Regional Gravity Modelling and Geohistory of the Parnaíba Basin (NE Brazil)

by

Mauro Andrade de Sousa

A thesis submitted for the degree of Doctor of Philosophy

Department of Physics
University of Newcastle upon Tyne

1996

I declare that no part of this work has previously been submitted for any degree at this, or any other, university.

Mauro Andrade de Sousa

Department of Physics
The University of Newcastle upon Tyne

TABLE OF CONTENTS

ABSTRACT

The Parnaíba Basin is one of the three large Palaeozoic intracratonic basins found in Brazil, the others being the Amazon and Paraná. Parnaíba is an oval-shaped basin situated in NE Brazil and its area is about 600.000 km^2.

Gravity data have been collected mainly along accessible roads crossing the Parnaíba Basin and merged with existing data bases of several Brazilian Institutions. The collection of all available geological and geophysical data included several gravity profiles crossing the eastern half of the basin. These profiles are part of a much larger data set forming polygons over a large proportion of the Brazilian territory. The whole gravity network has been internally adjusted and referred to the International Gravity Standardization Net 71. The net has been found precise to ± 0.041 mGal.

Although the distribution of gravity stations is not ideal, Bouguer and free-Air anomaly maps have been produced, these being the first gravity maps for the whole basin. Contrary to the basin physiography, the Bouguer map unexpectedly shows elongated gravity lows with NE-SW and NNW-SSE directions. These are parallel to the Transbrasiliano Lineament and subparallel to the Araguaia Fold Belt, respectively. A first attempt at interpreting the gravity anomalies resulted in the proposal of an anomalous, denser zone at lower crustal depths.

The tectonic subsidence in the basinal area was estimated through systematic backstripping using 22 boreholes which reached the metamorphic or sedimentary basement. A non-uniform lithospheric stretching model was used as a first approximation for the modelling of the tectonic regime. This procedure was suggested by the presence of several grabenlike structures, as confirmed by shallow seismic sections, exploratory boreholes and gravity maps.

Assuming an elastic rheology for the lithosphere, a regional W-E tectonic subsidence profile could be reproduced employing an axisymmetric subsurface load and a flexural ridigity of 0.2×10^{24} N m. Results of the present study are consistent with the apparent bimodality of the flexural ridigity of the continental lithosphere.

ACKNOWLEDGMENTS

I would like to thank Prof. R. W. Girdler and Dr. I. Wilkinson for many suggestions, criticisms and advice throughout the development of this project.

I am also indebted to, and would like to thank:

The Conselho Nacional de Desenvolvimento Científico e Tecnológico (CNPq) and Overseas Research Student (ORS Award) for financial assistance;

The Departamento de Geofísica of the Observatório Nacional in Rio de Janeiro for allowing me leave at the beginning and end of the project, for partial funding of fieldwork and continual support throughout this study;

The Department of Physics of the University of Newcastle upon Tyne for helping me to solve any problems I had while on leave in England;

PETROBRÁS, specifically Dr. Marco Polo B. Hora and Dr. Luis F. S. Braga for releasing the gravity and borehole data bases and to Francisco M. B. Cunha and Adson M. O. Góes for the release of an internal report on the Parnaíba Basin and for many useful discussions about the origin and evolution of intracratonic basins;

Dr. Naomi Ussami, Dr. Marcia C. L. Quintas and Dr. Duncan J. Hutt for many useful discussions, criticisms and help on different parts of this thesis; and

The millions of Brazilian taxpayers who allowed me free graduate and post-graduate studies.

Special thanks to Ms. Anne T. Codling for her invaluable support and friendship during the entire project and to Marilucia Quental and Diogo Quental for encouraging me in pursuing this research theme.

"The time has come", the Walrus said,
"To talk of many things"...

Lewis Carroll, *Through the Looking-Glass*

CHAPTER 1

INTRODUCTION

1.1 The Brazilian Intracratonic Basins

Most of the South American Platform was exposed at the end of the Ordovician (~440 Ma). Moderate subsidence in several sites began at about that time and by the end of the Silurian three major intracratonic basins had started being developed in Brazil, the *Amazon, Parnaíba and Paraná* (Fig. 1.1).

The margins of these intracratonic basins are defined by large marginal arches that started being formed in the Lower Silurian but were clearly defined only at the Lower Carboniferous. Thicknesses of 3,000 to 5,000 m of gently dipping sediments have been preserved in these basins (Fig. 1.1, schematic sections).

For all three basins there were three major periods of sedimentation: **i** ~445 to 410 Ma (Silurian); **ii** ~385 to 350 Ma (Devonian); **iii** ~310 to 235 Ma (Carboniferous-Triassic) and two less intense periods: **iv** ~180 to 155 Ma (Jurassic) and **v** ~120 to 100 Ma (Cretaceous). Regional variations in the sediment supply and tectonic regime allow for the differences in sedimentation rates. The Jurassic sequence, for instance, has not been found in the Amazon Basin. It must be stressed that important gaps that lasted for 20-40 Myr are also found in the stratigraphic record of these basins clearly indicating periods of non-deposition and/or erosion.

Interbasinal connection was still happening in the Palaeozoic during large marine transgressions. The Devonian was characterized in South America and, more specifically, in Brazil by the largest marine transgression ever. The Devonian sea allowed the three basins to be interconnected and palaeogeographic reconstruction maps have shown that Parnaíba and the Amazon Basins were interconnected through a large NW channel while a link to Paraná Basin was also established through a SW channel.

Structural arches delimiting the Parnaíba and Paraná Basins are usually associated with fold belts active during the Brasiliano Cycle (700-450 Ma) and these

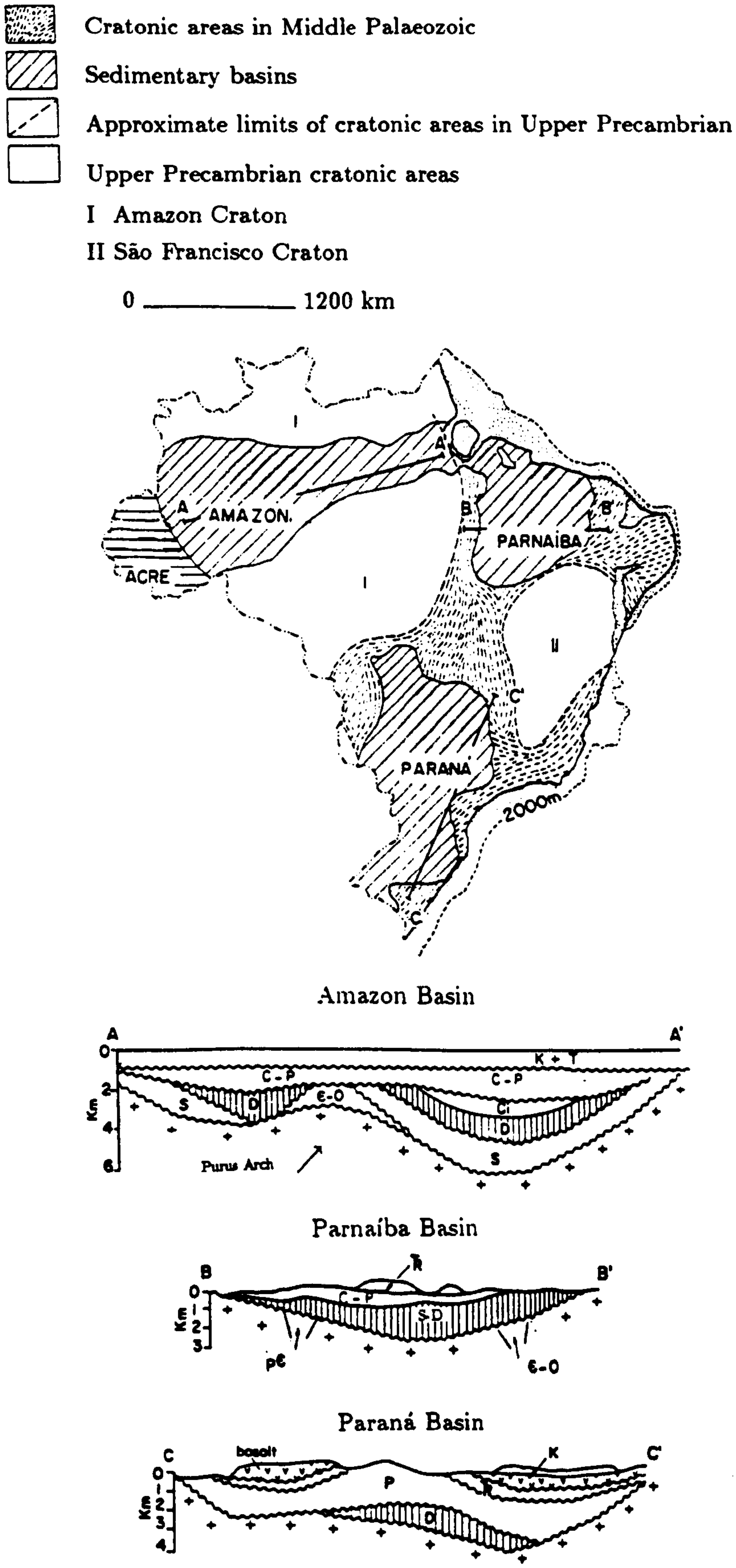

Fig. 1.1 Brazilian intracratonic basins (top) and schematic geological cross-sections (bottom). After Petri & Fúlfaro (1983).

Legend: T - Tertiary, K - Cretaceous, Ŧr - Triassic, P - Permian, C - Carboniferous, C_1 - Lower Carboniferous, D - Devonian, S - Silurian, O - Ordovician, ϵ-O - Cambro-Ordovician, ϵ - Cambrian, pϵ - Precambrian.

features suggest that these basins might have been in an embryonic phase at the end of Precambrian (~570 Ma).

The oldest dated sediments in these basins are Upper Ordovician-Lower Silurian with a marked marine character in the Devonian. Marine sediments are found in Parnaíba and the Amazon up to the Upper Carboniferous and up to Permian (~290 Ma) in the Paraná Basin. The basinal subsidence gradually declined after the Permian and, before these basins lost their individual characteristics, tectonic activity along the present-day coastline started in the Jurassic (~200 Ma), with the development of tectonic troughs and continental shelf sedimentation.

The main sedimentation scenario in Brazil after the Middle Cretaceous (~90 Ma) moved from the intracratonic basins to the coastal basins. The Cretaceous sediments had already transgressed the original basin boundaries, thus making the intracratonic basins lose their individualities.

The Phanerozoic geological history in Brazil is then mainly demarcated by five events:

1 The onset of large intracratonic basins in the Upper Ordovician-Lower Silurian;

2 A large marine transgression in the Devonian starting a thalassocratic phase in basinal development;

3 The disappearance of the large seas in the Carboniferous-Lower Permian bringing an end to the thalassocratic phase;

4 The development of coastal tectonic troughs in the Lower Jurassic; and

5 The loss of the intracratonic basin individualities in the Cretaceous.

1.2 The Development of Intracratonic Basins: Current Ideas

The study of sedimentary basins is important for both scientific and economic reasons. A geohistorical record of the tectonic, sedimentary and geochemical processes which have acted in a region for many millions of years is held in the accumulated sediment deposits. The use of the information held in these records help discriminate which basin-forming mechanisms were important during the whole development of a sedimentary basin. In particular, the initiation and evolution of intracratonic basins is still under debate.

Sedimentary basins are sites of prolonged and substantial subsidence on the continental or oceanic lithosphere. The location and evolution of sedimentary basins are intimately associated with the motion of the thin, relatively rigid lithospheric plates and are subject to complex stresses. These stresses are due to the fact that the lithospheric plates themselves are superimposed on a mantle slowly undergoing convection. Mantle convection is also the source of plate boundary forces which may be transferred considerable distances into the interior of plates.

Allen & Allen (1990) distinguish three main groups of sedimentary basins according to their origin. They are:

- basins due to *lithospheric stretching e.g.* the North Sea Basin and the Rhine Graben in Europe and the Rio Grande Rift in the United States;
- basins formed by *flexure of continental and oceanic lithosphere e.g.* the Appalachian Basin in the USA and Ganga Basin in India; and
- *strike-slip or megashear-related basins* caused by local stretching in complex fault zones *e.g.* Vienna Basin in Europe and Saint George Basin in the Bering Sea, Alaska.

These genetically different basins are the result of different basin-forming mechanisms. Some basins may be affected by more than one mechanism at different stages of their evolution. These *polyhistory* or *multicyclic* basins may show a rather complicated present-day scenario.

Subsidence models of intracratonic basins are still under debate. However, these basins have been observed (Bally & Snelson, 1980, Hartley & Allen, 1994) to quite often follow precursory troughs established on tectonically unstable zones of the Earth's crust. Once established, these weaknesses zones have a long-lasting, profound influence on the subsequent geological history of that particular area. This influence manifests itself as tectonic reactivations with or without magmatism. Structures formed by shear, compressional and extensional stresses are found in these zones, *e.g.* long normal faults regionally demarcating deep, ancient troughs.

Moreover, shear stresses may also involve some extension (*transtension*) or compression (*transpression*), further complicating the present-day basin scenario.

Several basin-forming mechanisms have been proposed to explain the creation and evolution of intracratonic basins. They fall into a number of categories not always mutually exclusive (modified after Hartley & Allen, 1994):

1 *Lithospheric stretching and thermal contraction.*

1.1 Rifting associated with a thermal plume *e.g.* McGinnis *et al.* (1976);

1.2 Thermal contraction following rifting *e.g.* Lindsay & Korsch (1989) and Nunn (1994);

2 *Crustal and mantle phase changes, metamorphism and intrusion.*

2.1 Phase changes and thermal metamorphism *e.g.* Haxby *et al.* (1976); Middleton (1980) and Hamdani *et al.* (1991);

2.2 Isostatically uncompensated excess mass in crust due to igneous intrusions *e.g.* De Rito *et al.* (1983) and Kolata & Nelson (1991);

2.3 Anorogenic granite emplacement associated with supercontinent break-up *e.g.* Klein & Hsui (1987) and Klein (1991);

3 *Changes in in-plane stress and tectonic rejuvenation.*

3.1 Changes of in-plane stress in an elastic or viscoelastic plate *e.g.* Karner (1986);

3.2 Tectonic rejuvenation of older structures *e.g.* De Brito Neves *et al.* (1984);

4 *Convective instabilities.* Development of mantle downwellings as convective boundary layer instabilities *e.g.* Middleton (1989); and

5 *Subaerial erosion.* Erosion over thermal uplift followed by sediment loading *e.g.* Sleep & Snell (1976).

All basin-forming mechanisms should be considered as *primary* in the sense that they initiate the local subsidence process. Water and sediment loading further amplifies the original tectonically-driven subsidence.

Finally, it must be said that although explanations about the origin and development of intracratonic basins are still controversial, the times of initiation of these basins and Palaeozoic passive margins are often coeval with the break-up of a late Precambrian supercontinent.

Systematic synchronous changes in sediment volume which characterize several Palaeozoic intracratonic basins have been observed not only in Brazil (Cunha, 1986; Raja Gabaglia & Milani 1990; Góes & Feijó, 1994; Quintas, 1995) but also in North America, the Russian Platform and North Africa (Sloss, 1972; Klein & Hsui, 1987).

The best-documented ancient intracratonic basins are those of the North-American Craton (Michigan, Illinois and Williston Basins) associated with the break-up of the Laurentian continental assembly in the Lower Palaeozoic (~530 Ma). These different observations suggest a commonality of intracratonic basin formation in time and space in response to global processes.

1.3 Aims of This Study

The study of sedimentary basins like Parnaíba is useful for the understanding of the thermo-mechanical evolution of the continental lithosphere and for defining viable exploration sites for minerals and energy resources.

The absence of regional geophysical models to describe the origin and evolution of the Parnaíba Basin led to the use of gravity and exploration well data as a first attempt to produce a coherent regional structural model. The joint use of gravity and exploratory borehole information help discriminate weakness zones associated with sources of extensional tectonics affecting the Parnaíba Basin.

There are no deep seismic lines across the Parnaíba Basin and shallow reflection lines have not been released by the Brazilian government owned company Petróleo Brasileiro S. A. - PETROBRÁS (oil and gas exploration). Some details about the Parnaíba Basin and surrounding geology are given in Chapter 2.

Gravity anomalies over sedimentary basins can be used to constrain depths, positions and sizes of loads that cause lithospheric flexure. These anomalies are due to:

- low-density sedimentary rocks infilling the basin;
- the driving load; and
- variations in depth to the crust/mantle (Moho) boundary.

A crucial phase of this study was preparing a homogeneous gravity data set for geophysical interpretation. The usefulness of selected mathematical algorithms capable of making a sub-set of the gravity data set consistent with modern sources of *datum* and scale (the IGSN 71 or the Absolute Gravity Stations) is shown in Chapter 3.

The basin geometry enables the use of axisymmetric 2.5D modelling which explores this geometry in the interpretation of gravity anomalies and the deduction of the regional basinal structure. The interpretation of the regional, resultant and residual gravity anomalies is presented in Chapter 4. A deep crustal model compatible with the isostatic condition of Parnaíba is proposed and is followed by a discussion of the effects of the Mesozoic magmatism.

A helpful tool in assessing the evolution of sedimentary basins is the use of their chrono-lithostratigraphic records. The application of the backstripping technique allows estimating the "true" tectonic subsidence from the observed, sediment-amplified basement subsidence. Also, lithospheric stretching models have been proposed for basins undergoing extensional tectonics with variable success in matching the deduced tectonic subsidence.

This is the first time that the backstripping technique has been systematically applied to oil and gas exploratory boreholes that reached the basement of the Parnaíba Basin. The information gathered allows the thermo-mechanical modelling of the computed tectonic subsidence, under the frames of uniform/non-uniform lithospheric stretching. It is anticipated, however, that the lack of detailed chrono-lithostratigraphic data and density logs for all wells in the basin introduce a fair degree of uncertainty on the results found. Erosional gaps also constitute a serious problem in the validity of final results.

The tectonic subsidence found poses the problem of lithospheric loading. Since the observed total subsidence has already been corrected for sedimentary loading, a driving load should be responsible for the computed tectonic subsidence. Again, the basin geometry allows the use of an axisymmetric loading model; thus an assessment of the lithospheric flexural ridigity or, equivalently, the lithospheric elastic thickness beneath Parnaíba can be made. These results are presented in Chapter 5.

Final conclusions are summarized in Chapter 6. Listings of selected computer programs used in this study can be found in the Appendix.

CHAPTER 2

THE PARNAÍBA BASIN

2.1 Geological Setting

The Parnaíba Basin is situated in northeast Brazil. It is roughly ellipsoidal in shape and covers an area of approximately 600,000 km^2. The basin has been named after the long river of the same name running approximately parallel to the major axis of the basin (Fig. 2.1a). The geological setting of Parnaíba Basin and its surrounding provinces is also shown in Fig. 2.1a. This is from the 1995 tectono-geological map of Brazil compiled by the Brazilian government owned Companhia de Pesquisa de Recursos Minerais (Company for Research on Mineral Resources)-CPRM. A bilingual (Portuguese/English) key to this map is found in Fig 2.1b on the following page. Note the progressive outcrop of older beds away from the coast line with Cenozoic sediments onlapping Mesozoic and the latter eventually onlapping Palaeozoic. The basin covers entirely two NE Brazilian states (Piauí-PI and Maranhão-MA) and parts of the adjacent states of Pará-PA, Tocantins-TO e Ceará-CE.

The intracratonic Parnaíba Basin is bounded by fold belts and structural arches. These belts are made of low to high-grade metasediments formed or reworked during the Brasiliano Cycle (700-450 Ma). Referring to Fig. 2.2, to the north, the smaller coastal Barreirinhas (A) and São Luis (D) Basins are separated from Parnaíba by the Ferrer (C) and Urbano Santos (B) Arches. To the northwest it is separated from the neighbouring Marajó Basin (F) by the Tocantins Arch (E). To the west it is separated from the Amazon Craton by the Araguaia Fold Belt (G). To the south it is separated from the São Francisco (I) and Lençóis (K) Basins by the basement high known as the Middle São Francisco Arch (J). Mesozoic sediments on the Mangabeiras Plateau obscure the exact contact between the Parnaíba and the São Francisco Basins. The Precambrian Borborema Province (L) demarcates the eastern border of the Parnaíba Basin.

The Parnaíba Basin is mainly Palaeozoic in age and filled with siliciclastics of mostly continental origin deposited in five great depositional cycles from Upper

Fig. 2.1a Tectono-geological map of the Parnaíba Basin and adjacent provinces. Note the decrease in basin width with time. Source: CPRM (1995) - Polyconic projection.

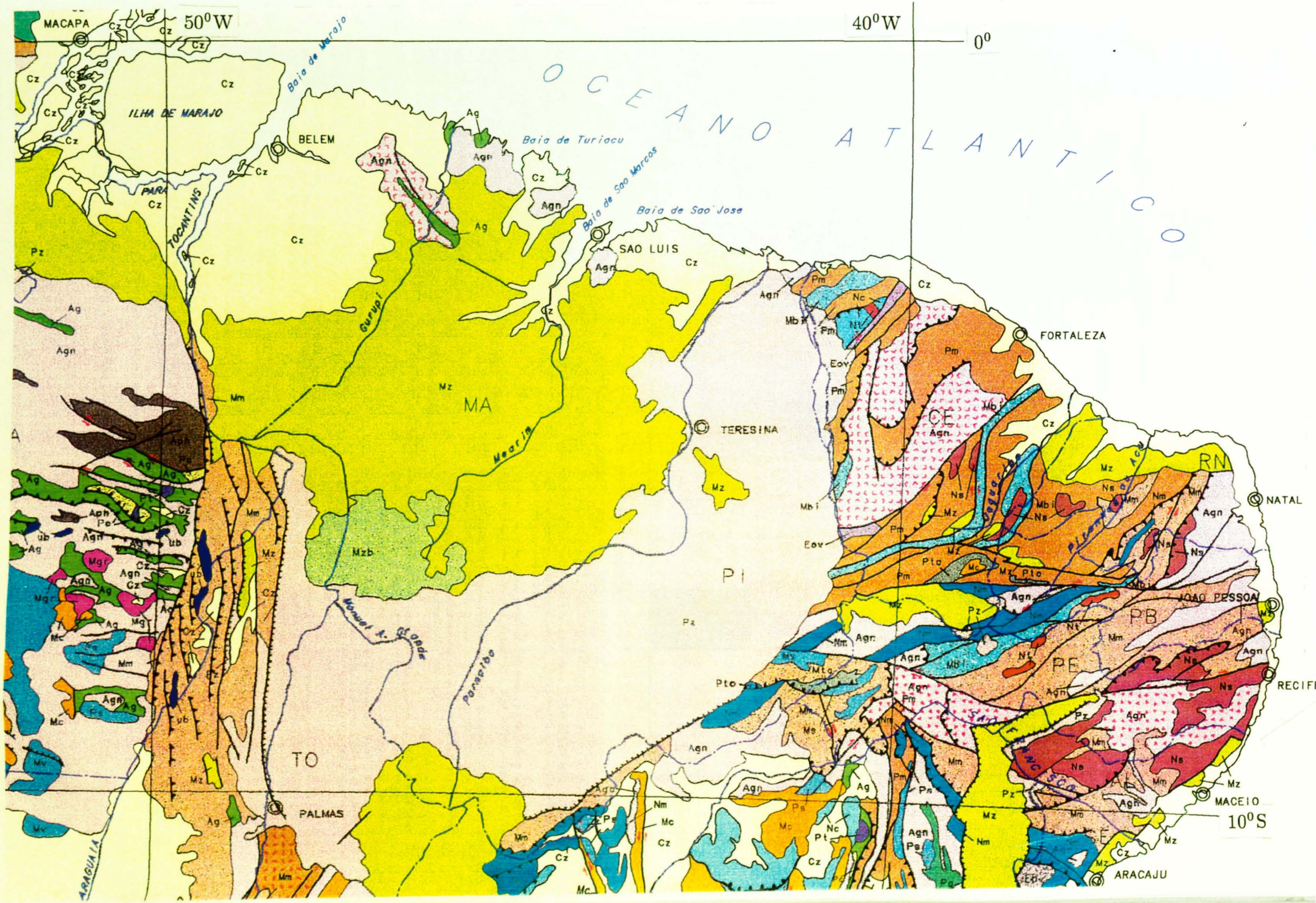

50°W
40°W
0°
10°S
OCEANO ATLANTICO
MACAPA
ILHA DE MARAJO
Baia de Marajo
BELEM
Baia de Turiacu
Baia de Sao Marcos
Baia de Sao Jose
SAO LUIS
FORTALEZA
TERESINA
NATAL
JOAO PESSOA
RECIFE
MACEIO
ARACAJU
PALMAS
MA
PI
CE
RN
PB
PE
AL
TO
PARA
TOCANTINS
Gurupi
Mearim
Parnaiba
ARAGUAIA
SAO FRANCISCO
Cz
Mz
Mzb
Pz
Agn
Ag
Aph
Mm
Pm
Ns
Nm
Nt
Nc
Mbi
Eov
Pto
Mc
Mv
Mgr
ub
Ps
Pt

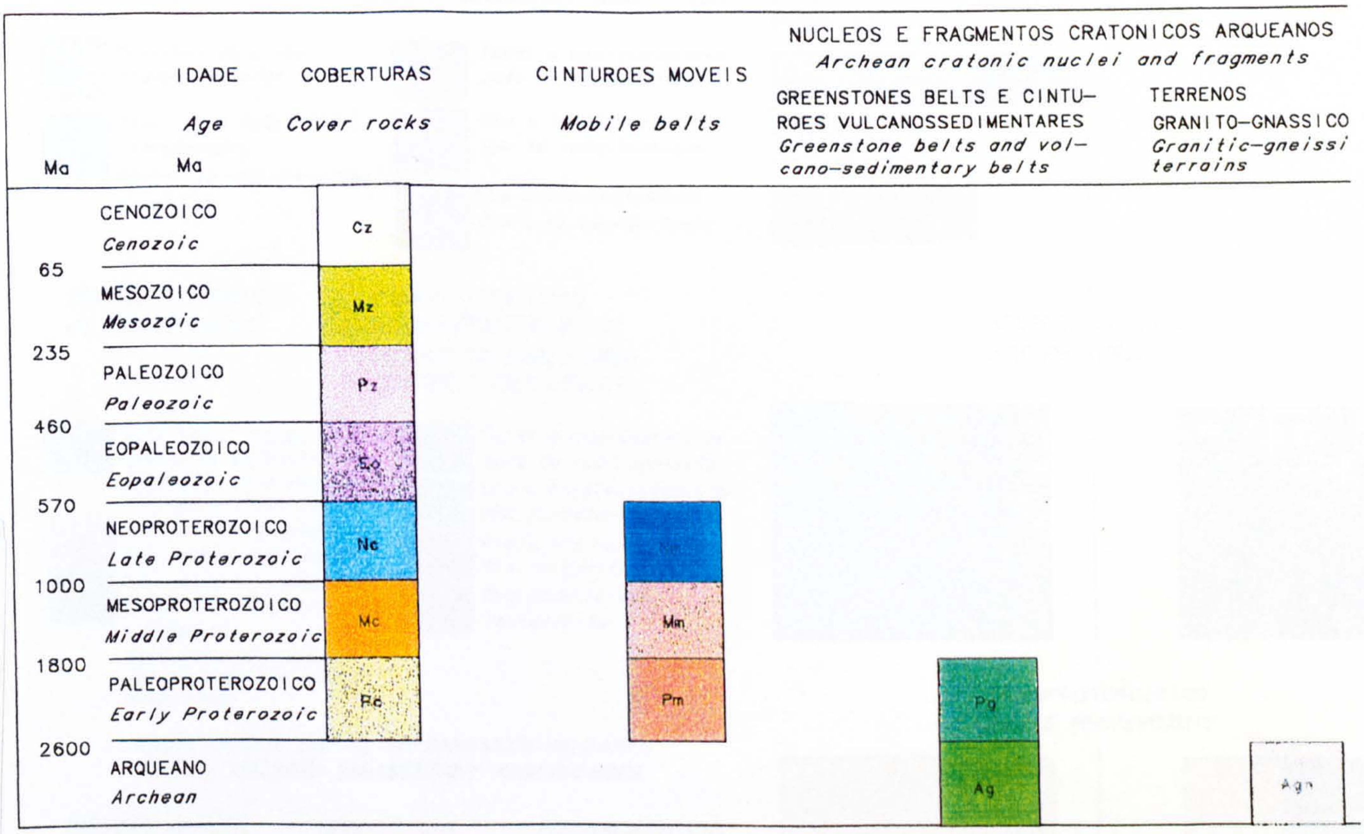

PRINCIPAIS ASSOCIAÇOES LITOLOGICAS
PRINCIPAL ROCK TYPES

Cz Sedimentos terrigenos, aluvioes e rochas lateriticas
Terrigenous sediments, alluvium and laterite

Mz Sequencia essencialmente terrigena (arenito, siltito, argilito), calcario e gipsita
Mostly terrigenous sequence (sandstone, siltstone, shale), limestone and gypsum

Pz Sequencia essencialmente terrigena (arenito, siltito, folhelho, diamictito), calcario e evaporitos
Mostly terrigenous sequence (sandstone, siltstone, shale, diamictite), limestone and evaporite

Eo Conglomerado, arenito e folhelho ('red beds')
Conglomerate, sandstone and shale (red beds)

Nc Sequencia pelito-carbonatica (calcario, dolomito, marga e folhelho), diamictito e arenito, localmente deformados e metamorfisados ('sub greenschist')
Pelitic-carbonate sequence (dolomite, limestone, marl and shale) diamictite and sandstone, locally deformed and metamorphosed (lower greenschist)

Mc Sequencia arenitica com conglomerados e folhelho, localmente deformada e metamorficada('sub greenschist')
Sequence of sandstone with conglomerate and shale, locally deformed and metamorphosed (lower greenschist)

Pc Sequencia filitica-metarenitica (incluindo xisto, metadolomito, magnesita e formacao ferrifera bandada)
Sequence of phyllite and metasandstone (including schist, metadolomite, magnesite and banded iron formation)

Nm Sequencia filitica-metacalcaria (incluindo xisto, metarenito e metadiamictito)
Sequence of phyllite and metalimestone (including schist, metasandstone and metadiamictite)

Mm Associacao de xistos e gnaisses (incluindo quartzito, metacalcario, metagrauvaca, anfibolito e rochas metamafico-ultramaficas)
Schist and gneiss (including quartzite, marble, metagra wacke, amphibolite and metabasic and metaultrabasic rock

Pm Associaçao de gnaisses, migmatito e granulito (incluind quartzito, rocha calcissilicatica e metabasica)
Gneiss, Migmatite and granulite (including quartzite, calcsilicate and metabasic rocks)

Pg,Ag Associaçoes metavulcanossedimentares tipo 'greenstone belt' (vulcanismo mafico-toleiitico / komatiitico e felsico-calcialcalino sucedido por sedimentos imaturos) e tipo rifte (vulcanismo bimodal associado com sedimentos clastoquimicos que transicionam para sedimentos pelito-psamiticos), metamorfisadas nas facies xisto verde e anfibolito
Meta-volcano-sedimentary greenstone belt-type rocks (mafic-tholeiitic / komatiitic and felsic-calcalkaline vol nism followed by immature sedimentary rocks) and rift- chemical sedimentary units, i.e. BIF, chert, that grade upward into shale and sandstone); metamorphosed greenschist and amphibolite facies

Agn Ortognaisses (sodicos e potassicos), migmatito e granulito (incluindo metabasicas, anfibolito e reliquias de rochas supracrustais)
Orthogneiss (sodic-and potassic-rich), migmatite and g nulite (including metabasic rocks, amphibolite, and re lics of supracustal rocks)

Fig. 2.1b Key for the tectono-geological map. Source: CPRM (1995).

Fig. 2.1b (cont.) Key for the tectono-geological map. Source: CPRM (1995).

ROCHAS IGNEAS E META-IGNEAS
IGNEOUS AND META-IGNEOUS ROCKS

ANOROGENICAS
ANOROGENIC

Regime Extensional
Extensional Regime

ROCHAS VULCANICAS
VOLCANIC ROCKS

Mzb — Basaltos de plato
Plateau basalts

Mv — Riolitos e andesitos plataformais
Rhyolites and andesites platforms

ROCHAS PLUTONICAS
PLUTONIC ROCKS

Mza — Alcalinas, subsaturadas, incluindo carbonatitos
Alkaline, undersaturated including carbonatites

Mgr — Granitoides anorogenicos
Anorogenic granitoids

Basicas e ultrabasicas (complexos estratiformes e zonados)
Basics to ultrabasics (stratiform and zoned complexes)

OROGENICAS
OROGENIC

Regime Compressional
Compressional Regime

GRANITOIDES NEOPROTEROZOICOS
LATE PROTEROZOIC GRANITOIDS

Nt — Tardi a pos-tectonicos
Late to post-tectonic

Ns — Sin a tardi-tectonicos
Syn to late-tectonic

Np — Pre a sin-tectonicos
Pre a to syn-tectonic

GRANITOIDES MESO A PALEOPROTEROZOICO
MIDDLE TO EARLY PROTEROZOIC GRANITOIDS

Mt / Pt — Tardi a pos-tectonicos
Late to post-tectonic

Ms / Ps — Sin a tardi-tectonicos
Syn to late-tectonic

Pp — Pre a sin-tectonicos
Pre to syn-tectonic

Aph — Charnockitoides
Charnockite

ASSOCIACOES (META) VULCANOSSEDIMENTARES
(META) VOLCANO-SEDIMENTARY ASSEMBLAGES

PRE-OROGENICAS
PRE-OROGENIC

Mbi — Bimodal, tipo rifte
Bimodal, rift type

Toleiitica, tipo Morb
Tholeiitic, Morb-type

OROGENICAS
OROGENIC

Nca / Mca / Pta — Calcialcalina, tipo arco
Calcalkaline, arc-type

Mta / Pca — Toleiitica, tipo arco de ilha
Tholeiitic, island arc-type

POS-OROGENICAS
POST-OROGENIC

Eov — Rochas acidas a intermediarias, alcalinas, vulcanicas e subvulcanicas, em bacias tipo 'pull-apart'
Acid to intermediate alkaline volcanic and subvolcanic rocks (in pull-apart basins)

SIMBOLOS ESTRUTURAIS
STRUCTURAL SYMBOLS

Contato
Contact

Falha
Fault

Falha de empurrao
Thrust fault

Falha normal
Normal fault

Falha transcorrente
Strike-slip fault

ZONAS DE RETRABALHAMENTO E SUPERPOSICAO DE EVENTOS TECTONICOS
REACTIVATED TECTONIC ZONES/OVERPRINTING OF TECTONIC EVENTS

Evento tectonico Brasiliano
Brasiliano tectonic event

Evento tectonico Uruaçuano
Uruaçuano tectonic event

Evento tectonico Transamazonico
Transamazonico tectonic event

CORRELACOES ENTRE UNIDADES
CORRELATION OF MAP UNITS

COBERTURAS E ROCHAS IGNEAS ANOROGENICAS
ANOROGENIC IGNEOUS AND COVER ROCKS

CINTUROES MOVEIS E ROCHAS IGNEAS OROGENICAS
OROGENIC IGNEOUS ROCKS AND MOBILE BELTS

MESOZOICO
MESOZOIC

EOPALEOZOICO
EOPALEOZOIC

NEOPROTEROZOICO
LATE PROTEROZOIC

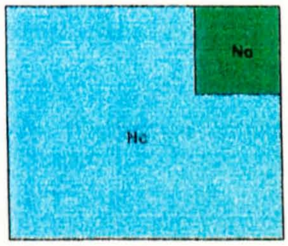

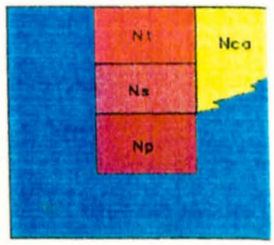

MESOPROTEROZOICO
MIDDLE PROTEROZOIC

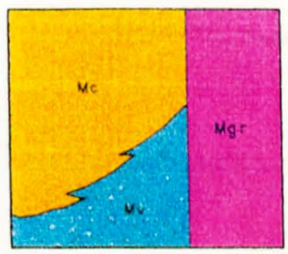

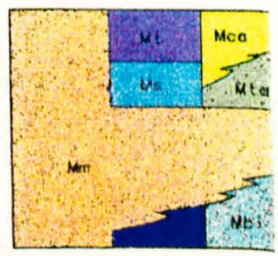

ARQUEANO A PALEOPROTEROZOICO
ARCHEAN TO EARLY PROTEROZOIC

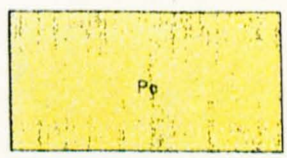

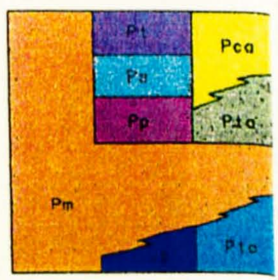

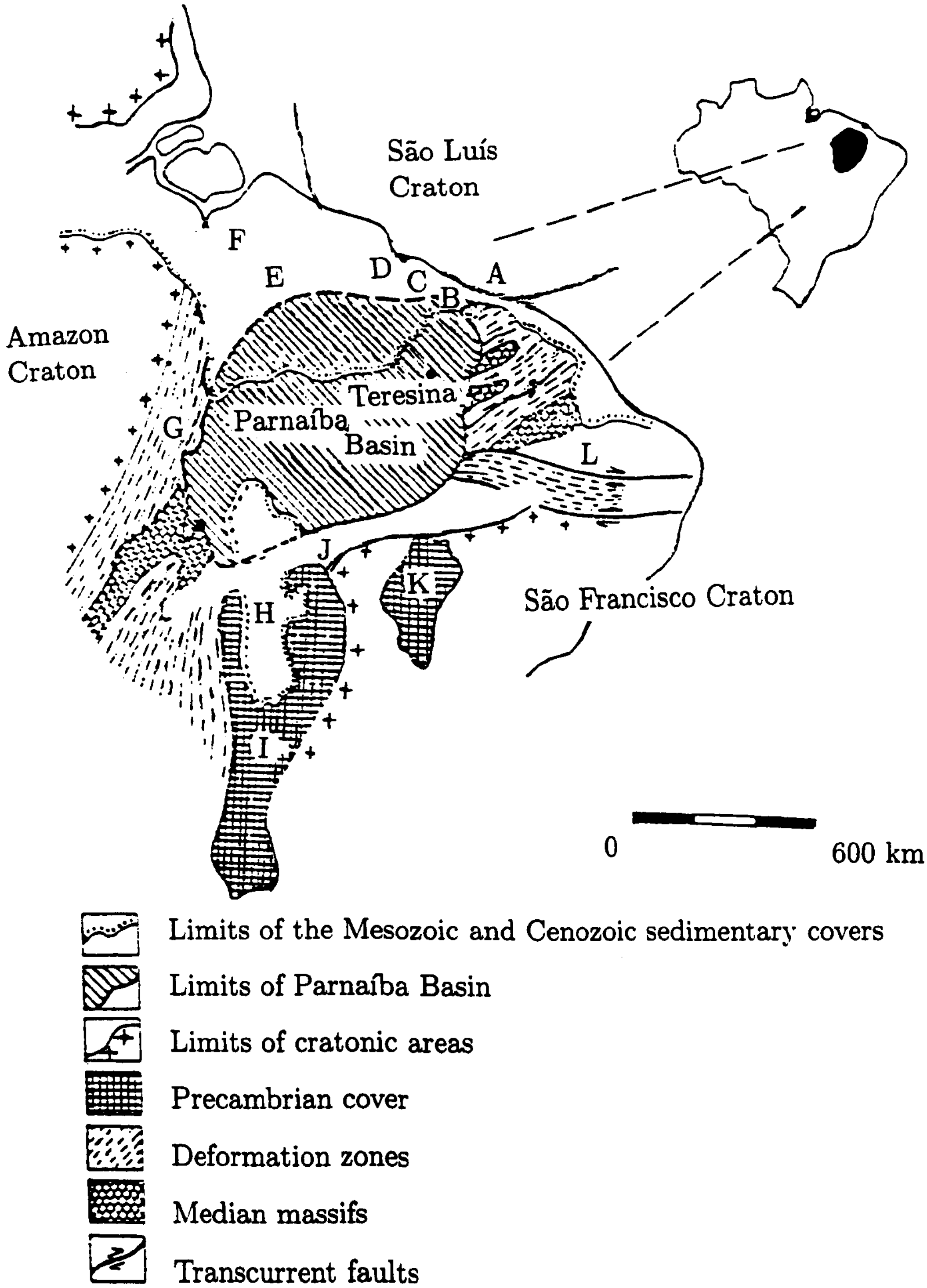

Fig. 2.2 Tectonic and structural setting of the Parnaíba Basin (after Cunha, 1986 and Góes *et al.*, 1993).

Ordovician to the Cretaceous. Regional uncomformities due to slow epeirogenic crustal movements have been recognized and the sedimentary cover has been intruded by volcanic rocks of Lower Jurassic and Lower Cretaceous ages. Palaeozoic sediments reach up to 2,900 m and are mainly sandstones with subordinate siltstones and shales. These rocks define broad and regionally distributed lithostratigraphic units with small facies variations. Carbonate beds and evaporites (gypsum and anhydrite) of Upper Carboniferous and Permian ages are sometimes found, indicating marine transgressions in a hot, arid environment. Mesozoic and Cenozoic sediments do not exceed about 600 m and are of lesser importance than in the neighbouring Barreirinhas Basin to the north, where they reach up to 9,000 metres.

A great number of geological similarities has been found between the northeast coast of Brazil and the west coast of Africa (Fig. 2.3). The analysis of tectonic style, metamorphism, geochronology, palaeontology and gravity anomalies indicates several correlations among large crustal blocks (Torquato & Cordani, 1981; Lesquer *et al.*, 1984). Figure 2.3 (Cunha, 1986) shows the relative position of tectonic units in Occidental Gondwana at the end of the Brasiliano/Pan-African Cycle. Evidence supporting this proposal is given by **i** the Palaeozoic sediments found to the south of Accra; **ii** the immature clastics found to the north of Accra and their close resemblance to their northeast Brazilian counterparts and **iii** the similar thermo-tectonic history of the Dahomeids (Africa) and Gurupí (Brazil) Fold Belts. Cunha (1986) has proposed that a precursory subsidence region might have existed in the region along the Transbrasiliano Lineament in Brazil and the Benin-Hoggar Lineament in Africa.

About 27% of the Parnaíba Basin has been mapped in detail and a general geological map including the structural arches is presented in Fig. 2.4. The Tocantins Arch has been interpreted as the result of uplifting and intense erosion (down to Permian rocks) from the Upper Jurassic (Malm, ~150 Ma) to Middle Cretaceous (Aptian, ~120 Ma). Likewise, the Ferrer and Urbano Santos Arches have been positioned in the Lower Cretaceous (Neocomian, ~135 Ma) as a result of the Gondwana rupturing and the opening of the Equatorial Atlantic Ocean. The presence of smaller deformational (transpressive) structures close to these arches have also been found in a few seismic sections.

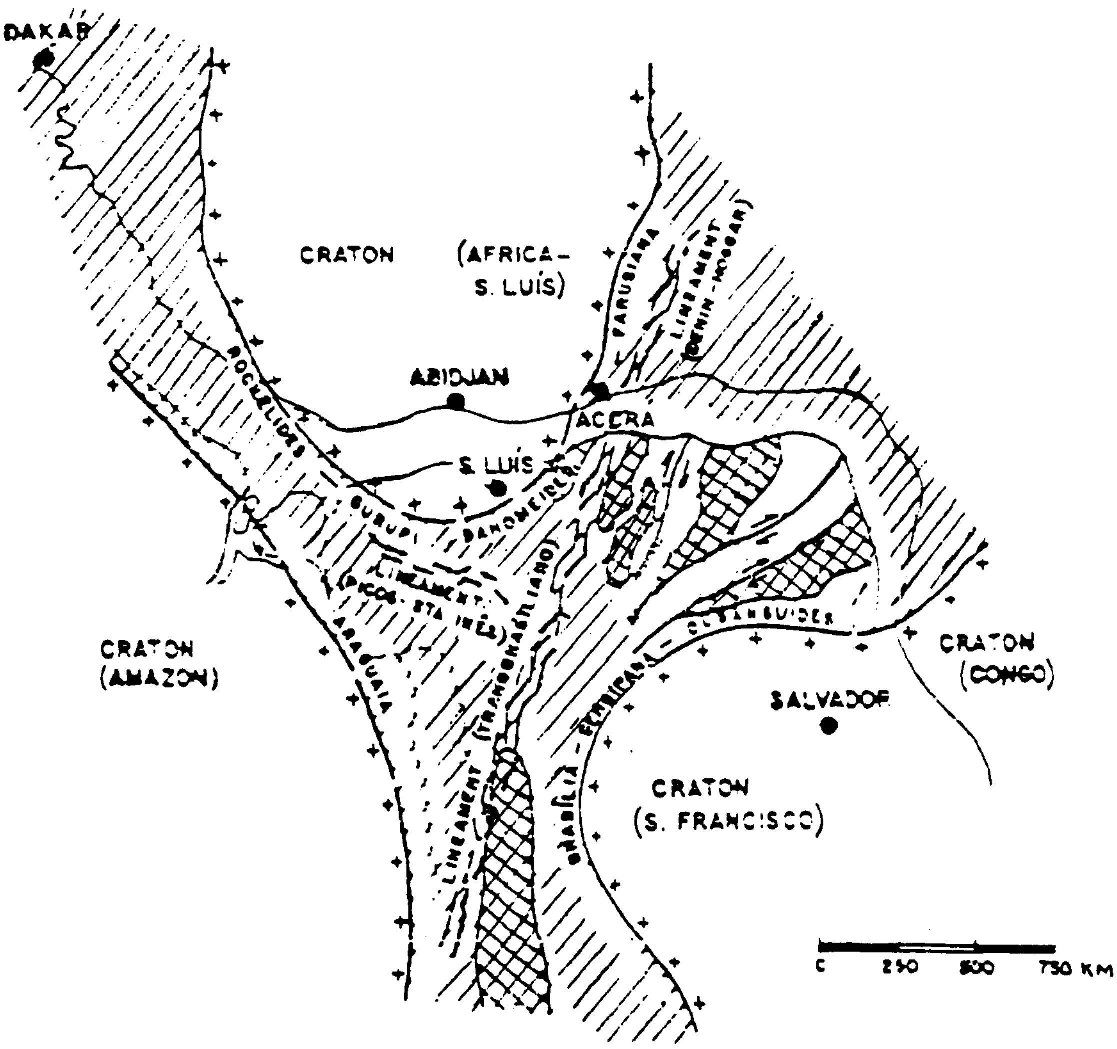

Metasediments formed and/or metamorphosed during the Brasiliano/Pan-African cycle

Median massifs

Transcurrent faults

Cataclastic belts

Fig. 2.3 Tectono-structural units in Occidental Gondwana reconstructed for the end of the Brasiliano/Pan-African Cycle. No Precambrian sedimentary covers are shown (after Cunha, 1986).

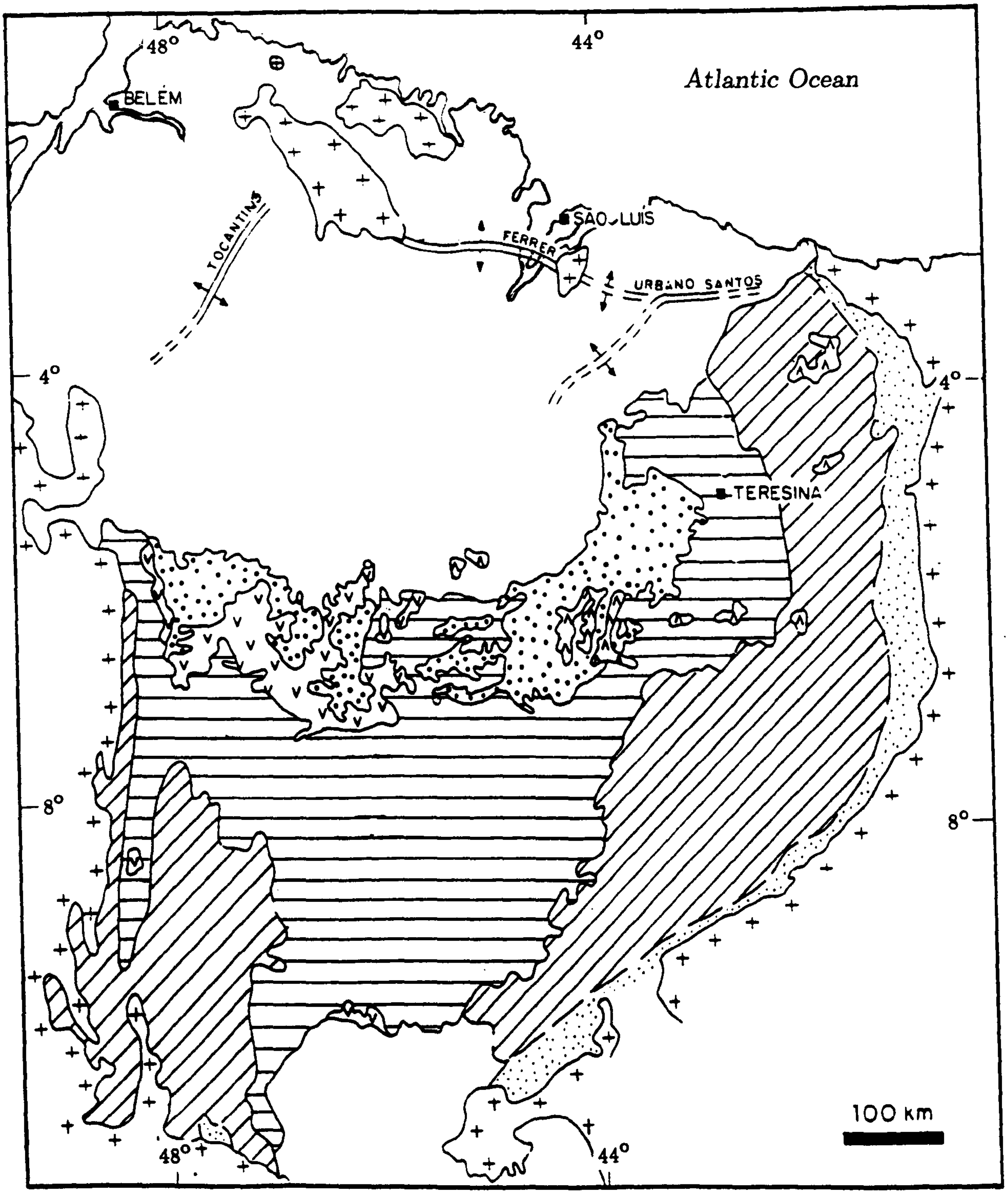

Itapecuru/Codó Fms. (*Cretaceous*)
Sardinha Fm. (*Lower Cretaceous basalts*)
Mearim Group (*Jurassic*)
Mosquito Fm. (*Lower Jurassic basalts*)
Balsas Group (*Carboniferous-Triassic*)
Canindé Group (*Devonian*)
Serra Grande Group (*Silurian*)
Basement

←||→ Arch (basement high)

Fig. 2.4 Schematic geological map of the Parnaíba Basin showing the depositional sequences and volcanic extrusives (after Góes et al., 1993).

2.2 Surface Structural Features

Surface structural features (Fig. 2.5) mapped so far show that the most important structural directions are NE and NNW (see rose diagram). The most frequent structural features are basinal fractures, especially in the east of Parnaíba which is locally highly fractured. Normal faulting prevails throughout the basin and the most important faults are 50-100 km in length, with a few (*e.g.* Bote and Meios Faults) extending to 110 km on the western and south-western borders. Fault throws are usually less than 50 m but occasionally 150 metres. Reverse faulting is less common and has been identified mostly southwest of Parnaíba.

The Parnaíba Basin shows some asymmetry with dip angles in the southern and southeastern borders being steeper than those in the northwest (Cunha, 1986). Dips in the basin are usually quite low, typically 3-4°. Folding is not a frequent structural feature and most of the folds observed in the geological mapping have been associated with sedimentary layers being disturbed by igneous bodies.

Regional faults and lineament traces have been recognized in the field and by using remote sensing tools. Radar images and TM-Landsat mosaics (black & white, bands 3 and 4, scale: 1:500,000) have been used to characterize basement-related structures. The interpretation of these images is found in an internal (unreleased) PETROBRÁS report: Cunha & Góes (1989).

A major tectonic feature that affected the development of the Parnaíba Basin is the NE-SW Transbrasiliano Lineament which is clearly seen on the aeromagnetic map shown in Fig. 2.6. This 75-100 km wide lineament extends through Brazil, Paraguay and Argentina in the NE-SW direction for about 2,700 km (Schobbenhaus, 1984). The morphostructural evidence of the Transbrasiliano Lineament in the Parnaíba Basin interior is given mainly by NE-SW faults cutting through Palaeozoic and Mesozoic sections and by Cretaceous diabase dykes in the same direction. This lineament is a complexly faulted shear zone including structural highs and grabens that possibly initiated in the Middle-Upper Proterozoic (Marini, 1984) and have been intermittently reactivated. Hasui *et al.* (1984) showed evidence of transcurrent dislocations that affected this complex faulting pattern during the Uruaçuano Cycle (1.3-1.0 Ga) and vertical reactivations at the end of the Brasiliano Cycle (700-450 Ma). Evidence of transcurrent syn-Brasiliano

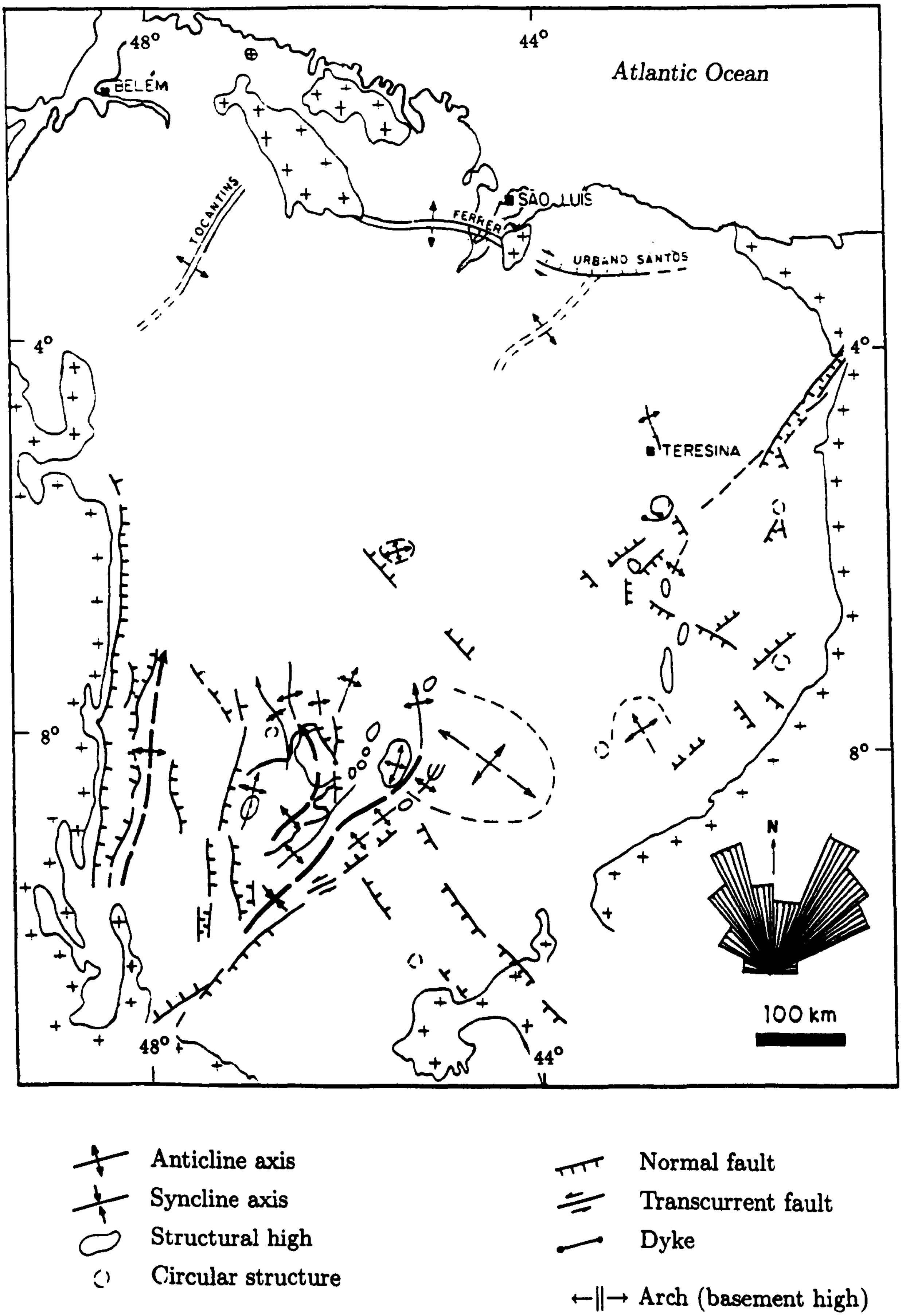

Fig. 2.5 Parnaíba Basin: surface structures features (after Góes *et al.*, 1993).

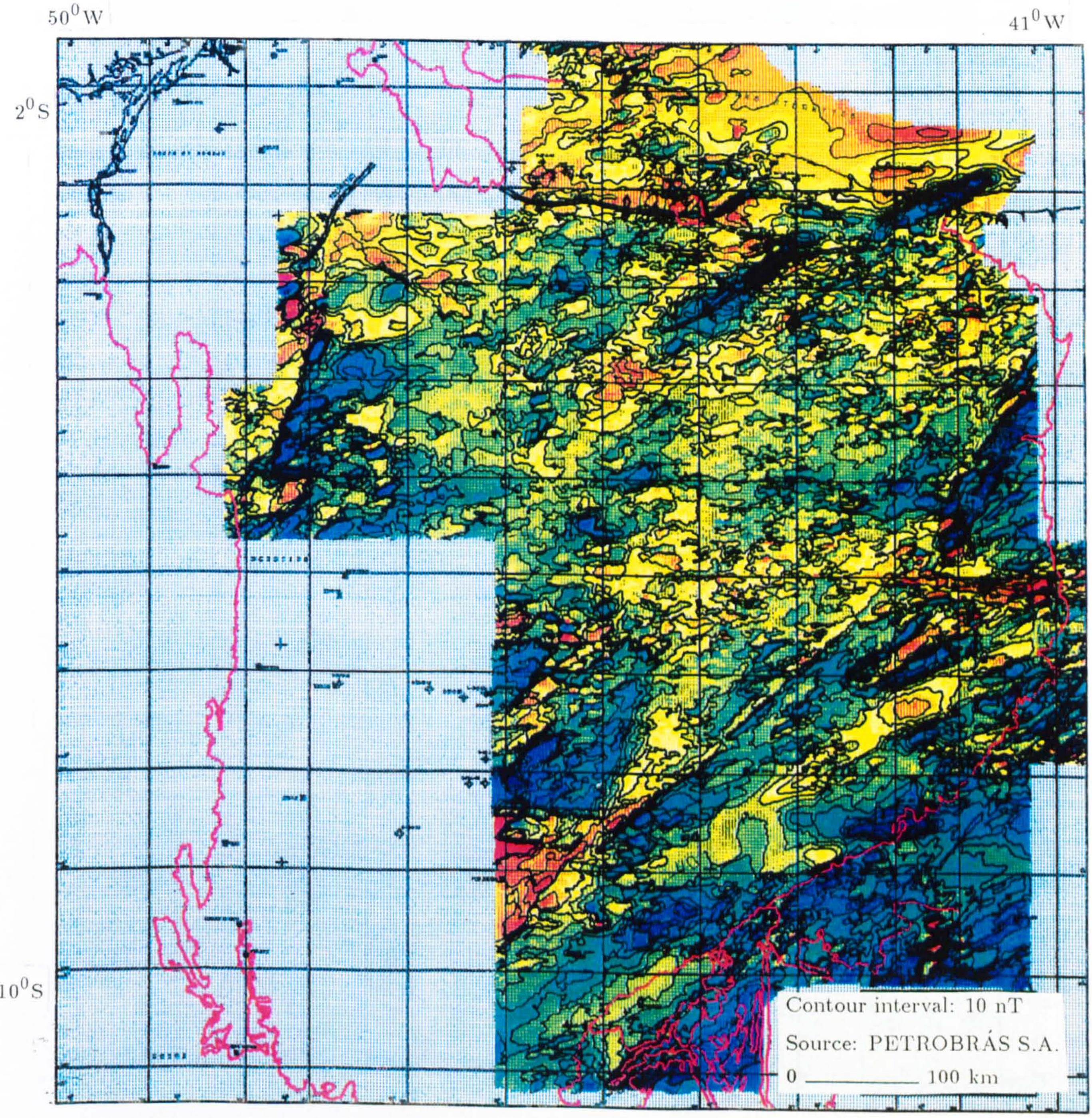

Fig. 2.6 Aeromagnetic map of the Parnaíba Basin (total intensity in nT). The continuous red line is the erosional basin boundary and the scattered crosses are borehole sites (after Góes *et al.*, 1993).

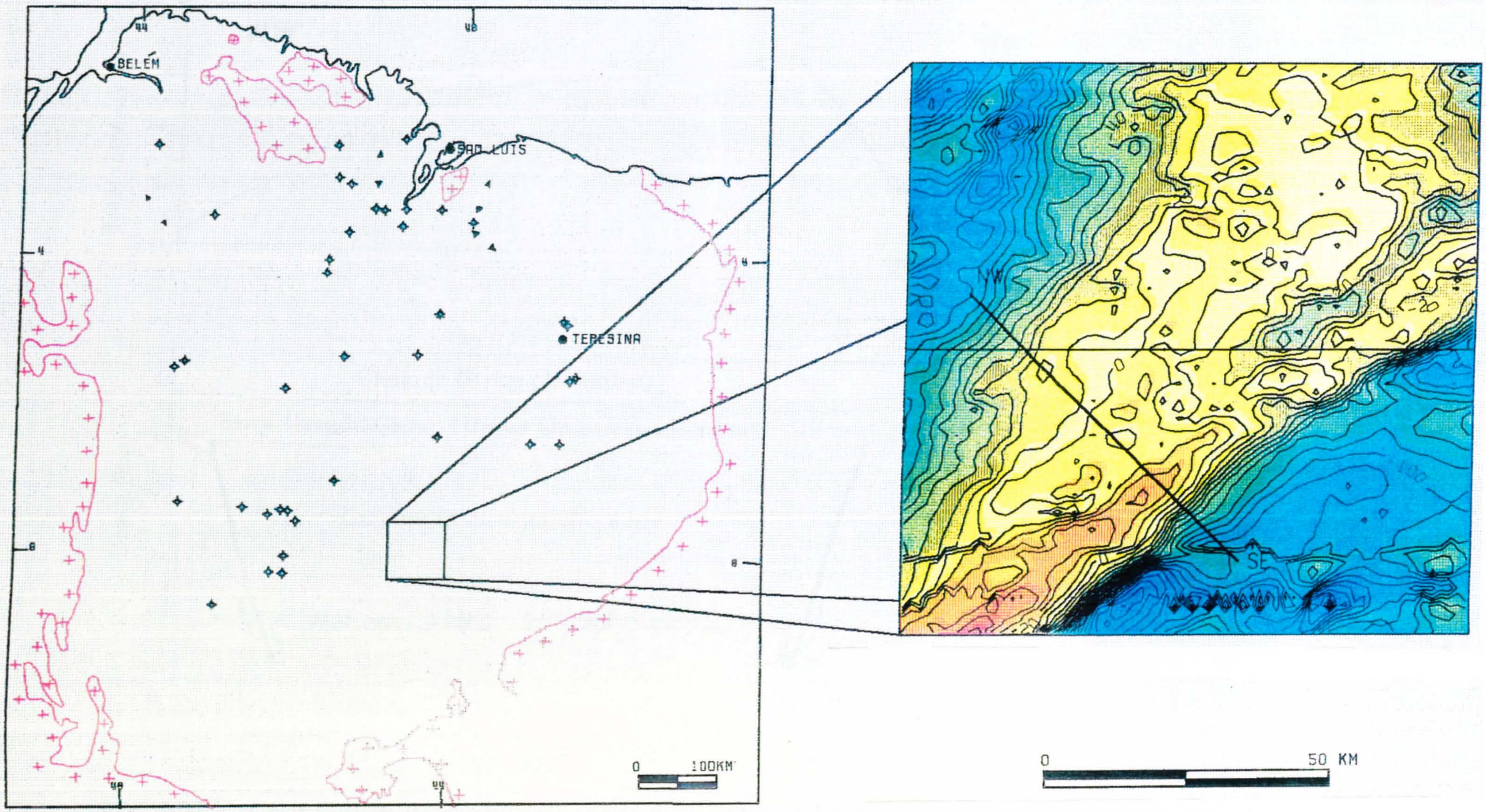

Fig. 2.7a Isolated magnetic anomaly on the Transbrasiliano Lineament (after Góes *et al.*, 1993).

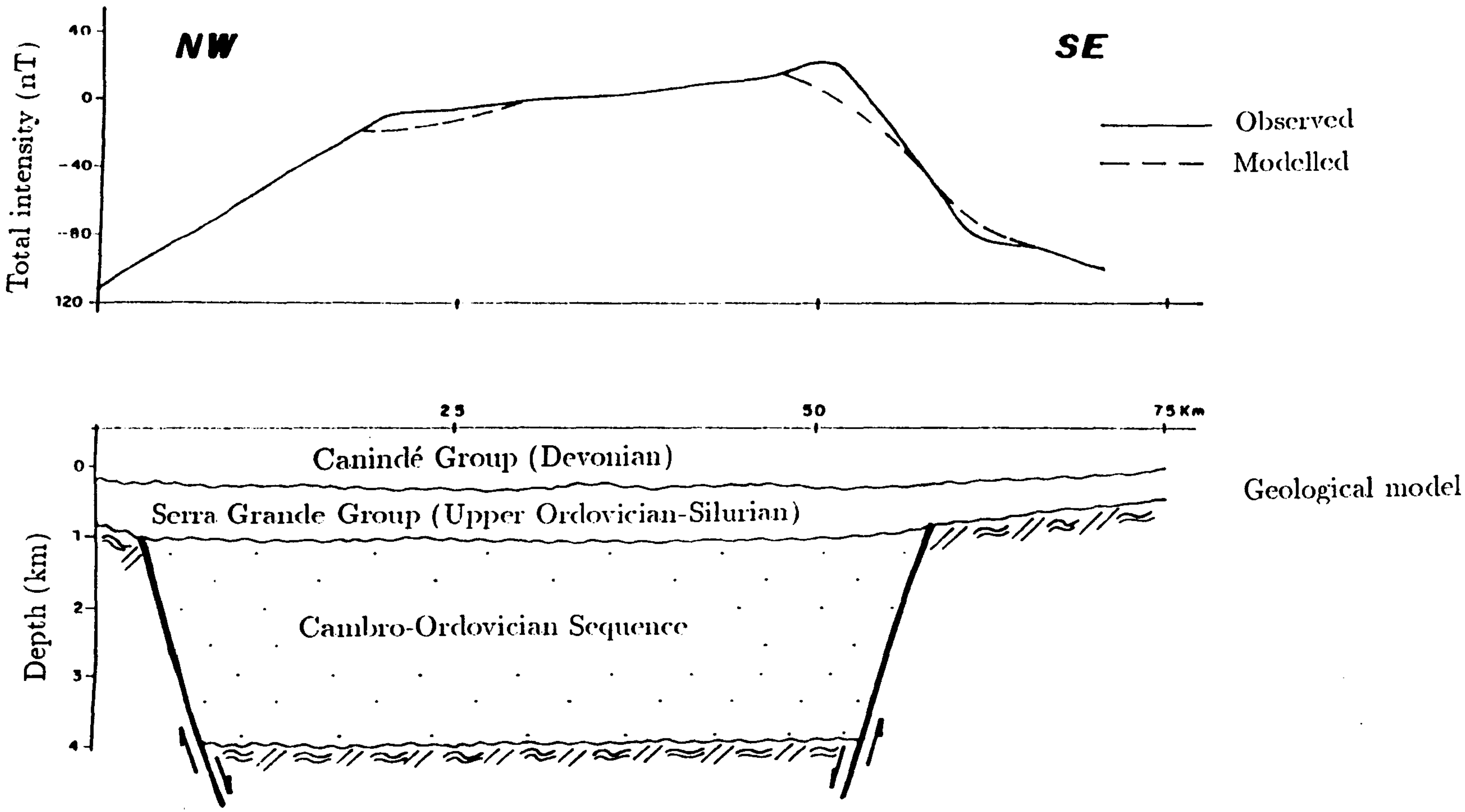

Fig. 2.7b Geological model for the isolated anomaly. Magnetic susceptibility contrast: 0.002 6 emu (after Góes *et al.*, 1993).

dislocations was recently presented by Fortes (1990, 1992). An isolated magnetic anomaly on the Transbrasiliano Lineament is shown in Fig. 2.7a and the geological model proposed by Góes *et al.* (1993) is shown in Fig. 2.7b.

Cunha (1986) was able to recognize in the contemporaneous morphology some NW-SE aligned river inflections due to faulting and the control of the mudlithic-arenaceous facies of Cretaceous sediments. His proposal of a NW-SE much less conspicuous surface structural feature (the "Picos-Santa Inês Lineament", from about 4°S, 40°W to 2°S, 46°W) has hardly any expression on the aeromagnetic map of Fig. 2.6. The isopach maps for the Silurian and Devonian sequences (see Figs. 2.17 and 2.18) show a NW-SE early depositional control. This seems to be the only evidence to link a present-day surface feature to the intermittent reactivation of an ancient crustal weakness zone.

Faulting is also evident on the aeromagnetic map to the NE of the Parnaíba Basin including the neighbouring coastal Barreirinhas Basin (Fig. 2.8). The anomaly pattern has been interpreted as due to the trace of a long transcurrent fault originating during the opening of the Equatorial Atlantic Ocean and subsequently being reactivated as a normal fault, leading to the development of the Barreirinhas Basin. A 60 km horizontal offset has been estimated from the displacement of prominent magnetic anomalies over the Urbano Santos structural high and the delta of the Parnaíba River.

2.3 Geology of the Basement Rocks

The Precambrian basement of the Parnaíba Basin has been demarcated by the study of outcropping rocks adjacent to the basin and those drilled in several exploratory boreholes. The basement mostly consists of folding belts, crustal blocks and median massifs similar to those found in the adjacent structural provinces and extending to the basin interior (Fig. 2.9), as confirmed by some wells. These rocks have been metamorphosed (and some produced) in the Brasiliano Cycle (700-450 Ma).

Basement rocks have been scarcely sampled in the Parnaíba Basin and Fig. 2.10 presents a distribution of 24 PETROBRÁS boreholes (6 on adjacent coastal

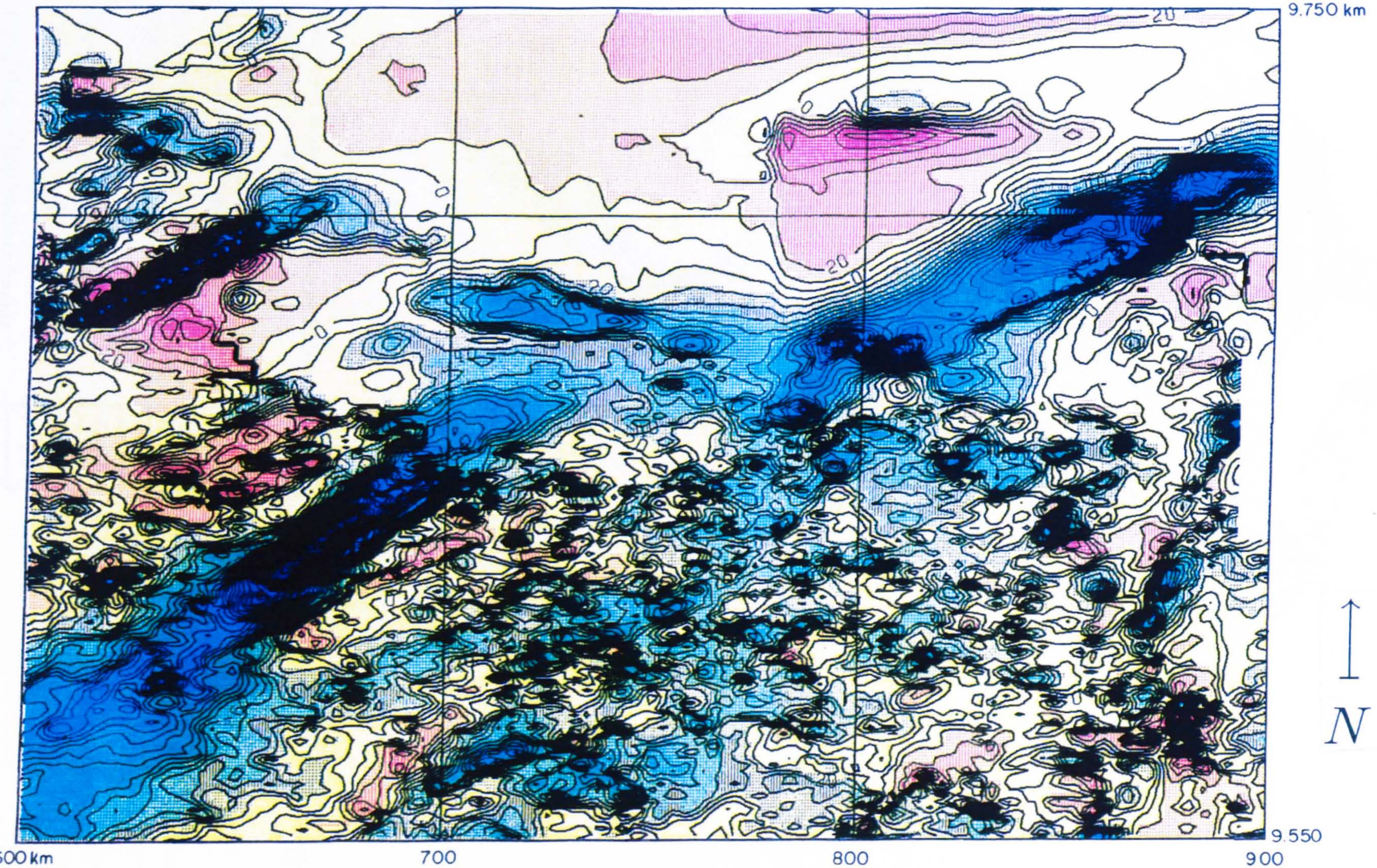

Fig. 2.8 Horizontal offset of ~60 km inferred from the displacement of the magnetic anomalies on the Urbano Santos structural high and the delta of the Parnaíba River (after Góes *et al.*, 1993).

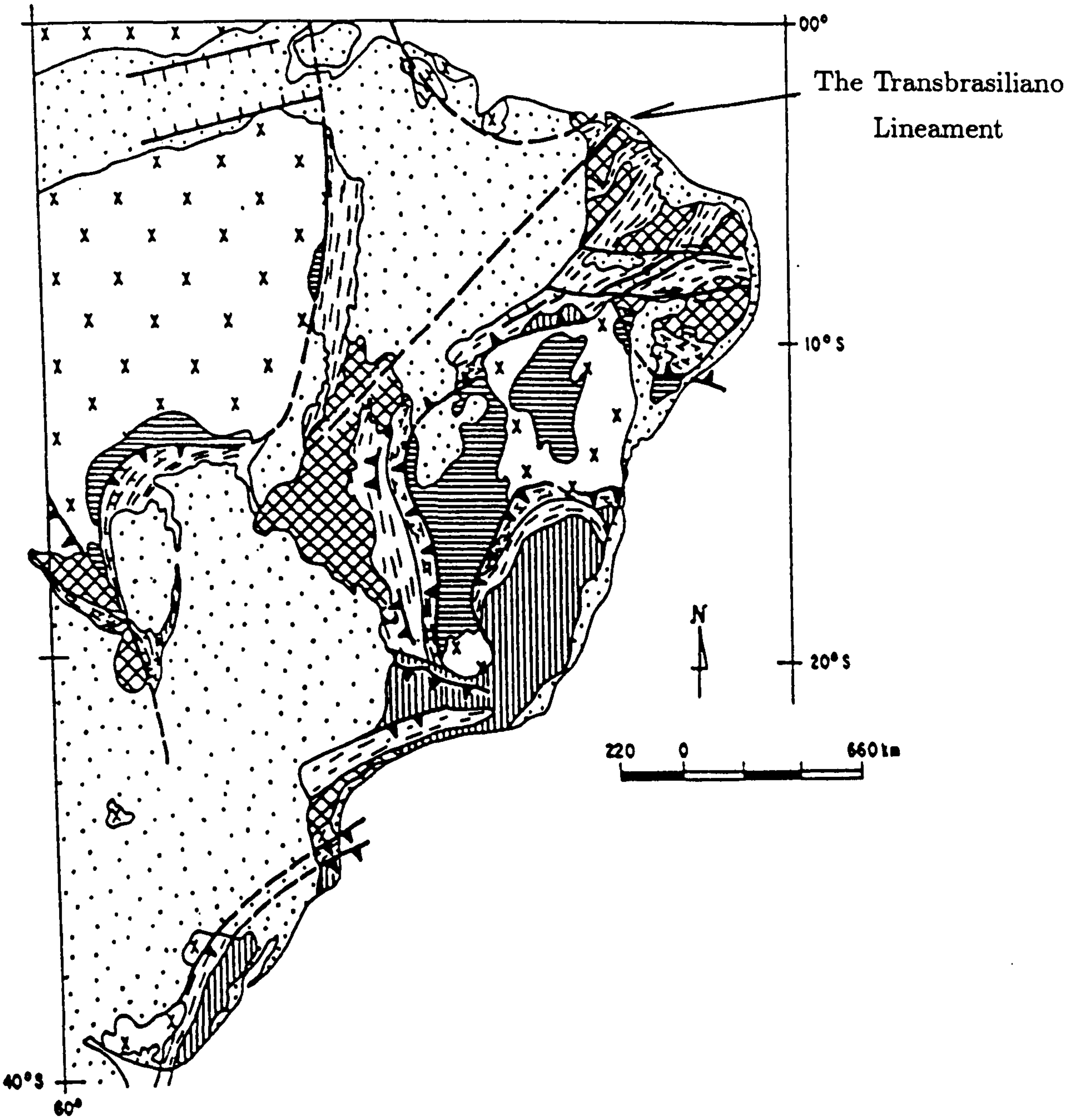

Syn-Brasiliano cratons. Upper Proterozoic continental plates

Median and marginal massifs (microplates and microcontinents)

Intensely metamorphosed basement and supracrustal rocks

Miogeoclinal, marginal systems

Rifts, forearc and backarc basins

Proterozoic, syn/post-Brasiliano covers. Foreland covers

Undifferentiated Phanerozoic covers

Collisional sutures and Brasiliano thrust traces

Main shear zones

Post-Brasiliano rifts

Fig. 2.9 Upper Proterozoic tectonic elements in Brazil (after De Brito Neves, 1990).

basins), their depths to basement rocks or ancient sedimentary covers, the available radiometric dates and lithological classification. The basement rocks of the Parnaíba Basin have been described as quartzites, metamorphosed limestones and schists affected in varying degrees by the Brasiliano Cycle.

An exploratory borehole (MS-1, 6.99°S, 45.49°W, Fig. 2.10) reached micaceous quartzite at a depth of 2,470 metres. This rock has been dated by the Rb/Sr (total rock) method giving an age of 1.42 Ga. This evidence and the observed metamorphic polarity* of the fold belts bordering the basin have led to the proposition that a *central cratonic nucleus* might be present beneath the Phanerozoic cover (Cordani *et al.*, 1984; Cunha, 1986).

A schematic map of the basement of the Parnaíba Basin (Góes *et al.*, 1993) is shown in Fig. 2.11. Precambrian rocks are found in the Granja and Goiás massifs and in the São Luís Craton. These outcrops define an ancient geological and geochronological domain related to the Transamazon Cycle (2.1-1.8 Ga). The São Luís Craton is bordered by low-grade metasediments, greenschist facies, defining the Gurupí Fold Belt. Rocks of this orogenic belt define a younger domain and have been related to the Brasiliano Cycle (700-450 Ma).

The Parnaíba Basin is also bounded to the west by the Araguaia Fold Belt. This is an ancient Proterozoic unit which has undergone tectonothermal events due to the Uruaçuano (1.3-1.0 Ga) and Brasiliano Cycles. Metamorphic polarity is directed to the Amazon Craton and, given the K/Ar age of 608 ± 21 Ma for a gneiss drilled at well CL-1 (7.34°S, 47.46°W, Fig. 2.10) it is believed that similar metamorphosed rocks might be found beneath the Phanerozoic sedimentary cover.

Middle to high metamorphic rocks (granulites) are found to the southwest of Parnaíba. They seem to be the core of the Araguaia Fold Belt and this fold belt is intersected in the south by a NE-SW cataclastic belt defining the Transbrasiliano Lineament. Upper Precambrian-Lower Cambrian deposits are found in local troughs.

---

* Use of the term "polarity" is made to point out the direction of decreasing metamorphism, orogenesis and magmatism, according to the definition of Loczy & Ladeira (1976).

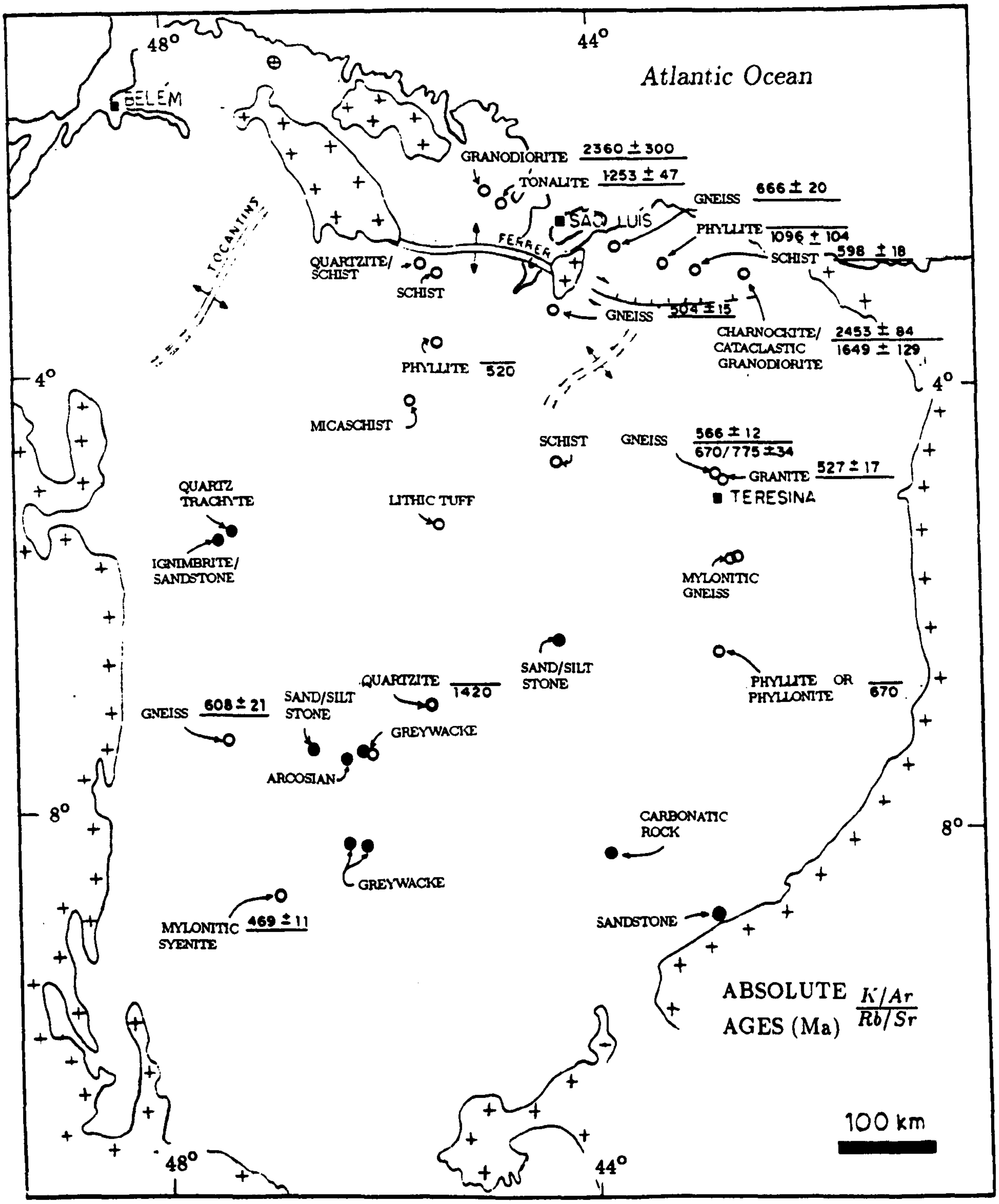

O METAMORPHIC BASEMENT

● ANCIENT SEDIMENTS

←||→ ARCH (BASEMENT HIGH)

Fig. 2.10 Parnaíba Basin: sampled basement rocks, petrology and radiometric ages (after Góes *et al.*, 1993).

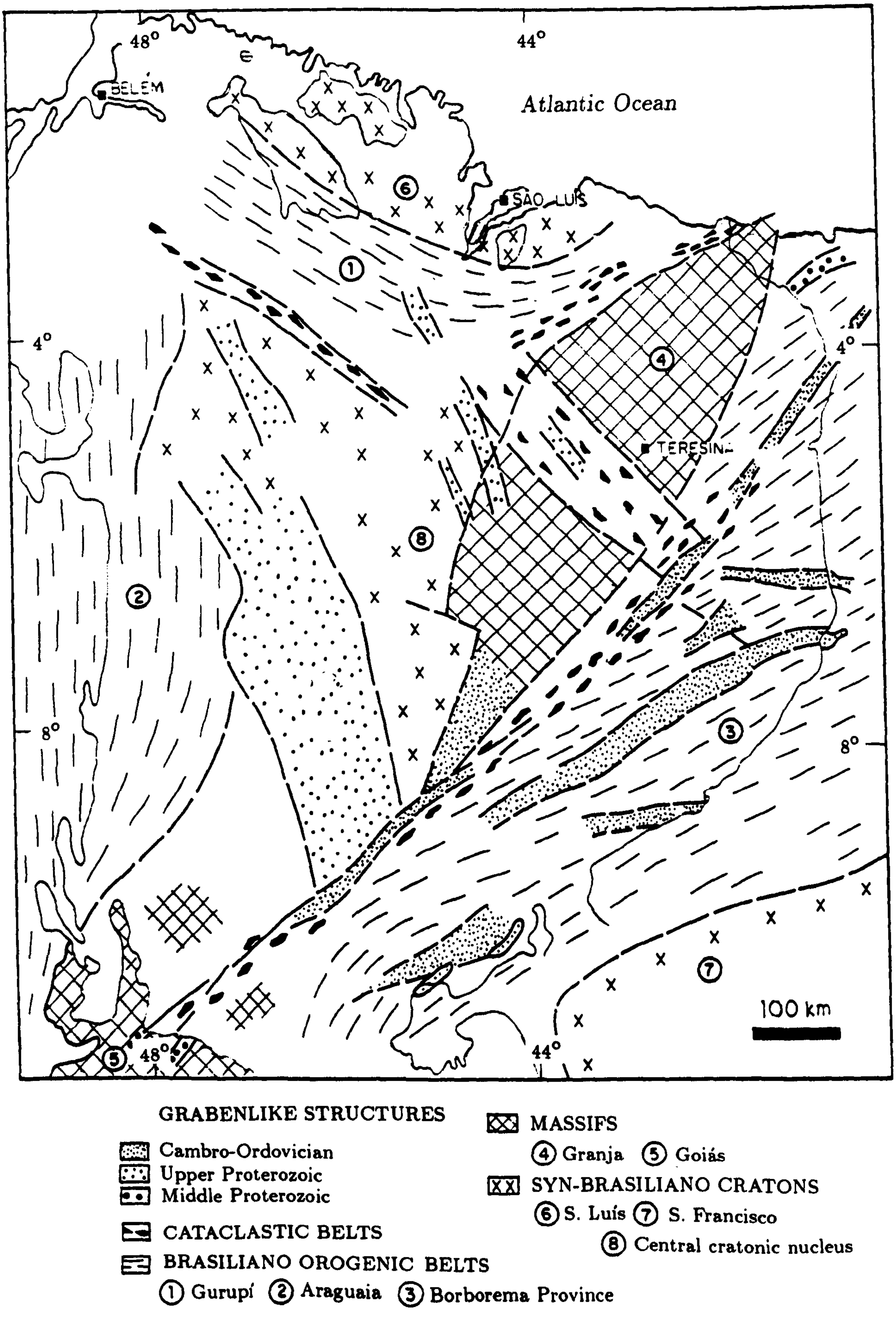

Fig. 2.11 Parnaíba Basin: basement geotectonic map (after Góes *et al.*, 1993).

Cretaceous covers to the south of the Parnaíba Basin preclude the direct observation of the contact between the Palaeozoic sediments and the Precambrian basement rocks.

To the southeast, basinal rocks overlay Upper Precambrian migmatites and gneisses. These rocks define orogenic belts in the adjacent Borborema Province and were deformed during the Brasiliano. Structural trends are NE-SW, subparallel to the southeast basin border and bounded by the São Francisco Craton. The observed tectonic zones lead to increased metamorphism towards the basin interior. Core rocks of these belts should be found beneath the basinal sequences.

The eastern embayment of the Parnaíba Basin is the west-southwest extension of the Borborema Province. This complex unit is formed by folds belts and median massifs delimited in several zones by (mainly) transcurrent faulting and extensive lineaments. The rocks of this unit present polyphasic metamorphism with gradations from greenschist to amphibolitic facies. The Borborema Province shows NE-SW structures reaching Parnaíba diagonally. Characteristic rocks of this province have been drilled in wells MA-1 (4.83°S, 42.80°W), MA-2 (4.85°S, 42.78°W), NLst-1 (5.60°S, 42.59°W) and FL-1 (6.46°S, 42.80°W), see Fig. 2.10. Some samples are very cataclastic and show ages related to the Brasiliano Cycle.

Cataclastic belts are also shown in Fig. 2.11. The NE-SW zone of cataclased rocks has been associated with the Transbrasiliano Lineament while a smaller NW-SE zone of cataclased rocks has been mapped by Hasui *et al.* (1984) to the south of the Gurupí Fold Belt.

In summary, the basinal substratum is mainly formed by metamorphic rocks originated in tectonomagmatic processes not older than Middle Proterozoic (1.6-0.9 Ga). Subordinate sedimentary rocks (showing varying degrees of metamorphism) are preserved in grabenlike structures of Upper Proterozoic and Cambro-Ordovician ages. These precursory sediments are discussed in more detail in the following section.

2.3.1 Ancient Sediments: The Riachão and Mirador Formations

The base of the first basinal sequence (the Upper Ordovician Serra Grande Group) was reached at -1,414 m at well VG-1R (7.40°S, 46.62°W, Fig. 2.12).

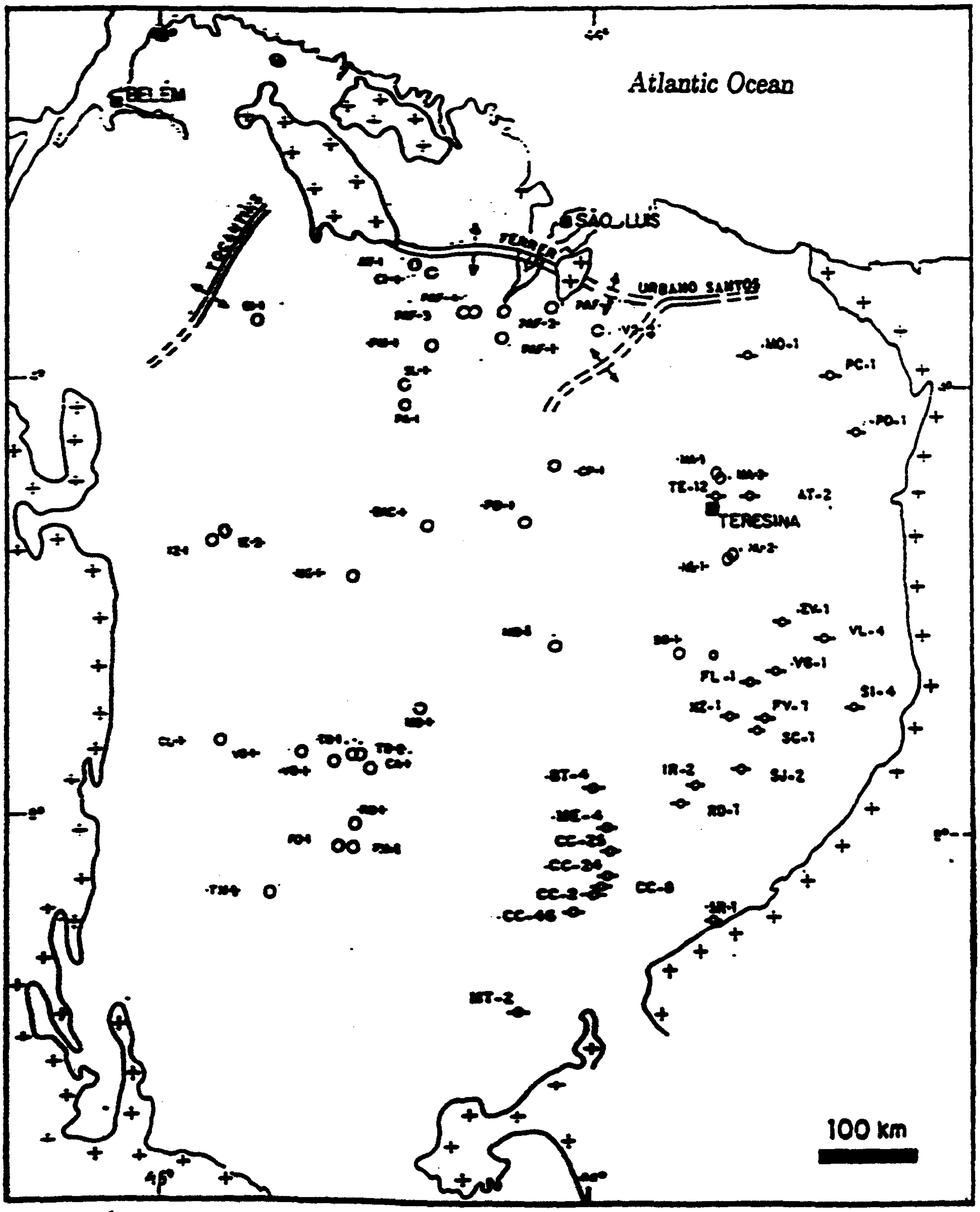

O Boreholes drilled by PETROBRÁS (36 for oil & gas)

-O- Boreholes drilled by CPRM (25 for groundwater)

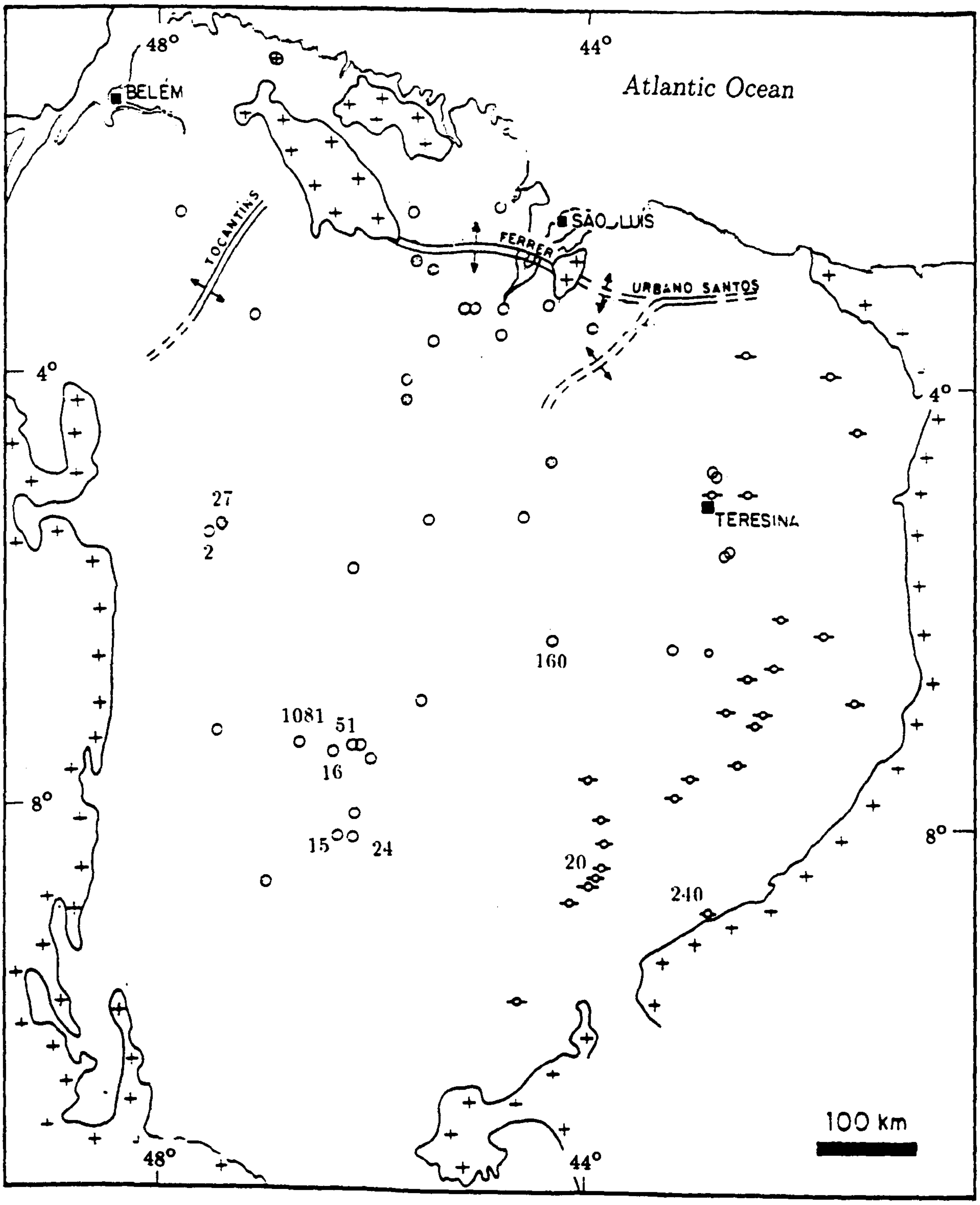

←||→ Arch (basement high)

Fig. 2.12 Location of exploration boreholes that reached ancient sediments beneath the Parnaíba Basin and drilled thicknesses in metres. The total thicknesses of these sediments are unknown (after Góes *et al.*, 1993).

From this depth down to -2,495 m (1,081 m drilled thickness) only immature sediments of the *Riachão Formation* were drilled. The drilling samples included greywackes, siltstones, red shales and ignimbrites typical of a *Molasse** sequence. This borehole did not reach metasediments or any other rocks belonging to the embayment of the Parnaíba Basin and the total thickness of the Riachão Formation is therefore unknown. The immature character of these clastics, their lithologic similarity, proximity and position below the Serra Grande Group suggest that this Formation correlates with the *Monte do Carmo Formation* which outcrops in terrains bordering the south-southwest Parnaíba Basin and with the platform covers of the Amazon Craton. The Monte do Carmo Formation is found in grabenlike structures showing signs of middle-grade metamorphism. Góes *et al.* (1993) has interpreted the few available seismic sections as showing evidence of carbonatic and pelitic facies in deeper parts of the Riachão Formation and tentatively assigned an Upper Precambrian (~700 Ma) age to this unit. Other PETROBRÁS wells (see Fig. 2.12) which reached the Riachão Formation are FM-1 (8.25°S, 46.09°W), FO-1 (8.26°S, 46.23°W), IZ-1 (5.45°S, 47.35°W), IZ-2 (5.53°S, 47.49°W), TB-1 (7.42°S, 46.10°W) and VB-1 (7.47°S, 46.30°W) with drilled thicknesses not exceeding 51 metres. Wells reaching the Riachão Formation yielded the largest heat flow estimates in Parnaíba, ranging from 60 to 90 mW m^{-2} (Pereira & Hamza, 1991).

A single exploratory borehole (MD-1, 6.38°S, 44.30°W, Fig. 2.12) also drilled 160 m of immature sediments which define the *Mirador Formation*. Metamorphic basement rocks were not reached. The Mirador Formation does not outcrop and seems to be restricted to the central-southeast part of the basin. Lithologically, it has been described as light grey-greenish to grey-whitish sandstones, with some intercalations at the top of extremely micaceous siltstones and greenish shales. Sandstones vary from fine to coarse-grained with quartz, quartzite and feldspar grains and pebbles scarcely distributed (Rodrigues, 1967). No fossils have been found in the Mirador Formation. Caputo & Lima (1984), tentatively established its age by correlation with rocks of the *Pacujá Formation* of the adjacent Borborema

* The later deposits of foreland basins are coarse-grained, predominantly shallow-water or continental sediments and typify the term "Molasse" (Allen & Allen, 1990, p. 246; Ricci-Lucchi, 1986.

Province (Fig. 2.11, Cambro-Ordovician grabenlike structures). The clastics of the Pacujá Formation are also immature and found below the sedimentary sections of the Serra Grande Formation in grabens outcropping to the east and northeast of Parnaíba. Diagenetic and low-grade metamorphic processes affected the Pacujá Formation at about 535 ± 27 Ma. These rocks are topped by a volcanic suite dated as 500-480 Ma and the whole graben section has been positioned in the Upper Precambrian-Middle Ordovician. Assuming the Mirador Formation is contemporaneous to Pacujá, it seems to have been deposited at Cambro-Ordovician times.

Two groundwater wells also drilled sediments not belonging to the basinal sequence. About 240 m of fine sandstones were drilled at well SR-1 (8.75°S, 42.90°W) and well CC-24 (8.35°S, 43.83°W) reached whitish carbonatic rock below the Serra Grande Group.

The well data summarized above and some evidence found in a few PETROBRÁS seismic sections lead Cunha (1986) to propose the existence of grabenlike structures within the basin which might have acted as precursory axes of subsidence. These structures would be the result of the activity along ancient fault lines either in the Precambrian (Riachão) or Cambrian (Mirador) times. Góes *et al.* (1993) reprocessed old seismic lines and used the information provided by more recent exploration wells (BAC-1, 5.30°S, 45.44°W) and (CP-1, 4.76°S, 44.30°W) to further support this proposal. The thicknesses of sediments infilling these grabenlike structures are still unknown and cannot be shown in an isopach map.

The deposition of the Mirador and Riachão Formations preceded the regional sedimentation of Parnaíba by ~60-300 Myr and supports the interpretation that this crustal block in northeastern Brazil was the site of intermittent extensional tectonics since (at least) the Upper Proterozoic.

2.4 Basin Stratigraphy and Tectonic Events

A concise presentation is first shown of the exploration tools that, along with basic geological mapping, were used in recognizing the different basinal strata, how they have been structured across the Parnaíba Basin and a reconstruction

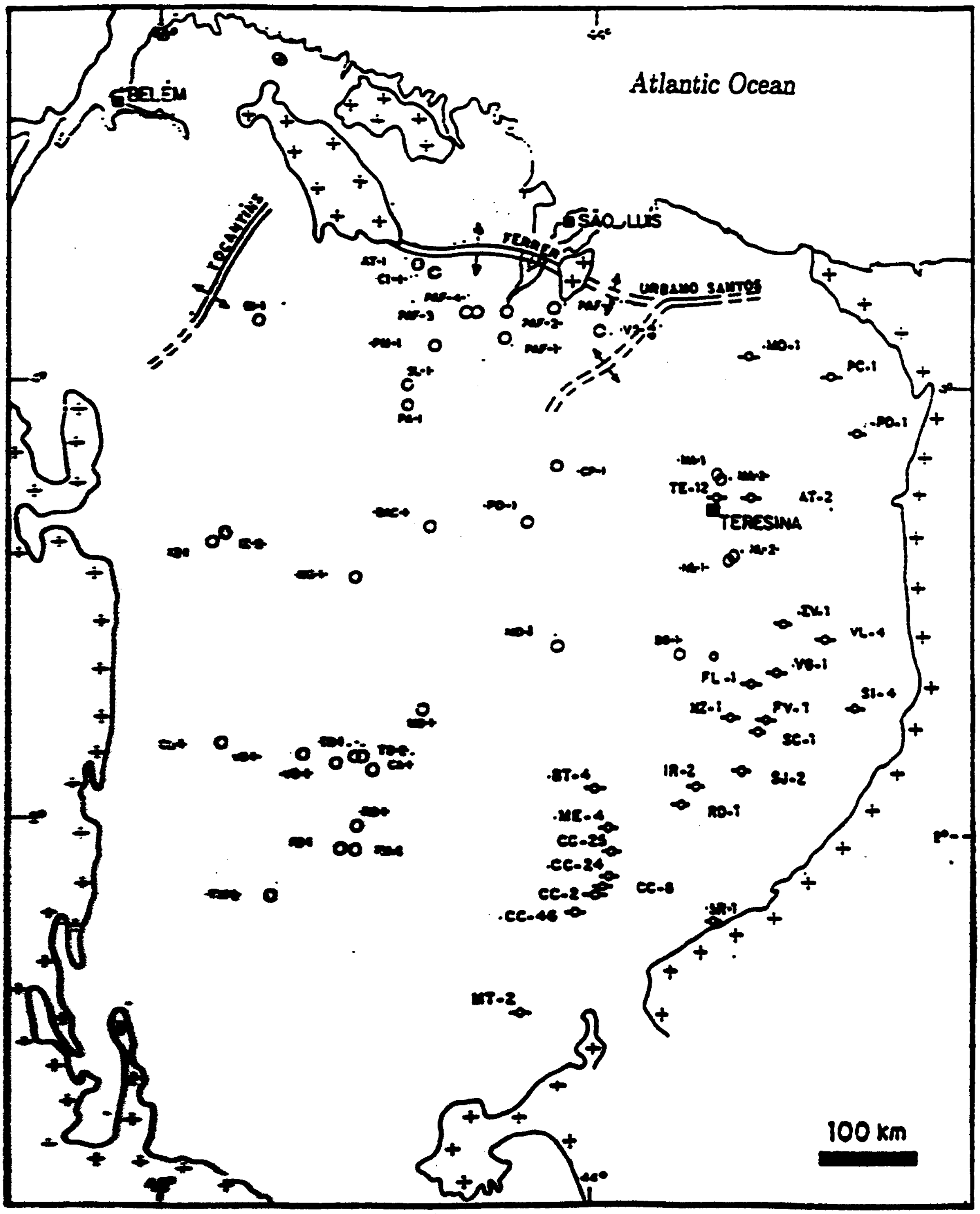

O Boreholes drilled by PETROBRÁS (36 for oil & gas)

-O- Boreholes drilled by CPRM (25 for groundwater)

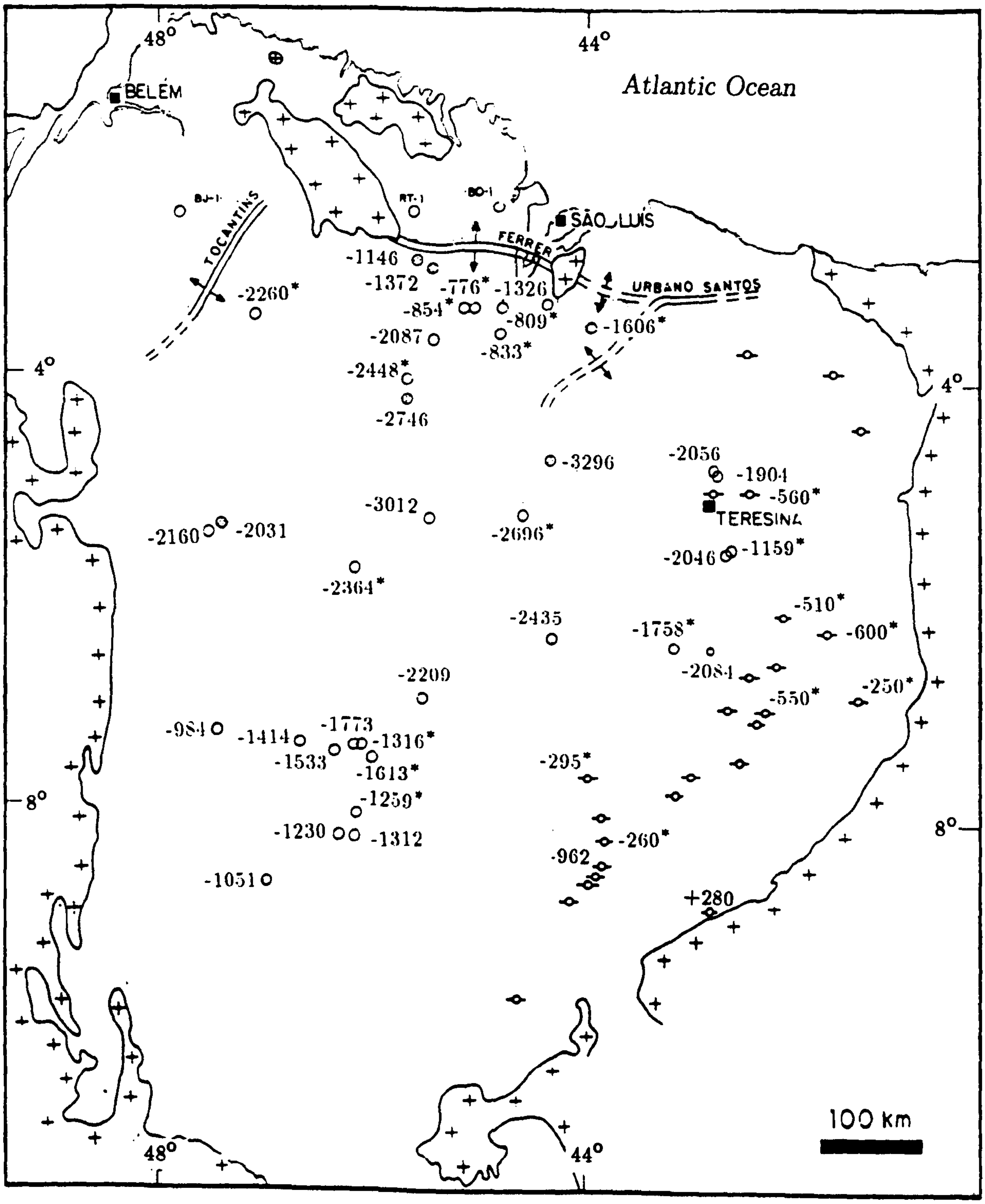

←||→ Arch (basement high)

Fig. 2.13 Exploratory boreholes drilled in the Parnaíba Basin. Figures are the known depths below sealevel (in metres) to the crystalline basement or to ancient sedimentary covers. Asterisks indicate total depths for those boreholes which did not reach the bottom (after Góes *et al.*, 1993).

of basinal sequences in time. The reference geologic time scales were taken from Hack & van Eysinga (1987) and Harland *et al.* (1990).

The location of all exploratory boreholes drilled by PETROBRÁS in the Parnaíba Basin is shown in Fig. 2.13. There are 36 wells, 22 of which reached basement rocks or precursory sedimentary covers. Also shown in this figure is the location of 25 shallow ground water exploration wells drilled by CPRM in the northeast, east and southeast of Parnaíba. Most of the depths of these wells cannot be shown because CPRM has not released them for the present study. However, Góes (1991, 1993) managed to include relevant information from these wells in the construction of isopach maps (Figs. 2.16-2.23). The density of exploratory wells is low (1 well/16,700 km^2) and Parnaíba is the least explored of the three Brazilian Palaeozoic basins.

Reflection seismic studies for oil exploration purposes in Parnaíba started in the 1950s with a few analog records. More systematic surveys began in 1975 in the area of the Ferrer Arch. Figure 2.14 shows the distribution of reflection seismic sections executed by PETROBRÁS up to 1989, *i.e.* the last executed. The total seismic coverage is only 7,866 km with a very low density of 0.013 km/km^2.

Surface geochemical prospecting was also executed by PETROBRÁS for oil exploration purposes in about 14% of the total basin area (Fig. 2.14). About 2,350 soil samples were collected on a (approximately) 5 x 5 km grid and have been analyzed for concentrations of gaseous hydrocarbons: methane, ethane, propane, butane and pentane. Vapours heavier than ethane ($C2^+$), pentane ($C5^+$) and total hydrocarbon contents have been also measured.

The sediments in the Parnaíba Basin form simple, thin sequences, with total thickness just over 3,500 metres. The predominantly sandy character and small number of fossils make it difficult to define the lithostratigraphic units and facies differences. The oldest strata defining the basin shape are Upper Ordovician-Lower Silurian and regional subsidence continued until the Cretaceous, when it was disrupted by the opening of the Equatorial South Atlantic Ocean. Similar depositional sequences are found in the Amazon and Paraná Basins. They have been also found roughly synchronous with the North-American Tippecanoe, Kaskaskia and Absaroka sequences (Nunn & Aires, 1988).

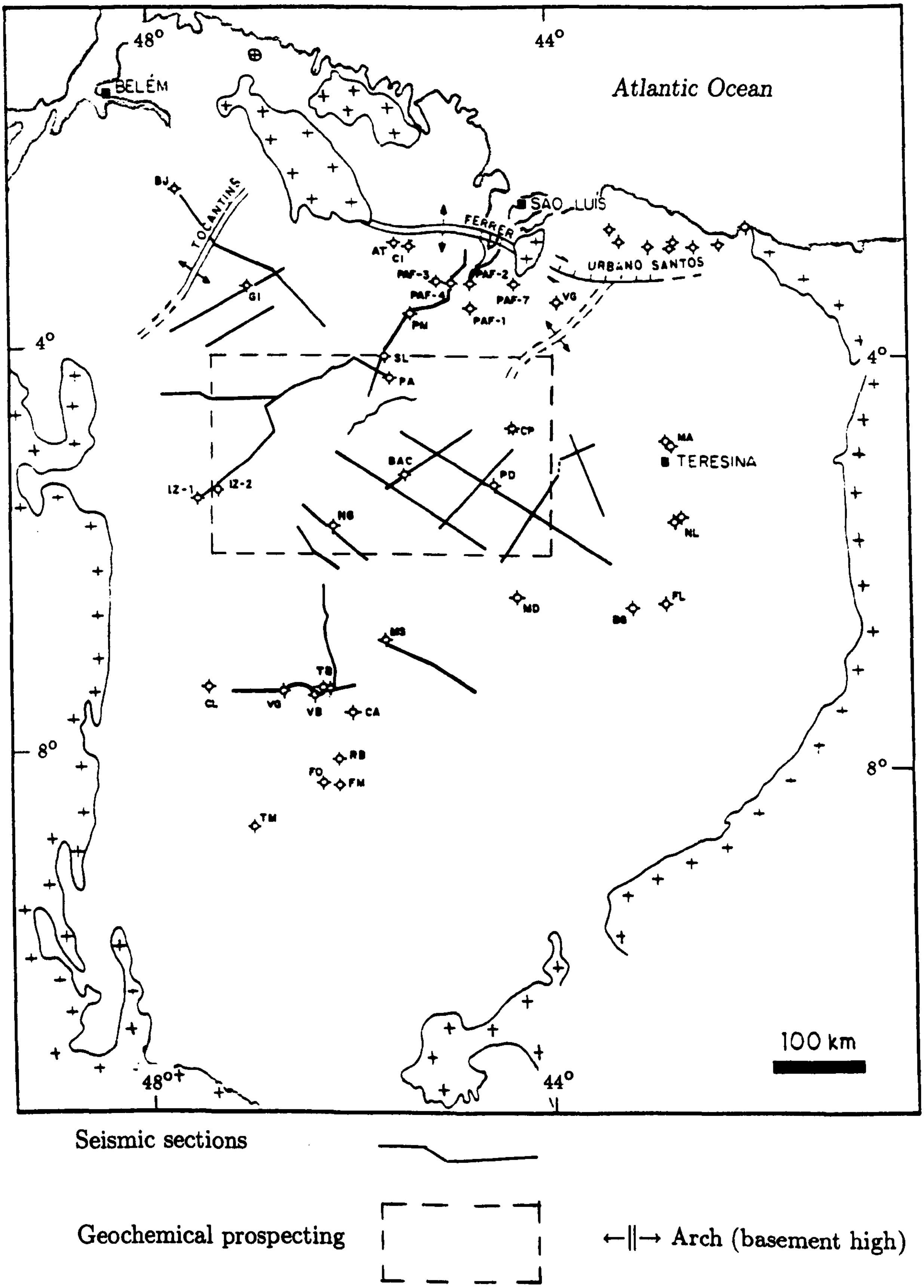

Fig. 2.14 Distribution of geochemical surveys and reflection seismic sections over Parnaíba Basin (after Góes *et al.*, 1993).

Of fundamental importance in the following sections is the geological concept of *depositional sequence* (Allen & Allen, 1990). Briefly stated, the fundamental meso-scale building blocks of stratigraphy are coherent and genetically related packets of strata known as *depositional sequences.* They are bounded by uncomformities or lateral comformities and are thought to have a chronostratigraphic significance. The boundaries of depositional sequences are of critical importance and the relation of the internal stratigraphic horizons to the depositional sequence boundary indicates the changes taking place that gave rise to the laying down of the new depositional sequence.

Data gathered from surface geology, geochemical surveys, exploratory wells and seismic sections were integrated to produce the chrono-lithostratigraphic chart by Góes & Feijó (1994). A schematic NW-SE basin section is presented in Fig. 2.15 along with the absolute ages, the formation names, the prevailing tectonic regimes and the depositional environments. The same data set allowed the construction of the total isopach map for the Parnaíba Basin (Fig. 2.16) and the characteristic oval shape of this basin is shown. A set of isopach maps for each depositional sequence of Parnaíba Basin as well as basalt/diabase and anhydrite cumulative thicknesses, *isoliths*, have been presented by Góes *et al.* (1993). These isopach maps are shown in the following sections.

The scarcity of wells and seismic sections do not give more than a regional significance to the isopach contour lines. The approximate depositional period for each sedimentary layer is also given.

2.4.1 Silurian Sequence: The Serra Grande Group

The strata forming the first depositional sequence of the Parnaíba Basin are those belonging to the *Serra Grande Group* (Fig. 2.17). The isopach map shows a strong depositional control along a NW-SE direction and, on a smaller scale, a NE-SW direction. This depositional pattern has been interpreted as clearly showing the prolonged influence of ancient crustal weakness zones on basinal development.

This Group overlays the metamorphic basement rocks and the molasses of Riachão and Mirador Formations uncomformably. The sedimentary assemblage of

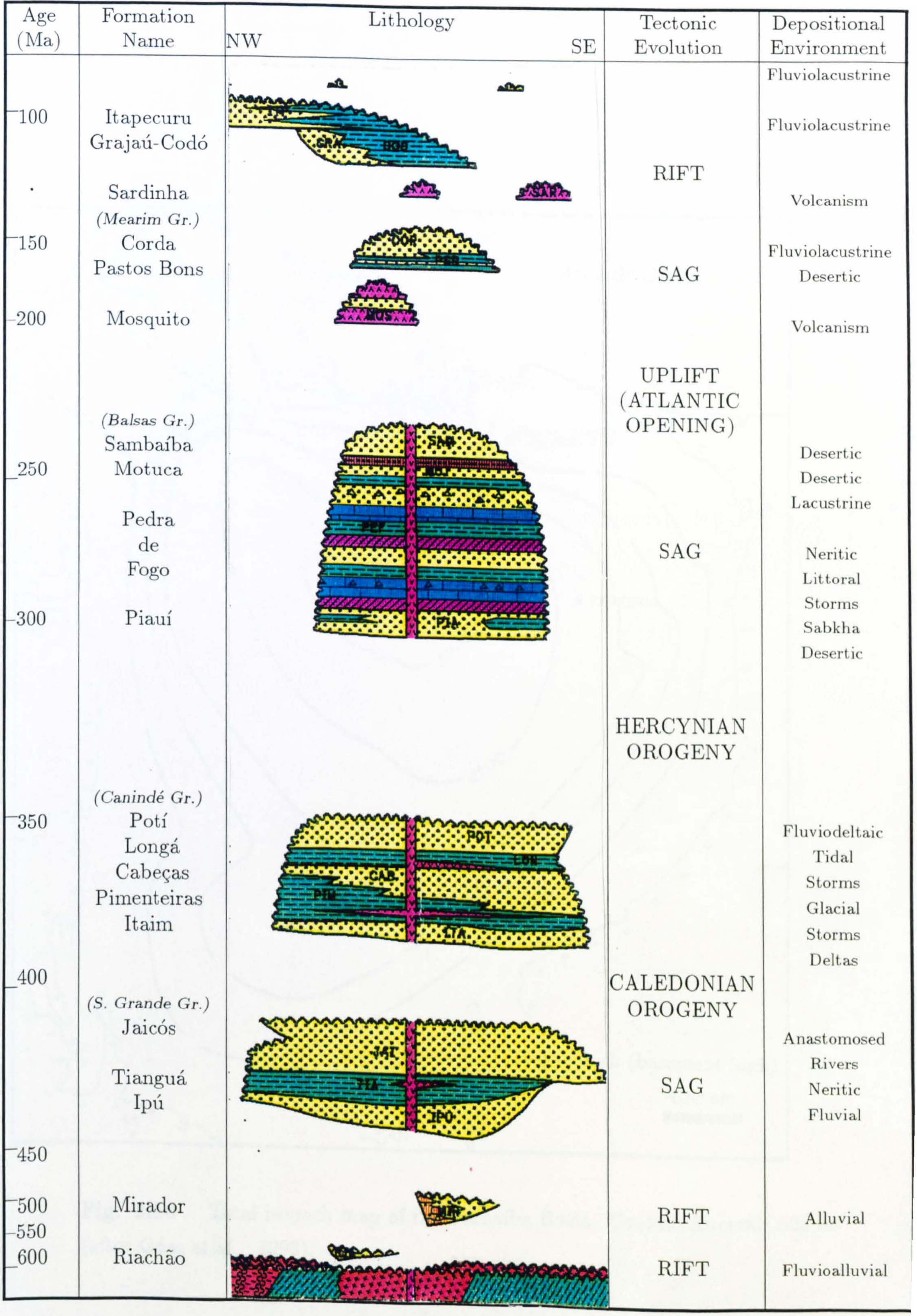

Fig. 2.15 Schematic NW-SE chrono-lithostratigraphic section of the Parnaíba Basin. Note the time scale on the left is not linear. (after Góes *et al.*, 1993).

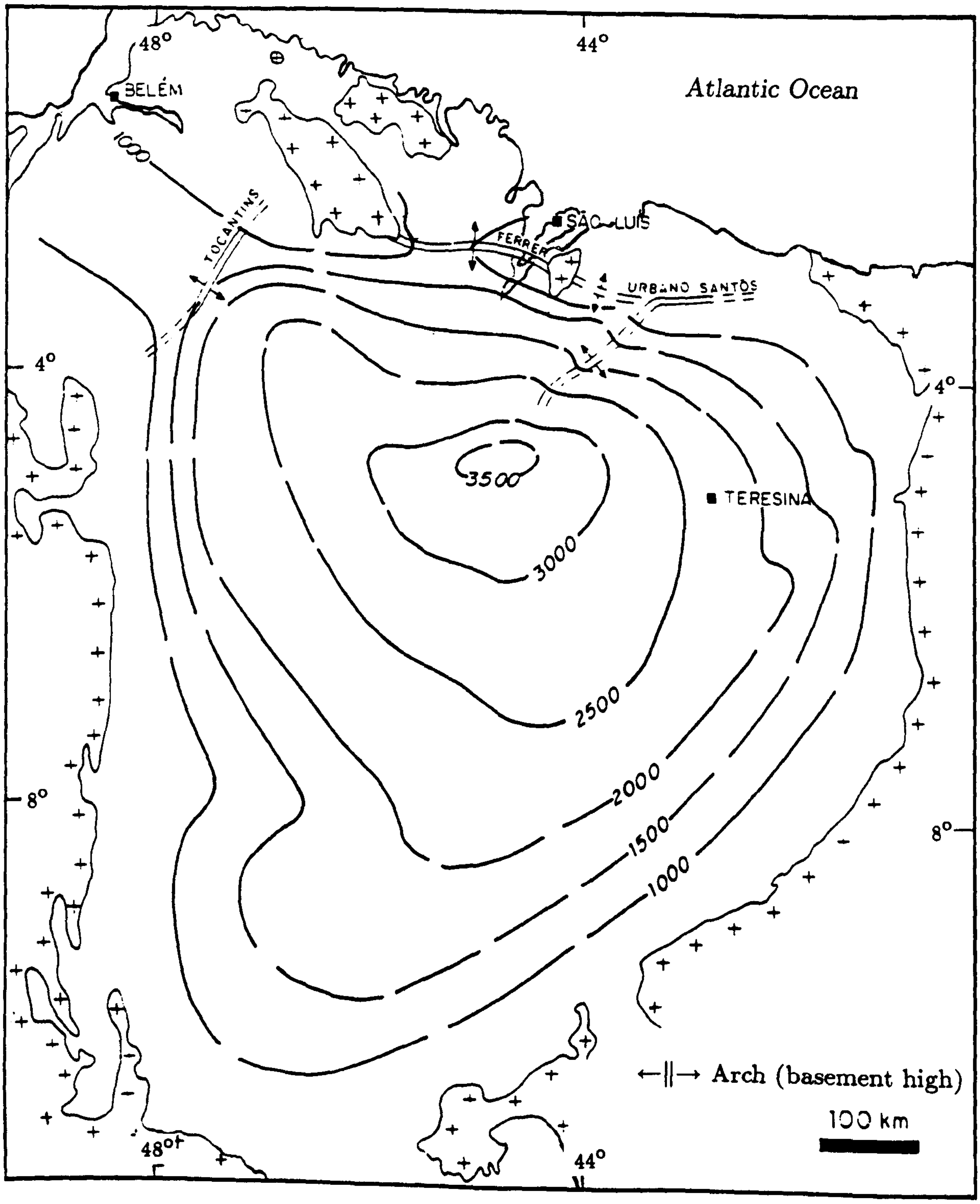

Fig. 2.16 Total isopach map of the Parnaíba Basin. Contour interval: 500 m (after Góes *et al.*, 1993).

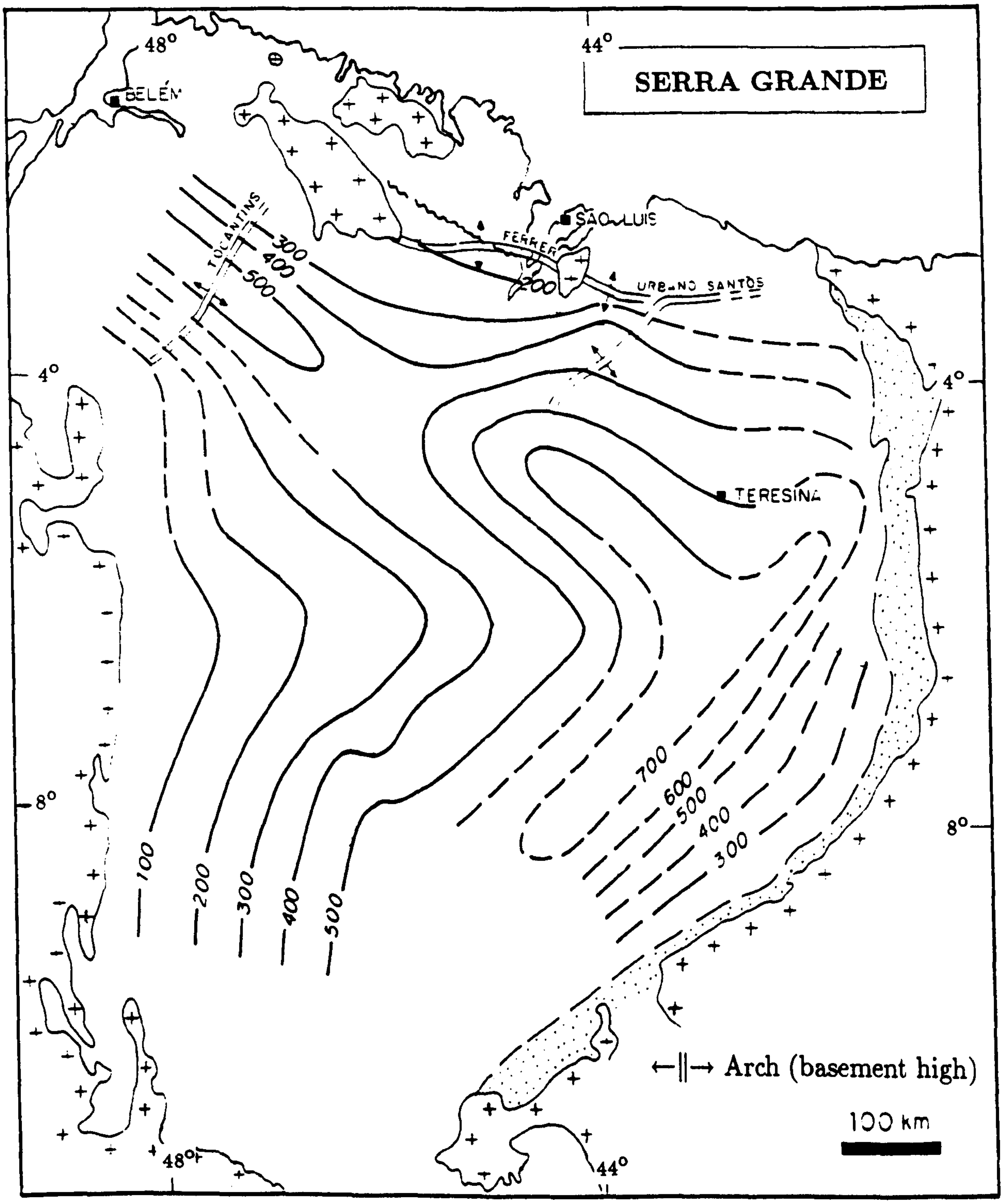

Fig. 2.17 Isopachs for the Serra Grande Group (*Upper Ordovician-Silurian*). Contour interval: 100 m (after Góes *et al.*, 1993).

this Group is mainly characterized by fluvial sandstones with subordinate siltstones, conglomerates, shales and rare diamictites. Caputo & Lima (1984) compiled chrono-lithostratigraphic data, geochemical analysis and updated palinological data and recognized three formations: *Ipu, Tianguá* and *Jaicós*. This depositional sequence records an entire transgressive-regressive cycle with Tianguá corresponding to the maximum flood surface and Jaicós being the regressive phase. The Serra Grande Group in Parnaíba has been correlated with the Trombetas Group in the Amazon Basin and the Rio Ivaí Group in Paraná Basin.

The Ipu Formation contains middle/coarse-grained sandstones and rare siltstones, shales and diamictites, showing signs of glacial and fluvioglacial influence. This Formation had been assigned a Lower Silurian age, but Cunha (1986) argued that it would be better positioned as Upper Ordovician-Lower Silurian, due to some similarities found by Caputo & Lima (1984) to Upper Ordovician lithostratigraphic units found in Occidental Africa. The maximum drilled thickness of Ipu is 350 m and it has been deposited between 445 and 435 Ma.

The Tianguá Formation has been described as extremely micaceous sandstone, sometimes erroneously interpreted as shales, some siltstones and grey shales deposited on a neritic environment at Middle Silurian (435-425 Ma) Its maximum drilled thickness is 200 metres.

The Jaicós Formation overlaies the Tianguá Formation comformably and encloses medium to coarse-grained sandstones and pelites deposited in the Upper Silurian (425 and 410 Ma) with a maximum drilled thickness of 360 metres.

The transition from Silurian to Devonian is related to the Caledonian Orogeny which brought strong modifications to the depositional environment of the basin, from continental to marine, with pronounced glacial influence. At the end of the Silurian a marine regression caused the clastics of the next sequence to be uncomformably deposited on the eroded surface of the Jaicós Formation. This is an easily recognized parallel uncomformity, well seen where both units outcrop and inferred from palaeontology, lithology changes, salinity contrasts and electrical logs elsewhere. An erosional gap of $\sim$25 Myr has been associated with this uncomformity.

2.4.2 Devonian Sequence: The Canindé Group

The *Canindé Group* includes the Devonian and Lower Carboniferous sequence and is the main target for oil exploration (Fig. 2.18). The isopachs still show some preferred depositional directions, although less prominent than the Silurian sequence.

Representative facies of this Group are sandstones, shales, siltstones and diamictites witnessing another transgressive-regressive cycle with deposits in continental, transitional and marine environments. Glacial influence is recognized in these clastics and marine deposits were usually affected by storm waves and ocean currents. The Canindé Group includes the *Itaim, Pimenteiras, Cabeças, Longá* and *Poti Formations.*

The Itaim Formation is of Middle Devonian (385-380 Ma) age and has fine, whitish sandstones and gray to dark grey shales deposited in storm-dominated deltaic environments. Its maximum drilled thickness is 260 metres.

The Pimenteiras Formation consists of thick, organically rich, dark-grey to black, radioactive shales with thin layers of very fine-grained sandstones deposited in a neritic, storm-dominated shelf environment. An Upper Devonian age (380-370 Ma) was assigned to this formation and this is the most promising target for oil exploration with a maximum drilled thickness of 320 metres.

A similar Upper Devonian age (370-365 Ma) was assigned to the Cabeças Formation, made up of fine sandstones deposited on a neritic, wave-dominated shelf environment and showing glacial influence. The maximum drilled thickness is 350 metres.

The Longá Formation is Upper Devonian-Lower Carboniferous (365-360 Ma). It includes fine sandstones, shales and siltstones also deposited on a storm-dominated, neritic environment. Its maximum drilled thickness is 220 metres.

The last unit in the Group, Poti Formation, has been described as grey-whitish sandstones, with intercalations of shales and siltstones, mostly deposited in occasionally storm-influenced deltas in the Lower Carboniferous (360-350 Ma). The maximum drilled thickness is 220 metres.

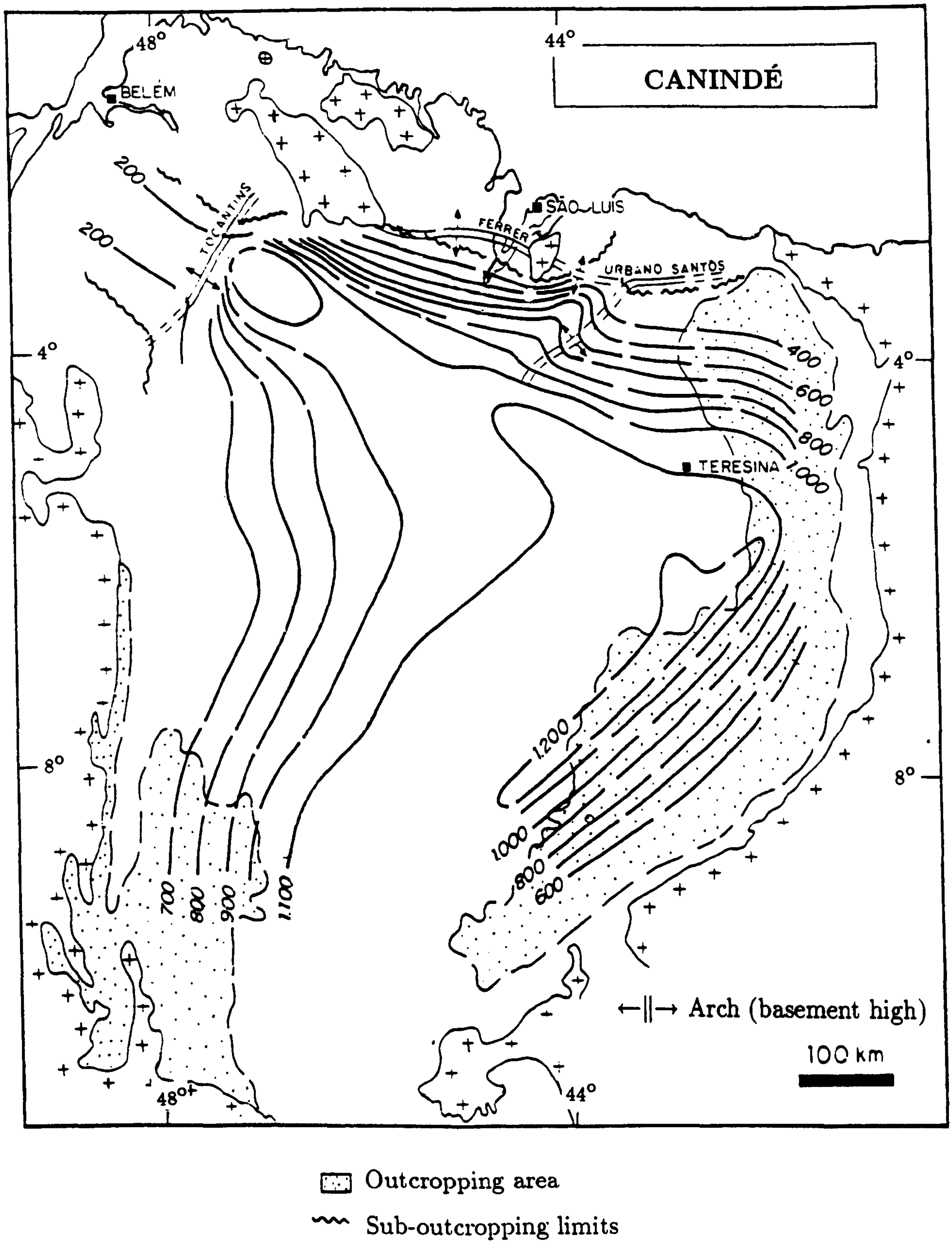

Fig. 2.18 Isopachs for the Canindé Group (*Devonian*). Contour interval: 100 m (after Góes *et al.*, 1993).

The Canindé Group overlaies the Serra Grande Group uncomformably, except in the extreme east, where it is in direct contact with basement rocks. It has been correlated to the Urupadí and Curuá Groups in the Amazon Basin and to the Paraná Group of Paraná Basin.

After the deposition of the Poti Formation the basin was totally exposed and a new uncomformity was imprinted upon the sediments, accompanied by major changes in climate and depositional conditions. The marine, open-sea environment, with cold to temperate climate, of the Silurian-Devonian changed into a continental, arid environment in the Carboniferous-Triassic with a remanent, epicontinental sea. This disruption of the subsidence pattern has been related to the Hercynian Orogeny and seems to have lasted for $\sim$40 Myr.

2.4.3 Carboniferous-Triassic Sequence: The Balsas Group

The next depositional sequence is the *Balsas Group* which includes the *Piauí, Pedra de Fogo, Motuca* and *Sambaíba Formations* (Fig. 2.19). As seen in the isopach map, an uplift of the eastern basin border and reactivation of NW-SE weaknesses zones caused an orientation change in the depositional pattern of this sequence, bringing it closer to the present depocentre. The Carboniferous-Triassic basin, quite different from the Siluro-Devonian sequence, reached the characteristic ellipsoidal shape of Parnaíba Basin. The Balsas Group has been correlated with the Tapajós Group of the Amazon Basin and with the Itararé, Guatá e Passa Dois Groups of Paraná Basin.

The Piauí Formation consists of middle to fine-grained, grey-whitish sandstones which eventually become conglomeratic, red shales and whitish limestones. These rocks were deposited under severe arid conditions in continental, littoral environments and have been assigned an Upper Carboniferous age (310-290 Ma). The maximum drilled thickness is 220 metres.

The Pedra de Fogo Formation consists of silex and limestones interbedded with fine/middle-grained yellowish sandstones, gray shales and white anhydrite of Lower Permian age (290-255 Ma). Silicified trunks of ***Psaronius Brasiliensis***, a Permian

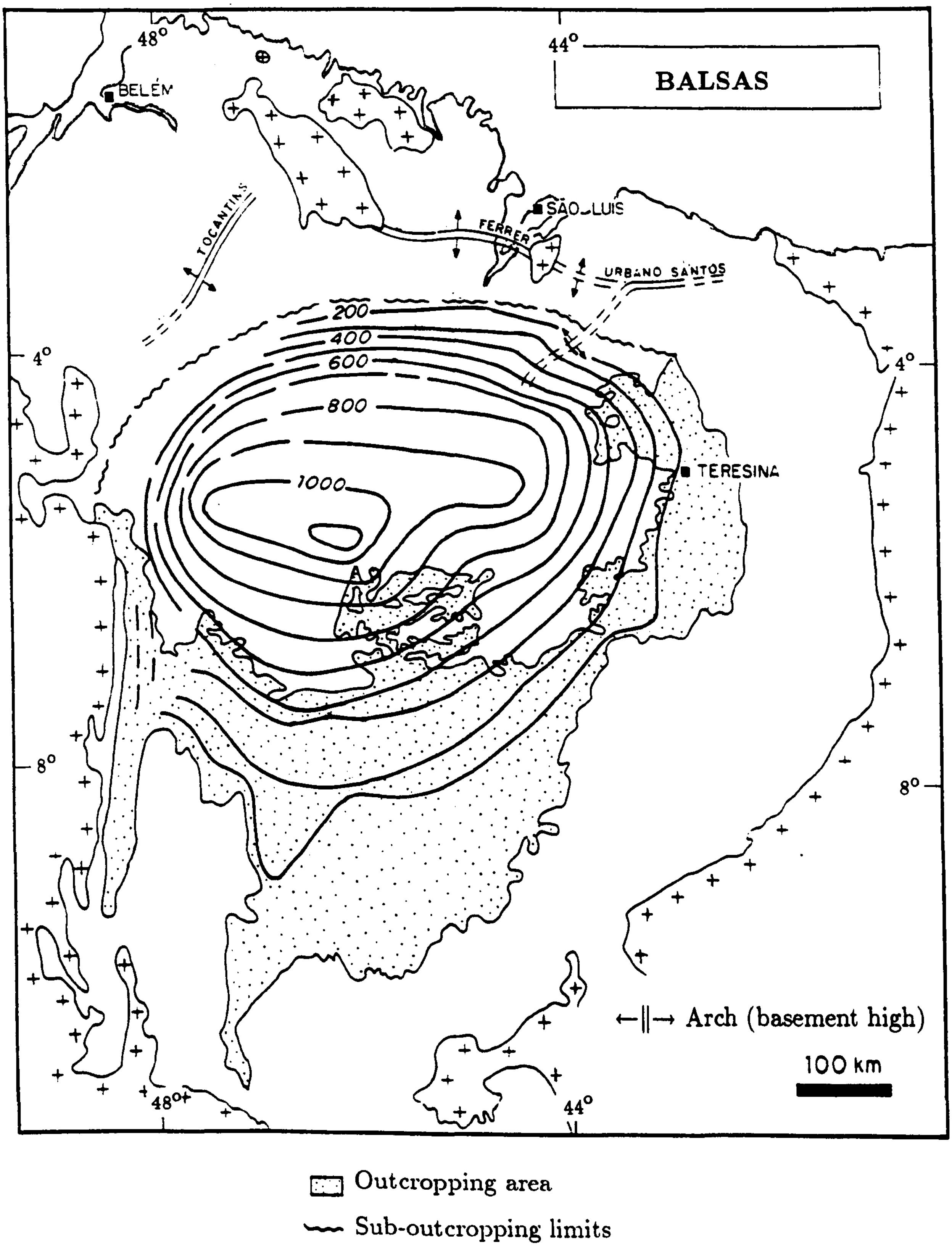

Fig. 2.19 Isopachs for the Balsas Group (*Upper Carboniferous-Lower Triassic*). Contour interval: 100 m (after Góes *et al.*, 1993).

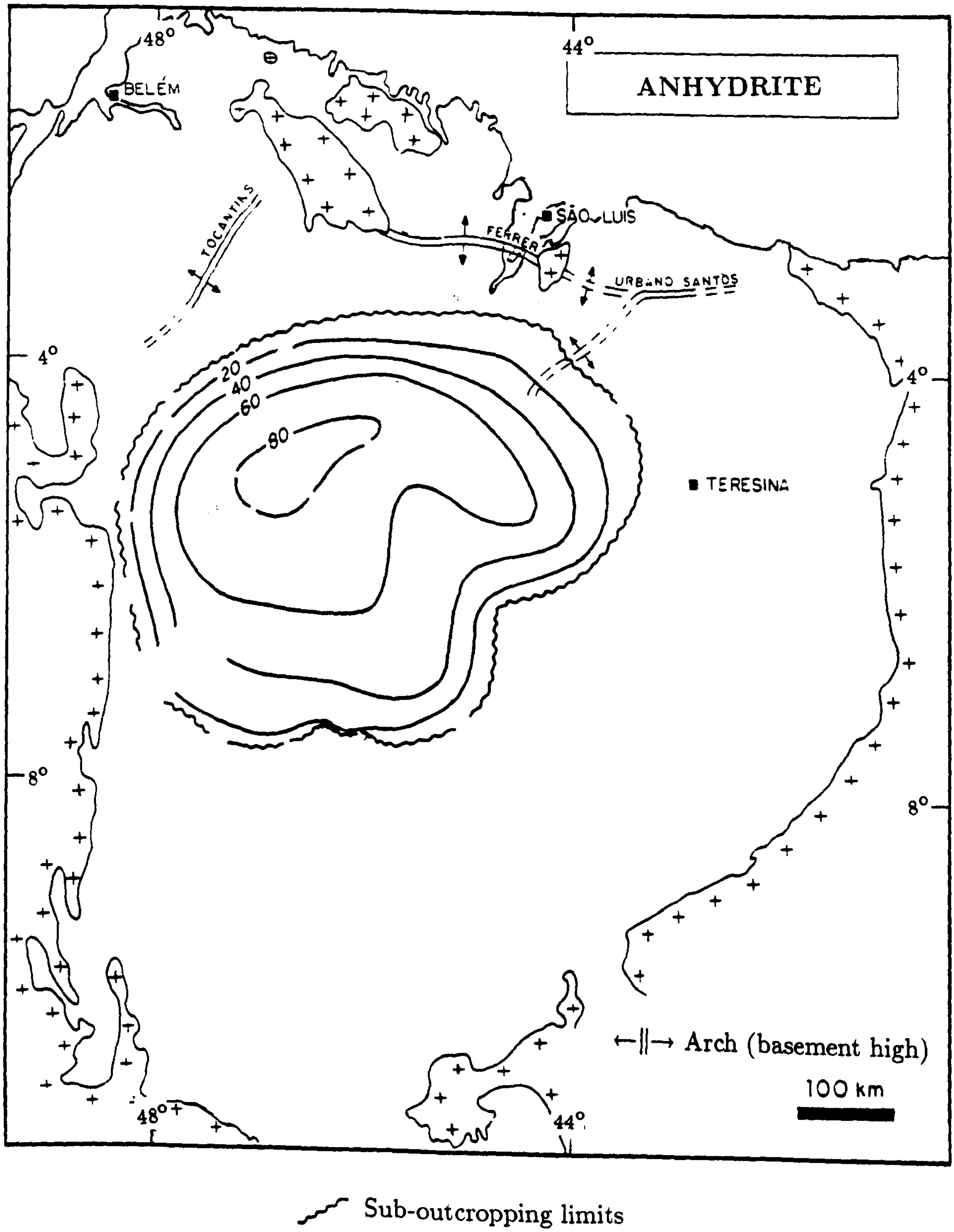

Fig. 2.20 Anhydrite isoliths. Contour interval: 20 m (after Góes *et al.*, 1993).

fossil index are found in this layer. The depositional environment of this formation is neritic, shallow to littoral, with *sabkha* flatlands sometimes being storm-influenced. The maximum drilled thickness is 240 metres.

The Motuca Formation is made up of reddish and brown siltstones, fine/middle-grained white sandstones, white anhydrite and very rare limestones deposited in a lacustrine-controlled, desertic, continental environment during the Upper Permian (255 to 245 Ma). The maximum drilled thickness of this formation is 280 metres. A map of anhydrite isoliths is shown in Fig. 2.20.

The afossiliferous Sambaíba Formation is made up of yellow to reddish, fine/middle-grained sandstones, showing large cross-stratification and was deposited by aeolic systems in a desertic environment. A Lower Triassic age (245-235 Ma) has been assigned to this formation and its maximum drilled thickness is 440 metres.

As a consequence of the thermal uplift that occurred during the opening of the Equatorial Atlantic Ocean, the basin was again exposed putting an end to this sedimentary cycle. Intense erosion followed for ~30 Myr and the first signs of magmatism further obscured basinal development. The basalts of the Mosquito Formation are stratigraphically positioned between the Carboniferous-Triassic and the Jurassic sequences. A much smaller basaltic flow known as the Sardinha Formation overlays the Jurassic depositional sequence. The magmatism in Parnaíba Basin is discussed in more detail in section 2.3.

2.4.4 Jurassic Sequence: The Mearim Group

The last large depositional sequence is the *Mearim Group*, which includes the *Pastos Bons* and *Corda Formations* (Fig. 2.21). Rocks of the Mearim Group were deposited in a continental, desertic environment controlled by fluviolacustrine systems. The fossiliferous contents is poor but the occurrence of ostracods, and ***Lepidotus Piauhyensis*** helped assigning a Middle Jurassic age to this group.

The limnic sedimentation of the Mearim Group includes siltstones and green, brown-reddish shales/claystones. Quartz grains are embedded in the rock matrix of the Pastos Bons Formation. Sandstones appear as subordinate rocks in this unit which shows a maximum drilled thickness of 77 m and has been deposited between 180 and 170 Ma.

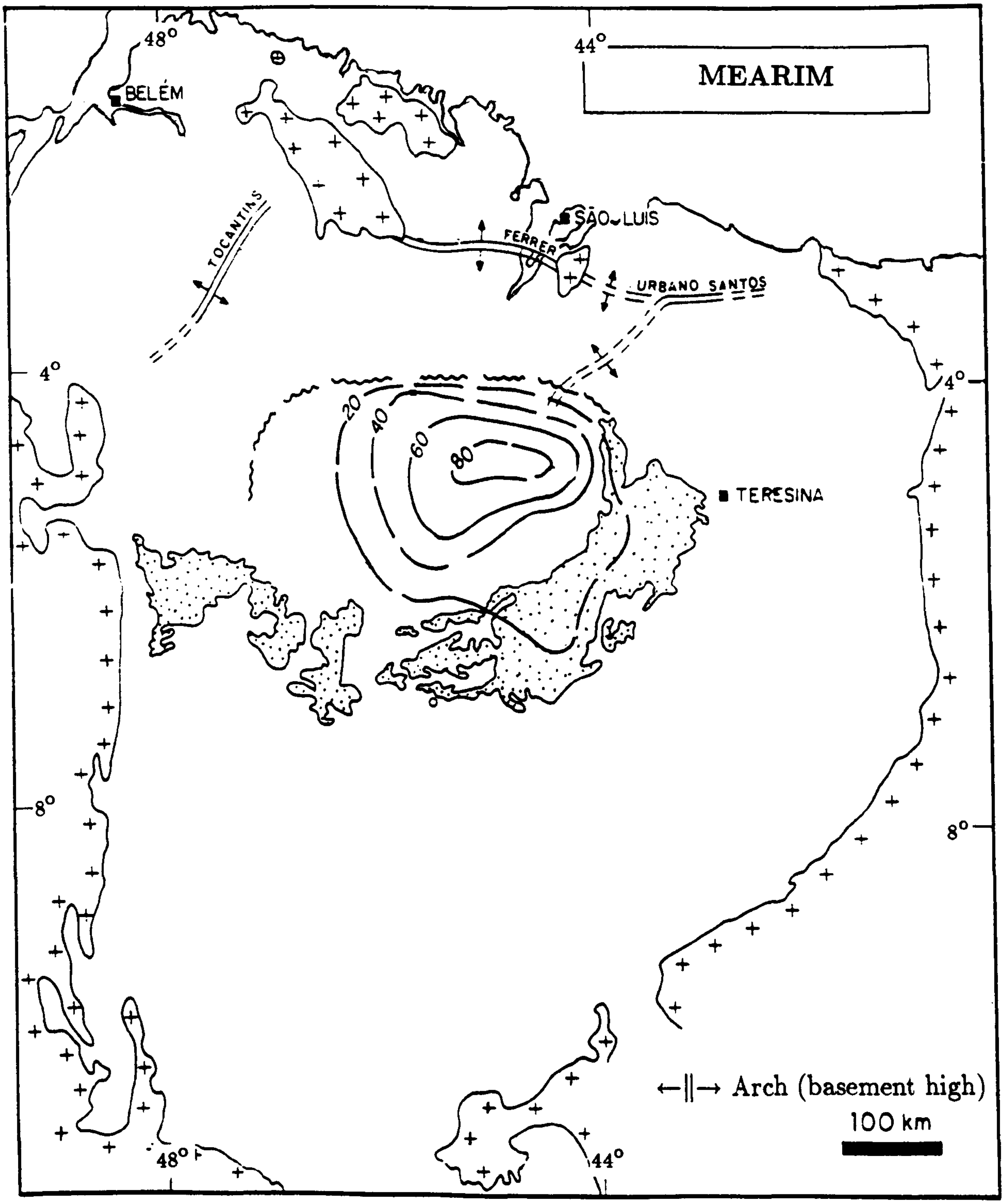

Outcropping area

Sub-outcropping limits

Fig. 2.21 Isopachs for the Mearim Group (*Jurassic*). Contour interval: 20 m (after Góes *et al.*, 1993).

The Corda Formation is characterized by grey-whitish and reddish, fine/coarse-grained sandstones. The maximum drilled thickness is 29 m and it has been deposited between 170 and 155 Ma.

The Mearim Group rocks show uncomformable contacts with the subjacent Mosquito basalts and a small erosional gap of ~4 Myr has been estimated. The Group is also uncomformably overlaid by the Sardinha basalts after an interval of ~15 Myr. Rocks of the Mearim Group have been tentatively correlated to the Botucatú Formation of Paraná Basin. No equivalent sediments have been found in the Amazon Basin.

2.4.5 Cretaceous Sequence: The Grajaú/Codó and Itapecuru Formations

The Cretaceous sedimentation in Parnaíba Basin is represented by the *Grajaú*, *Codó* and *Itapecuru Formations* (Fig. 2.22). The rupture of the Brazilian equatorial margin in the Lower Cretaceous (Neocomian, ~135 Ma) allowed a new, short transgression/regression cycle with further basin subsidence. Sedimentation is restricted to the central-north part of the basin.

The Grajaú Formation is made of fine to conglomeratic, whitish sandstones interfingered with the bituminous shales, limestones and some anhydrite of the Codó Formation. The Codó sediments were deposited in a shallow marine environment interbeded with littoral sediments of the Grajaú. These formations have been deposited in the Middle Cretaceous approximately from 120 to 110 Ma and their maximum combined drilled thickness is 237 metres.

The Itapecuru Formation has been described as reddish, middle to coarse-grained sandstones and brown-reddish mudstones not exceeding 724 metres. This last sedimentation occurred in the Upper Cretaceous (110-100 Ma) with the deposition of the Itapecuru rocks in fluviolacustrine, estuarine and deltaic environments under a semi-arid climate.

Sedimentation cycles in the Parnaíba Basin eventually ended in the Upper Cretaceous (Senonian, ~85 Ma). The north equatorial coast was affected by tectonic activity related to the complete separation of the South American and African continents. Zones of NW-SE and NE-SW weaknesses experienced shear causing

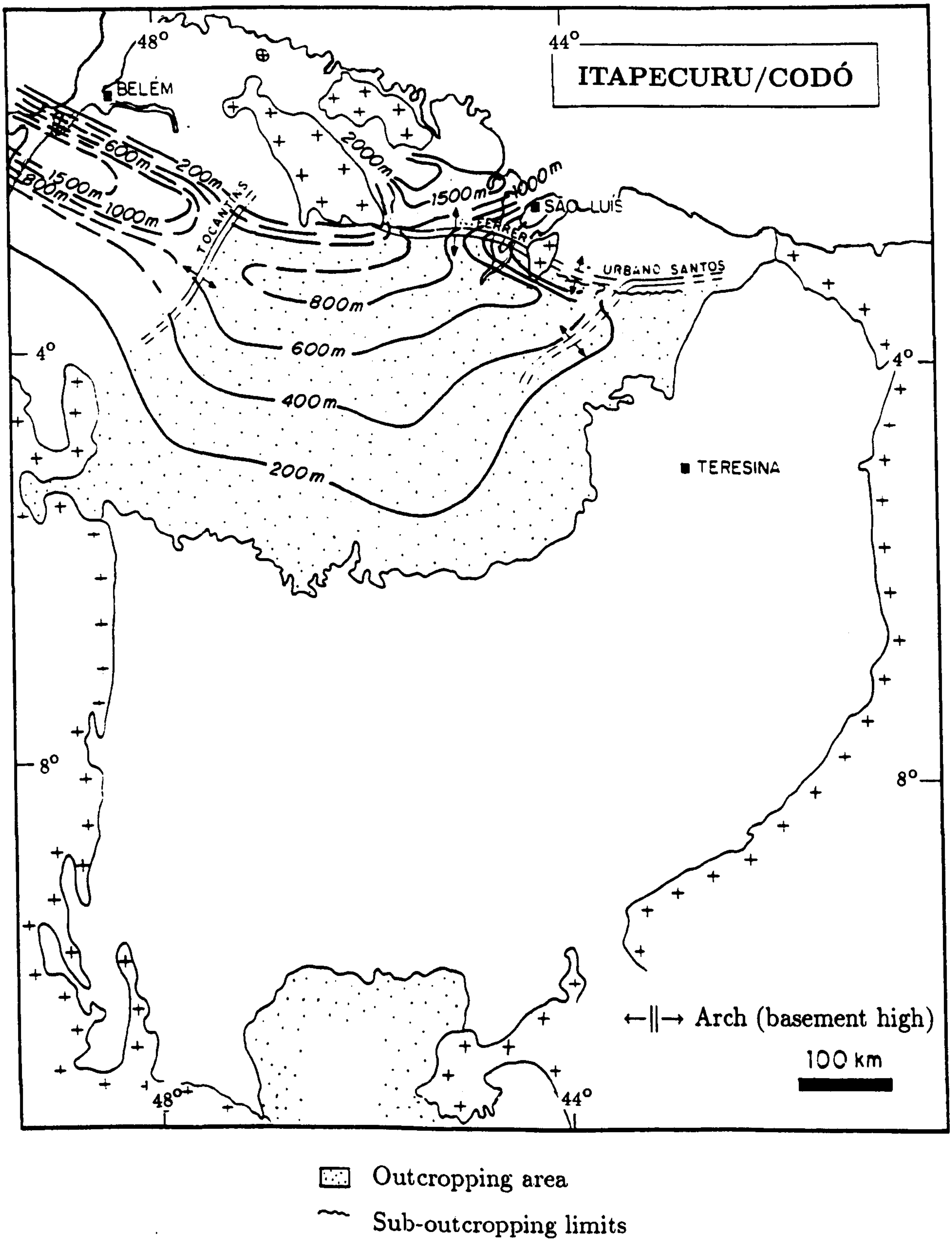

Fig. 2.22 Thicknesses of the Itapecuru/Codó Formations (*Cretaceous*). Contour interval: 100 m (after Góes *et al.*, 1993).

transcurrent dislocations, asymmetric anticlines and associated reverse faulting. This tectonic event ends the evolutionary history of the Parnaíba Basin.

2.4.6 Magmatism in the Parnaíba Basin: The Mosquito and Sardinha Formations

The initial stages of the rupturing of Gondwana reactivated N-S faults to the west of Parnaíba and NE-SW faults to the east. The magmatism in the Parnaíba Basin (Fig. 2.23) seems to have happened in pulses from the Lower Jurassic to the Middle Cretaceous. These intrusive and extrusive volcanics show radiometric ages from 215 to 110 Ma (Fig. 2.24), thus Parnaíba seems to have the longest record of volcanic activity affecting a Brazilian intracratonic basin.

About 90% of the observed sills intrude the Devonian sequence (Canindé Group) with the Silurian sequence (Serra Grande) taking the remaining 10%. Seismic and well data have shown that diabase sills do not reach the Carbonif-erous-Triassic strata. This has been associated with insufficient magmatic pressure as well as being due to the arenaceous barriers posed by the Poti and Piauí Formations, top and base of the Devonian and Carboniferous sequences, respectively. The diabases have not been grouped as individual units due to their non-specific stratigraphic position in the basin but are obviously associated with the magmatic pulses.

The extrusive magmatism of the Parnaíba Basin is bimodal in age and is represented by two-pyroxene flood basalts, the *Mosquito* and the *Sardinha Formations.*

The Lower-Middle Jurassic Mosquito Formation has been described as tholeiitic, amigdaloidal, black basalts, sometimes interfingered with red sandstones and silex beds and occurs between the Balsas and Mearim Groups. The Mosquito basalts outcrop to the west of Parnaíba and have been dated at 215-180 Ma.

The Mosquito flood basalts are characterized by low TiO_2 (< 2 wt.%) and incompatible element contents. Regarding Sr-Nd isotope data, the Mosquito tholeiites show initial $^{87}Sr/^{86}Sr$ (R_0) and present day $^{143}Nd/^{144}Nd$ (Nd_*) ratios in the ranges 0.7030-0.7075 and 0.51293-0.51248, respectively. These ratios suggest that the Mosquito basalts experienced low-pressure crustal contamination.

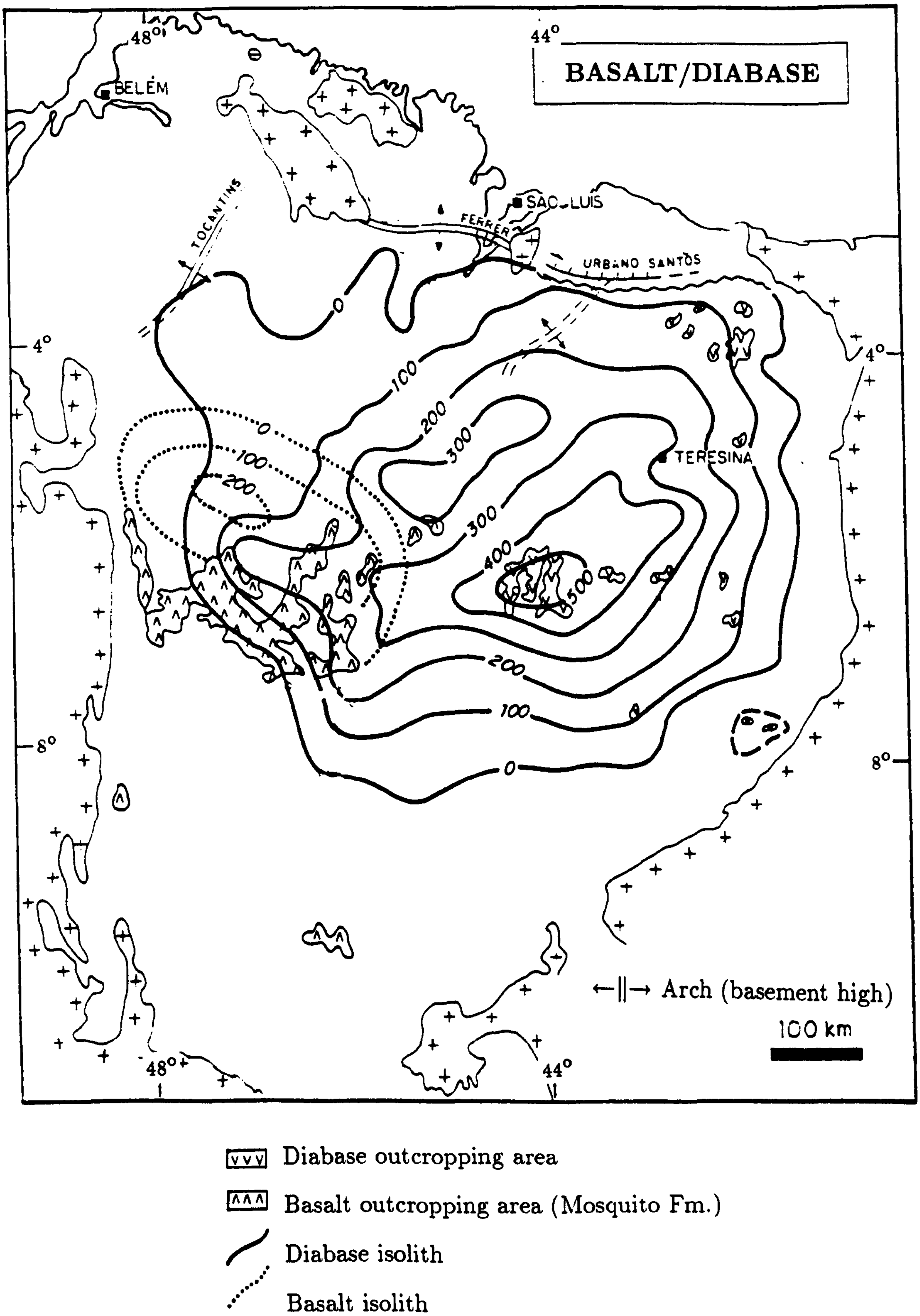

Fig. 2.23 Diabase/basalt isoliths. Contour interval: 100 m (after Góes et al., 1993).

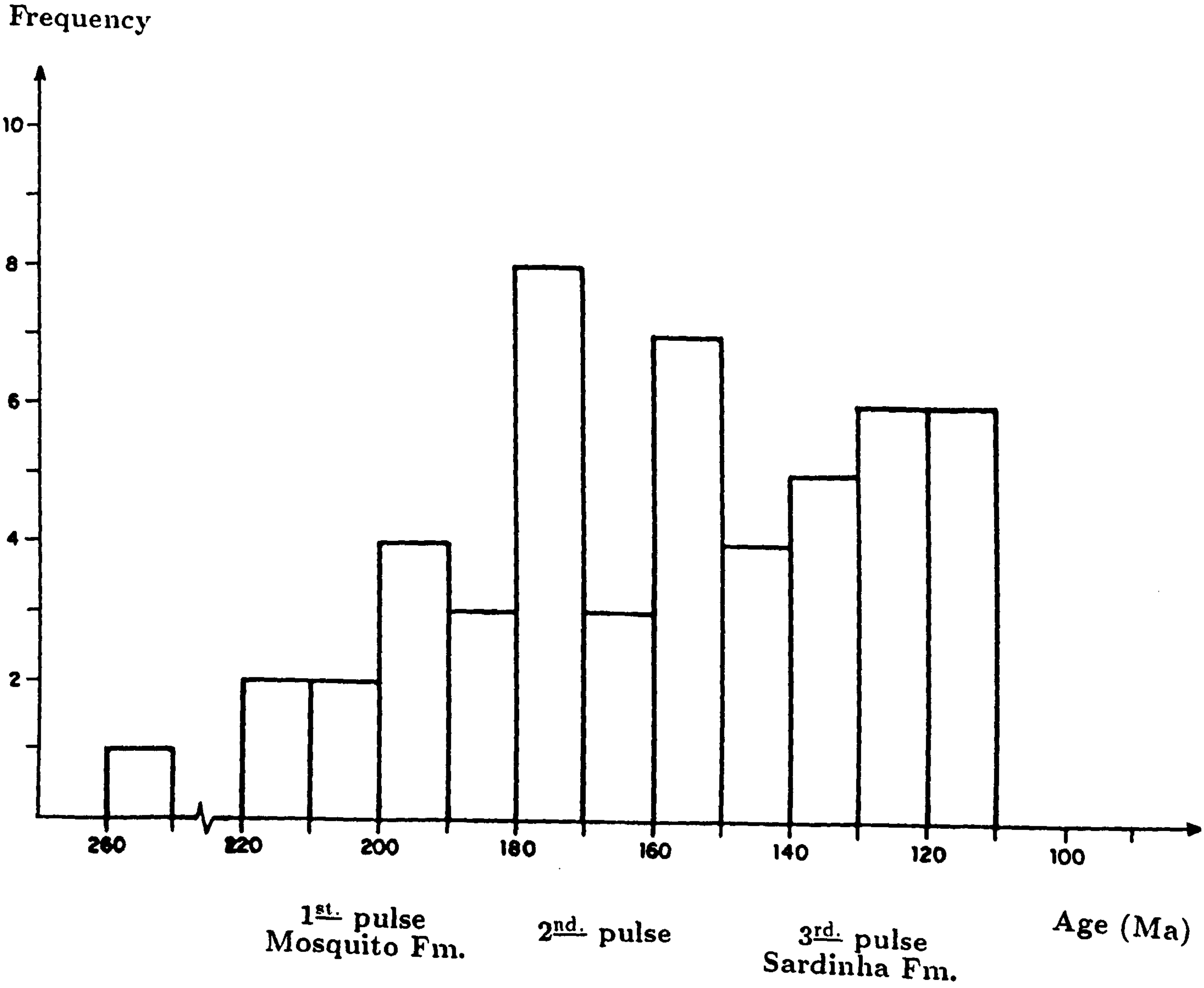

Fig. 2.24 Histogram of K-Ar dates for basalts and diabases sampled in the Parnaíba Basin (after Góes *et al.*, 1993).

The Sardinha Formation is made of Lower Cretaceous, black, amigdaloidal basalts overlaying the Mearim Group and subadjacent to the Grajaú/Codó Formations. Restricted outcropping occurs to the east of Parnaíba and its stratigraphic positioning is still controversial due to ill-defined contacts. The Sardinha basalts have been positioned as post-Corda and tentatively dated as 140 to 125 Ma.

The Sardinha basalts are high in TiO_2 (> 2 wt.%) and incompatible elements. Moreover, their R_0 and Nd_* ratios vary in restricted ranges (0.7054-0.7059 and 0.51247-0.51245, respectively) and do not show significant correlations with major and trace elements, thus suggesting appreciable crustal contamination. The associated intrusives have been found to correspond to Lower Cretaceous dyke swarms of the northeastern Borborema Province and to the coeval Benue Trough in west Africa (Bellieni *et al.*, 1992). Therefore, they may be related to early rifting events of the Equatorial South Atlantic. According to Popoff (1988), the time elapsed from eo-rift to complete oceanization in the Equatorial Domain was ~20-25 Ma.

In general, the Parnaíba basalt rock types show important mineralogical, chemical and Sr-Nd isotope similarities with the Lower Cretaceous two-pyroxene tholeiitic flood basalts of the Paraná Basin, in the south of Brazil (Bellieni *et al.*, 1990). The Mosquito basalts correspond chemically to the southern Paraná basalts (low Ti-type), whereas the Sardinha basalts are similar to those of high Ti-type of northern Paraná (De Sousa, 1983, Mantovani *et al.*, 1985).

2.5 Summary and Discussion

The geology of the Parnaíba Basin shows a broad, regional subsidence that initiated in the Upper Ordovician. Ancient aulacogenic covers have been drilled in a few boreholes and detected in (unreleased) seismic sections (Góes *et al.*, 1993). Schematic geological cross sections are shown in Fig. 2.25. They summarize the geological knowledge about the basin with data gathered from surface mapping, exploration boreholes, seismic sections, geochemical analysis and the interpretation of aeromagnetic anomalies. These sections also show the inferred location of ancient, precursory sedimentary covers. Figure 2.25a shows the approximate position of the Transbrasiliano Lineament crossing the section and an associated graben, according to the interpretation by Góes (1993) of the aeromagnetic map.

Fig. 2.25a Schematic W-E geological section across the Parnaíba Basin showing the sites of ancient sedimentary covers and magmatism (after Góes *et al.*, 1993).

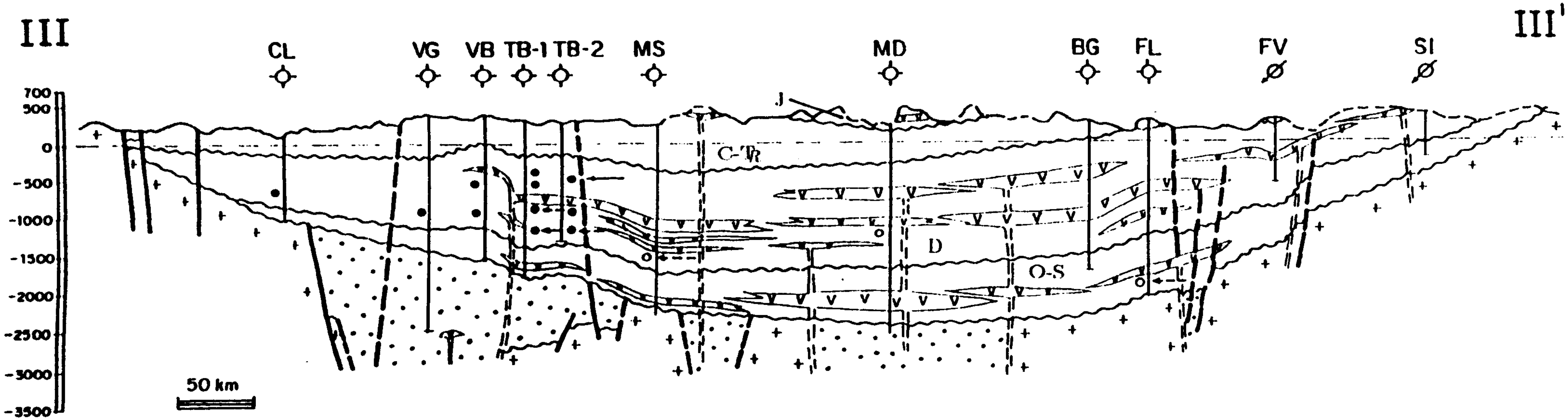

LEGEND

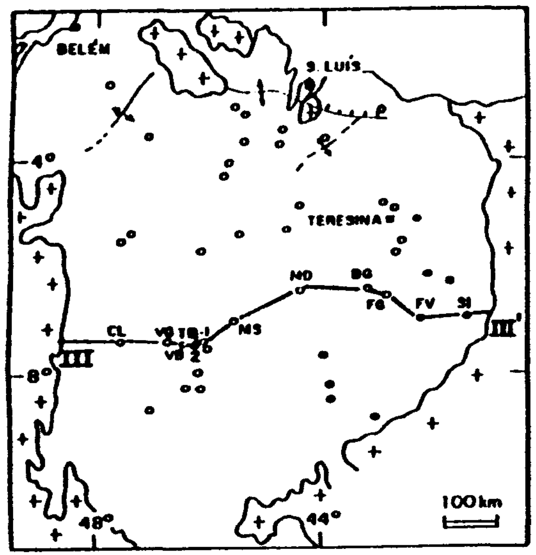

- K — CRETACEOUS
- J — JURASSIC
- BASALT/DIABASE
- C-TR — CARBONIFEROUS-TRIASSIC
- D — DEVONIAN
- O-S — UPPER ORDOVICIAN-SILURIAN
- PRESILURIAN
- BASEMENT
- OIL TRACE
- GAS TRACE
- FORMATION TEST (OIL)
- FORMATION TEST (GAS)
- OIL & GAS WELL
- GROUNDWATER WELL

Fig. 2.25b Schematic N-S geological section across the Parnaíba Basin showing the sites of ancient sedimentary covers, magmatism and basement highs (after Góes *et al.*, 1993).

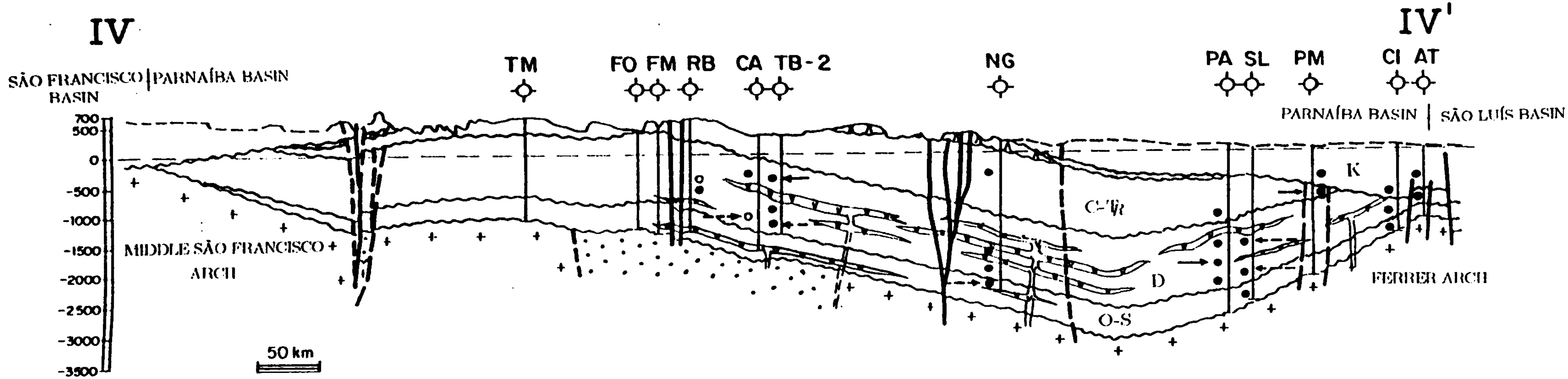

LEGEND

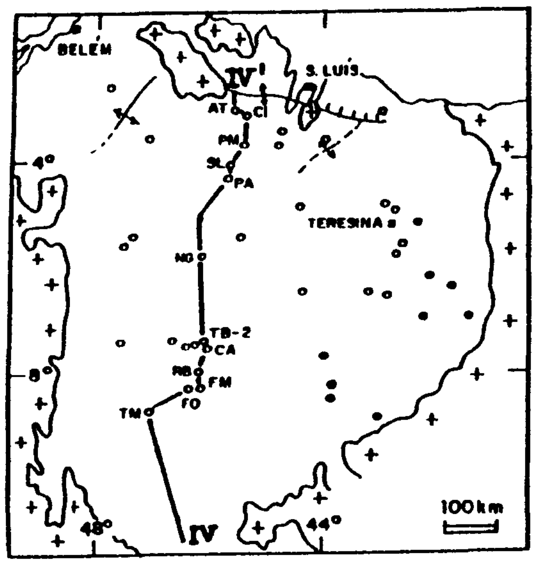

K	CRETACEOUS
J	JURASSIC
	BASALT/DIABASE
C-TR	CARBONIFEROUS-TRIASSIC
D	DEVONIAN
O-S	UPPER ORDOVICIAN-SILURIAN
	PRESILURIAN
	BASEMENT

- OIL TRACE
- GAS TRACE
- FORMATION TEST (OIL)
- FORMATION TEST (GAS)
- OIL & GAS WELL
- GROUNDWATER WELL

Figure 2.25b shows the truncation that Parnaíba suffered at the opening of the Equatorial Atlantic Ocean. Most of the Cretaceous sedimentation seems to be the reflex of isostatic accommodation following the strong erosion suffered during the thermal uplift.

The ancient, immature sediments found from the southwest up to the northwest of Parnaíba have been correlated with the Middle-Upper Proterozoic covers of the Amazon and the São Fancisco Cratons. It is possible that this grabenlike structure is associated with a general NW-SE faulting pattern as seen evident in the early phases of basinal development.

Strong NE-SW shear zones have been detected by geological mapping, satellite images, aerophotogrammetry, total intensity magnetic anomalies and, as will be seen in the Chapter 3, also by the Bouguer anomalies. These crustal discontinuities are of a polyciclic nature and were noticeably active during the Brasiliano Cycle. Several examples of sediment accumulation and volcanism have been recognized in grabens outcropping to the east, the northeast and to southwest of Parnaíba.

The NE-SW structures represent another important fault system affecting the basement of Parnaíba. These structures and the NW-SE oriented fractures of the Proterozoic grabens are the underlying tectonic fabric inherited from the Brasiliano and where the Parnaíba Basin initiated its development.

Several authors have discussed the possible break-up of a supercontinent in Upper Proterozoic time. The surviving record of early Palaeozoic sediments implies that by the Lower Cambrian the total length of passive margins was considerable, and a major widespread episode or episodes of rifting had occurred (Lindsay *et al.*, 1987; Lindsay, 1991; Klein & Hsui, 1987; Klein, 1991; Hartley & Allen, 1994). There is, however, some uncertainty in the precise timing of this break-up, with some workers suggesting that it occurred between 850 and 560 Ma (*e.g.* Piper, 1983) and others positioning it as 625-555 Ma (*e.g.* Bond *et al.*, 1984).

In Brazil, Cordani *et al.* (1984) and De Brito Neves *et al.* (1984, 1990) have called attention to the importance of tectonic rejuvenation of older structures, mainly at the latest phases of the Brasiliano Cycle, and their relationship to the subsequent Phanerozoic basins.

The main targets for oil exploration in the Parnaíba Basin are the Palaeozoic sandstones of Ipu, Itaim, Cabeças and Piauí Formations as well as the shales interbedded with sandstones of the Pimenteiras Formation (Petri & Fúlfaro, 1983; Cunha, 1986; Góes *et al.*, 1993). All exploration oil and gas wells drilled in this basin have been classified by PETROBRÁS as *dry*. Only three of them showed evidence of oil and gas during formation tests (Figs. 2.13 and 2.25):

- Well 2-CP-1-MA. Gas was found in fractured diabases intruding the Pimenteiras Formation and in sandstones of the Itaim Formation;
- Well 1-TB-2-MA. Up to 6 m of oil-soaked sandstone samples of the top of Cabeças Formation were recovered. Formation tests also produced water with oil traces; and
- Well 1-FL-1-MA. Gas and water were found in sandstones of the Ipu Formation with gas burning during reverse circulation.

The basinal stratigraphy of Parnaíba is reasonably well known. Source and reservoir rocks have been recognized but the basin is still classified as *virtually unknown* regarding oil traps.

The main mineral deposits in the Parnaíba Basin include alluvional gold and diamonds derived from the sandstones of the Serra Grande Group. Precious stones are explored to the northeast of Parnaíba, mostly associated to the Lower Palaeozoic magmatism present in outcropping grabens.

CHAPTER 3

GRAVITY DATA

3.1 Previous Gravity Data

The Parnaíba Basin is the least known of all Brazilian Palaeozoic basins and most of the geophysical data collection work in the area has been done by PETROBRÁS as part of their oil-exploration activities in the basin. This company is responsible for the largest gravity, aeromagnetic and exploratory boreholes data bases and is the only reference for seismic sections.

Besides PETROBRÁS, other Institutions which have gathered geophysical data in selected parts of the basin are: the CPRM (geological mapping/gravity/groundwater exploration boreholes); the Instituto Brasileiro de Geografia e Estatística-IBGE (gravity/geometric levelling); the Instituto de Pesquisas Tecnológicas [Technological Research Institute]-IPT (geothermics); the Brazilian government owned holding Empresas Nucleares Brasileiras [Brazilian Nuclear Companies]-NUCLEBRÁS (aeromagnetism/aerogammaspectrometry), the Observatório Nacional-ON (gravity/magnetotelluric) and the Universidade Federal do Pará-UFPa (gravity/ geological mapping).

The present study of the Parnaíba Basin covers a 12° by 12° square with the SW corner at (12°S, 50°W) and NE corner at (0°, 38°W).

There are 9,658 PETROBRÁS gravity stations used in this study, these being a sub-set of their original 78,746 station data base. The sampling procedure used did not cause any loss of quality in the distribution of the gravity stations and simply reduced their number to a more tractable data set, compatible with the regional interpretation sought after. The PETROBRÁS gravity measurements were made with a Worden gravimeter and were originally tied to the Potsdam 1930 *datum* through Woollard base stations in Brazil (Fachetti, 1961; Woollard *et al.*, 1954).

Gravity stations established by CPRM, IBGE and UFPa are tied to the Brazilian Gravity Reference Network-BGRN which has been referred either to the IGSN

71 or to the Absolute Gravity Stations Network established in Brazil. These Institutions used only LaCoste & Romberg gravimeters for their measurements. There are 1,892 stations established by CPRM, 2,702 by IBGE and 1,162 by UFPa, bringing the total number of already existing gravity stations over the selected area to 15,414.

Fig. 3.1 shows the distribution of gravity stations. Although the total number is reasonable, its distribution is inadequate, clearly showing the *aligned random* and *aligned stratified random* patterns usually seen in land gravity surveys (Eckstein, 1989). These patterns usually occur because land gravity surveys tend to avoid regions with steeper relief.

The altimetric control of the gravity stations was given by:

- geometrical levelling on IBGE gravity stations which are coincident with bench marks of the Brazilian Levelling Reference Network. The reported error is better than 0.01 m;
- trigonometric levelling on PETROBRÁS gravity stations with a reported error (Fachetti, 1961) better than 2.0 m; and
- barometric levelling on CPRM and UFPa stations located on roads devoid of bench marks. Height values of these stations are accurate to ±5 m.

The positioning of all gravity stations has been done on 1:100,000 or 1:250,000 scale maps.

3.1.1 Data Reduction

All gravity values have been referred to the International Gravity Standardization Net 1971-IGSN 71 (Morelli, 1972). The PETROBRÁS measurements were made consistent with the IGSN 71 by adding a constant value of -15.0 mGal* as proposed by De Sá & Blitzkow (1986).

---

* The present thesis adheres to SI units. Nevertheless, for the sake of tradition, the mGal was adopted in the text with the known equivalence 1 mGal = 10^{-5}m s^{-2}.

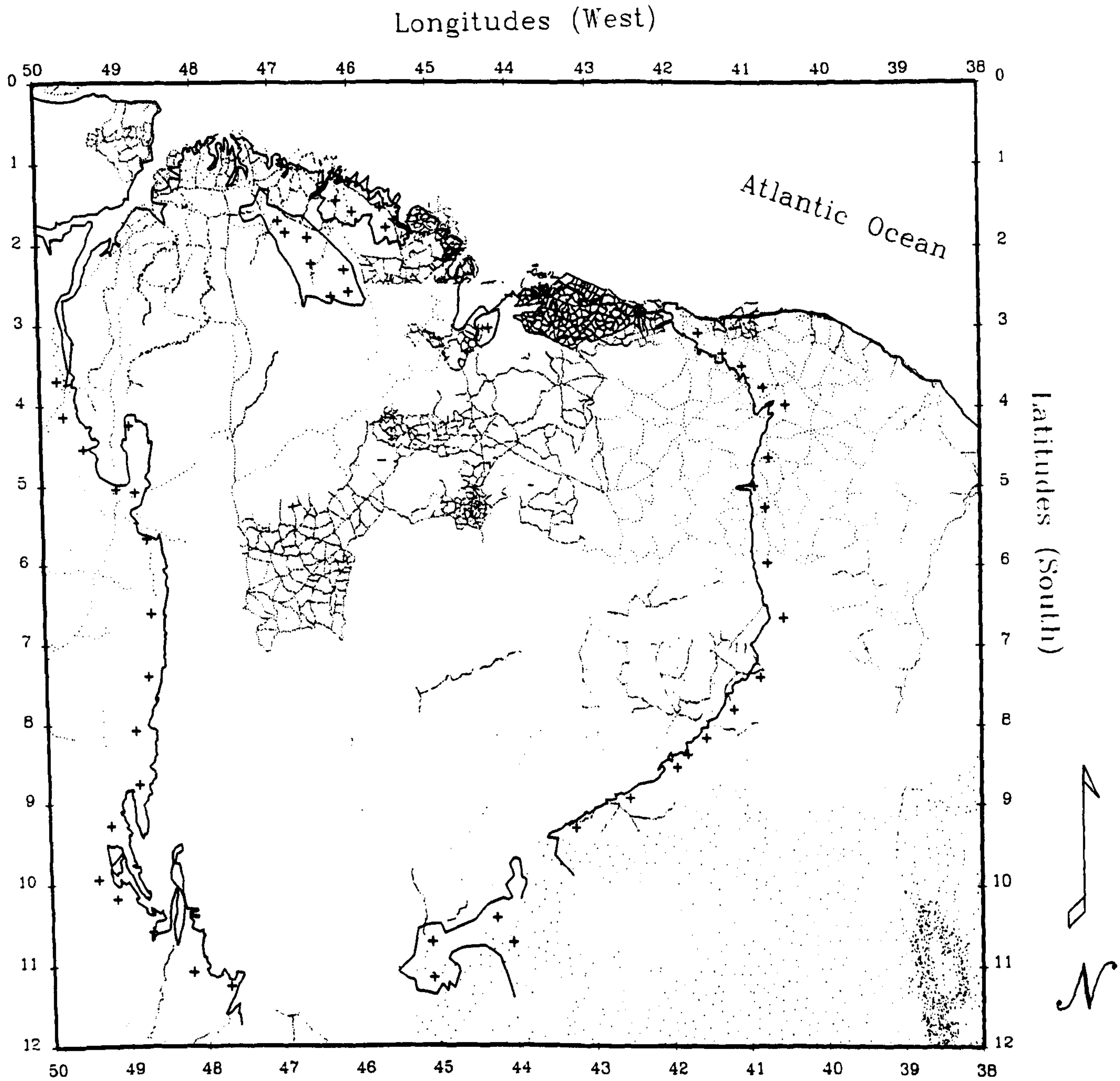

Fig. 3.1 Previous gravity stations (15,414) over the Parnaíba Basin and adjacent geological provinces. Data sources: PETROBRAS (9,658), IBGE (2,702), CPRM (1,892) and UFPa (1,162). Conic projection.

The latitude correction was carried out using the 1967 International Gravity Formula. Given the latitude range of the study area and a maximum error in the positioning of 200 m, an accuracy better than 0.1 mGal can be expected for the latitude correction.

The main error source in gravity reductions is usually the uncertainty in altitude. The free-air correction was computed using a vertical gradient of -0.3086 mGal m^{-1}. Considering the worst case of a height uncertainty of 8 m and taking 2,670 kg m^{-3} as a representative density of upper crustal rocks, the error in the combined elevation correction can be as much as ± 1.6 mGal. Whilst the error due to the uncertainty in altitude can be regardered as random, an incorrect choice of the density value for the Bouguer correction introduces a systematic error (Ussami, 1986). A correlation between Bouguer anomalies and shorter wavelength topographic features may be observed in regions of significant topographic variation. Since the average altitude in the Parnaíba Basin is about 200 m, an error of ± 50 kg m^{-3} in the Bouguer density introduces a systematic error of 0.42 or -0.42 mGal.

Bouguer anomalies computed by PETROBRÁS for their stations used a density value of 2,200 kg m^{-3}. Similarly, CPRM computed Bouguer anomalies employing a density value of 2,600 kg m^{-3}. Since these densities seemed to be too low to be representative of the basement rocks beneath the basin, a more appropriate density value was used instead. The chosen value was 2,670 kg m^{-3}, the standard Bouguer density, since this is a well known average crust density over large continental areas, allowing direct comparison of gravity anomalies found in Parnaíba with those found elsewhere. The chosen value is compatible with density measurements on 158 crystalline rocks of the adjacent São Francisco Craton. Ussami & Padilha (1982) reported a mean value of 2,710 $\pm$ 60 kg m^{-3}, similar to the value obtained by Gibb (1968) for the Canadian Shield rocks. This density value characterizes an upper crust of granodioritic to dioritic composition and samples of these rocks have already been drilled in the basement of the Parnaíba Basin (see Fig. 2.10).

Terrain corrections were not applied to the Bouguer anomalies, given the usual modest topography of the Parnaíba Basin. Fachetti (1961) computed terrain corrections for PETROBRÁS stations yielding a maximum value of 0.51 mGal to the east border of Parnaíba, where the roughest relief is found.

To summarize, the maximum random error in the Bouguer anomalies is 1.0 mGal for stations with barometric heights and the maximum systematic error does not exceed 0.5 mGal.

3.2 Fieldwork Data

Since the available gravity data distribution was not adequate for quantitative interpretation, it was necessary to do fieldwork in those areas devoid of or with very little data. Several campaigns were directed mainly to the west, southwest and southeast basin borders. Land surveys were carried out using 1 or 2 LaCoste & Romberg gravimeter(s), 5 American Paulin or 4 Thommen precision altimeters for measuring heights at gravity stations and 2 other sets of Wallace & Tiernen precision altimeters, for the dual base or "hi-lo" method (Hodgson, 1979). Each set included 3 W & T barometers. Gravimeter readings were taken preferably on bench marks at an average distance of 3 km. When barometric levelling was needed, gravimeter/barometer readings were taken every 5 km between departure and arrival bases, the distance between bases being 50-60 km. Base sites were always bench marks and air-pressure readings were taken every 10 minutes.

Computer code had to be written for appropriate gravity and topography field data reduction. Barometric heights of the gravity stations were computed by subtracting the diurnal pressure variation recorded at bases A and B, separated by distance d, from the mean barometric reading at a given gravity station. The correction for the diurnal pressure variation was obtained after a linear combination of the records at both bases with weighting factors given by the distances of the gravity station (roving altimeters) to the two bases, *i.e.*

$$Correction = \frac{(d-l)DV_A + lDV_B}{d},$$

where l is the distance between the roving altimeters and base A and DV_A, DV_B are the diurnal variation records at bases A and B, respectively. This dual base method was used to correct for diurnal pressure variation and improve the quality of height determinations with errors better than 5 m. Occasionally, errors in the range of 8-10 m were sometimes detected, when height values were computed for a few bench marks found in a given barometric levelling line. This was probably due to sudden equatorial microclimatic changes causing instabilities in the barometric cells.

Program **GRR.FOR** (De Sousa & Seixas, 1995) computes gravity values for all stations measured during a fieldwork session and refers them to the BGRN (IGSN 71). Given the reported (Sevilla *et al.*, 1990) different behaviour of gravimeters when kept at rest for a period of time (*static drift*) and when subject to vibrations of a moving platform (*dynamic drift*), the algorithm developed corrects the total instrumental drift through a two-step procedure. Firstly, the static drift (in mGal) is sequentially removed by taking out those small differences in gravity readings at the same station with the gravimeter not being transported (usually overnight measurements). Secondly, after filtering out the static drift and the corresponding rest periods of the gravimeter, the dynamic drift is accounted for by computing ratios (in mGal h^{-1}) given by differences in gravity readings at the same station and the time interval between them. Each ratio is associated to the mean time of the readings and this procedure allows sampling the temporal behaviour of the meter, including possible non-linearities in the drift (Pennybaker, 1988). After ordering these ratios in time and performing linear interpolation between them, numerical integration from $t = 0$ (the beginning of the campaign) to $t = t_{Max}$ (end of the campaign) produces the drift correction *plus noise*. Given the known long-term stability of gravimeters, a low-pass filter applied to the time-integrated curve is able to remove the noise caused by operational errors. The smoothed curve in time obtained from $t = 0$ to the time of the gravity observation produces the amount of *dynamic drift correction* to be added to that reading.

A total of 2,060 new gravity stations were established in the study area, wherever access was possible, and their distribution is shown in Fig. 3.2. Several data gaps persist in the gravity coverage because access was beyond the logistic capabilities of the surveys.

The new gravity stations also had their gravity anomalies computed using the International Gravity Formula 1967; the normal gravity gradient of -0.3086 mGal m^{-1} and an average upper crust density of 2,670 kg m^{-3}. Likewise, the maximum systematic error did not exceed 1.0 mGal and the maximum random errors were 2.0 mGal.

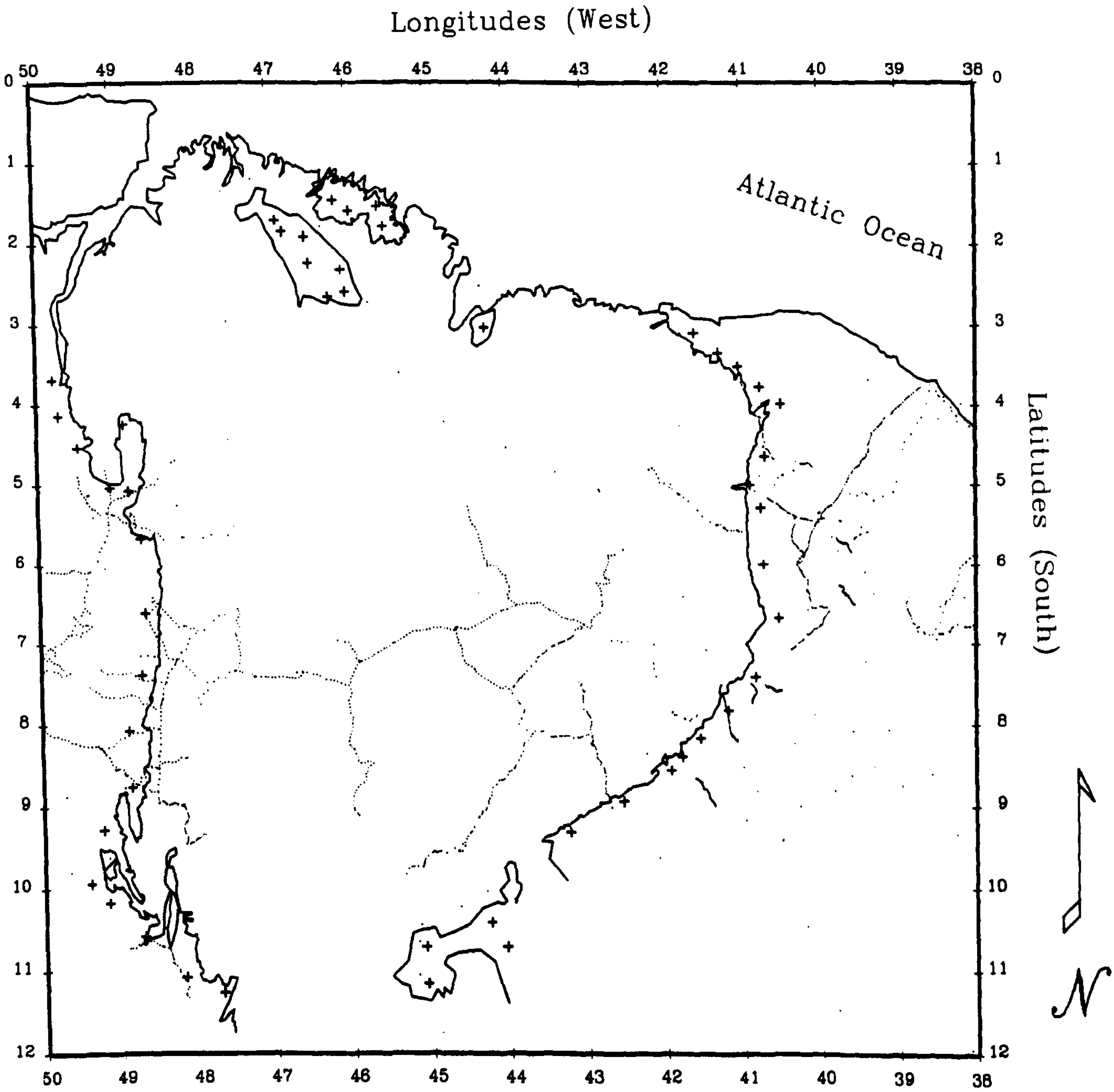

Fig. 3.2 Gravity stations (2,160) established in fieldwork campaigns in the Parnaíba Basin. Conic projection.

3.3 The LC & R 61 Gravity Network

An agreement with the Departamento de Geofísica of the Observatório Nacional in Rio de Janeiro not only granted partial funding of necessary fieldwork but also allowed the release of gravity stations already measured in the selected area - provided their whole data set (4,090 LaCoste & Romberg measurements on 1,484 stations and 7,258 Worden measurements on 1,635 stations) covering a large area of the Brazilian territory - was adequately reduced and referred to a modern *datum*. These gravity measurements were still tied to the Potsdam 1930 *datum* and a single absolute gravity value (the Rio de Janeiro station) had been used to derive the absolute gravity values of all the other stations in the net.

Reduction of part of this data set has been accomplished (De Sousa & Moreira, 1994). There are 660 LC & R gravity stations within the study area (Fig. 3.3) and all are bench marks (no Worden gravity stations). The LC & R 61 gravity network is shown in Fig 3.4. All gravity measurements have been adjusted and referred to the IGSN 71. The criteria employed and the methodology followed in computing absolute gravity values for all stations forming the polygons of this large net are discussed in the next sections.

3.3.1 Mathematical Models for Gravimetric Adjustment

The algorithms used for gravity network adjustment are usually based on the least-squares method (the L_2 norm), where an *economized* (Uotila, 1976) mathematical structure is sought to compute the maximum likelihood estimators of physical observables. The mathematical structure relates measured quantities and functions of some parameters either explicitly or implicitly. For a given set of n measured quantities the number of u mutually independent parameters is kept fixed and the structure is said to be economized when u is kept as small as possible. An adjustment is necessary when $n > u$ and the difference $n - u = r$ is the number of mutually independent conditions. Strictly speaking, the gravity readings are actually the available observed (measured) independent quantities while the gravity intervals are formed by their differences. Although the gravity intervals are not strictly independent they are usually considered to be the appropriate input data for gravity adjustment with a diagonal variance-covariance matrix.

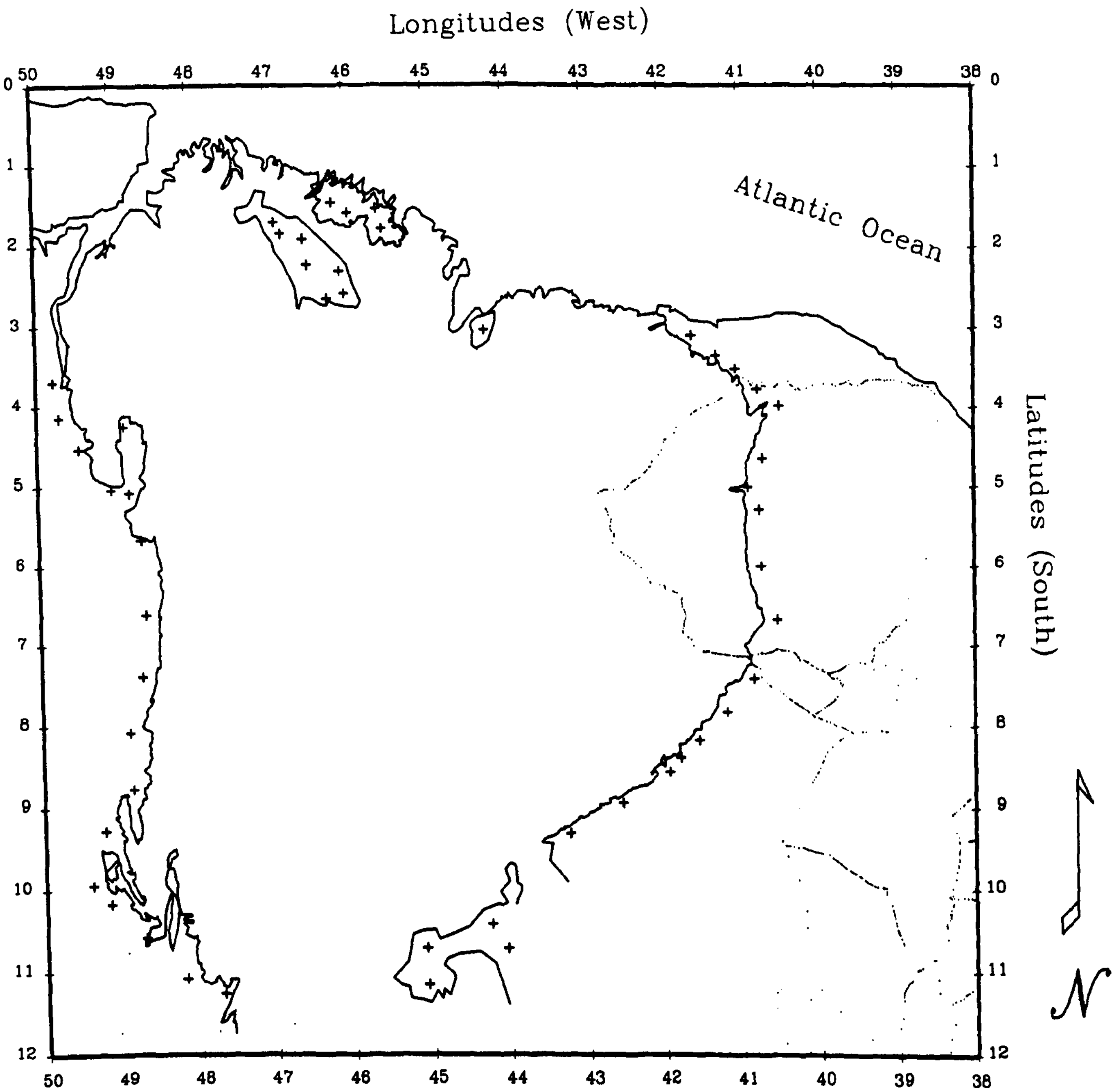

Fig. 3.3 LaCoste & Romberg 61 gravity stations (660) in the Parnaíba Basin and adjacent areas. Conic projection.

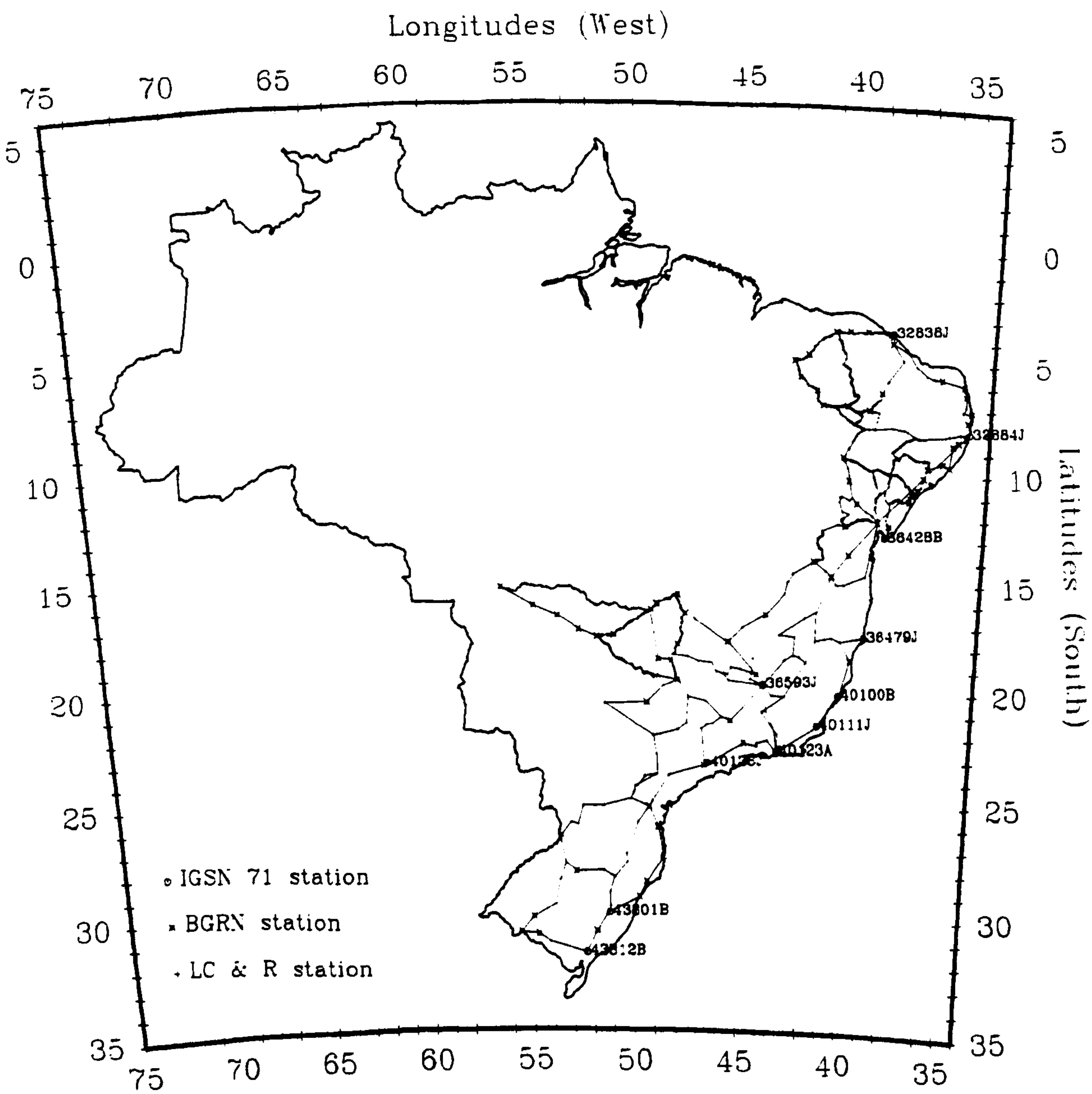

Fig. 3.4 The LaCoste & Romberg 61 gravity network (De Sousa & Moreira, 1994) comprising 32 polygons and 1,484 gravity stations. Conic projection.

The following matrix notation is used in adjustment theory:

$X_0 = (x_{0_i})$, approximate values for the parameters which are numerical values selected before the adjustment;

$X_a = (x_{a_i})$, values obtained as results of the adjustment;

$L_b = (l_{b_i})$, observed values of quantities;

$L_0 = (l_{0_i})$, computed values of the observed quantities taking a mathematical structure as a function of X_0; and

$L_a = (l_{a_i})$, adjusted values of the observed quantities.

Using the notation above the following differences can be established:

$X = X_a - X_0$ or $X_a = X_0 + X$, vector X: the corrections vector;

$L = L_b - L_0$, the discrepancy before the adjustment; and

$V = L_a - L_b$, the vector of residuals.

A mathematical model can be expressed as (Uotila, 1976; Lugnani, 1983):

$$F(X_a, L_a) = 0, \tag{3.1}$$

where $F = (f_i)$, $i = 1, 2, \ldots, m$ is a vector of functions associating the adjusted parameters $X_a = (x_{a_i})$, $i = 1, 2, \ldots, u$ to the adjusted values for the observables $L_a = (l_{a_i})$, $i = 1, 2, \ldots, n$. The mathematical model can be linear or non-linear whereas it has to be linearized in order to find its solution.

Considering the linear case when the vector of approximate parameters $X_0 = (x_{0_i})$, $i = 1, 2, \ldots, u$ and the vector of observed quantities $L_b = (l_{b_i})$, $i = 1, 2, \ldots, n$, are sufficiently close to X_a and L_a, respectively, the model described by Equation 3.1 can be approximated by a Taylor series development around X_0, L_b and truncated in the linear term,

$$F(X_a, L_a) = F(X_0, L_b) + X\left(\frac{\partial F}{\partial X_a}\right)_{X_a = X_0, L_a = L_b} + V\left(\frac{\partial F}{\partial L_a}\right)_{X_a = X_0, L_a = L_b}$$

or

$$AX + BV + W = 0, \tag{3.2}$$

where

$$A = \left(\frac{\partial F}{\partial X_a}\right)_{X_a=X_0, L_a=L_b},$$

$$B = \left(\frac{\partial F}{\partial L_a}\right)_{X_a=X_0, L_a=L_b}$$

and

$$W = F(X_0, L_b).$$

Being m the number of equations in the system, u the number of parameters and n the number of observations, Equation (3.2) can be written as

$$_mA_{uu}X_1 +_m B_{nn}V_1 +_m W_1 = 0, \tag{3.3}$$

which is a consistent system of linear equations with $n+u$ unknowns and $m < n+u$ equations to be solved for X and V.

Solution of Equation (3.3) under the least-squares criteria (the L_2 norm) is obtained by including a vector K composed of Lagrange multipliers and minimizing the function

$$\Phi = V^TPV + 2K^T(AX + BV + W). \tag{3.4}$$

Here P is a weight coefficient matrix for the observations. If all observations have the same precision then $P = I$ (the Identity matrix). Note that when Equation (3.3) is satisfied the parenthesis in (3.4) is also nulled.

Imposing the usual condition that the derivatives of Φ with respect to X and V should be zero,

$$A^TK = 0,$$

$$PV + B^TK = 0,$$

These relationships can be combined with Equation (3.3), leading to a consistent set of $u+n+m$ equations with the same number of unknowns that can be written as

$$\begin{pmatrix} P & B^T & 0 \\ B & 0 & A \\ 0 & A^T & 0 \end{pmatrix} \begin{pmatrix} V \\ K \\ X \end{pmatrix} + \begin{pmatrix} 0 \\ W \\ 0 \end{pmatrix} = 0, \tag{3.5}$$

making a system of normal equations.

For small problems this system can be directly solved by inverting the coefficient hypermatrix. Assuming that no singularities are present for Cayley inversion,

$$\begin{pmatrix} V \\ K \\ X \end{pmatrix} = \begin{pmatrix} P & B^T & 0 \\ B & 0 & A \\ 0 & A^T & 0 \end{pmatrix}^{-1} \begin{pmatrix} 0 \\ W \\ 0 \end{pmatrix}.$$

This solution is not computationally attractive due to computer storage needs and processing time - proportional to the cube of the rank of the matrix. The solution of the system (3.5) is usually sought rewriting it as

$$NY + U = 0,$$

which can be partitioned as

$$\begin{pmatrix} N_{11} & N_{12} \\ N_{21} & N_{22} \end{pmatrix} \begin{pmatrix} Y_1 \\ Y_2 \end{pmatrix} + \begin{pmatrix} U_1 \\ U_2 \end{pmatrix} = 0.$$

Assuming N_{11} non-singular, this can be further developed as

$$\begin{aligned} N_{11}Y_1 + N_{12}Y_2 + U_1 &= 0, \\ N_{21}Y_1 + N_{22}Y_2 + U_2 &= 0, \\ \implies Y_1 &= -N_{11}^{-1}(U_1 + N_{12}Y_2) \end{aligned}$$

resulting in

$$(N_{22} - N_{21}N_{11}^{-1}N_{12})Y_2 + (U_2 - N_{21}N_{11}^{-1}U_1) = 0.$$

The application of the development above to the system of normal equations (3.4) leads to the solution

$$X = -[A^T(BP^{-1}B^T)^{-1}A]^{-1}A^T(BP^{-1}B^T)^{-1}W$$

with the following expressions for the matrix of residuals,

$$V = -P^{-1}B^T(BP^{-1}B^T)^{-1}(AX + W)$$

and for the variance of unit weight,

$$\sigma_0 = \frac{V^TPV}{(m-u)}.$$

If it is assumed that $A = 0$ in Equation (3.2) we get the so called method of *condition equations* or *correlates* for the adjustment of observations only, with no parameters involved. It is desired to find out the best estimates for the observed (measured) quantities. In the specific case of a gravity network these observables are the gravity intervals measured between stations and the condition is imposed that the circulation of the gravity field along any closed path is zero. Condition equations are usually applied as a preliminary adjustment since they deal only with actually measured quantities, not being affected by sources of errors external to the gravity network. This allows having a pure estimate of the quality of observations avoiding error propagation from other sources. On the other hand, at least one known absolute gravity value is needed to assign g values to all other gravity stations.

The corresponding mathematical model Uotila (1976) for the condition equations is

$$F(L_a) = 0$$

and its linearized form can be written as

$$BV + W = 0,$$

where

$$B = \left(\frac{\partial F}{\partial L_a}\right)_{L_a = L_b}$$

and $W = F(L_b)$.

The vector of residuals V, assumed small, should be added to the vector L_b of observed values to get the vector of adjusted observations L_a. Then, given an appropriate weight matrix P for the observations L_b,

$$L_a = L_b + V,$$

with

$$V = P^{-1}B^T K,$$
$$K = -M^{-1}W, \quad \text{and}$$
$$M = BP^{-1}B^T.$$

The variance-covariance matrix Σ_{L_a} for the adjusted observations is

$$\Sigma_{L_a} = \sigma_0^2 P^{-1}(I - B^T M^{-1} B P^{-1}),$$

where $\sigma_0^2 = V^T PV/m = -K^T W/m$ and m is the number of condition equations. The rank of the coefficient matrix M is given by the number of polygons in the network. It is much smaller than the number of unknown gravity stations, what greatly reduces the computing effort when compared either to the implicit or to the parametric model.

When $A \neq 0$ and $B = -I$ we get the *parametric* or *observation equations* method with the corresponding mathematical structure, *e.g.* Lugnani (1983),

$$L_a = F(X_a),$$

where F is a generically non-linear functional.

The problem is usually linearized by performing a Taylor series expansion around the approximate values X_0,

$$AX = L + V$$

with

$$A = \left(\frac{\partial F}{\partial X_a}\right)_{X_a = X_0}.$$

Since $F(X_a) = L_b + V, F(X_0) = L_0$ and $L = L_b - L_0$, the solution can be found by minimizing the function $\Phi = V^T PV$ in the L_2 sense. The corrections vector X and the residuals are then given by

$$X = (A^T PA)^{-1} A^T PL,$$
$$V = AX - L.$$

Given the generic non-linear nature of F and the linear approximation taken, the final solution is found iteratively by establishing,

$$X_a = X_0 + X \longrightarrow X_0'$$

$$X_a' = X_0' + X'$$

until convergence is eventually reached.

After the final set of adjusted values for the parameters is obtained their dispersion can be estimated through

$$\sigma_0^2 = \frac{V^T P V}{n-u}$$

with the variance-covariance matrix given by

$$\Sigma_X = \sigma_0^2 (A^T P A)^{-1}. \tag{3.6}$$

3.3.2 Adjustment of the LC & R 61 Network to the IGSN 71

The gravity intervals measured with the LC & R 61 were provisionally adjusted using the condition equations method applied to the 32 polygons defined by the network in Fig. 3.4. There are 88 gravity intervals defining the polygons and 6 additional intervals tying the network to IGSN stations. Table 3.1 shows the misclosures for each circuit before the adjustment. The polygons were defined by node stations which were considered as those gravity stations with at least three ties to neighbouring stations. This helped diminish the size of the matrices involved in the problem.

Table 3.1 Polygon misclosures (in mGal).

#	Miscl.	#	Miscl.	#	Miscl.	#	Miscl.
1	.027	9	-.083	17	-.119	25	-.428
2	.056	10	.109	18	-.018	26	.471
3	.057	11	.191	19	-.096	27	.065
4	.268	12	-.187	20	.178	28	.115
5	-.108	13	.076	21	-.076	29	.142
6	.211	14	.205	22	.292	30	.097
7	-.065	15	-.010	23	.098	31	-.450
8	-.061	16	.015	24	-.218	32	.206

Since the observer was always the same for all measurements and most gravity intervals of the network had the same number of determinations (and were usually measured twice), the precision might be considered as the same for all intervals, i.e. the weight matrix could be set to the Identity matrix. However, the number of subintervals between two node stations is quite different, imposing a different precision to the total gravity interval. As a first approximation the weight matrix was set to I and an initial variance of unit weight σ_0^2 as well the residuals could be estimated. After that, a diagonal weight matrix was iteratively fitted as

$$P = \sigma_0^2 \Sigma_{L_b}^{-1} = \sigma_0^2 \begin{pmatrix} \frac{1}{\sigma_1^2} & 0 & \dots & 0 \\ 0 & \frac{1}{\sigma_2^2} & \dots & 0 \\ \vdots & \vdots & \ddots & \vdots \\ 0 & 0 & \dots & \frac{1}{\sigma_{88}^2} \end{pmatrix}$$

with elements σ_i^2, $i = 0, 1, \dots, 88$ being recomputed at each step.

The application of the method of correlates produced a variance of unit weight, $\sigma_0^2 = 0.00170916$ mGal^2, which can be considered as an estimate for the variances of all conditionally adjusted intervals with an adequate weight matrix. The standard deviation was found to be 0.041 mGal and this is an estimate of the quality (precision) of the LC & R 61 measurements. Table 3.2 shows that the largest residuals are found in intervals #10, 14, 17, 19, 31, 52, 57, 68, 76, 79 and 85 as result of the iterative least-squares procedure adopted.

Table 3.2 Conditionally adjusted gravity intervals.

Interval	Value (mGal)	Residual (mGal)	Variance (mGal^2)
1	-355.434	.014	.00092758
2	50.922	.012	.00101369
3	466.120	-.026	.00116813
4	-161.607	-.026	.00116813
5	-541.357	-.040	.00097063
6	185.923	-.002	.00091915
7	-72.274	-.008	.00103331
8	309.119	-.039	.00114285
9	-126.810	-.031	.00141423
10	-143.942	-.184	.00259616
11	-98.689	-.006	.00134254
12	203.050	-.025	.00122557
13	94.116	-.031	.00141423
14	-37.598	.088	.00186670
15	240.648	-.005	.00126946

Table 3.2 (continued) Conditionally adjusted gravity intervals.

Interval	Value (mGal)	Residual (mGal)	Variance ($mGal^2$)
16	-63.655	-.013	.00118277
17	-80.465	-.041	.00108205
18	12.509	-.038	.00130815
19	59.928	-.082	.00110612
20	71.682	-.038	.00130815
21	59.928	-.017	.00110612
22	-43.186	.029	.00073607
23	43.186	.032	.00073607
24	-32.158	.028	.00117858
25	-164.276	.038	.00103031
26	72.782	.004	.00123516
27	97.684	-.010	.00117593
28	-93.272	-.027	.00113267
29	-168.688	-.034	.00115366
30	-123.991	-.003	.00132138
31	-10.424	-.100	.00231861
32	153.299	-.021	.00139192
33	-421.232	.021	.00089427
34	-315.838	-.029	.00097033
35	-105.394	-.026	.00087647
36	-68.904	-.013	.00139747
37	-79.171	-.013	.00139747
38	-177.291	-.013	.00139747
39	-72.146	-.013	.00139747
40	65.406	.000	.00110706
41	16.269	.003	.00109021
42	-144.010	-.003	.00099476
43	54.886	-.009	.00102523
44	-69.263	-.013	.00115076
45	-9.342	-.006	.00107694
46	-137.009	.000	.00113010
47	33.313	-.008	.00133877
48	-212.005	-.007	.00134198
49	54.169	.018	.00103453
50	66.372	-.007	.00134198
51	86.966	-.009	.00109178
52	-86.966	.105	.00109178
53	-37.209	-.031	.00088849
54	4.411	-.025	.00119254
55	-75.600	.039	.00095392

Table 3.2 (continued) Conditionally adjusted gravity intervals.

Interval	Value (mGal)	Residual (mGal)	Variance (mGal^2)
56	38.391	.006	.00103931
57	-105.268	-.241	.00299181
58	-43.734	.021	.00118701
59	-6.878	.000	.00127094
60	80.280	-.033	.00138884
61	-58.890	-.028	.00118800
62	42.240	-.027	.00110352
63	-27.083	-.021	.00110191
64	131.386	-.026	.00139202
65	-242.716	-.026	.00139202
66	-52.828	.001	.00127615
67	35.866	-.027	.00137579
68	-40.608	.423	.00264615
69	-5.846	.006	.00132222
70	28.835	-.031	.00137500
71	-205.850	-.019	.00132474
72	136.407	.002	.00132047
73	56.938	-.021	.00132668
74	18.092	-.023	.00122038
75	21.571	-.033	.00136936
76	-95.671	-.141	.00385028
77	-91.197	-.012	.00140938
78	37.956	-.002	.00139608
79	-94.045	-.173	.00348663
80	128.649	.016	.00122939
81	21.444	-.010	.00144098
82	98.225	-.026	.00125498
83	19.631	-.030	.00124855
84	10.792	-.026	.00114837
85	-95.803	.416	.00253561
86	115.434	.004	.00144801
87	12.456	.000	.00145837
88	-195.275	.000	.00145837

After correcting for misclosures the parametric method was iteratively applied to the node stations, taking the gravity values for the IGSN 71 stations as fixed. The IGSN 71 has been used as the source of *datum* and scale in the present work and Table 3.3 lists the eleven IGSN 71 stations tied to the LC & R 61 network. A difference in scale between the IGSN g values and the previously published (Gama, 1971, 1972, 1973) g values is clearly seen in this table.

Table 3.3 IGSN 71 stations tied to the LC & R 61 network.

IGSN 71 Gravity Station		Latitude (°South)	$g_{IGSN\ 71}$ (mGal)	g_{Gama} (mGal)	$g_{Gama} - g_{IGSN\ 71}$ (mGal)
32838J	Fortaleza	-3.73	978067.81	978083.12	15.31
32884J	Recife	-8.09	978151.25	978166.58	15.33
36428B	Salvador	-12.98	978311.31	978326.57	15.26
36479J	Caravelas	-17.63	978511.46	978526.69	15.23
36593J	Belo Horizonte	-19.91	978385.50	Not available	Not computed
40100B	Vitória	-20.31	978641.83	978657.04	15.21
40111J	Campos	-21.70	978717.49	978732.58	15.09
40123A	Rio de Janeiro	-22.90	978789.90	978805.00	15.10
40136J	São Paulo	-23.56	978627.29	Not available	Not computed
43801B	Porto Alegre	-30.04	979305.00	979320.06	15.06
43812B	Pelotas	-31.76	979466.63	979481.65	15.02

The functional chosen was

$$F : \kappa \delta g_{ij} = g_i - g_j,$$

where κ is the appropriate linear scale coefficient for the LC & R 61 gravimeter, δg_{ij} is the adjusted gravity interval and g_i, g_j are the adjusted absolute gravity values.

Square and cubic scale coefficients were not included in the mathematical model due to their possible lack of statistical significance, given the fact that occasional non-linearities in the apparatus are already considered in the Calibration Table for the gravimeter (the LaCoste & Romberg Table). Also, according to McConnell *et al.* (1972), these non-linearities are undetected unless gravity intervals larger than 2,000 mGal are measured. Since the largest gravity interval in the network is 1,398.82 mGal between the IGSN stations of Fortaleza (32838 J) and Pelotas (43812 B) the use of scale coefficients other than the linear term was thought to be unnecessary.

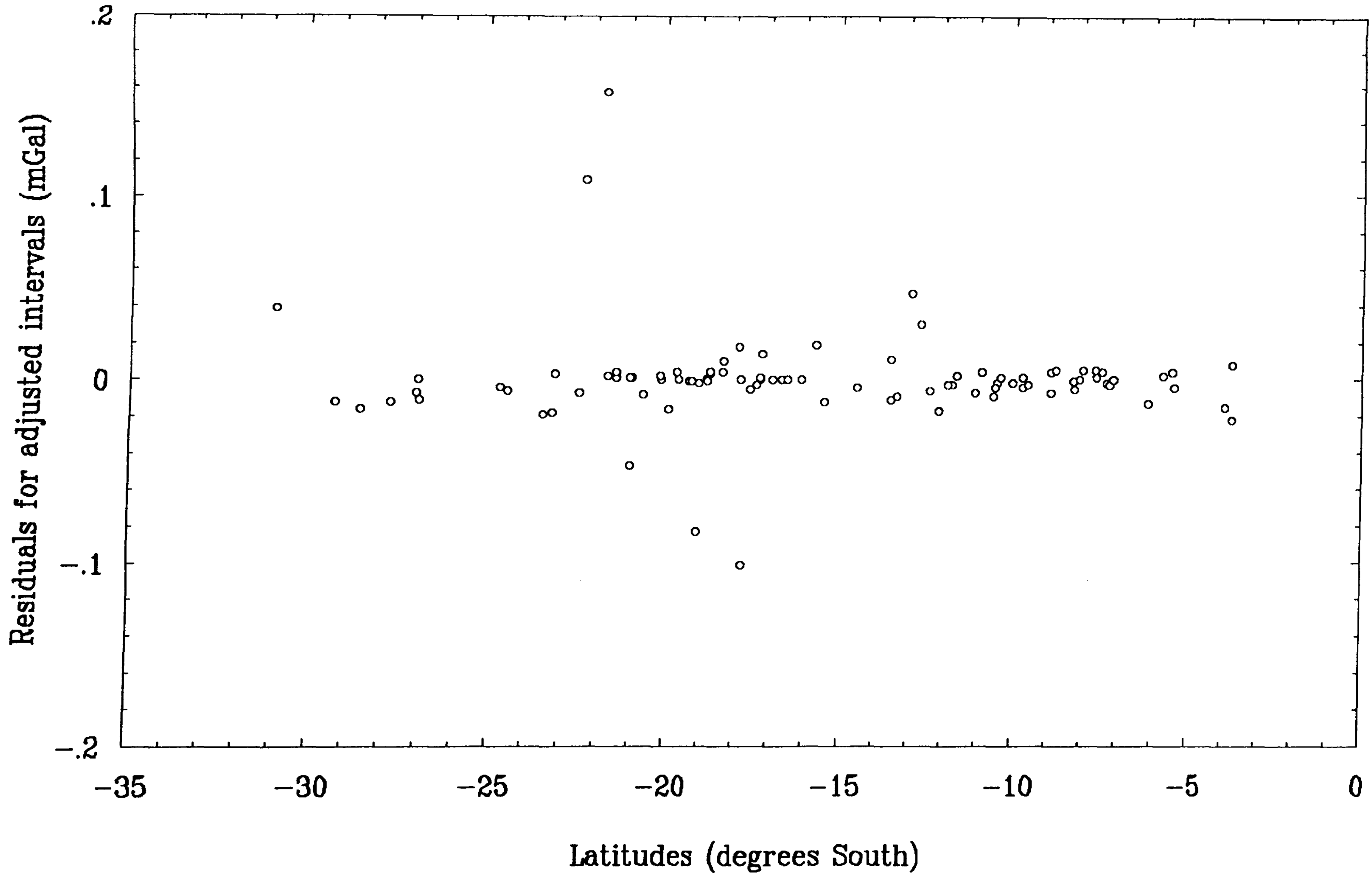

Fig. 3.5 Distribution of the residuals of conditionally adjusted intervals against geographical latitudes.

Rewriting F as $\delta g_{ij} = (g_i - g_j)/\kappa$ and considering that the adjusted values are not available, the following approximate values were taken: δg_{ij}^0 given by the output of the condition equations; g_i^0, g_j^0 obtained by transporting the absolute value of the IGSN station 40123 A (Rio de Janeiro) to all node stations and 1.0 for the linear scale coefficient.

For the present problem the number of parameters was 53 (52 node stations and 1 scale coefficient) and the number of gravity intervals was 94. Since the gravity intervals were already properly weighted in the conditional adjustment, the weight matrix for this step was simply taken as a diagonal matrix with elements $p_{ii} = \sigma_0^{-2}$, $i = 1, 2, \ldots, 88$ with σ_0^{-2} as given by the correlates. In this second step the *a posteriori* variance of unit weight should be close to 1.0. The value actually found was 0.9326 which can be considered as an indication that the weight matrices considered were appropriate.

Since the g values for the IGSN 71 stations were kept fixed throughout the adjustment process, the variance-covariance matrix, as given by the parametric method, underestimated the dispersions involved. More realistic estimates were obtained by considering the intrinsic errors in the IGSN 71 stations. The total standard deviation for the node stations was computed by the expression

$$\sigma_{total_i} = (\sigma_i^2 + \overline{\sigma_{IGSN\ 71}}^2)^{1/2}, \tag{3.7}$$

where σ_i is the standard deviation given by the i-th element of the main diagonal of the variance-covariance matrix Σ_X, as defined by (3.6), and $\overline{\sigma_{IGSN\ 71}}$ is the average standard deviation for the eleven IGSN stations tied to the net.

Figure 3.5 shows that the residuals found for the adjusted gravity intervals are smaller than 0.16 mGal with no systematic dependence on latitude. The apparent larger dispersions towards the south is due to the much smaller number of polygons measured with the LC & R 61 in that region (the W 178 was used instead) as compared to the northeast and east regions. Unfortunately, the LC & R 61 is not available any more for remeasuring those gravity intervals with poorer results.

The final step in the adjustment procedure was the computation of absolute gravity values for the internode stations. The parametric method was again applied but no *a priori* approximate values were used, with no iterations involved. Each time the algorithm was employed, only one side of a polygon was adjusted with the linear scale coefficient already known. The gravity values for the node stations were kept fixed and the functional F, as defined above, was used with known κ. The number of parameters varied according to the number of gravity stations between the nodes with a maximum of 148. Again, a more realistic estimate of the standard deviation of the gravity values for the internode stations was found by applying an equation similar to (3.7) with the mean deviation for the two node stations defining the side of the polygon being considered and σ_i is given by the appropriate diagonal element of the matrix Σ_X. Although the matrices involved in the calculations were sparse no instabilities were found in the Gauss-Jordan inversion algorithm (Subroutine **GAUSSJ**, Press *et al.*, 1992) utilized. The linear scale coefficient for the LC & R 61 compared to the IGSN 71 was found to be 1.000761 $\pm$ 0.000052.

3.3.3 Discussion

The procedures presented above allowed the computation of absolute gravity values of 1,484 stations distributed over Brazil, including the eastern side of the Parnaíba Basin. These measurements have been now referred to the IGSN 71 and the techniques developed are currently being applied to the LC & R 257 and W 178 data sets.

It is also possible to approach the problem of adjusting gravity observations using the *implicit* or *combined model* applying Equation (3.1) directly with a functional F generically non-linear. However, since three different meters were used in assembling the old gravity network of the Observatório Nacional, with a few differences in field methodology, the three-step procedure was taken as the best way to compare qualitative differences in the data sets.

A quick transformation rule can also be used to convert the old g_{Gama} values into IGSN-compatible ones using the data shown in Table 3.3. Figure 3.6 shows a best fit regression line (in the L_2 sense) relating the two scales. The equation for the straight line is

$$g_{IGSN\ 71} = -233.32020 + 1.0002229.g_{Gama} \quad (\mathrm{r}^2 = 0.999995)$$

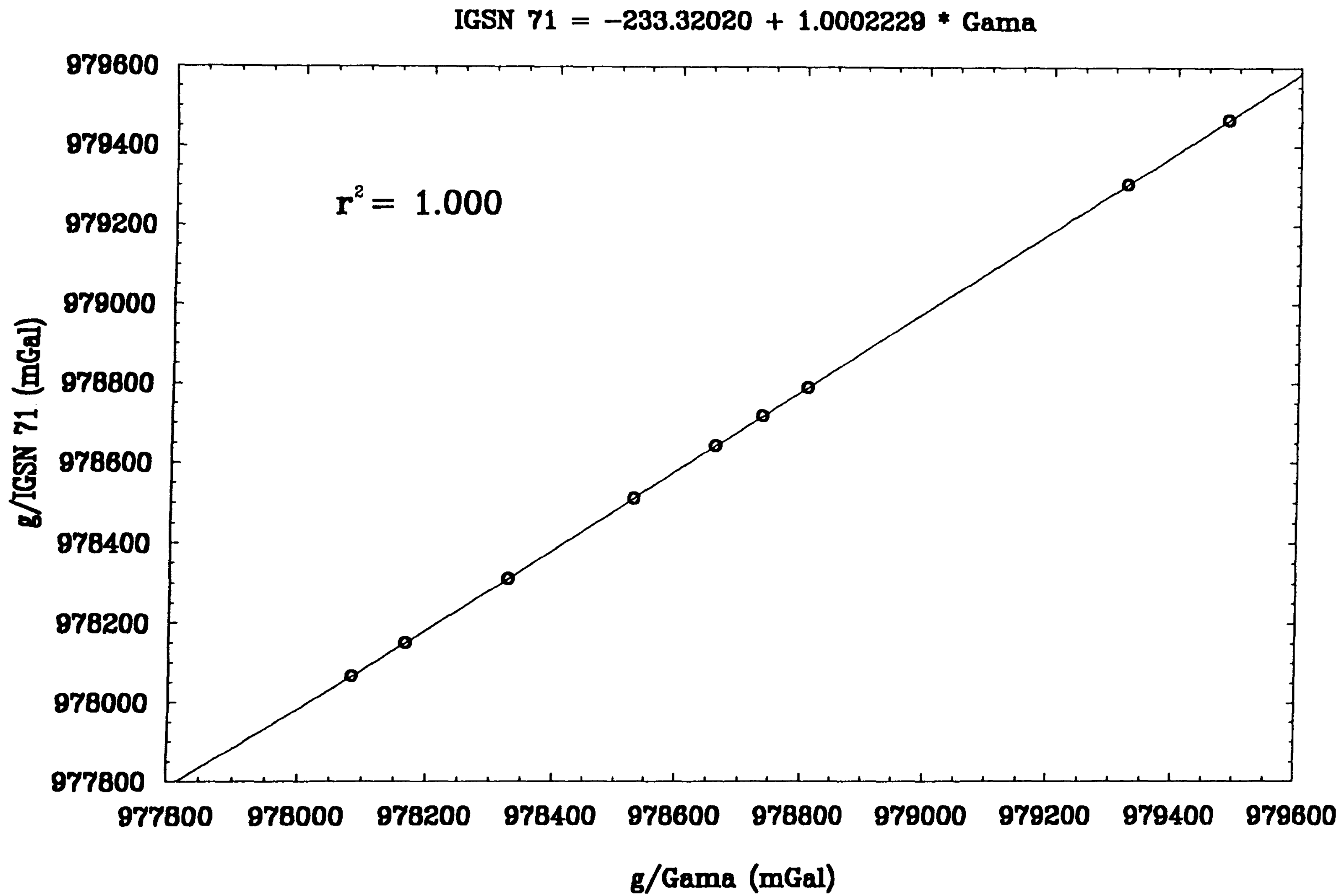

Fig. 3.6 Best-fit regression line (in the L_2 sense) for the correlation between g_{Gama} and $g_{IGSN\,71}$.

This relationship is in close agreement with the transformation rule proposed by De Sá & Blitzkow (1986) for converting the Woollard Gravity Network in Brazil to the IGSN 71. The WGN also conforms to the Potsdam *datum* and a mean correction of -15.0 mGal seems to make it consistent with the IGSN 71.

Absolute gravity measurements at seven different sites allowed for the establishment of a preliminary absolute gravity calibration network in Brazil (Gemael *et al.* 1990). These stations have been tied to the Brazilian Gravity Reference Network and a readjustment of the BGRN, taking the absolute gravity stations as source of *datum* and scale has been done, (I. P. Escobar, personal communication, 1993).

Considering that 72 gravity stations of the BGRN are coincident with the LC & R 61 network, a comparison between their gravity values obtained in the present work and those adjusted to the absolute *datum* could be made. A histogram of the differences found is shown in Fig. 3.7 with mean difference of 0.0 mGal and a standard deviation of 0.1 mGal. Since the accuracy of the LC & R 61 network is also of ±0.1 mGal it is seen that the gravity values computed are consistent with the absolute *datum* at this level of accuracy.

Ebong (1981, 1985), working with the levelling network of Nigeria, concluded for the apparent superiority of the application of the adjustment methods based on the minimization of the sum of absolute residuals (the L_1 norm) instead of their least squares. The absence of a constraint that the observables follow a normal distribution would be an advantage with the more intense computational effort producing more realistic results. That would be particularly true for sets of measurements involving several sets of equipment and observers, different field methodologies and surveys spanning several years; a situation similar to the measurements composing the gravity network of the Observatório Nacional. Claerbout & Muir (1973), Barrodale & Young (1966) and, more specifically, Fuchs (1983), analyzing the problem of adjustment of large geodesic networks, proposed an algorithm for minimizing the function $\Phi = V^T PV$ in the L_1 sense by turning the problem equivalent to a linear programming optimization process, solved by the SIMPLEX method. The viability of using robust statistic techniques to the adjustment of gravity networks is planned to be investigated.

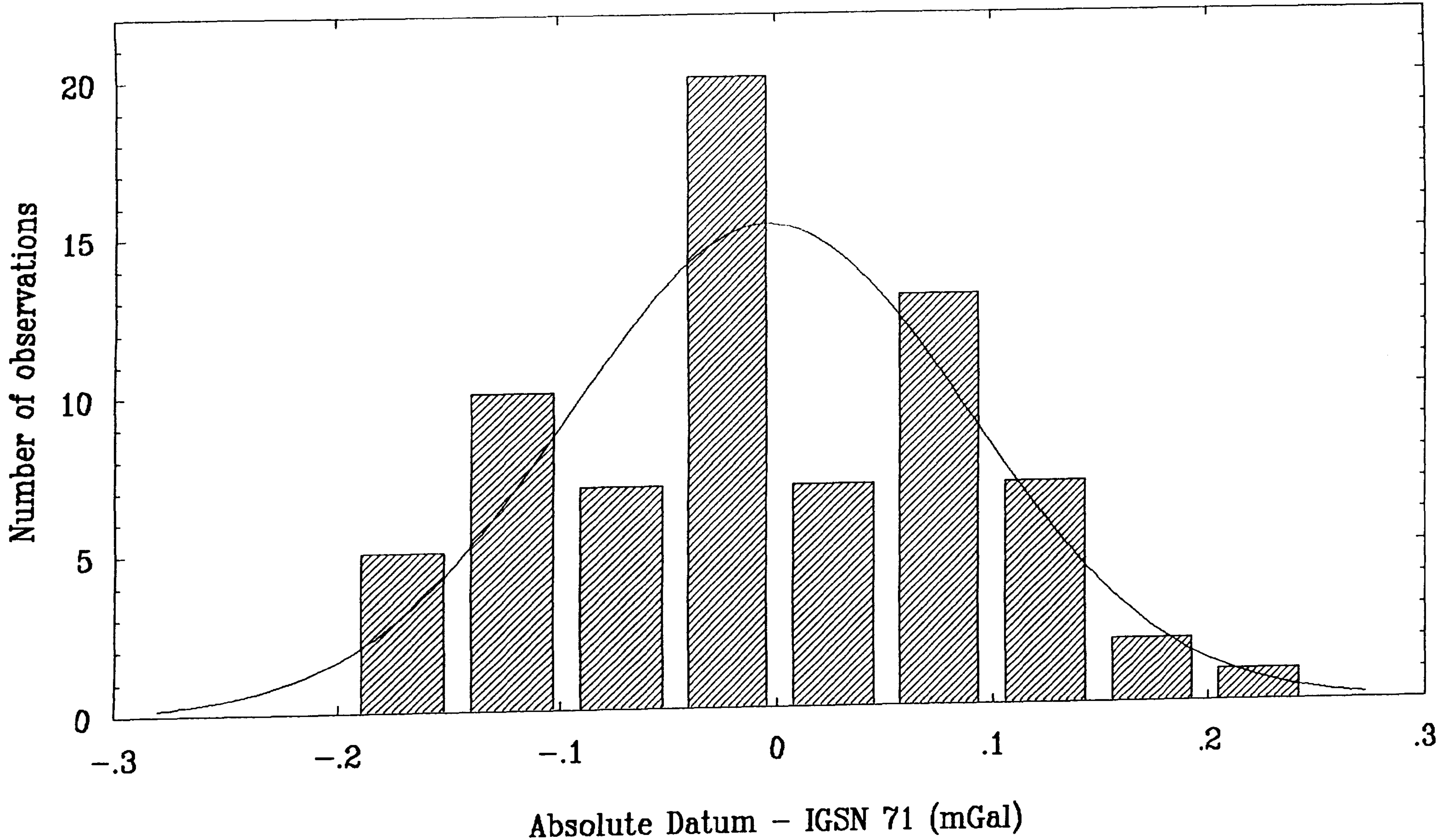

Fig. 3.7 Histogram of the differences (in mGal) between the absolute gravity stations and the IGSN 71 in Brazil (72 cases, mean = 0.0 ± 0.1 mGal).

A digital file was created holding all gravity station identification codes, plani-altimetric coordinates, g values, standard deviations and gravity anomalies. This file is available upon request on a floppy disk under the IBM-PC format at the Departamento de Geofísica of the Observatório Nacional.

3.4 Summary

The entire gravity data set used in the present study comprises 18,234 stations and their distribution is shown in Fig. 3.8. Table 3.4 summarizes all contributing gravity data sources.

Table 3.4 Sources of gravity data used in this study.
In total: 18,234 gravity stations.

Institution	Gravity stations
PETROBRÁS	9,658
ON	2,820
IBGE	2,702
CPRM	1,892
UFPa	1,162

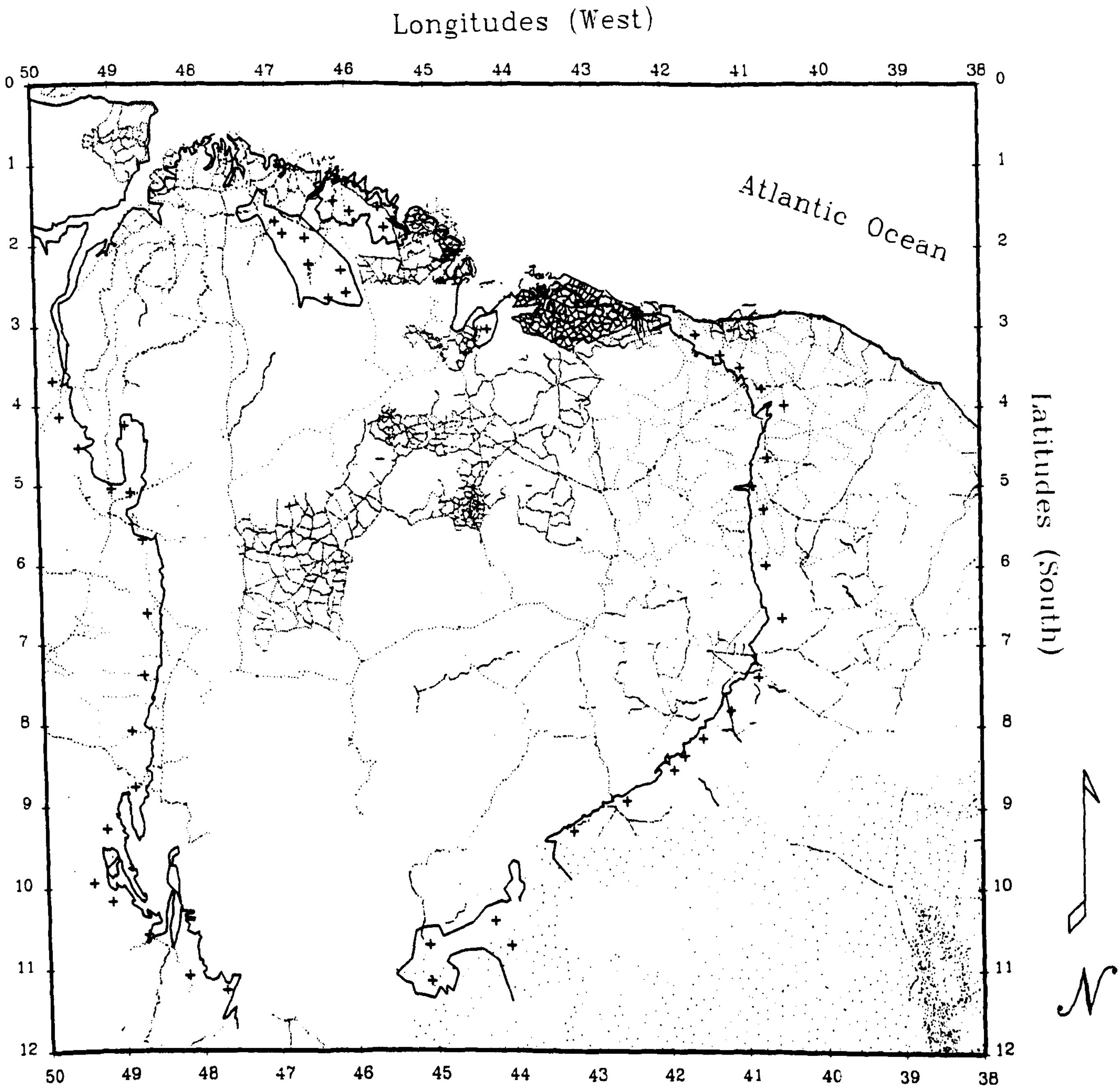

Fig. 3.8 Gravity data set (18,234 stations) used in the present study of the Parnaíba Basin. Conic projection.

CHAPTER 4

GRAVITY MODELLING

4.1 Topographic and Gravity Anomaly Maps

In order to produce free-air and Bouguer anomaly maps, the gravity stations were projected onto a plane by transforming their geographical coordinates into conical coordinates. The Lambert conical projection was chosen so that a direct comparison of the anomaly maps with the available geological/tectonic maps could be made. A computer subroutine for the Lambert conical projection was written and the required mathematical formulae were obtained from Richardus & Adler (1972).

The irregularly distributed data points were interpolated onto a regular grid of $15' \times 15'$ using a two-dimensional interpolation subroutine provided by the graphics library **PLOT 88** (Young & Van Woert, 1990). A hand-made $15'$-gridded Bouguer map was used to help choose the best parameters for automatic contouring, avoiding spurious short-wavelength anomalies in regions with poor coverage and giving accurate contouring where the coverage is good. The first topographic, free-air and Bouguer anomaly maps for the entire Parnaíba Basin are shown in Figures 4.1, 4.2 and 4.3, respectively.

The free-air map produced shows more details than the 1°-gridded map for South America presented by Hinze *et al.* (1982). A regional gravity low ($\leq$-20 mGal, Fig. 4.4) is associated with the Parnaíba Basin.

Examination of the Bouguer map shows a regional gravity low associated with the Parnaíba Basin and a rapid increase of the Bouguer gravity values towards the coast. Other conspicuous anomalies are clearly visible in this map (see the overlay of Fig. 4.3). They are:

- localized gravity lows associated with the sedimentary basins of Tucano, Araripe, Barreirinhas and São Luís;
- gravity highs associated with the structural arches of Urbano Santos, Ferrer, Tocantins and the most prominent of all, the Middle São Francisco Arch;

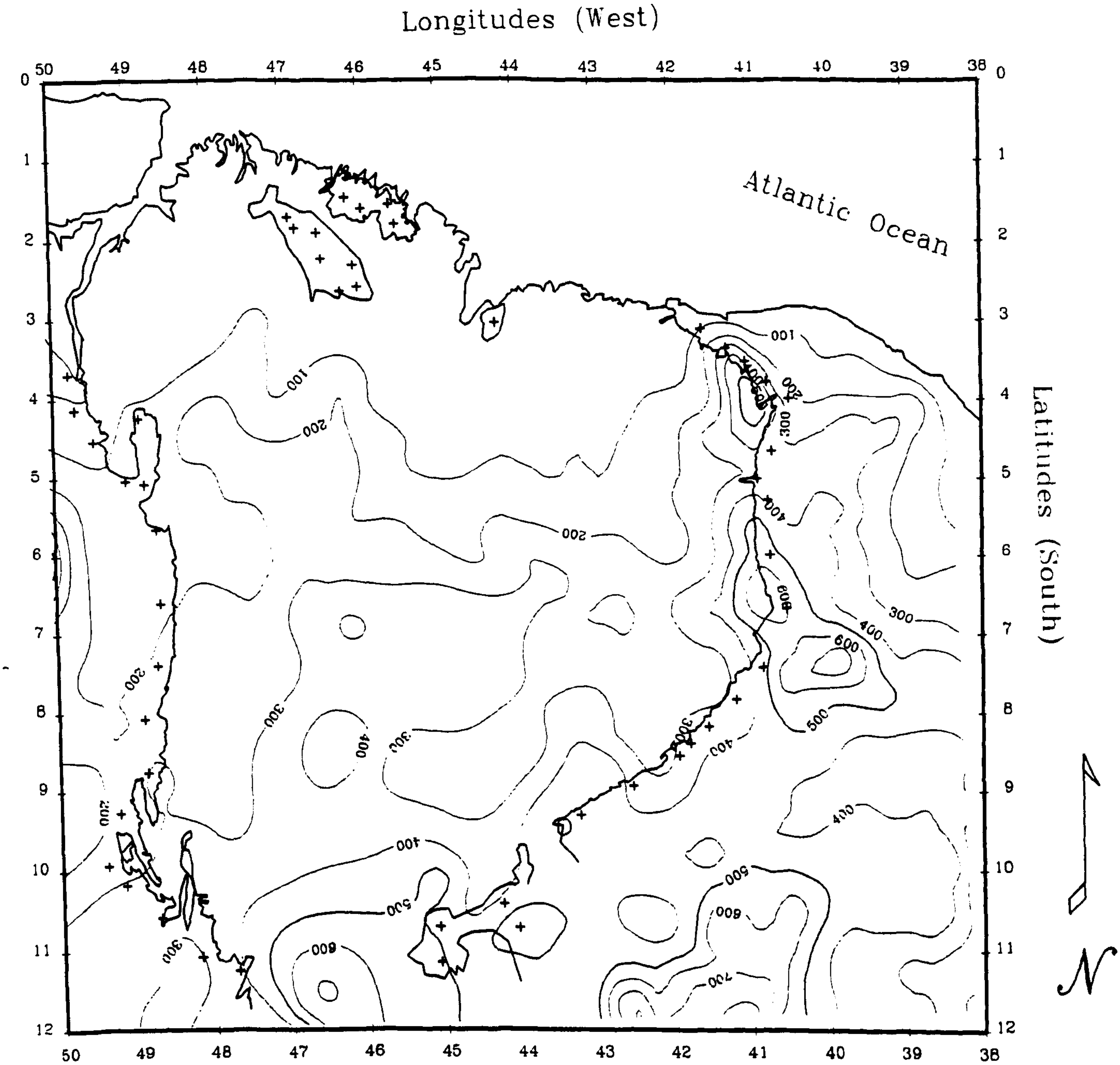

Fig. 4.1 Topographic map of the Parnaíba Basin. Contour interval: 100 m, conic projection.

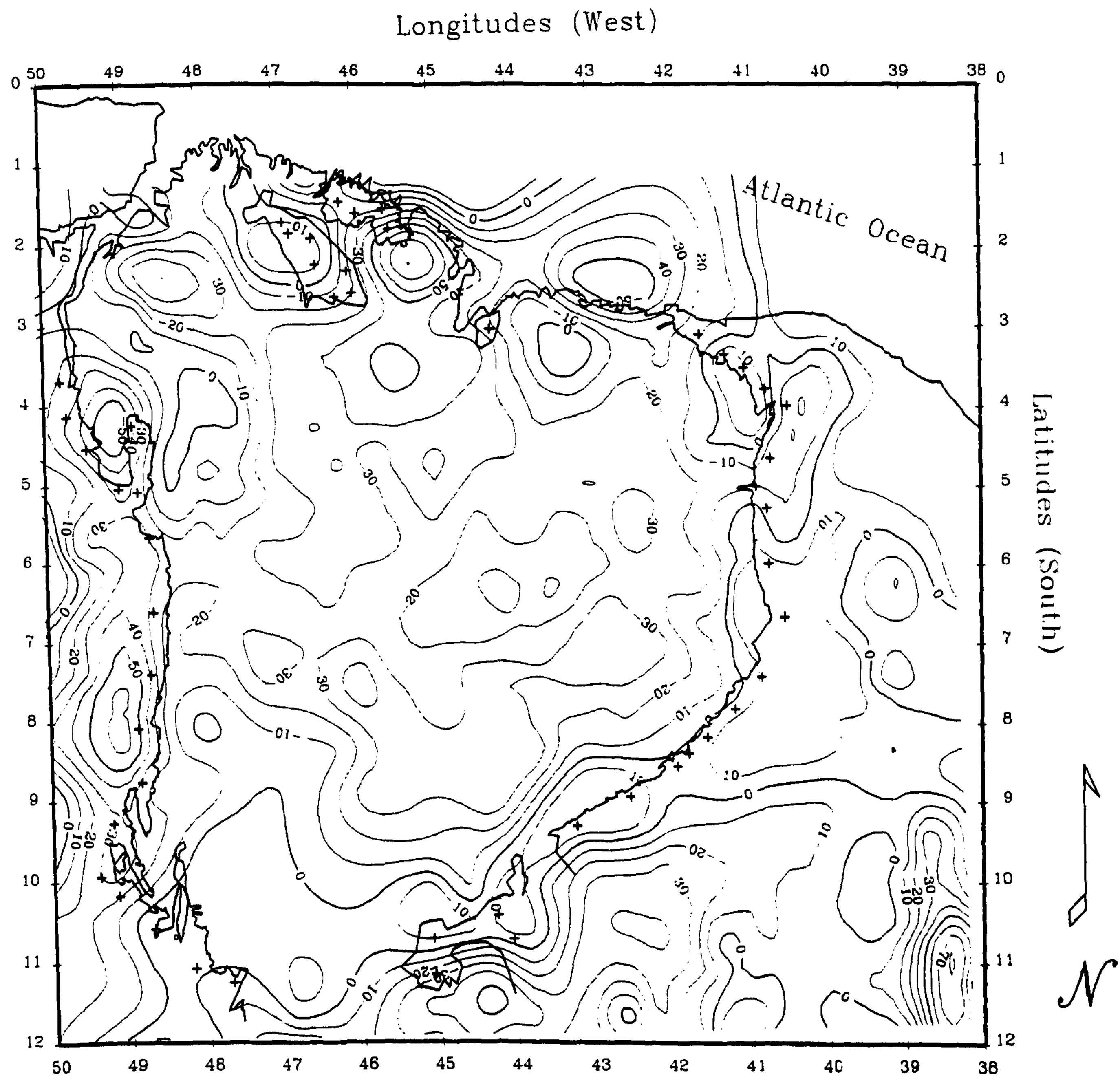

Fig. 4.2 Free-air gravity anomaly map of the Parnaíba Basin. Contour interval: 10 mGal, conic projection.

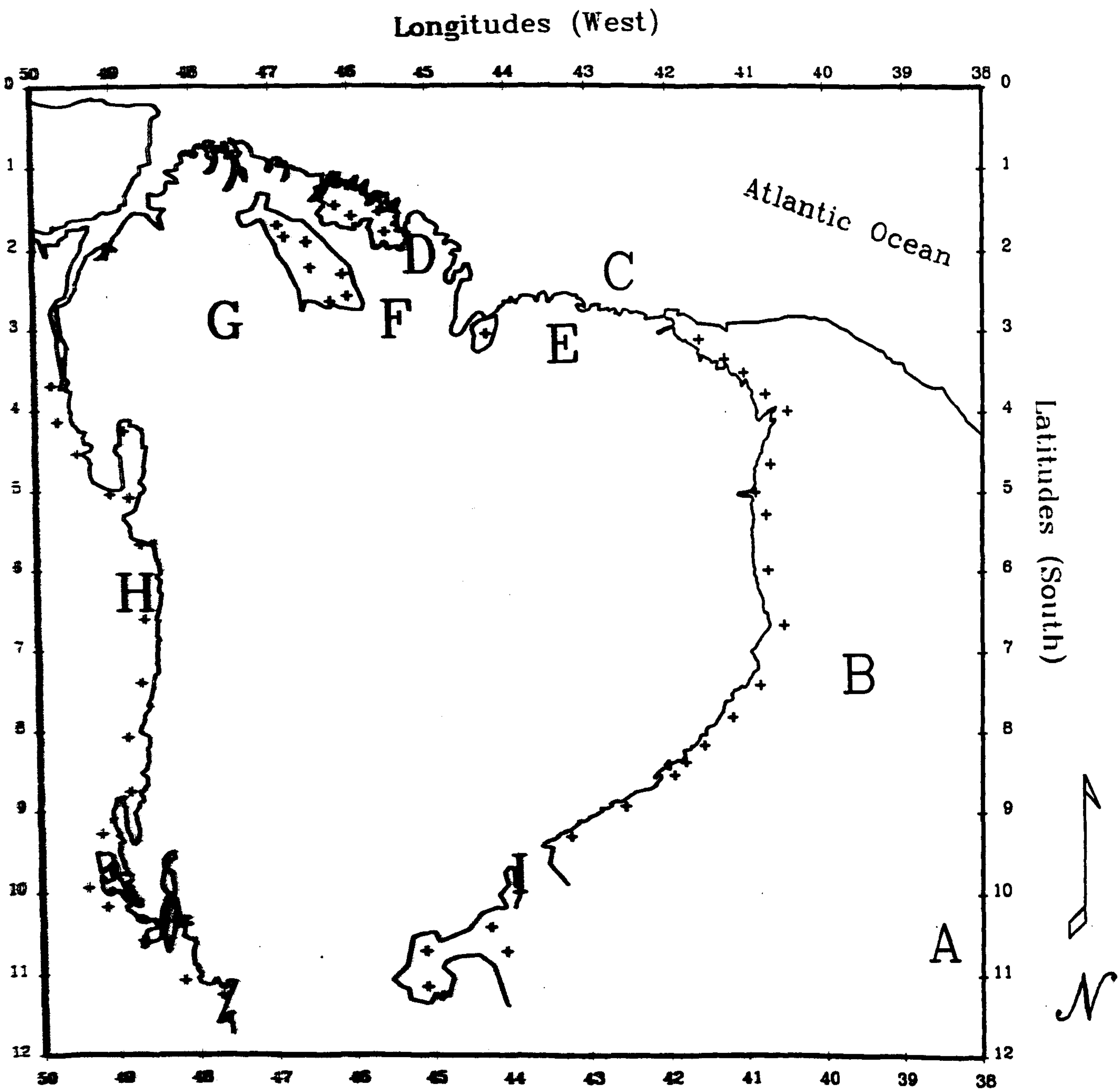

Overlay for Fig. 4.3 showing the Bouguer gravity expression of some geological structures within the study area.

A	-	**Tucano Basin**	**F**	-	**Ferrer Arch**
B	-	**Araripe Basin**	**G**	-	**Tocantins Arch**
C	-	**Barreirinhas Basin**	**H**	-	**Araguaia Fold Belt**
D	-	**São Luís Basin**	**I**	-	**Middle São Francisco Arch**
E	-	**Urbano Santos Arch**			

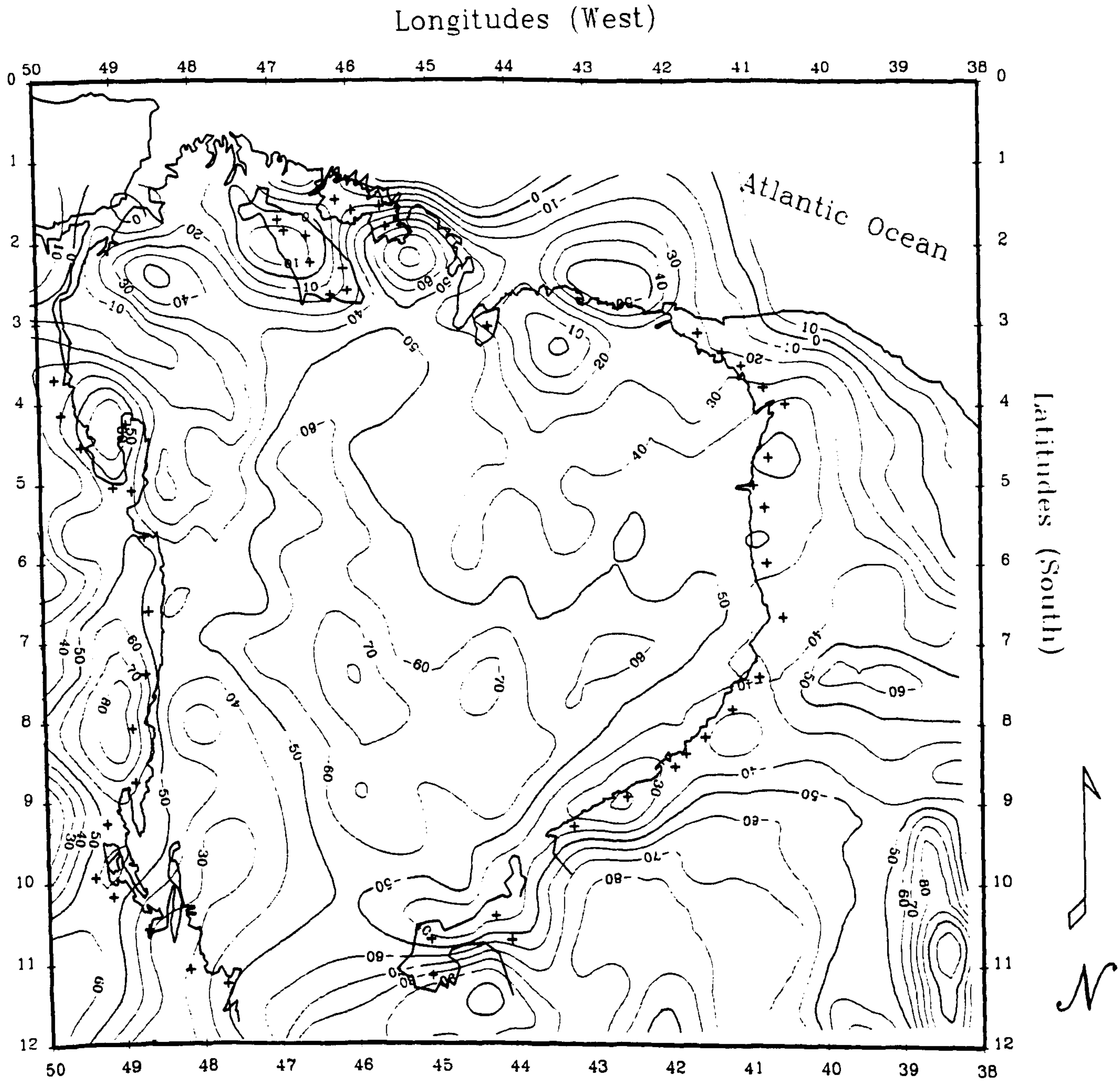

Fig. 4.3 Bouguer gravity anomaly map of the Parnaíba Basin. Contour interval: 10 mGal, conic projection.

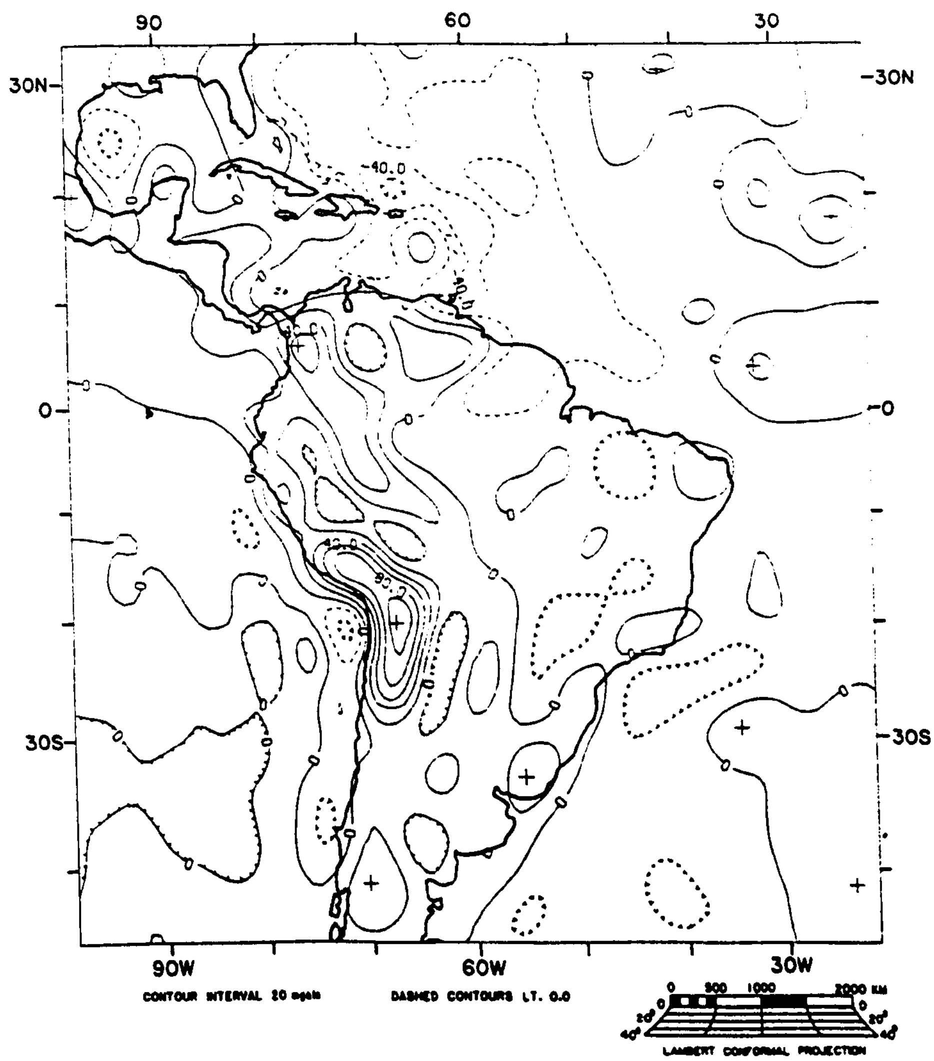

Fig. 4.4 Long-wavelength-pass ($\lambda \geq 8^0$) filtered surface free-air gravity anomaly map of South America and adjacent areas. Contour interval: 20 mGal (Hinze *et al.*, 1982, Fig. 2).

• the N-S trend of the Araguaia Fold Belt;

The -50 mGal contour line has been emphasized because it shows reasonably well two trends of NE-SW and NNW-SSE elongated gravity lows associated with the Transbrasiliano Lineament and the Upper Proterozoic precursory sediments (Fig. 2.11), respectively.

The relative central gravity high depicts the close presence of the Urbano Santos and Ferrer basement highs and does not contradict the existence of a remanent, central cratonic nucleus underneath the basinal strata, as discussed in section 2.3. This cratonic nucleus subsided during the development of the basin, but as the adjacent areas experienced extension thicker sequences of sediments in them produce even larger negative anomalies. Moreover, if this area is in-between extensional events it should be expected to be coincident with the largest lithospheric attenuation. Therefore, the existence of mantle/differentiated crustal rocks closer to the surface would contribute to the relative gravity high.

The Bouguer map of the Parnaíba Basin is in marked contrast to the corresponding map of the Amazon Basin and shows some similarities to the one of Paraná Basin. Quintas (1995) presents a Bouguer map of Paraná where the average anomalies are ~20 mGal more negative than Parnaíba with recognized crustal weakness zones showing even more negative (10-20 mGal) anomalies. The average heights in Paraná are ~500 m higher than in Parnaíba and maximum sediment thickness is just over 5,000 m. The massive Upper Jurassic volcanism in the Paraná Basin, locally reaching up to 2,000 m in the stratigraphic column, produces positive anomalies, a feature not observed in the Parnaíba Basin. Nunn & Aires (1988) show a Bouguer map of the Middle Amazon Basin where a chain of gravity highs (+40-+90 mGal) transects the basin roughly coincident with the axis of maximum deposition. The positive anomalies are flanked by gravity lows of -40 $\pm$ 20 mGal and some short-wavelength anomalies caused by shallow ultrabasic intrusions are also seen. Up to 7,000 m of Palaeozoic sediments are found along the basin axis.

De Sá *et al.* (1993) produced gravity anomaly maps for Brazil as a whole (Fig. 4.5). These maps did not include gravity surveys used in the present study and some areas to the centre, east and south of Parnaíba were reported as *incomplete* or *empty* with 1°-2° resolution. Therefore, it is expected that the specific Parnaíba

Free-air gravity anomaly map of Brazil.

Bouguer gravity anomaly map of Brazil.

Fig. 4.5 Free-air and Bouguer maps of Brazil (De Sá *et al.*, 1993, Figs. 12 and 13). Note the absence of gravity expression for the Transbrasiliano Lineament and the Upper Proterozoic graben structures. Contour interval: 10 mGal, polyconic projection.

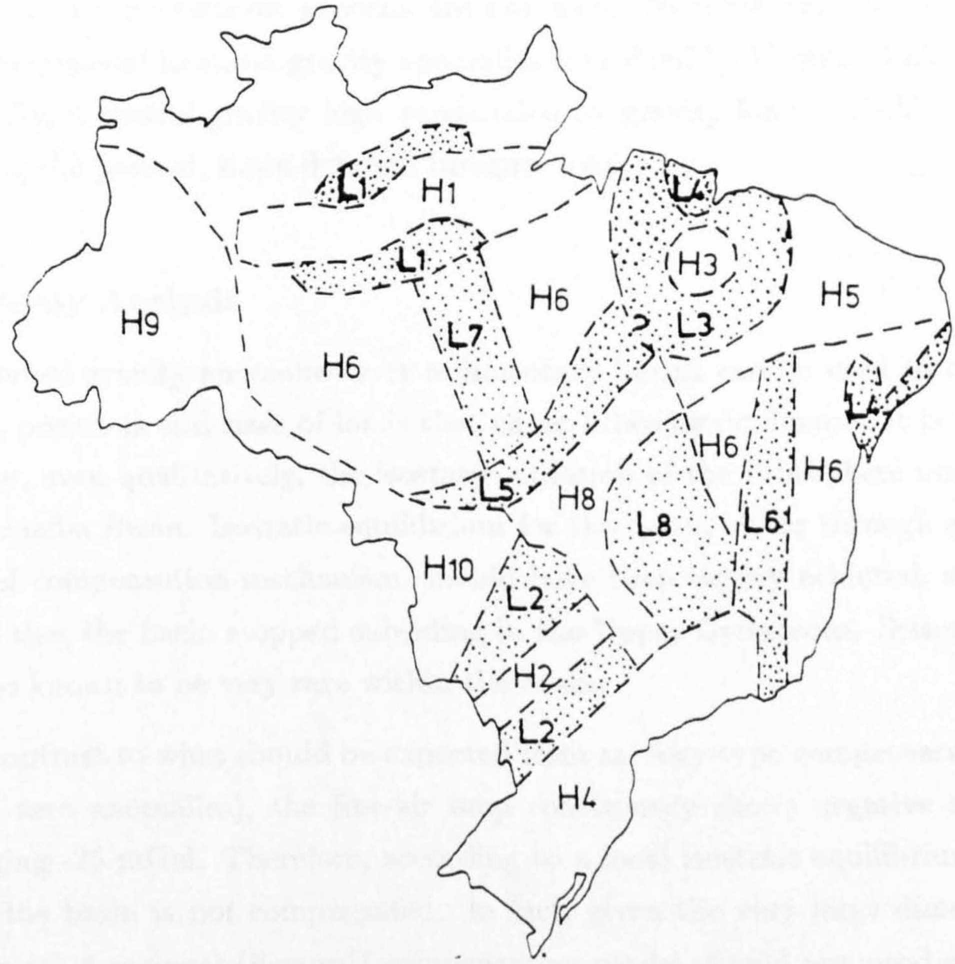

Fig. 4.6 Residual isostatic gravity anomalies over Brazil (Ussami *et al.*, 1993, Fig. 11). H is for highs and L for lows. Note the central high H3 bounded by lows L3 and L4 in the area of the Parnaíba Basin. Numbers apply to anomalies over major Brazilian tectonic and geological units: (H1/L1) Palaeozoic Amazon Basin; (H2/L2) Palaeozoic Paraná Basin; (H3/L3) Palaeozoic Parnaíba Basin; (H4) eastern Paraná Basin (Lower Cretaceous crustal underplating?); (L4) coastal Lower Cretaceous-Tertiary basins; (H5) Proterozoic Borborema Province and northeastern fold belts; (L5) Proterozoic Araguaia Fold Belt and Palaeozoic Parecís-Alto Xingú Basins; (H6) Archean-Lower Proterozoic high-grade metamorphic basement within the Amazon and São Francisco Cratons; (L6) Middle-Upper Proterozoic Espinhaço Thrust Belt; (L7) Lower Proterozoic granites and acid volcanics; (H8) Archean Goiás Massif; (L8) Middle Proterozoic Uruaçú and Upper Proterozoic Brasília Fold Belts; and (H9, H10) foreland basins of the Andean System.

Basin section of these maps does not compare well with the ones produced here. For instance, note that the gravity signatures of the Transbrasiliano Lineament and the Upper Proterozoic grabens are not seen. Nonetheless, Fig. 4.6 reproduces the residual isostatic gravity anomalies contoured by Ussami *et al.* (1993). Essentially, a central gravity high surrounded by gravity lows is visible, roughly matching the present, more detailed Bouguer map.

4.2 Gravity Analysis

Observed gravity anomalies over sedimentary basins can be used to constrain depths, positions and sizes of loads that cause lithospheric flexure. It is useful to consider, even qualitatively, the isostatic situation of the lithosphere underneath the Parnaíba Basin. Isostatic equilibrium for the basin, either through a local or regional compensation mechanism, should have been largely achieved, since it is known that the basin stopped subsiding in the Upper Cretaceous. Seismic events are also known to be very rare within the basin.

In contrast to what should be expected from an Airy-type compensation model (mean zero anomalies), the free-air map consistently shows negative anomalies averaging -25 mGal. Therefore, according to a local isostatic equilibrium mechanism, the basin is *not* compensated. In fact, given the very large dimensions of this basin, a regional (flexural) compensation model should not produce gravity anomalies substantially different from a local, Airy-type model, assuming that the surface topography is the only load acting on the lithosphere.

These observations indicate the inadequacy of a simple local compensation, crustal thinning model for the Parnaíba Basin.

In order to examine the form of the regional compensation present beneath the basin, six long radial gravity profiles have been considered (Fig. 4.7). This figure superimposes the distribution of gravity stations to the Bouguer map, since the availability of a reasonable number of stations that could be projected onto a given line, controls the choice of possible azimuths.

Before any gravity anomalies could be calculated, it was necessary to establish reasonable density values for the various layers assumed in the models.

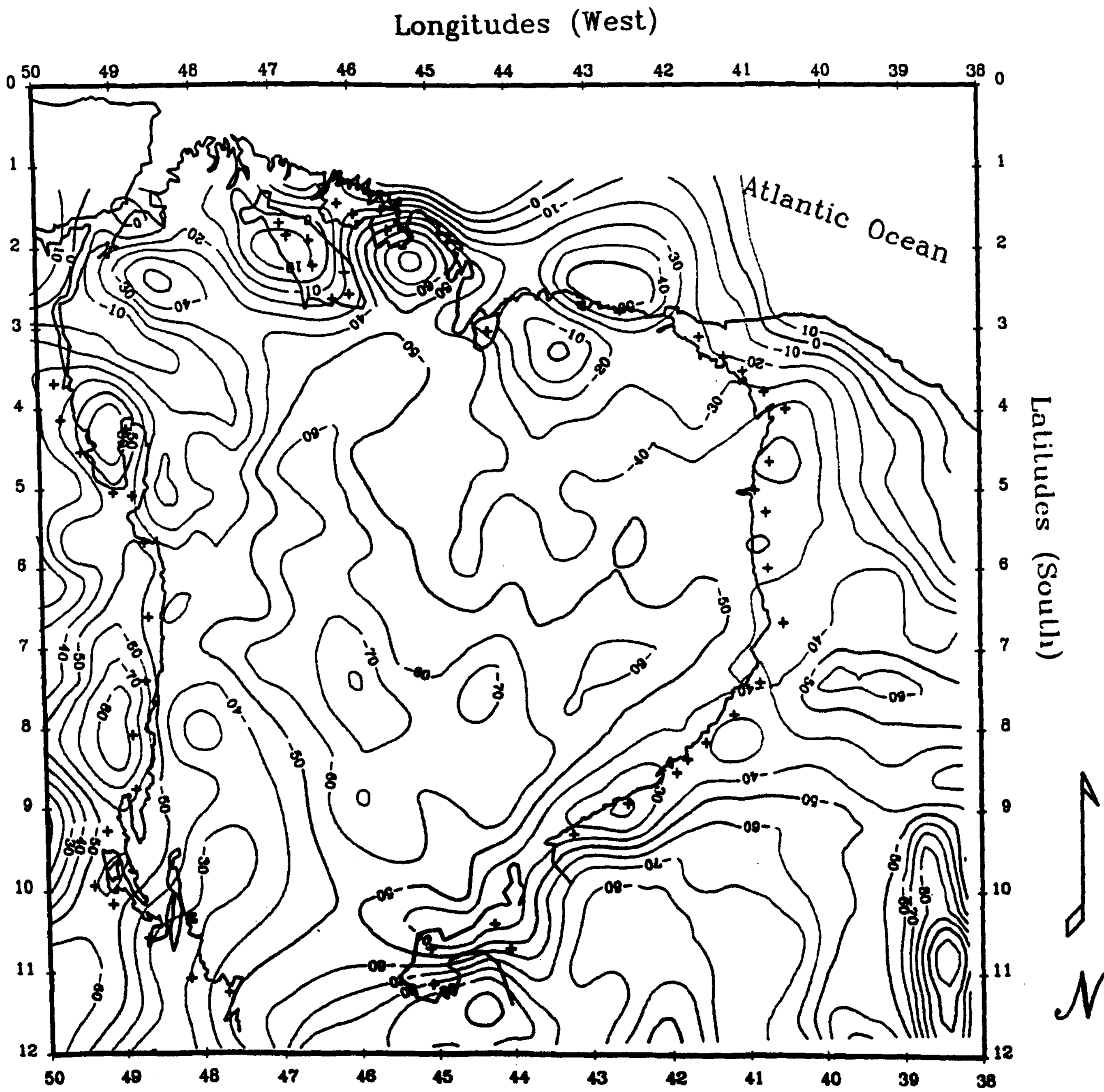

Longitudes (West)
Latitudes (South)
Atlantic Ocean
N

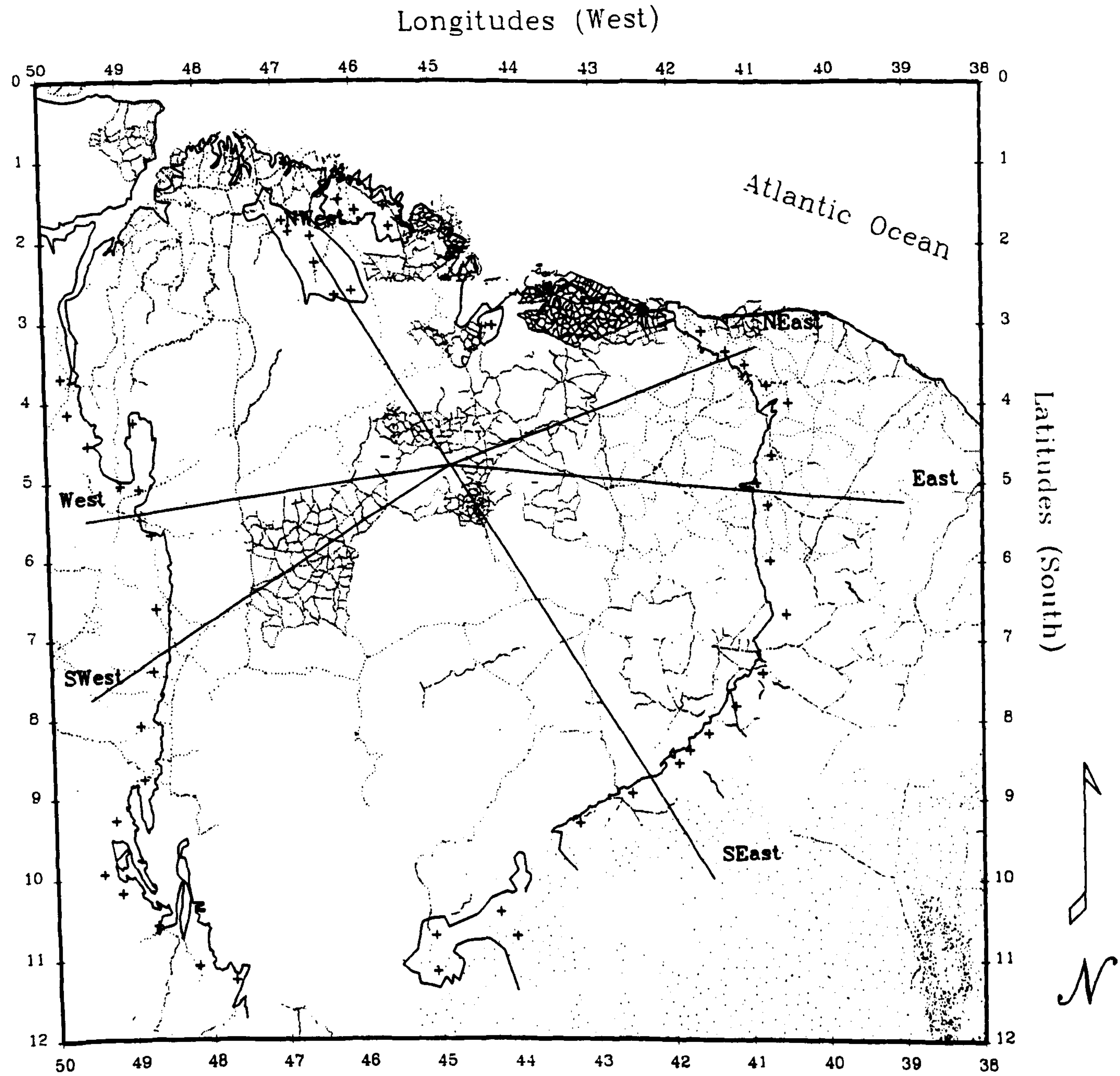

Fig. 4.7 Radial gravity profiles across the Parnaíba Basin superimposed to the distribution of gravity stations and the Bouguer map. Contour interval: 5 mGal, conic projection.

A single exploratory borehole (1-PA-01-MA, 4.2°S, 45.7°W, Fig. 2.10) has a formation density log (FDC) and is the only available source of density vs. depth information in the basin. Sediments infilling basins gravitationally compact with depth and time and this process should be taken into account in forward basin modelling. Cowie & Karner (1990) have already pointed out that the amplitude of gravity anomalies across extensional basins may primarily reflect compaction of the sedimentary infill.

It is known that the predominant lithologies are sandstones, with subordinate shales and siltstones and it was assumed that the depth dependence of the porosity of these sediments follows the empirical results of Athy (1930),

$$\phi = \phi_0 \exp(-cz),$$

where ϕ is the rock porosity at any depth z, ϕ_0 is the surface porosity and c is a lithology dependent coefficient associated with the rate at which the exponential decrease of rock porosity varies with depth. This is the sediment compaction relationship most used in basin modelling. It is difficult, however, to derive equations for calculating gravity anomalies in the spatial domain using an exponential depth-dependence for rock porosity.

Alternative relationships include the use of hyperbolic functions in computing weighted averages of sediment densities, weights being the different formation thicknesses - the *effective density* concept of Litinsky (1989). Rao (1986) advocated the use of a quadratic function in depth to approximate measured sediment density values. The main advantage of both formulations is allowing the computation of the anomaly equation in closed form in the spatial domain. Analytical expressions in the wavenumber domain have been obtained by *e.g.* Xia & Sprowl (1995).

It can be shown (see Chapter 4 for more details about rock porosity and its implications for sediment thicknesses varying with depth through geological time) that the density $\rho(z)$ of a (homogeneous) sedimentary layer at depth z is

$$\rho(z) = \rho_{sg} - (\rho_{sg} - \rho_w)\phi_0 \exp(-cz), \tag{4.1}$$

where ρ_w is the sea water density (= 1,030 kg m^{-3}), ρ_{sg} is the density of the dry sediment matrix grain (= 2,720 kg m^{-3} for the lithology being considered), ϕ_0 = 0.3140 $\pm$ 0.0812 and c = 0.6312 km^{-1}.

From Equation (4.1) the density contrast in kg m^{-3} could be written as

$$\Delta\rho_{sed}(z) = 50 - 530.66\exp(-0.6312z), \qquad 0 \leq z \leq 3.65 \qquad (4.2)$$

with the depth z expressed in kilometres.

Several workers e.g. Litinsky (1989), use the infinite-slab anomaly formula, $\Delta g = 2\pi G\Delta\rho H$, where H is the slab thickness, in practically any gravity modelling of sedimentary basins. This is somewhat justified since basins' width (W) to depth (D) ratios are often large. In most cases, sedimentary basins on platforms have $W/H \geq 10$ and the error in using the slab formula is less than 2.5%. In the specific case of Parnaíba, $W/H \approx 23$, but an even better approximation can be used. Although the Parnaíba Basin is not a purely cylindrical geological structure, its approximate ellipsoidal shape suggests that it is advantageous to consider the use of an axisymmetric 2.5D approach in defining the regional gravity model. Commercial 2.5D modelling softwares consider the whole basin as a rectangular block and use a single density contrast for the entire sedimentary infill; therefore being of little use in this study.

Considering expression (4.2) and the total isopach map of Fig. 2.16, the basin sediments were regionally modelled by piling up a series of concentric disks centered on the present depocentre. As the deepest section in the basin reaches just over 3,500 m, the entire sedimentary pack was divided into 72 disks, each 50 m thick. The radius for each disk was given by a linear interpolation between the nearest higher and lower isopach values along the profile line. Summation of (4.2) over the sedimentary section gives an excellent approximation to the sediment gravity effect and no end-corrections are needed at the basin edges. Nearly continuous sediment compaction can be taken into account through this approach.

The gravity attraction of a disk has been given by several authors, e.g. Parasnis (1961); Rao & Radhakrishnamurty, (1966) and Singh (1977). The most appropriate expression is the one given by Singh (1977), where the vertical component of

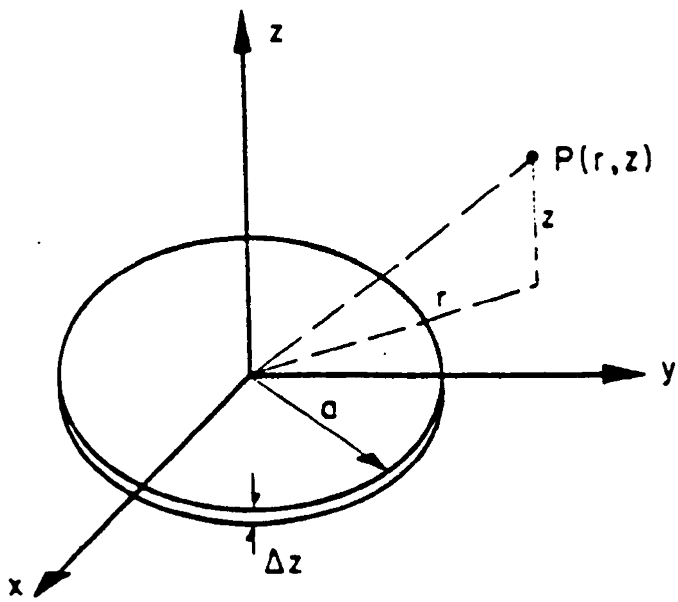

Fig. 4.8 Geometry of the problem of gravity atraction of a disk.

gravity is computed in closed form by making use of the complete elliptic function of first kind, $K(k)$, and Heuman's Lambda function, Λ_0 (Eason *et al.*, 1955).

Considering the geometry of Fig. 4.8, the expression for the vertical component of gravity, g_z, at $P(r,\ z)$ is:

$$g_z = 2\pi G \Delta\rho_{sed} \Delta z \Omega'$$

where G is the gravitational constant, $\Delta\rho_{sed}$ is the uniform density contrast of the disk of radius a, thickness Δz at depth z and Ω' is given by

$$\Omega' = \begin{cases} -z\dfrac{F_0(k)}{2[(a+r)^2+z^2]^{1/2}} - \dfrac{1}{2}\Lambda_0(\alpha,\beta) + 1, & a > r \\ -z\dfrac{F_0(k)}{2(4a^2+z^2)^{1/2}} + \dfrac{1}{2}, & a = r \\ -z\dfrac{F_0(k)}{2[(a+r)^2+z^2]^{1/2}} + \dfrac{1}{2}\Lambda_0(\alpha,\beta), & a < r \end{cases}$$

$$\sin^2 \alpha = k^2,$$

$$\sin^2 \beta = \frac{z^2}{(a-r)^2 + z^2},$$

and

$$F_0(k) = \frac{2}{\pi} K(k).$$

Heuman's Lambda function, $\Lambda_0(\alpha, \beta)$, was computed through appropriate parameterization of the general and complete elliptic integral and the computer code written for the gravity modelling makes use of the FORTRAN function **CEL** (Press *et al.*, 1992).

The nearest data points within a maximum distance of 30 km from the profile line were projected onto it and the choice of azimuths was primarily determined by the availability of a representative amount of gravity stations along the selected profile. Figure 4.9a shows the observed Bouguer anomalies and the gravity model for the basin sediments along the East radial profile. The continuous line depicts the gravity signal produced by the concentric disks model with density contrast in the range -481 kg m^{-3} (at the surface) to -3 kg m^{-3}(at a depth of 3,650 m). The average density contrast is -157 kg m^{-3}. This signal is seen to drop rapidly outside the basin boundary and although this may be due partially to the presence of neighbouring outcropping grabens in the adjacent Borborema Province, a deeper mass deficiency should result in the long-wavelength anomaly. The observed Bouguer anomalies systematically decrease (in the arithmetic sense) from $\sim$-5 to $\sim$-55 mGal for over 200 km towards the basin. A slight increase from $\sim$-55 to $\sim$-40 mGal towards the depocentre is also observed, despite the continuous increase in thickness of low density sediments. In Fig. 4.9b the long-wavelength resultant anomaly, obtained by subtracting the effect of the sediments from the observed anomalies, has been explained by the replacement of part of the normal lower crust by differentiated, denser material. It is also necessary to consider the basinal sag and a fraction of the upper mantle has been replaced by the differentiated, lighter anomalous crust. This anomalous crust was positioned at an average depth of 35 km, coincident with the Moho interface. Figure 4.9c shows that by including both effects of the sediments and of the proposed zone of modified crustal material it is possible, at least on a regional basis, to account for the observed

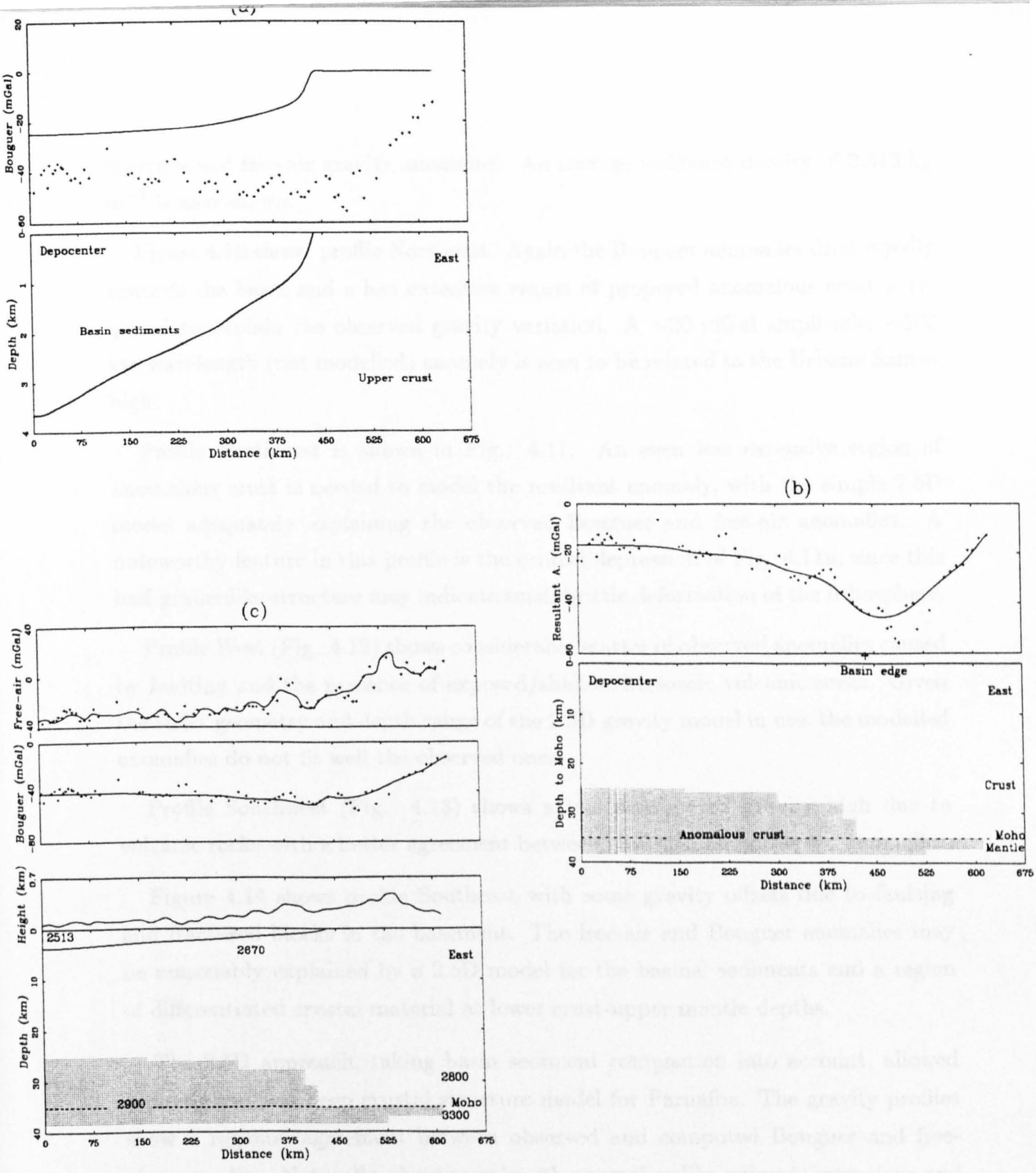

Fig. 4.9 East radial gravity profile across the Parnaíba Basin: (a) Note the systematic fall of gravity anomalies towards the basin and the slight increase within it. The continuous line depicts the gravity signal produced by the sediments model; (b) Resultant gravity anomaly obtained from subtracting the sediment effect from the observed Bouguer anomalies. The continuous line is the modelled anomaly; (c) Gravity model including sediments and zone of anomalous crust showing general agreement between observed and calculated gravity anomalies. Densities in kg m^{-3}.

Bouguer and free-air gravity anomalies. An average sediment density of 2,513 kg m^{-3} is also shown.

Figure 4.10 shows profile Northeast. Again the Bouguer anomalies drop rapidly towards the basin and a less extensive region of proposed anomalous crust is required to explain the observed gravity variation. A $\sim$20 mGal amplitude, $\sim$200 km wavelength (not modelled) anomaly is seen to be related to the Urbano Santos high.

Profile Northwest is shown in Fig. 4.11. An even less extensive region of anomalous crust is needed to model the resultant anomaly, with the simple 2.5D model adequately explaining the observed Bouguer and free-air anomalies. A noteworthy feature in this profile is the central depression of Fig. 4.11a, since this half-grabenlike structure may indicate small brittle deformation of the lithosphere.

Profile West (Fig. 4.12) shows considerable scatter of observed anomalies caused by faulting and the presence of exposed/shallow Mesozoic volcanic rocks. Given the strict geometry and depth range of the 2.5D gravity model in use, the modelled anomalies do not fit well the observed ones.

Profile Southwest (Fig. 4.13) shows a less pronounced gravity high due to volcanic rocks with a better agreement between modelled and observed anomalies.

Figure 4.14 shows profile Southeast with some gravity offsets due to faulting and fractured blocks in the basement. The free-air and Bouguer anomalies may be reasonably explained by a 2.5D model for the basinal sediments and a region of differentiated crustal material at lower crust-upper mantle depths.

The 2.5D approach, taking basin sediment compaction into account, allowed building the first deep crustal structure model for Parnaíba. The gravity profiles show a regional agreement between observed and computed Bouguer and free-air anomalies. Naturally, short-wavelength anomalies like volcanic intrusions and block faulting cannot be modelled under the geometrical restrictions of the 2.5D axisymmetrical model.

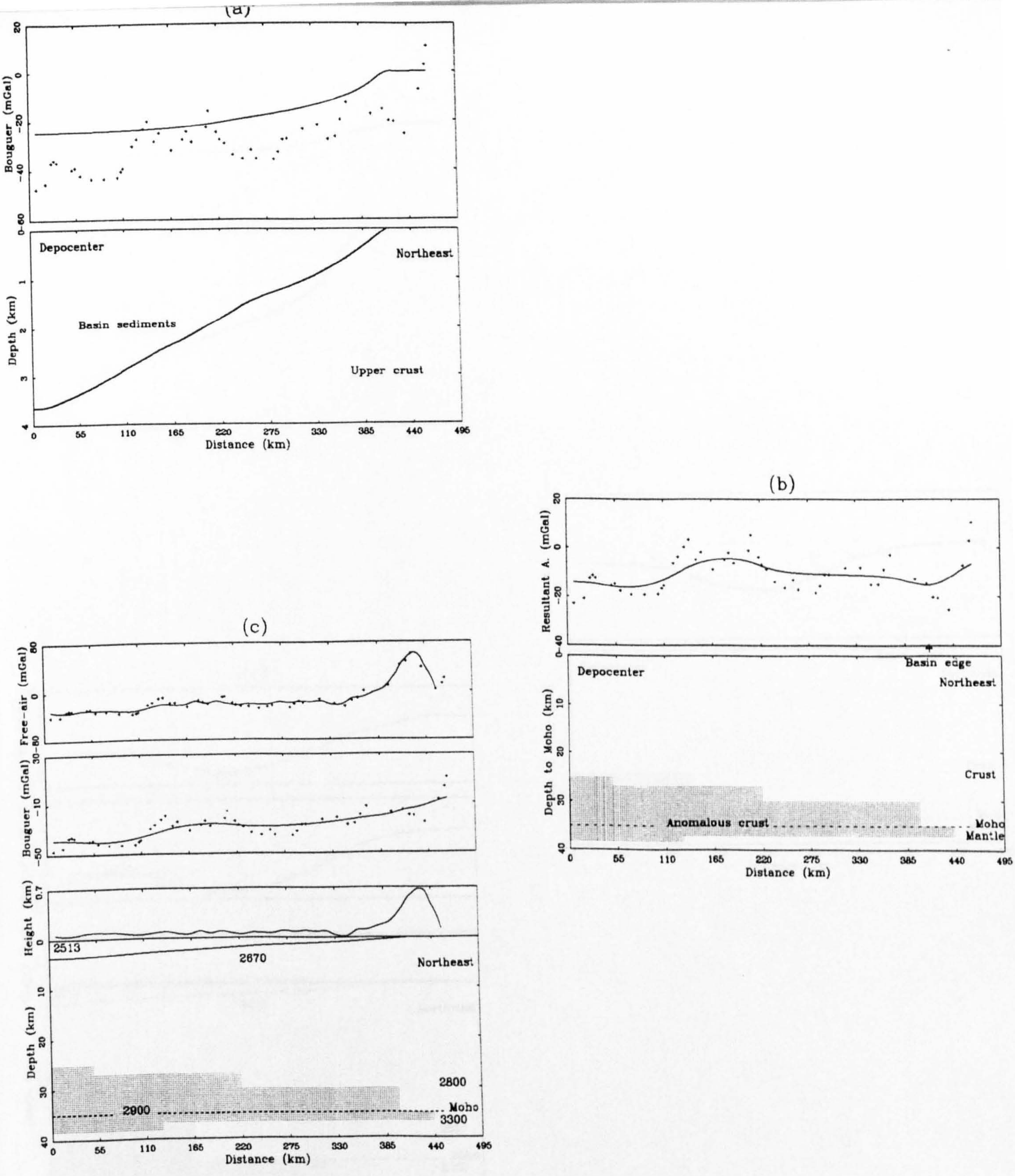

Fig. 4.10 Northeast radial gravity profile: (a) Observed Bouguer anomalies and the gravity signal produced by sediments. Note the short-wavelength anomaly caused by the Urbano Santos basement high; (b) Resultant anomaly interpreted as due to a zone of anomalous crust material. The continuous line is the modelled anomaly; (c) Gravity model including sediments and zone of anomalous crust showing general agreement between observed and calculated gravity anomalies. Densities in kg m^{-3}.

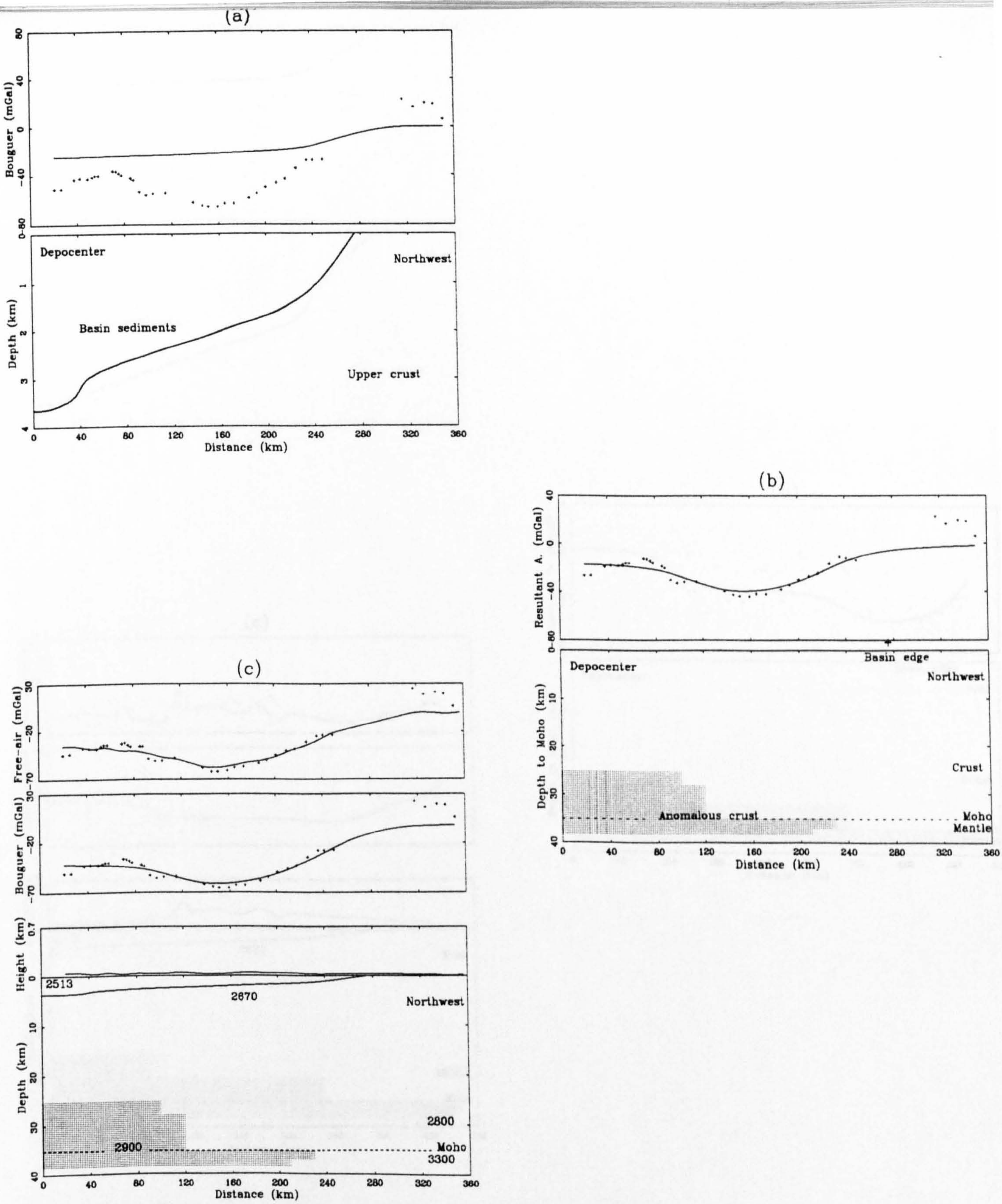

Fig. 4.11 Northwest radial gravity profile: (a) Observed Bouguer anomalies and the gravity signal produced by sediments; (b) Resultant gravity anomaly (continuous line) produced by the zone of anomalous crust; (c) Gravity model including sediments and zone of anomalous crust. Densities in kg m^{-3}.

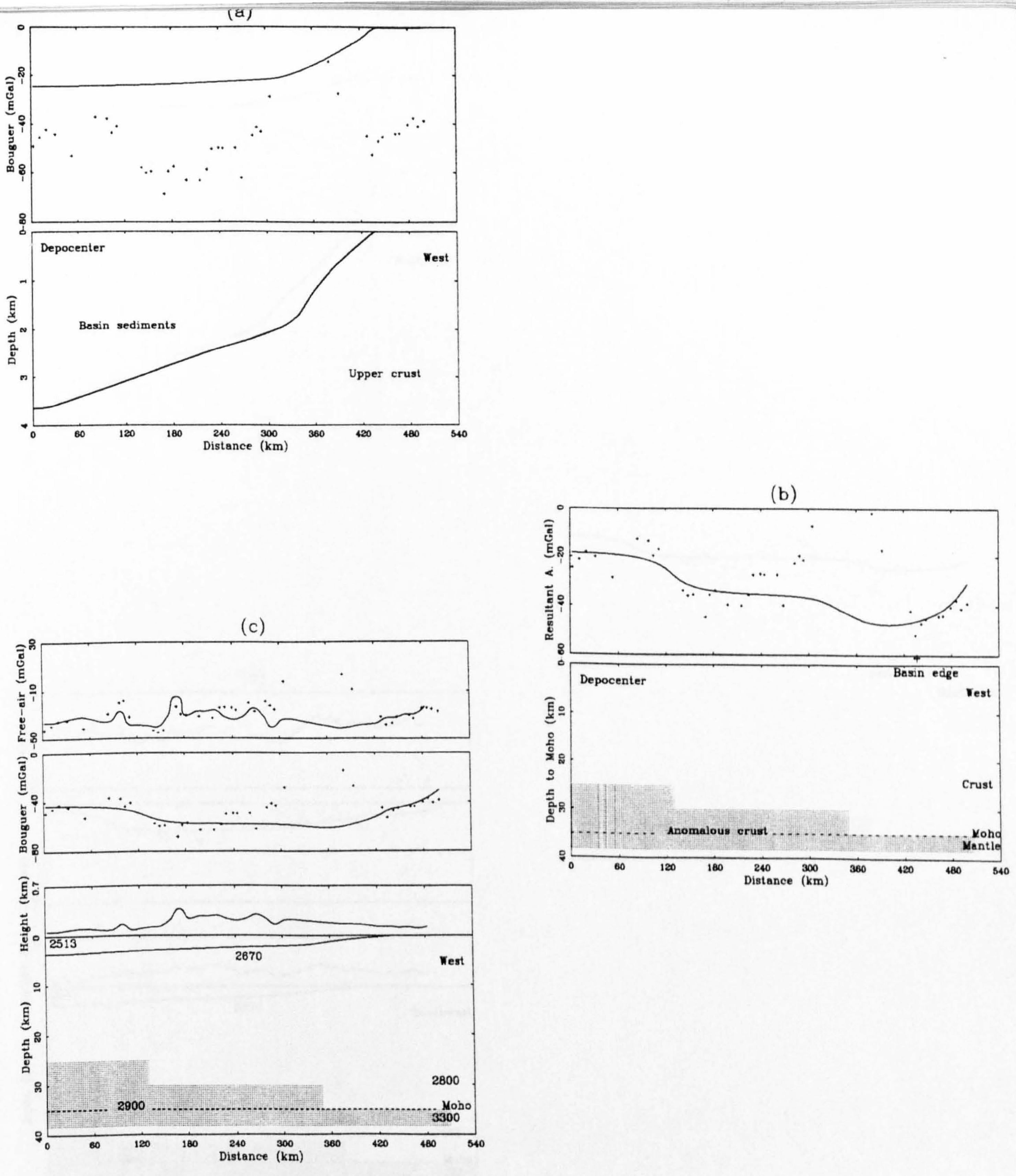

Fig. 4.12 West radial gravity profile: (a) The observed scatter of the Bouguer anomalies are due to faulting and volcanic intrusions. The ~40 mGal amplitude, ~240 km wavelength gravity high is caused by the Mosquito Fm. extrusives and exposed/shallow diabases; (b) Resultant anomaly vs. modelled (continuous line) anomalies; (c) Gravity model including sediments and zone of anomalous crust. Densities in kg m^{-3}.

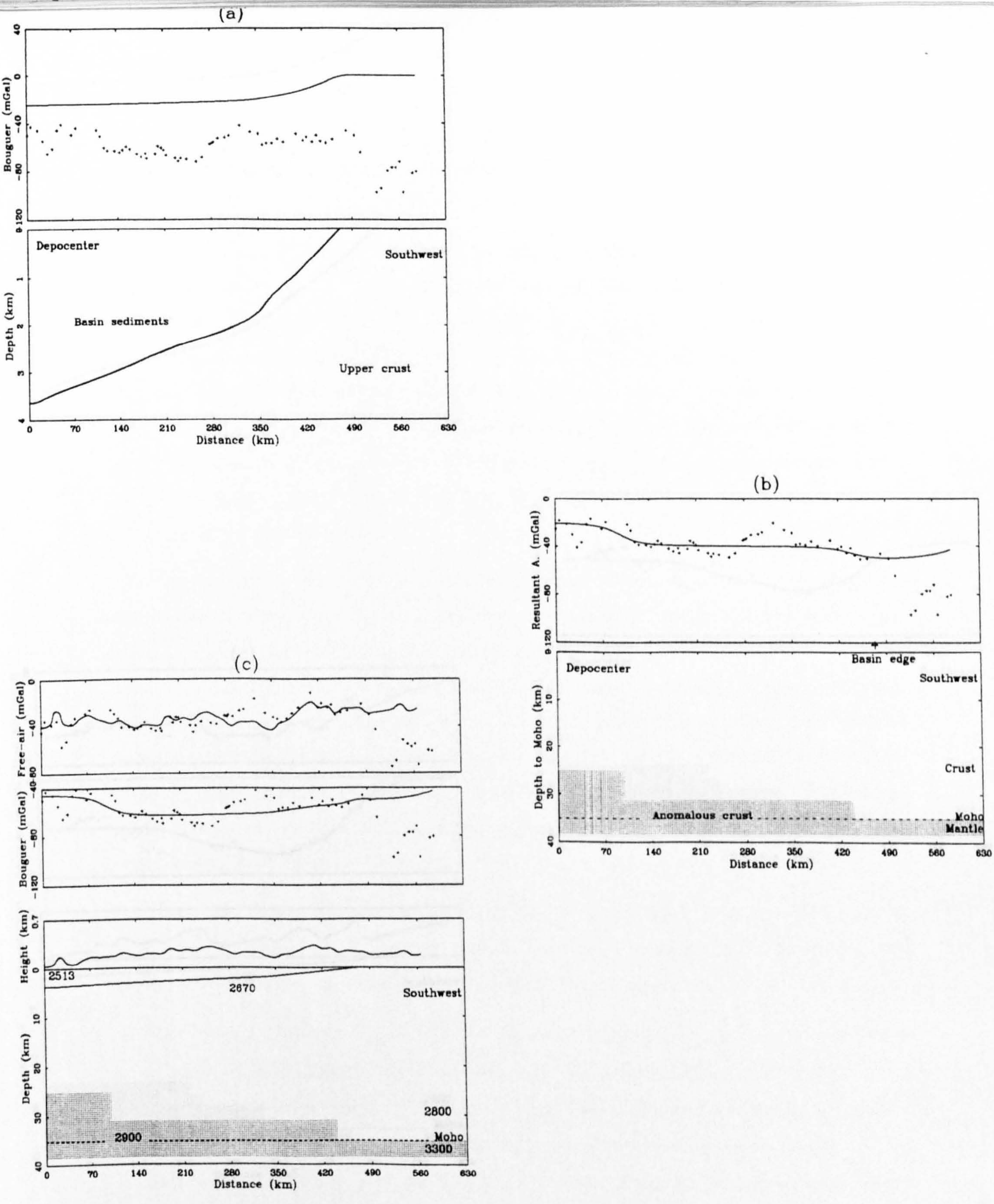

Fig. 4.13 Southwest radial gravity profile: (a) The observed Bouguer anomalies still show short-wavelength highs due to faulting and volcanic intrusions; (b) Resultant anomaly vs. modelled (continuous line) anomalies; (c) Gravity model including sediments and zone of anomalous crust. Densities in kg m^{-3}.

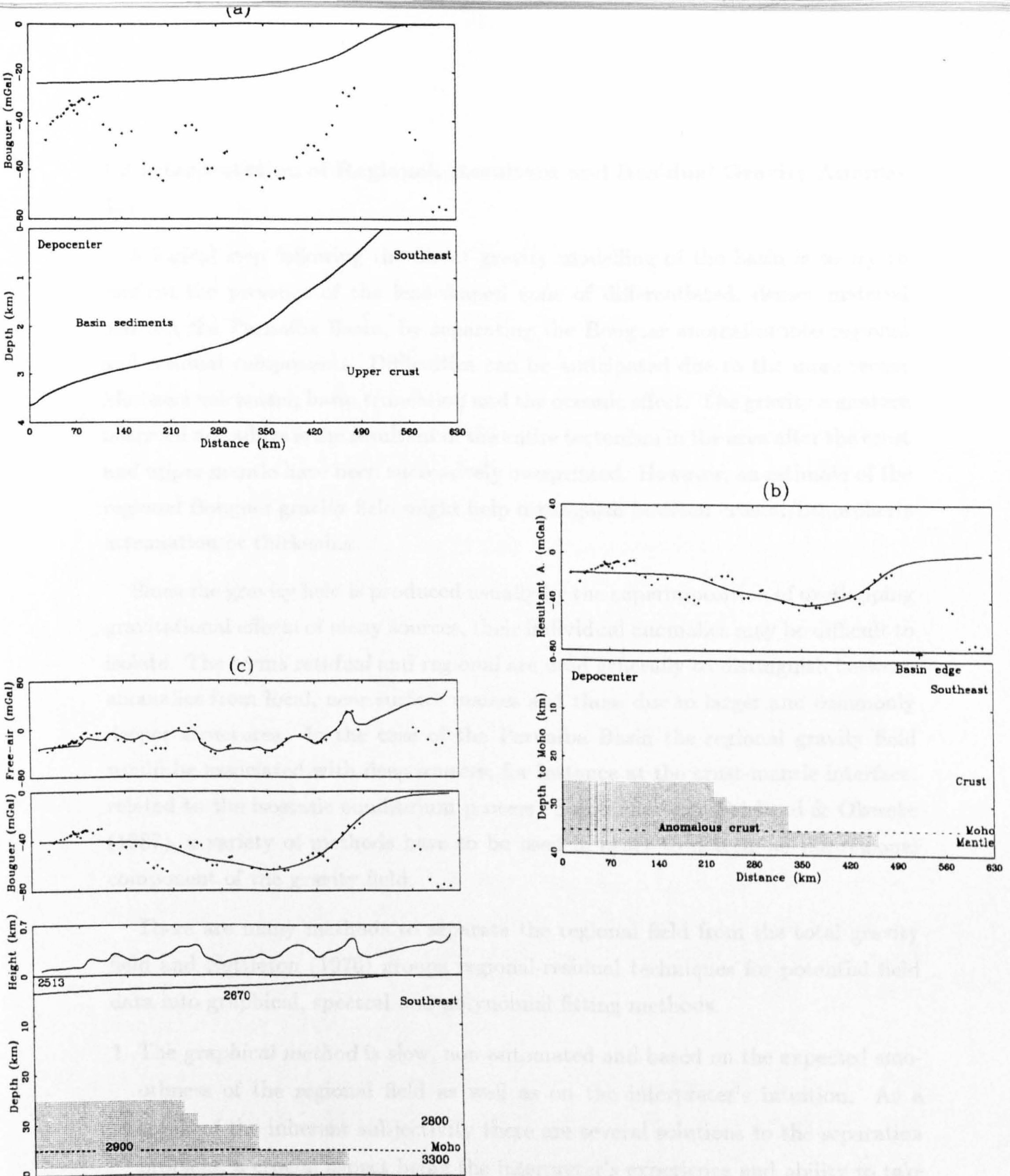

Fig. 4.14 Southeast radial gravity profile: (a) Observed Bouguer anomalies and short-wavelength highs due to faulting and the gravity signal produced by sediments (continuous line); (b) Resultant anomaly vs. modelled (continuous line) anomalies; (c) Gravity model including sediments and zone of anomalous crust. Densities in kg m^{-3}.

4.3 Interpretation of Regional, Resultant and Residual Gravity Anomalies

A logical step following the direct gravity modelling of the basin is to try to confirm the presence of the lens-shaped zone of differentiated, denser material beneath the Parnaíba Basin, by separating the Bouguer anomalies into regional and residual components. Difficulties can be anticipated due to the more recent Mesozoic volcanism, basin truncation and the oceanic effect. The gravity signature observed nowadays is the resultant of the entire tectonism in the area after the crust and upper mantle have been successively overprinted. However, an estimate of the regional Bouguer gravity field might help distinguish between crustal/lithospheric attenuation or thickening.

Since the gravity field is produced usually by the superimposition of overlapping gravitational effects of many sources, their individual anomalies may be difficult to isolate. The terms *residual* and *regional* are used generally to distinguish between anomalies from local, near surface masses and those due to larger and commonly deeper structures. In the case of the Parnaíba Basin the regional gravity field would be associated with deep sources, for instance at the crust-mantle interface, related to the isostatic equilibrium process. Sometimes *e.g.* Fairhead & Okereke (1987), a variety of methods have to be used in order to determine the regional component of the gravity field.

There are many methods to separate the regional field from the total gravity field and Nettleton (1976) groups regional-residual techniques for potential field data into graphical, spectral and polynomial fitting methods.

1 The *graphical method* is slow, non-automated and based on the expected smoothness of the regional field as well as on the interpreter's intuition. As a result of the inherent subjectivity there are several solutions to the separation problem, a crucial aspect being the interpreter's experience and ability to take into account relevant geological information about the regional field (*e.g.* Gupta & Ramani, 1980).

2 *Spectral methods* take advantage of the known predominance of the low-frequency spectral content of the regional field to quantitatively estimate its smoothness. They are faster and less subjective than the graphical method obtaining

the separation through the application of a suitable low-pass filter to the total field. A complete separation is not attainable due to the overlap of the regional and residual spectra resulting in signal distortion and noise transmission being always present. The filtering procedure causes signal distortion when it eliminates part of the signal spectral content. It also causes noise transmission as the result of the incomplete removal of the noise. Jacobsen (1987) showed that the use of Wiener filtering can minimize the total effect of these errors. Pawlowski & Hansen (1990) performed the gravity anomaly separation by Wiener filtering and incorporating geologic information from the study area to the specification of the filter's transfer function.

3 *Polynomial fitting methods* apply polynomial surfaces to model the regional field whose smoothness is controlled by the polynomial order (Zeng, 1989; Beltrão *et al.*, 1991). Any attempt to model a complex regional field by a high-order polynomial will produce an effect similar to noise transmission of spectral methods. On the other hand, a smooth but irregular regional field cannot be modelled by a very low-order polynomial due to an effect similar to signal distortion.

Recently, Beltrão *et al.* (1991) proposed the use of robust polynomial fitting to perform the regional-residual separation. It employs *a priori* information assuming that isolated gravity anomalies are locally either positive or negative, but not both. The application of this method to an area in the Borborema Province adjacent to Parnaíba allowed the removal of the prevailing NE-SW regional trend due to the Transbrasiliano Lineament. Local gravity anomalies due to outcropping granulites were then made visible.

According to Zeng (1989), a stable and unbiased estimate of the regional field can be obtained by upward continuation of surface gravity anomalies up to heights where the regional field predominates. Consider fitting (in the L_2 sense) polynomials

$$P_d(x_i, y_i) = a_0 + a_1 x_i + a_2 y_i + a_3 x_i^2 + a_4 x_i y_i + \ldots + a_k y_i^d$$

to the function

$$f(x_i, y_i), \ i = 1, 2, \ldots, L,$$

with

$$k = \frac{1}{2}(d+1)(d+2) - 1, \quad d = 1, 2, \ldots, n.$$

The variance σ_d is

$$\sigma_d = \frac{1}{L}\sum_{i=1}^{L}[f(x_i, y_i) - P_d(x_i, y_i)]^2$$

and it can be shown (see proof in the Appendix of Zeng, 1989) that if $f(x_i, y_i)$ is an nth-order polynomial, in fitting $P_d(x_i, y_i)$ $(d = 1, 2, \ldots, n-1, n, n+1, \ldots)$ to $f(x_i, y_i)$ the variance σ_d decreases when d increases in the interval $0 < d < n$ and $\sigma_d = 0$ for $d \geq n$. Figure 4.15a shows that the point of discontinuity of the gradient of the plot of σ_d against d yields the degree n of the polynomial.

Since gravity anomalies can be represented by the sum of finite Fourier series, they can also be represented by a finite polynomial of sufficiently high degree, because sines and cosines can be expressed as Taylor series. When a set of polynomials $P_d(x, y)$ $(d = 1, 2, \ldots, D)$ is fitted to the gravity anomalies $\Delta g(x, y)$, the point of discontinuity of the gradient of σ_d against d allows estimating the optimum degree d_n, as shown in Fig. 4.15b.

Bouguer anomalies, Δg_B, can be regarded as the superimposition of anomalies from sources at varying depths

$$\Delta g_B = \Delta g_1 + \Delta g_2 + \ldots + \Delta g_l,$$

with Δg_1 denoting the contribution from the deepest disturbing mass, Δg_2 the next deepest, ... and Δg_l being the shallowest. After computing the upwardly continued anomalies $\Delta g_B(h_1)$ and $\Delta g_B(h_2)$ at heights h_1 and h_2 respectively, the degree of the polynomial representing Δg_1 can be estimated by fitting polynomials P_d $(d = 1, 2, \ldots, n)$ to $\Delta g_B(h_1)$ or $\Delta g_B(h_2)$.

The optimal height value for the upward continuation can be calculated considering that at and above this height the regional field is reasonably smooth with low lateral change rates. Given $\Delta g_B(h)$, the upward-continued Bouguer anomaly at height h, the number of points (*Zeng's extremal points*) on the continuation map with gradient

$$\left(\frac{\partial \Delta g_B}{\partial x, y}\right) \approx 0$$

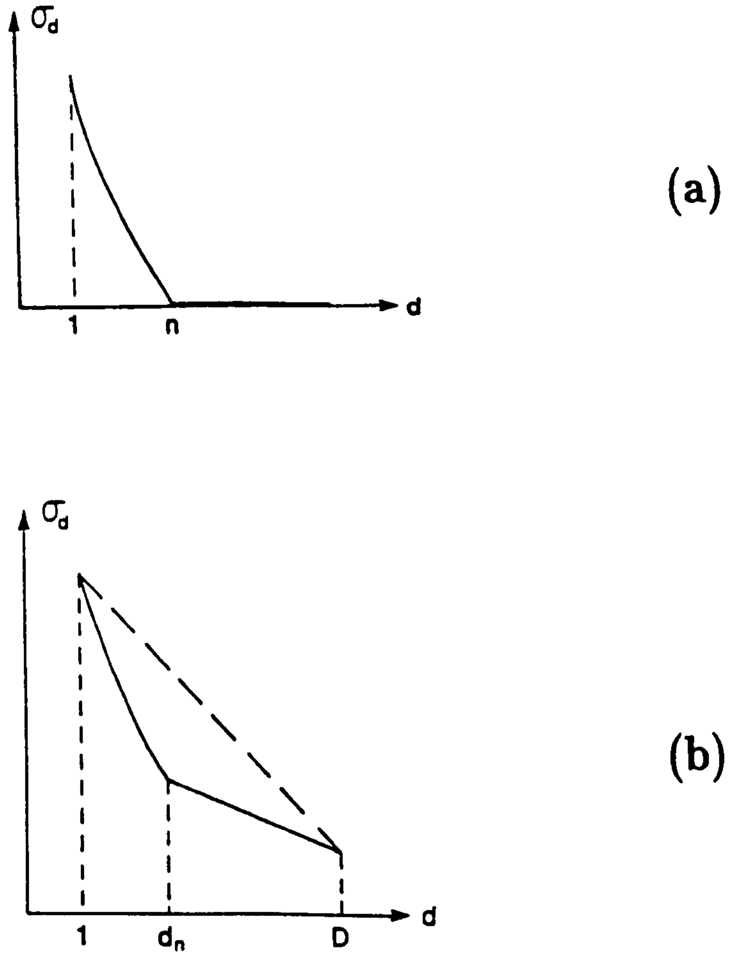

Fig. 4.15 Fitting polynomials to functions $f(x,y)$; (a) Variance σ_d against polynomial degree d for an nth-degree polynomial $f_n(x,y)$; (b) Variance σ_d against polynomial degree d for gravity anomaly $\Delta g(x,y)$ (after Zeng, 1989).

can be counted and this number should be asymptotically constant.

The main deep density boundaries in the study area are the Moho and the differentiated/lower crust discontinuity. The basinal strata and the sediment infill of precursory grabens produce less deep discontinuities with upper crust rocks. Then, ignoring short-wavelength anomalies due to shallow structures, the total Bouguer anomaly Δg_B can be approximated by

$$\Delta g_B = \Delta g_M + \Delta g_{crust} + \Delta g_{sed},$$

where Δg_{sed}, Δg_{crust} and Δg_M are anomalies due to the sediment infill, the anomalous crust structure and the Moho discontinuity, respectively. The aim is to separate the anomaly Δg_M from the total Bouguer anomaly. The sediment infill constitutes a problem in the process of isolating Δg_M and its long-wavelength anomaly must be filtered out. This was accomplished by fitting a seventh-degree polynomial surface $Z_7(\phi, \lambda)$, shown in Fig. 4.16, to the digitized total isopach map. Parameters (ϕ, λ) are the geographic latitude and longitude and use was made of the routine **SURFACE.FOR** (Balch & Thompson, 1989). Depths to the basement of all data points could then be estimated and the simple Bouguer slab with a density contrast of $\Delta\rho$ = -157 kg m^{-3} was used to estimate the sediment gravity component. These rather simple assumptions, although crude for forward gravity modelling, provide a first approximation to Δg_{sed} and, in the process of upward continuation, the (second-order) deviations are expected to be smoothed.

Considering the simple Bouguer approximation, the gravity component due to the sediments was computed as

$$\Delta g_{sed} = 2\pi G \Delta\rho Z_7(\phi, \lambda), \tag{4.3}$$

with all parameters already defined.

After appropriate gridding the area, the number of extremal points could be found as those satisfying the inequality:

$$\left| \frac{\partial \Delta g_B}{\partial x, y} \right| \leq \epsilon,$$

where ϵ is a small non-negative value in mGal km^{-1}. In the present study ϵ was set to 0.1 mGal km^{-1} and Fig. 4.17 shows the number of Zeng's extremal points

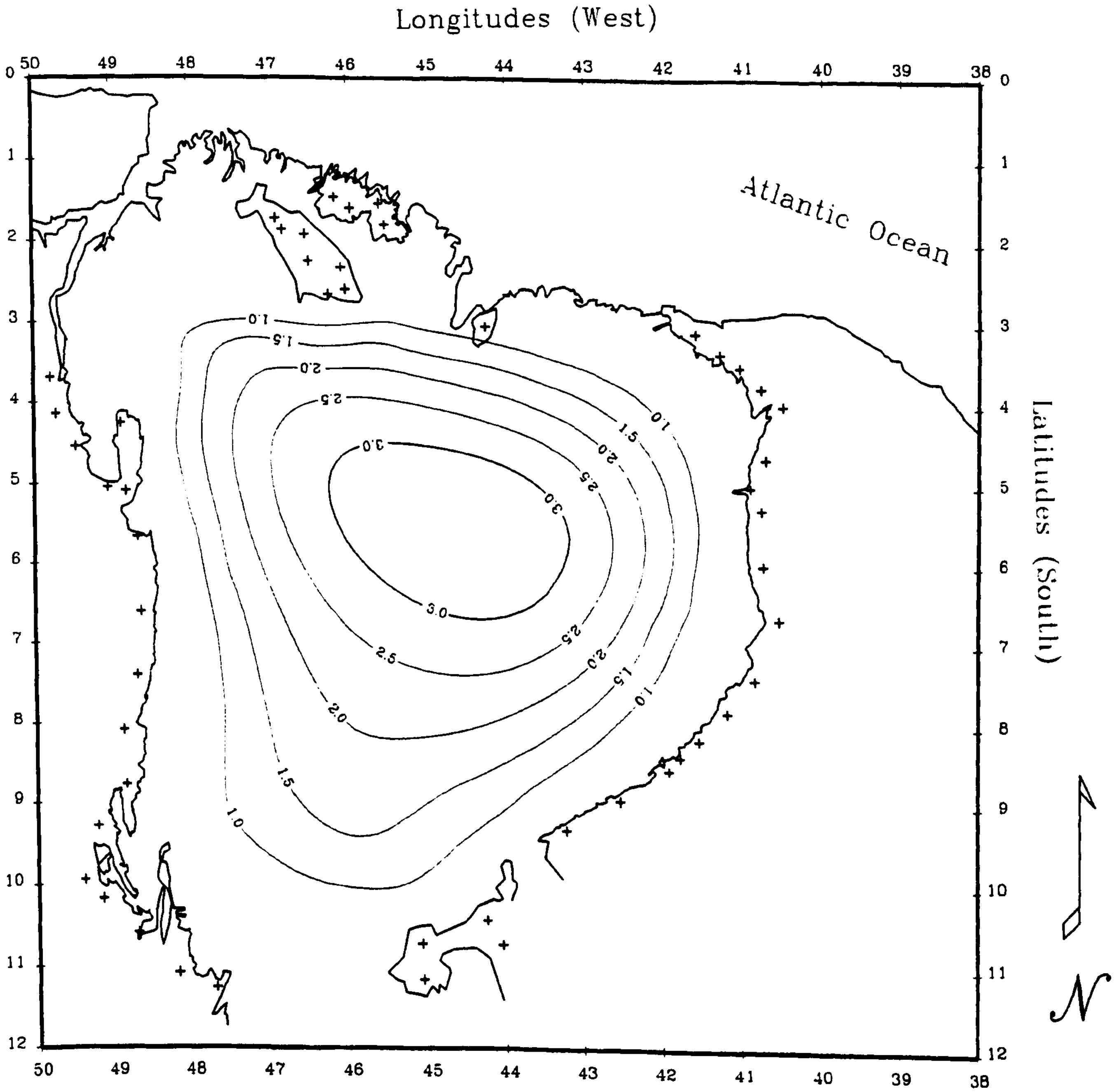

Fig. 4.16 Polynomial surface of degree 7 in latitude and longitude $Z_7(\phi, \lambda)$, fitted to the digitized total isopach map of the Parnaíba Basin and used to estimate the sediment component of the Bouguer anomalies. Contour interval: 0.5 km, conic projection.

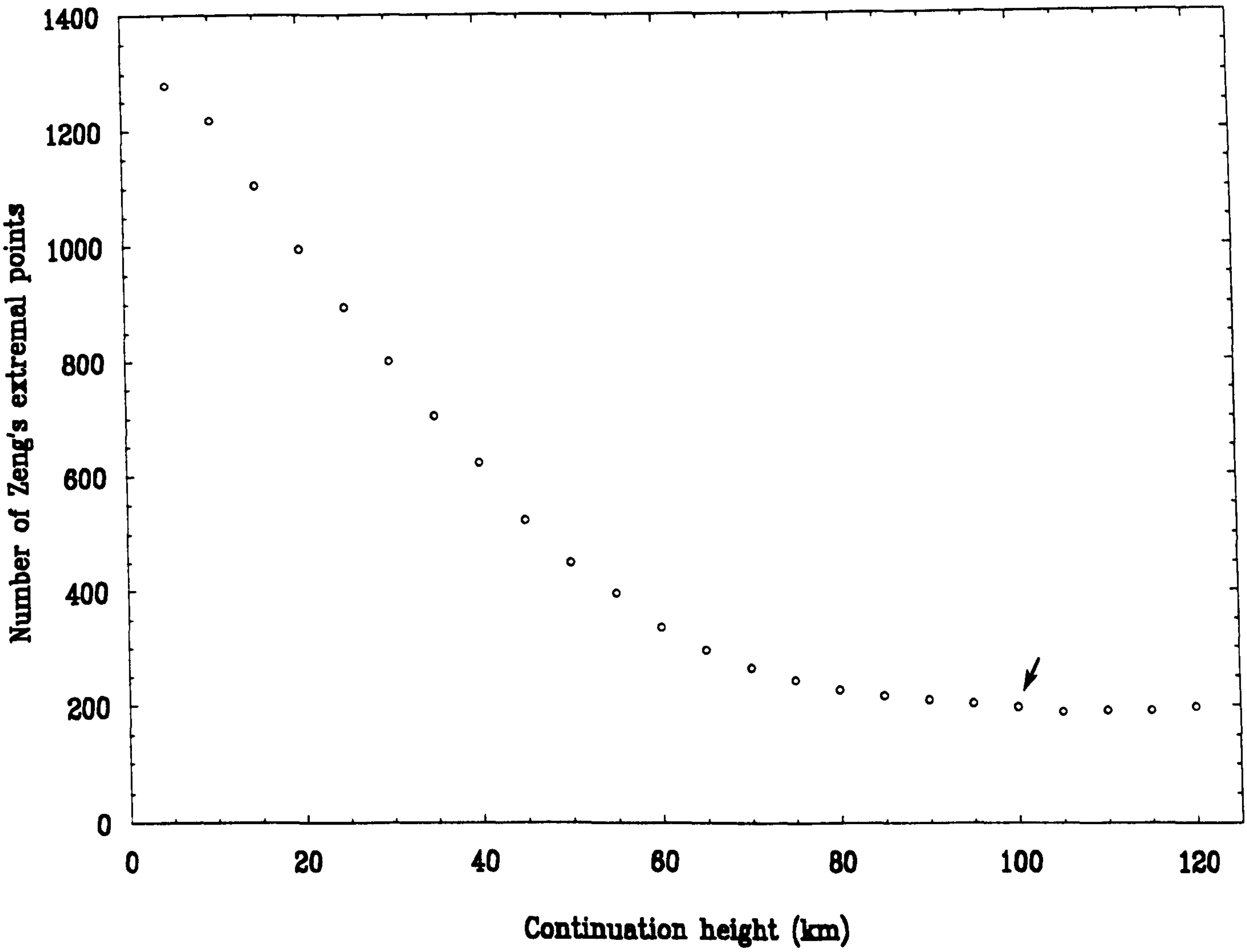

Fig. 4.17 Number of Zeng's extremal points against the continuation height of the Bouguer anomalies over Parnaíba. The arrow points to the chosen optimal height.

against height. It is seen that for heights above 100 km these points tend to be asymptotically constant.

The coefficients $C(k,n)$ for the upward continuation of the resultant anomalies were calculated according to the expression given by Baranov (1975, Equation 6.12) and coded in program **COEFF.FOR** in the Appendix.

$$C(k,n) = \frac{1}{2\pi^2}\int_{-1}^{1} du \int_{0}^{\pi} \exp -\alpha h(1+u^2)^{1/2}\alpha[\cos(k+nu)\alpha + \cos(ku+n)\alpha]d\alpha,$$

where $(k,n) = -N,\ldots,0,\ldots,N$ are the appropriate grid indexes for the continuation coefficients; h is the continuation height and the double integral was solved by Romberg's quadrature (Subroutine **QROMB**, Press *et al.*, 1992)

The whole 12^0 by 12^0 square was gridded N-S, E-W with the same interval of $15'$ used for constructing the gravity anomaly maps and the continuation filter was truncated in $N = 10$ due to data coverage limitations. The summation $\sum_{k,n=-10}^{10} C(k,n)$ was kept normalized to 1.0 for the entire range of continuation heights. In order to minimize border effects the effective area for upward continuation and mapping of the regional field was limited to an 8^0 by 8^0 square, centered at the surface data square. Several computer codes were developed to calculate the upward continuation coefficients, grid the input surface data, perform the upward continuation of the Bouguer anomalies and produce a map of the regional Bouguer field.

The upward-continued Bouguer field at the height of 100 km was modelled by fitting a polynomial surface with independent variables given by the longitude, latitude pairs for each grid point. A graph showing the variance versus polynomial degree is shown in Fig. 4.18. By examining this graph from higher to lower degrees a break in the curve is seen at degree 4 and, according to Zeng (1989), this break would define the best-fitting surface for the regional field.

The regional Bouguer map over the Parnaíba Basin is shown in Fig. 4.19. The long-wavelength anomalies have been interpreted in terms of Moho topography as a regional thickening of the crust underneath the basin and its rapid attenuation towards the coast. A thicker crust underneath the São Francisco Craton is also denoted in the map. The steep E-W gradient seen over the Tucano Basin to the

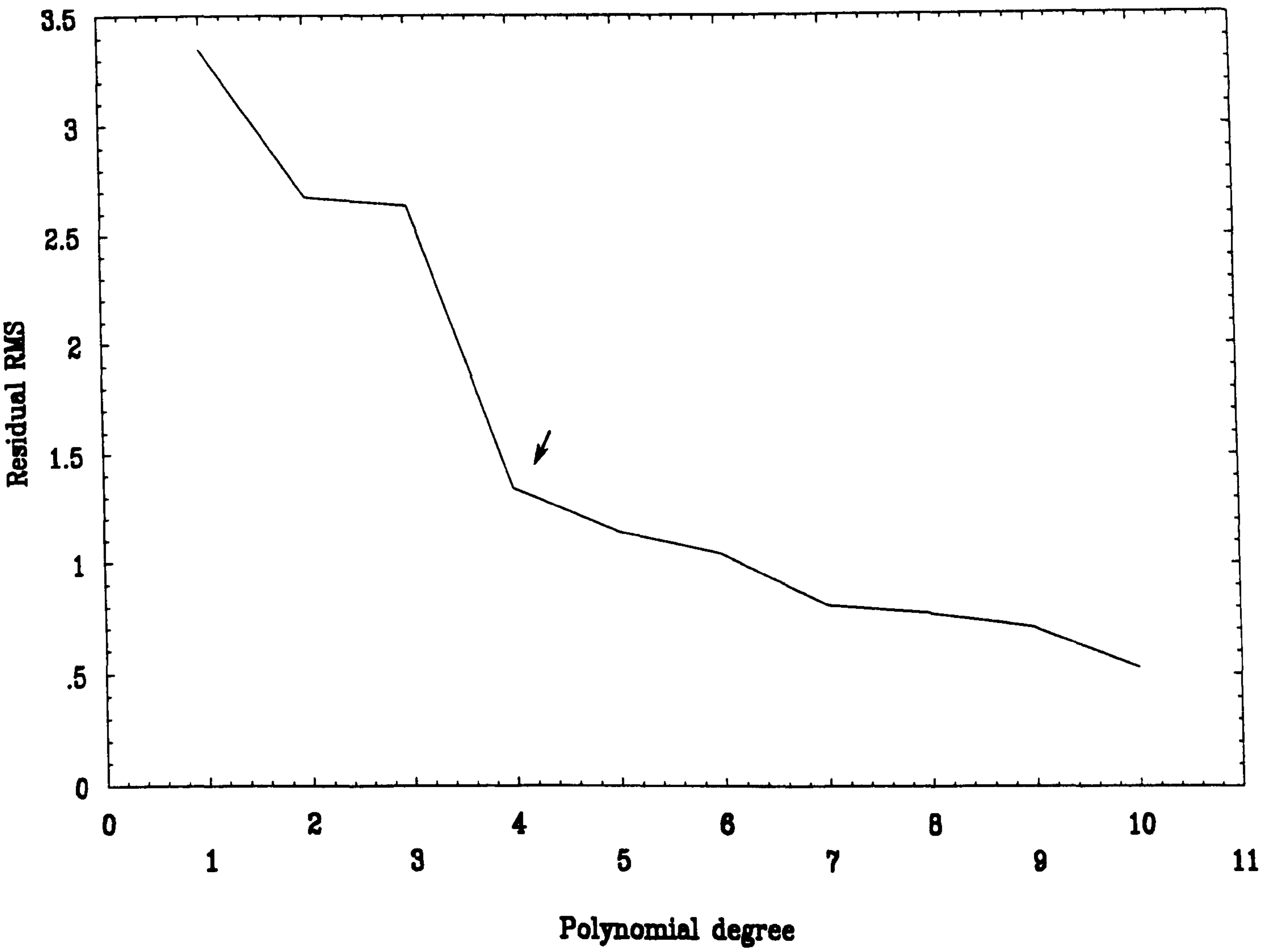

Fig. 4.18 Variances (residual RMS) of polynomial surface models of the regional Bouguer field over Parnaíba. The arrow indicates the preferred degree.

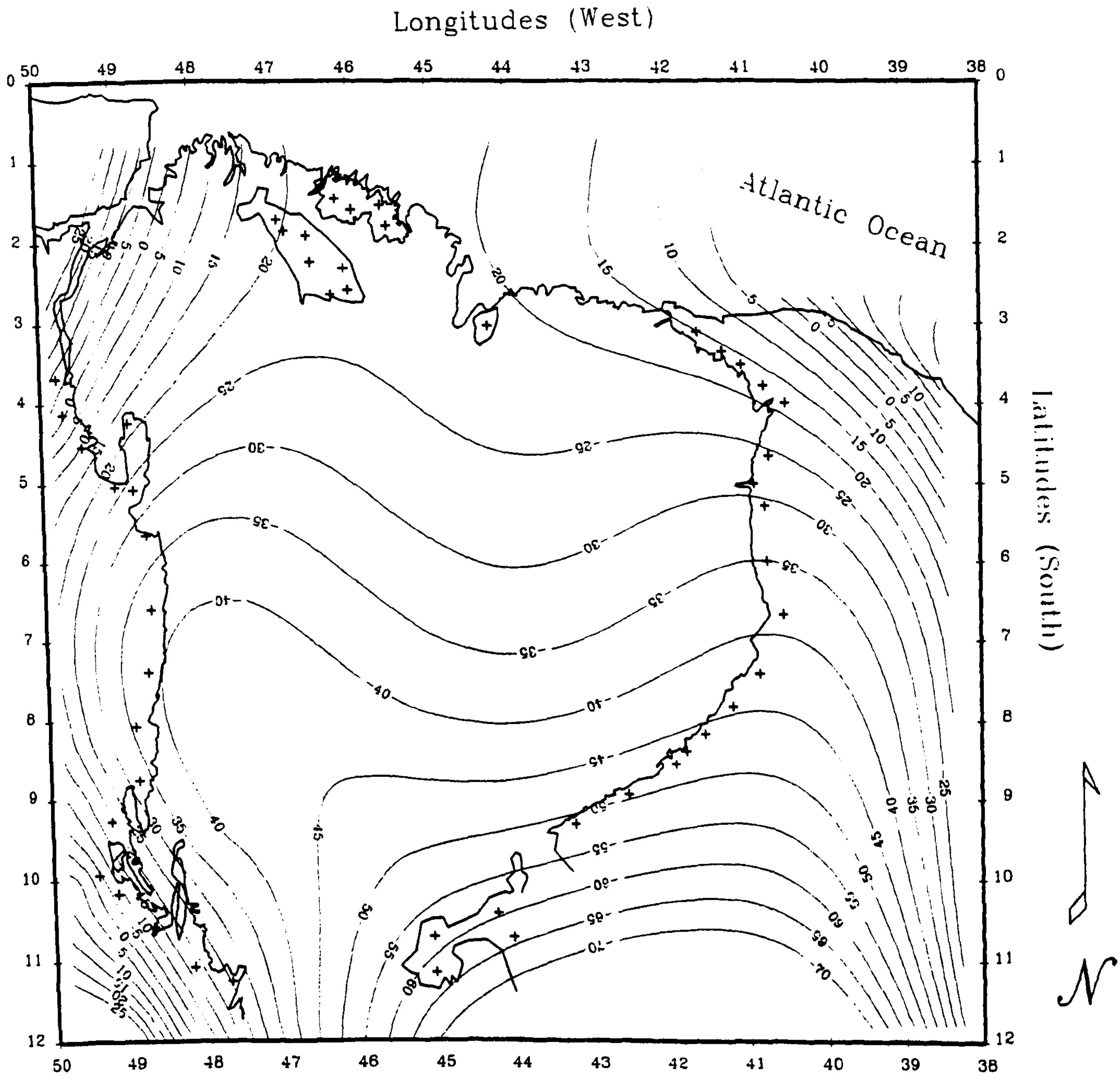

Fig. 4.19 Regional Bouguer map of the Parnaíba Basin. Contour interval: 5 mGal, conic projection.

SE of Parnaíba was previously detected by Meneses (1990). The present resolution of the gravity data coverage does not allow a finer estimate of the regional field.

A resultant anomaly map is shown in Fig. 4.20. The resultant anomalies were produced by removing the sediment gravity component computed through Equation (4.3) from the Bouguer anomalies. As expected, the gravity signals due to basement structures are enhanced. The -40 mGal contour line to the east and northeast of Parnaíba delineates the influence of subsiding structures (grabens and half-grabens) associated with the Transbrasiliano Lineament. Note this elongated low ignores the basin boundary to the northeast and effectively provides geophysical evidence of the continuation of prebasinal sediments outcropping in the Borborema Province deposited and/or reworked during the Brasiliano Cycle.

An even lower gravity anomaly (-50 mGal) to the southwest is associated with the inferred NNW-SSE grabens. Locally, -60 mGal is mapped and demarcates the maximum deposition of Upper Proterozoic molassic sequences. Outside Parnaíba, the resultant map has no sediment component removed and is identical to the ordinary Bouguer map.

The viability of inverting gravity anomalies to model depths to the basement over sedimentary basins with variable density contrast has been discussed by *e.g.* Rao (1986) and Rao & Babu (1991). These workers presented very satisfactory results for small basins like the São Jacinto Graben (North America), Vienna and Pannonian Basins (Central Europe). This inversion technique has been also applied with success to the small Camaquã Basin in the south of Brazil (Costa, 1995). Unfortunately, results for the Parnaíba Basin were unsatisfactory and are related to the very large dimensions of this basin and lack of detailed Bouguer and regional anomaly maps. Also, in order to get analytical expressions for the gravity anomalies in the spatial domain, the inversion algorithm makes use of a quadratic density function to account for the variation of the density contrast with depth (Thompson & Balch, 1988) and this approximation may contribute to inaccurate depths to the basement.

A better approach in the present case is inverting the gravity signal in separate sections linking borehole sites where the basement was actually reached. Narasimha Rao *et al.* (1995) proposed an inversion algorithm based on the

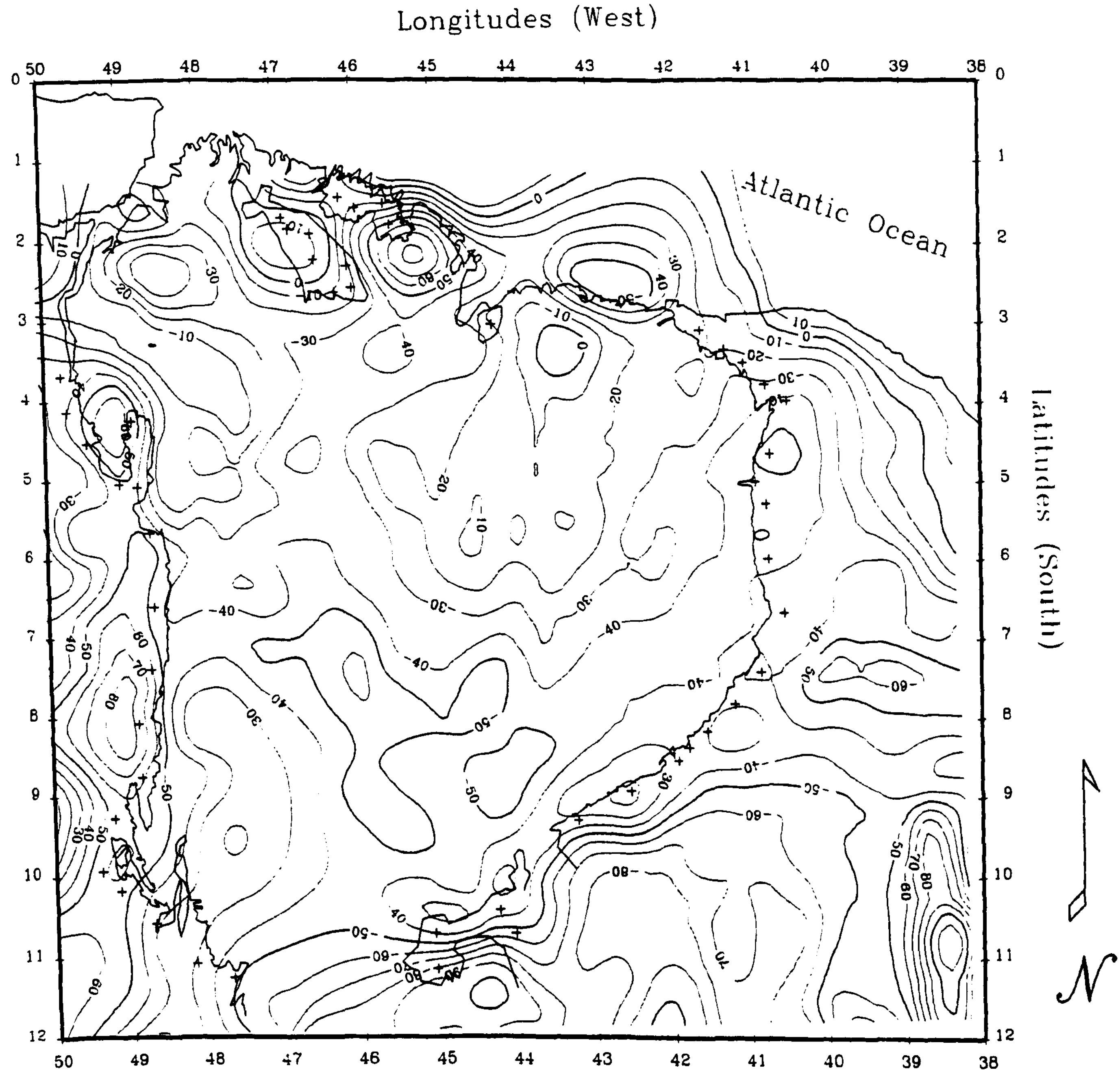

Fig. 4.20 Resultant anomaly (observed Bouguer less sediment gravity component) map of the Parnaíba Basin. Contour interval: 10 mGal, conic projection.

damped approximate technique which can make use of *a priori* geologic information. Recently, Narasimha Rao *et al.* (1996) suggested the use of the Hartley Transform to achieve basement mapping with the additional capability of directional filtering. Published examples of the successful application of both techniques are restricted to small regions and the viability of applying them to Parnaíba is currently being investigated.

The residual anomaly map shown in Fig. 4.21 was produced by removing from the Bouguer both the regional field and the sediment component. Despite the limitations in the gravity coverage a positive, central anomaly is clearly visible. The anomaly pattern is compatible with the existence of differentiated, denser crustal material closer to the surface at about the basin depocentre. Other positive anomalies seen to the NW and SW that might be related to the upwelling of aesthenosphere or partial basaltic melt do not correlate well with the Upper Proterozoic NNW-SSE deposits. The gravity coverage is poor in this area of the basin.

4.4 Discussion

The present work introduces the first gravity anomaly maps and the deep crustal model of the Parnaíba Basin. Although severe limitations in the gravity data coverage are recognized, the areal extent of the Transbrasiliano Lineament and the NNW-SSE grabens could be assessed. The use of 2.5D gravity models exploring the near-axisymmetric basin geometry allowed the proposal of the first deep crustal structure model for Parnaíba. Analysis of gravity data suggests that the Parnaíba Basin is underlain by a lens-shaped zone of dense material in the lowermost part of the crust uppermost part of the mantle. Up to $\sim$10 km of the lower continental crust in this zone seems to be partially replaced/intruded by material intermediate in density between normal lower continental crust and upper mantle. This anomalous, denser zone may result from intrusion/partial replacement of the lower crust by mantle material, continental underplating (Furlong & Fountain, 1986) or passive upwelling of partial melt (not aesthenosphere) during rifting and extension of the lithosphere (Buck & Mutter, 1987). The use of a slightly different density contrast between normal lower crust and altered crust would change the size but not the shape of the proposed anomalous crust zone. The lack of a homogeneous gravity coverage over the basin and adjacent provinces and uncertainties in the sediment thickness and effective density preclude more refined, detailed gravity models to be presented for the time being.

A summary of the gravity model proposed for Parnaíba is shown in Fig. 4.22. Although not unique, this model satisfies both the observed Bouguer and free-air anomalies thus providing a good crustal structure model and illustrating the isostatic condition of the basin. The proposed deep crustal model compensates the surface topography and the sedimentary load by flexural downwarp of up to 13.5 km of anomalous crust. It is possible that the topography observed at the flanks of the basin is partially created by this flexural downwarp.

Gravity studies of other areas where the continental lithosphere underwent extensional tectonics indicated simple crustal thinning *e.g.* the North Sea Basin, Donato & Tully, 1981. Fairhead *et al.* (1991) were able to produce a gravity model for the Mamfe Basin in West Africa, predicting simple crustal thinning, although a rather low ($\Delta\rho = 170$ kg m^{-3}) crust/mantle density contrast had to be used. Also, Mamfe is about 100 km wide and local equilibrium is a valid assumption in this case. Thick continental crust intruded by denser material at depth has been reported by Halls (1982) and Mooney *et al.* (1983) regarding the midcontinent gravity high and the Mississippi Embayment in North America.

In Brazil, Nunn & Aires (1988) proposed the existence of an elongated, riftlike zone of dense (3,000 kg m^{-3}) material, up to 45 km in thickness beneath the Middle Amazon Basin, not necessarily below the basin axis. Molina *et al.* (1989) pointed out the need in gravity analysis to take into account not only the Bouguer evidence but also the isostatic condition using the free-air anomalies. Their gravity study of the northern Paraná Basin, where intense Mesozoic volcanism occurred, led to the proposal of a *crustal underplating* situation with the lowermost crust being contaminated by mantle material. Hurter & Pollack (1995) further considered this underplate model in their assessment of the temperature history and surface heat flow of the Paraná Basin. They showed that the thermal disturbance in the sediments caused by the cooling of sill-like bodies and extrusive basalts lasts for less than 1 Myr and temperatures above 100°C cannot be locally maintained for over than 200 kyr. Effects on basin temperatures and heat flow due to a large underplate reach a maximum of ~10°C and 5 mW m^{-2}, respectively, at about 10

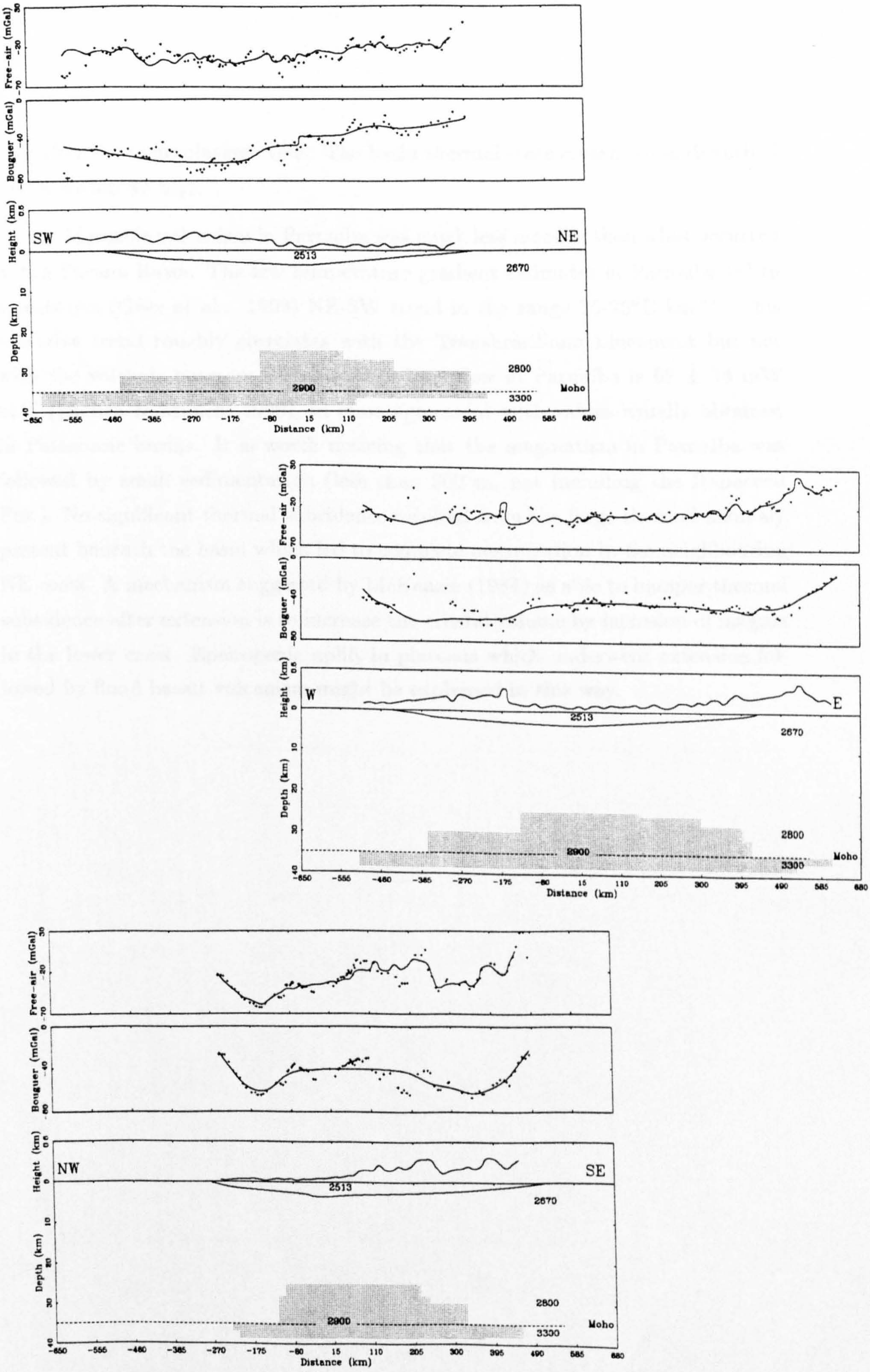

Fig. 4.22 Gravity model for the Parnaíba Basin along profiles SW-NE, W-E and NW-SE. Scattered crosses are the observed anomalies and the continuous lines are the predicted anomalies. Densities in kg m^{-3}.

Myr after the underplating event. The basin thermal state returns to undisturbed values within 80 Myr.

The Mesozoic volcanism in Parnaíba was much less massive than what occurred in the Paraná Basin. The few temperature gradient estimates in Parnaíba led to a tentative (Góes *et al.*, 1993) NE-SW trend in the range 15-25°C km^{-1}. This tentative trend roughly correlates with the Transbrasiliano Lineament but not with the volcanic outcrops. The average heat flow in Parnaíba is 62 $\pm$ 14 mW m^{-2} (Hamza & Muñoz, 1996), in close agreement with values usually obtained in Palaeozoic basins. It is worth noticing that the magmatism in Parnaíba was followed by small sedimentation (less than 300 m, not including the Itapecuru Fm.). No significant thermal subsidence resulted from the large thermal anomaly present beneath the basin which led to complete oceanization in the neighbouring NE coast. A mechanism suggested by McKenzie (1984) as able to hamper thermal subsidence after extension is to increase the crustal volume by intrusion of magma in the lower crust. Epeirogenic uplift in plateaus which underwent extension followed by flood basalt volcanism might be explained in this way.

CHAPTER 5

GEOHISTORY ANALYSIS

5.1 Borehole Data

The borehole data set used in the present study of geohistory of the Parnaíba Basin was released by PETROBRÁS. Stratigraphic information, including thicknesses of drilled layers, of 22 boreholes which reached the metamorphic or sedimentary basement of Parnaíba was used to assess the tectonic subsidence pattern in the basin. The distribution of boreholes is shown in Fig. 5.1. As previously mentioned, a single well in the basin (1-PA-01-MA, 4.2°S, 45.7°W) provides density vs. depth information derived from a FDC log, as shown in Table 5.1.

Table 5.1 Input parameters for backstripping well 1-PA-01-MA. Source: PETROBRÁS S.A.

Stratigraphic Unit	Top (km)	Thickness (km)	Density (kg m^{-3})	Absolute Age (Ma)
Itapecuru	-0.093	0.312	2,200	100
Codó	0.219	0.095	2,234	110
Grajaú	0.314	0.091	2,254	115
Pastos Bons	0.405	0.056	2,362	170
Motuca	0.461	0.056	2,362	245
Pedra de Fogo	0.681	0.243	2,390	255
Piauí	0.881	0.384	2,467	290
Poti	1.174	0.371	2,496	350
Longá	1.459	0.069	2,508	360
Cabeças	1.528	0.261	2,548	365
Pimenteiras	1.622	0.359	2,590	370
Itaim	2.148	0.098	2,595	380
Jaicós	2.298	0.210	2,473	410
Tianguá	2.456	0.131	2,665	420
Ipu	2.587	0.159	2,463	435
Basement	2.746	0.023*	2,544	445

(* - drilled thickness)

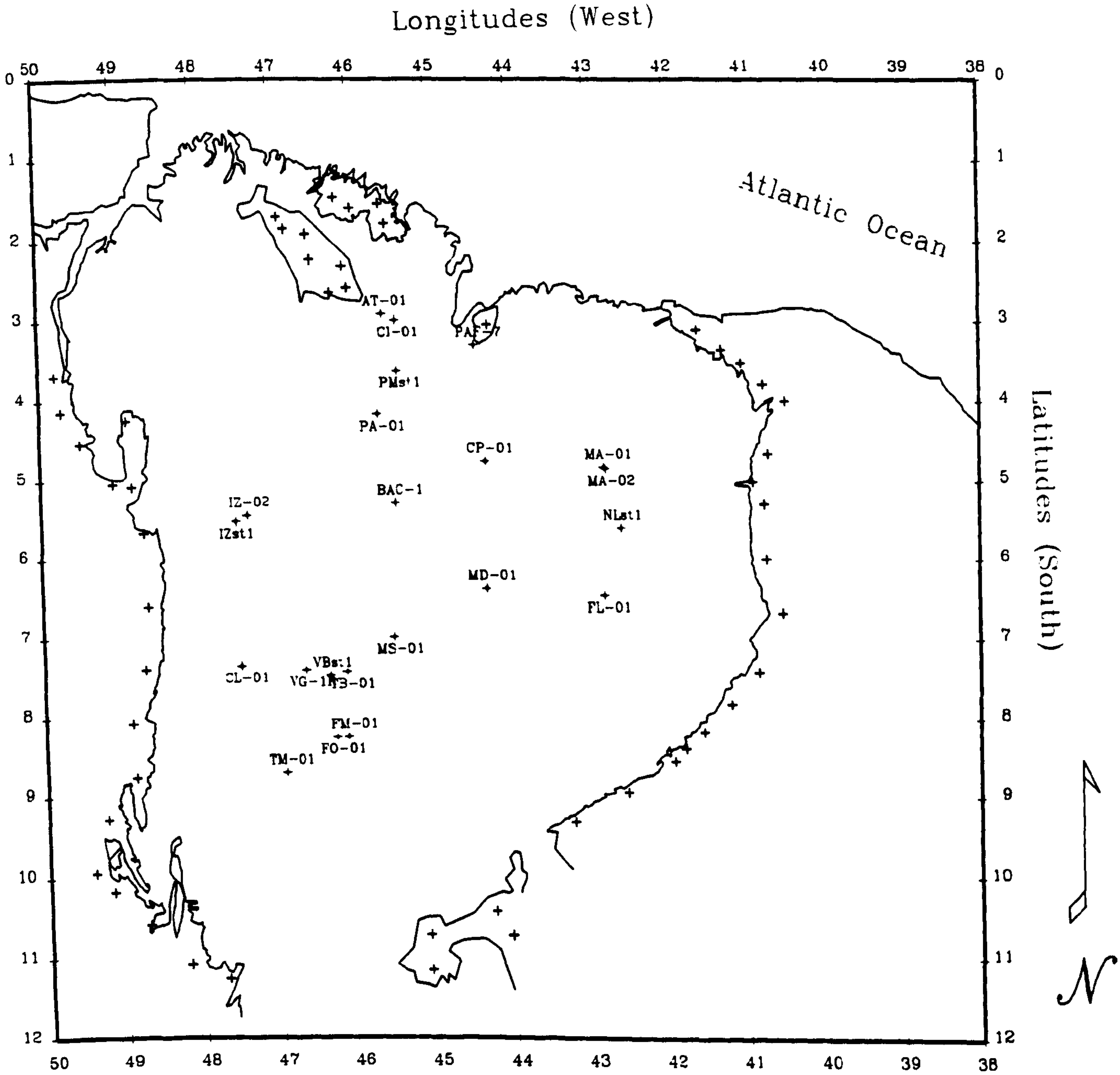

Fig. 5.1 PETROBRÁS boreholes (22) used in the present geohistory assessment of the Parnaíba Basin. 1-PA-01-MA is the only well in the basin with a FDC (gamma) density log. Conic projection.

The main uncertainties in this data set are due to:

- sediment heterogeneity either laterally or with depth; and
- lack of a better, more detailed chronostratigraphic chart.

Samples of the drilled sediments were not made available for this study. The chrono-lithostratigraphic data gathered were used to reconstruct the depths to the basement through geological time.

5.1.1 Erosion Estimates

Uncomformities in the basin have been dated. Erosional intervals have been recognized in the periods ~100 Ma to the present time, ~155-140 Ma, ~184-180 Ma, ~245-215 Ma, ~350-310 Ma and ~410-385 Ma. A total erosional (non-depositional) period of ~214 Myr may have regionally affected Parnaíba. Erosion is certainly a fundamental process in the production of sediments and how they are deposited in an evolving sedimentary basin. Erosional effects should be estimated if one wants to predict basin development. Yet quantifying erosion is extremely difficult, mainly due to the lack of suitable observable constraints (Karner, 1993).

The simplest model of erosion directly relates the erosion rate to the height of topography,

$$\frac{dE}{dt}\ \alpha\ k_e E,$$

where k_e^{-1} is the erosion time constant, E is the elevation and (dE/dt) is its rate of change. For an initial elevation E_0, the predicted erosion is then

$$E = E_0 \exp(k_e^{-1} t).$$

Certainly $k_e \ll 0$ but choosing the correct k_e is problematical, with reported literature values e.g. Stephenson (1984), being in the range 50-100 Myr. The very small erosion rates cause asymmetry in the predicted stratigraphy of basins; whereas sediment deposition often keeps pace with subsidence, erosion of the flexural outer bulges and basin sediments, when the sea level falls, does not. Reasonable, on first thought, this simple model simply does not agree with topographic features ranging in scale from mesas to the Tibetan Plateau. Sediments are currently being deposited in the interior of the Tibetan Plateau, which is at a mean elevation of 5,000 metres.

More sophisticated denudation models, with particular interest to the studies of erosion of topographic forms like mountains, is the *diffusive model*. According to this model, erosion diffuses outwards with time, like heat, and the topographic form is proportional to the curvature of the topography.

Simple erosion estimates *e.g.* Steckler & Watts (1978), state that the eroded column in a basin is at least 10% of the remaining sedimentary column. Then, for a sediment thickness of 3,000 meters at a given borehole in Parnaíba, an erosional rate of 1.40 m Myr^{-1} could be associated with that particular site. Certainly, erosion is not constant through geologic time and asymmetry should be expected in erosional rates affecting such a large basin. Nonetheless, this preliminary approximation can be used when no other information is available.

5.2 The Backstripping Technique

The stratigraphic record of a sedimentary basin witnesses the effect of compaction of sediments through time. *Geohistory analysis* aims at producing a curve for the subsidence and sediment accumulation rates through time. This quantitative analysis requires three corrections to the present-day stratigraphic thicknesses (Allen & Allen, 1990):

1 *Decompaction of sediments*, since observed compacted thicknesses must be corrected to account for the progressive loss of rock porosity with depth of burial;

2 *Palaeobathymetry*, the water depth at the time of deposition determines its position relative to a *datum, e.g.* the present-day sea level; and

3 *Absolute sea level fluctuations*, changes in the palaeosea level relative to today's may be needed.

The application of these corrections allows comparisons among boreholes in the sedimentary basin and the resulting subsidence curves can indicate the nature of the driving force responsible for basin formation and development.

The addition of a sediment load to a sedimentary basin causes additional subsidence of the basement as a simple consequence of replacing sea water by sediment. The total subsidence can then be separated into:

1 the tectonic driving force; and

2 the sediment load.

This partitioning depends on the nature of the lithospheric response to the applied load. The simplest and most commonly used approach is the assumption that the lithosphere has no lateral strength and the load is supported locally (Airy isostasy). Alternatively, if the lithosphere is able to transmit stresses and deformations, then the same load will produce a smaller subsidence on a lithosphere that deforms by regional flexure. The technique of removing the effects of the sediment load from the total subsidence is called *backstripping* and backstripped subsidence curves are useful in investigating basin-forming mechanisms. The backstripping technique was applied to 22 boreholes in the Parnaíba basin in order to assess the mechanism driving subsidence. Assuming that the stratigraphic record is the result of extensional processes, lithospheric stretching models can be tested to check the consistency of the deep crustal model derived for Parnaíba from the gravity studies shown in Chapter 4.

The decompaction of a stratigraphic unit seeks to remove the progressive effects of rock volume changes with time and depth. It requires the knowledge of the variation of rock porosity with depth. Estimates of porosity from borehole logs e.g. Athy (1930), suggest that normally pressured sediments, in particular micaceous/clastic sandstones and chalks exhibit an exponential relationship of the form given by

$$\phi = \phi_0 \exp(-cz), \tag{5.1}$$

where ϕ is the rock porosity at any depth z, ϕ_0 is the surface porosity and c is a lithology dependent coefficient associated with the rate of exponential decrease of rock porosity with depth.

In normally pressured sediments it is assumed that the pore fluids are at a pressure equivalent to a hydrostatic column and the grain-grain contacts are supporting the formation. Overpressuring occurs when porefluids trapped in the formation inhibit compaction. Overpressured stratigraphic units cause strong deviations from the expected porosity-depth curve. Given at least one density log for a representative borehole in the basin, the parameters ϕ_0 and c can be estimated and used to calculate the thickness of sedimentary layers at any time in the past.

Figure 5.2 shows the graph of the estimated porosity versus depth for borehole 1-PA-01-MA assuming an exponential dependence as in Equation 4.1. A resistant regression is also shown and the observed scatter has been interpreted as being due to possible overpressuring sections in the well and/or discrepancies in the assumed lithology (shaley sandstones). Results obtained for the porosity parameters were

$$\phi_0 = 0.3140 \pm 0.0812 \quad \text{and} \quad c = 0.6312\,\mathrm{km}^{-1}.$$

The computation of decompacted thicknesses is briefly described in Sclater & Christie (1980) and Allen & Allen (1990). Essentially, each sediment layer has been moved up the appropriate porosity-depth curve, being equivalent to sequentially removing overlaying layers and allowing the stratigraphic unit of interest to decompact. This process keeps mass constant and considers volume changes and therefore thicknesses. The compaction process is assumed to be one-dimensional (1D) in the discussion below. The effects of geothermal gradients and diagenetic processes are omitted. A more detailed mathematical model for sediment compaction including constitutive laws (mainly for argillaceous sediments) for the solid and fluid phases can be found in e.g. Audet & McKonell (1992).

Consider a sediment layer between present depths z_1 and z_2 which is to be moved vertically to new shallower depths z_1' and z_2' (Fig. 5.3). Taking into account Equation (5.1) the volume of water V_w present in a column of unit cross-sectional area is

$$\begin{aligned} V_w &= \int_{z_1}^{z_2} \phi_0 \exp(-cz)dz \\ &= \frac{\phi_0}{c}[\exp(-cz_1) - \exp(-cz_2)]. \end{aligned}$$

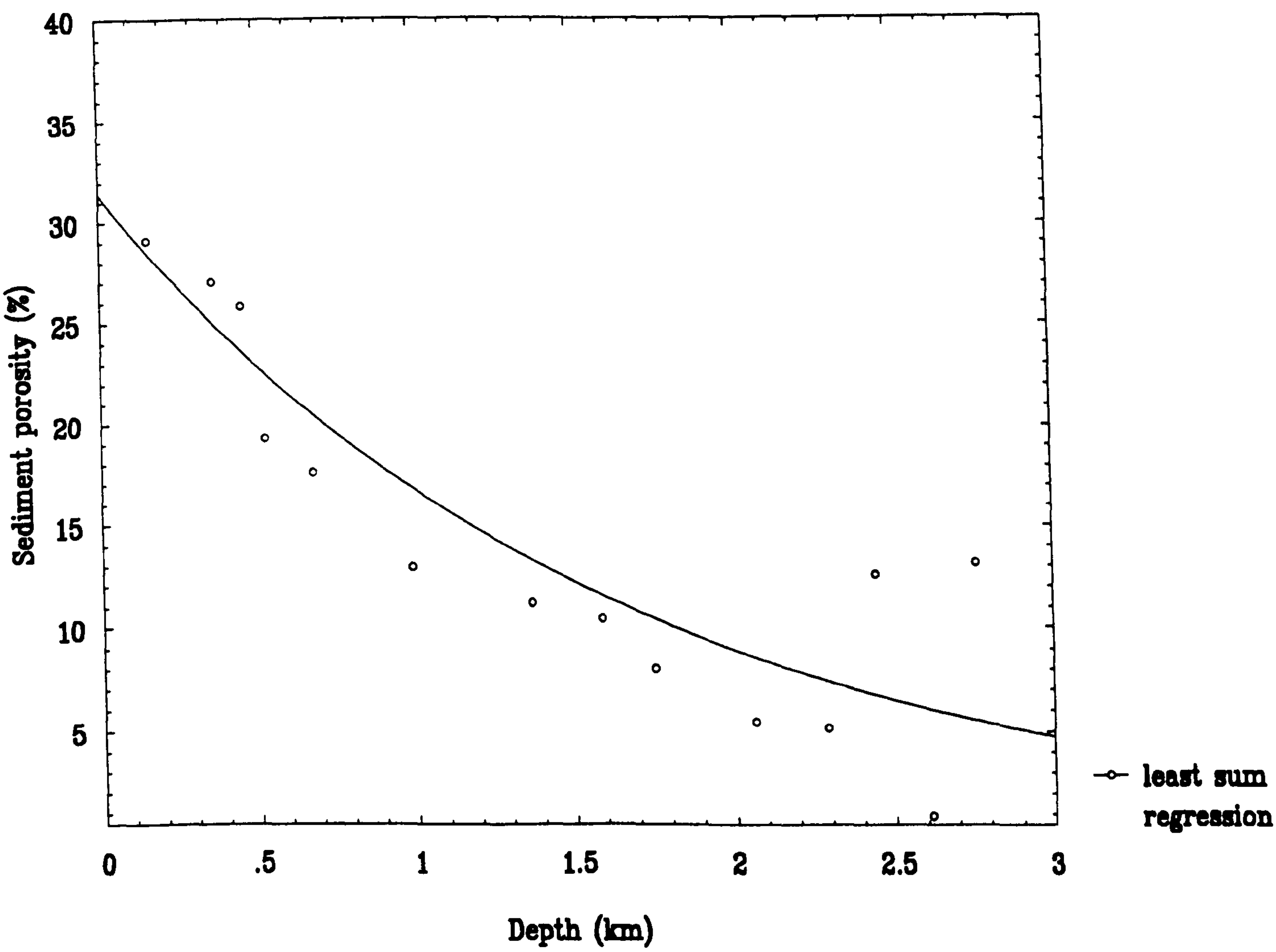

Fig. 5.2 Exponential dependence of the porosity, ϕ, of sediments of the Parnaíba Basin on depth. Sediment density values from well 1-PA-01-MA.

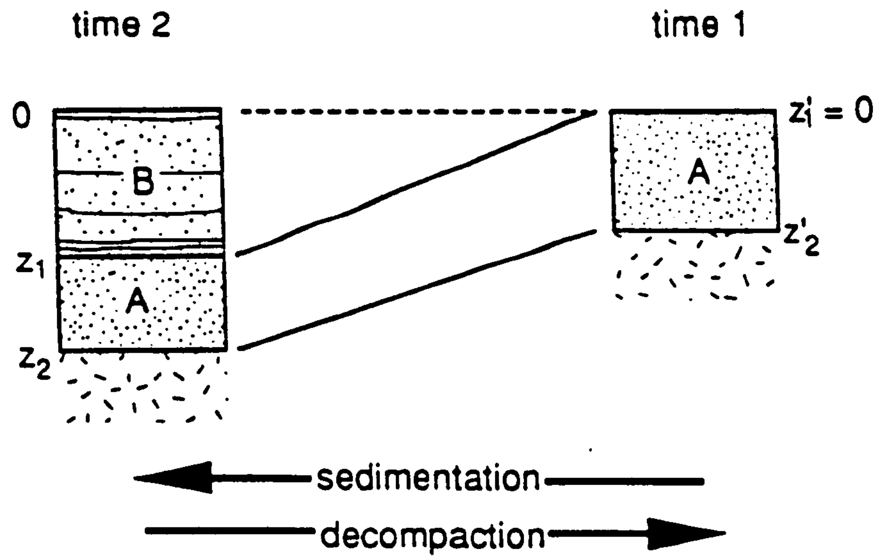

Fig. 5.3 When unit B is analytically removed from the section, bringing unit A from depth and decompacting it, the thickness of A increases according to its lithological porosity.

Since the total volume of the unit column, V_{w+sg}, is equal to the volume of water plus the volume of the sediment grains, V_{sg}. the height of the sediment grain column z_{sg} becomes

$$V_{sg} = V_{w+sg} - V_w$$
$$\Longrightarrow z_{sg} = z_2 - z_1 - \frac{\phi_0}{c}[\exp(-cz_1) - \exp(-cz_2)].$$

When sediments are removed from above, the sediment in the column absorbs water and expands, although the actual volume of sediment grains remains constant. The height of water z'_w in the column with unit cross-sectional area lying between depths z'_1 and z'_2 is given by

$$z'_w = \frac{\phi_0}{c}[\exp(-cz'_1) - \exp(-cz'_2)]$$

with the total height of the sediment column $z'_2 - z'_1$ being given by

$$\begin{aligned} z'_2 - z'_1 &= z_{sg} + z'_w \qquad (5.2) \\ &= z_2 - z_1 - \frac{\phi_0}{c}[\exp(-cz_1) - \exp(-cz_2) - \exp(-cz'_1) + \exp(-cz'_2)]. \end{aligned}$$

As parameters c and ϕ_0 are already known and z_1 and z_2 define the present layer thickness, the difference $z'_2 - z'_1$ can be evaluated because z'_1 is the bottom of the previous layer. After working down the sedimentary column and calculating z'_1, z'_2 can be estimated by numerical methods.

Consider, for example, the case when all sedimentary units except the first have been removed, with the top of this layer being brought up to sea level *i.e.* $z'_1 = 0$. Then, Equation (5.2) becomes

$$z'_2 - z_2 + z_1 + \frac{\phi_0}{c}[\exp(-cz_1) + \exp(-cz'_2) - \exp(-cz_2) - 1] = 0 \qquad (5.3)$$

with all parameters, but z'_2, known. This transcendental equation can be solved by *e.g.* Newton's Method (Demidovich & Maron, 1976), which allows calculating roots of equations of the form

$$f(z) = 0.$$

The roots are found iteratively and for the jth-iteration,

$$z_j = z_{j-1} - \frac{f(z_j)}{f'(z_j)},$$

where the prime denotes the derivative (df/dz). It can be shown that convergence is assured provided that, for $z > 0$,

- $f''(z)$ does not change sign; and
- $f(z)f''(z) > 0$.

Equation (5.3) fulfills both conditions and the algorithm can be readily implemented as a computer program. The application of Equations (5.2) and (5.3) allows the calculation of the thickness of a sediment layer since its time of deposition to the present-day. Therefore, a decompacted subsidence curve can be plotted using the boundaries of stratigraphical units as input data with known absolute ages and their present-day thicknesses. As outlined above, it must be noted that all depths are relative to the present-day mean sea level.

Further refinements include the application of palaeobathymetric and eustatic corrections. The palaeobathymetric correction to the decompacted subsidence curve considers the difference in height between the depositional surface and the regional *datum*. The eustatic correction accounts for variations in the ambient sea level compared to today's.

Differences in the initial and ensuing palaeobathymetric conditions in a sedimentary basin can change the stratigraphy dramatically. Intracratonic basins, however, are known to develop in neritic environments with usually shallow marine conditions. In the case of Parnaíba, except for a brief period in the Devonian when an open-sea environment prevailed, its development occurred in the restricted marine conditions of an epicontinental sea.

The eustatic correction is due to global sea level fluctuations and, as pointed out by Allen & Allen (1990), it is hazardous to apply. The precise significance of the first-, second- and third- order cycles of Vail *et al.* (1977) and the short- and long-term curves of Haq *et al.* (1987) are not well understood. The first-order cycle should be related to volume changes in the ocean ridge system and the effects of glaciations/deglaciations. However, the figures involved are debatable and a simple transferral from the Vail/Haq curves is not recommended. Given the mostly shallow depositional environment of Parnaíba, often tidal in range, water depths variations can be largely ignored. Eustatic sea level effects are almost impossible to distinguish from basin dynamics. Sea level changes seem to be relatively small ($< 10\%$) than the observed subsidence and can probably be disregarded on the assumption that their effects are minimal and synchronous throughout the basinal region. Subsidence was normalized so that all depths were set to zero at 445 Ma.

Having computed z'_1 and z'_2, the mean porosity $\bar{\phi}$ of the decompacted layer is

$$\bar{\phi} = \frac{\phi_0}{c} \frac{\exp(-cz'_1) - \exp(-cz'_2)}{z'_2 - z'_1}.$$

This expression can then be used to calculate the density ρ_s of the decompacted layer,

$$\rho_s = \bar{\phi}\rho_w + (1 - \bar{\phi})\rho_{sg}$$

and the mean sediment density $\bar{\rho}_s$ for the total column is

$$\bar{\rho}_s = \frac{\sum_i [\bar{\phi}_i \rho_w + (1 - \bar{\phi}_i)\rho_{sg_i}]\Delta z'_i}{S},$$

where S is the total thickness of the column corrected for compaction and $\Delta z'_i$ is the individual layer thickness.

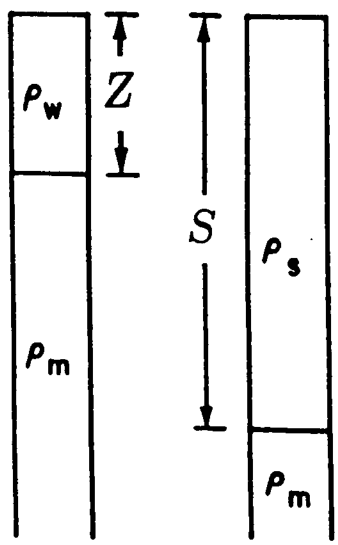

Fig. 5.4 Depth of a water-filled basin Z compared with the depth S due to isostatic subsidence when the basin is filled with sediments. The crust is not shown because its thickness is assumed to remain constant.

The final step is to evaluate the true tectonic subsidence, since it is known that the sediment load acts as an excess weight causing further subsidence. Considering the geometry of Fig. 5.4 the depth to basement Z can be corrected for the loading due to the sediments by

$$Z = S\left(\frac{\rho_m - \bar{\rho}_s}{\rho_m - \rho_w}\right)$$

where ρ_m is the density of mantle. After applying all corrections the true tectonic subsidence can then be obtained as

$$Z = \Phi\left[S\left(\frac{\rho_m - \bar{\rho}_s}{\rho_m - \rho_w}\right) - \Delta_{SL}\left(\frac{\rho_w}{\rho_m - \rho_w}\right)\right] + (W_d - \Delta_{SL}), \qquad (5.4)$$

where Δ_{SL} is the palaeosea level relative to the present *datum*; W_d is the palaeowater depth; and Φ is the basement function equal to unity for Airy isostasy.

The basement function Φ varies from 0 to 1 according to the degree of compensation of the load imposed by the sediments on the lithosphere. Turcotte

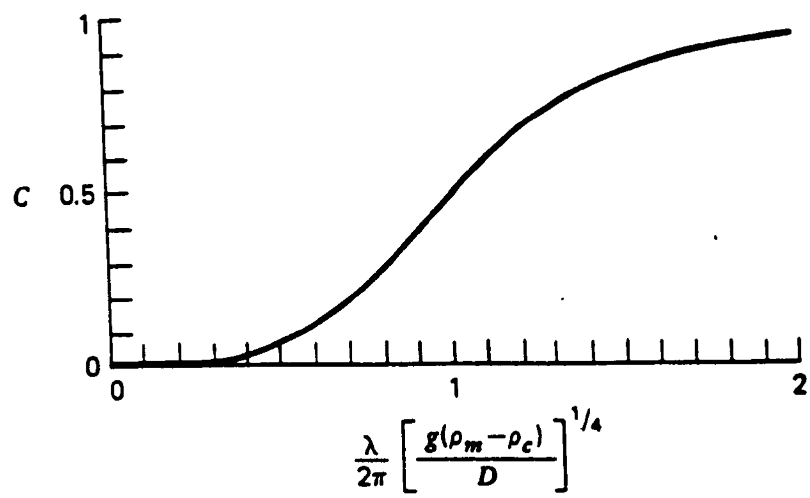

Fig. 5.5 Dependence of the degree of compensation, C, on the non-dimensional wavelength of periodic (sinusoidal) topography (after Turcotte & Schubert, 1982). Parameters as defined in the text.

& Schubert (1982) discuss the case of a periodic (sinusoidal) load with a corresponding periodic lithospheric response and the degree of flexural loading can be predicted by the *compensation coefficient* C given by

$$C = \frac{\rho_m - \rho_c}{\rho_m - \rho_c + \dfrac{D}{g}\left(\dfrac{2\pi}{\lambda}\right)^4}, \tag{5.5}$$

with all parameters as already defined, except D, the effective flexural ridigity of the lithosphere, g, the (mean) gravity value and λ, the wavelength of the load.

The dependence of the compensation coefficient C on the non-dimensional wavelength of periodic (sinusoidal) topography is shown in Fig. 5.5. For a lithosphere with elastic thickness 25 km, Poisson's ratio 0.25, Young's modulus 70 GPa, ρ_m = 3,300 kg m^{-3} and ρ_c = 2,800 kg m^{-3}, the topography is 50% compensated (C = 0.5) if its wavelength is λ = 420 km. Topography with a wavelength shorter than this is substantially supported by the ridigity of the lithosphere; topography with a longer wavelength is only weakly supported. Considering a sinusoidal load, therefore, Φ in Equation (5.4) can be replaced by the compensation coefficient C.

The backstripping curves for well 1-PA-01-MA are shown in Fig. 5.6. The lower curve shows the depths to the basement taking into account the decompacted sedimentary load while for the upper curve this load has been removed and the "true" tectonic subsidence is shown. Notice that a local equilibrium model (Airy) was used to compute the backstripping curves. This is justified due to the large dimensions of the Parnaíba Basin. Considering expression (5.5) and typical values as $D = 10^{24}$ N m, $(\rho_m - \rho_s) = 800$ kg m^{-3} and $\lambda/2 = 400$ km we get $C = 0.91$ for the compensation coefficient. This means that the whole basin is only weakly supported by the underlying lithosphere with Airy-type isostasy being approached. It is true that C depends strongly on D; for instance for $D = 10^{25}$ N m we get $C = 0.51$ with a clear flexural behaviour of the lithosphere. However, such an extreme high D value is unlikely to have ever occurred in the tectonic regime of Parnaíba.

A FORTRAN program (**STRIPP.FOR**) was written to systematically apply the backstripping technique to the PETROBRÁS boreholes. Erosional (non-depositional) gaps which affected the whole basin as well as intrusions of volcanics in the stratigraphic column have been considered in the algorithm developed. Volcanic layers were accounted for by taking their thicknesses (small, as compared to the total column) back to the basement level.

Decompacted sediment and backstripped plots for all wells are grouped in Fig. 5.7. Note steeper total and tectonic curves for the Devonian (Canindé Group) in all wells and the overall thermal decay appearance first recognized by Sleep (1971) and Sleep & Snell (1976). The larger Devonian subsidence rates may be associated with a second rifting event occurring at 400-385 Ma. The tectonic subsidence curves show a similar pattern, *i.e.* a long-term regular trend with a short Devonian acceleration. Tectonic subsidence values are also modest, generally between 0.5 and 1 km.

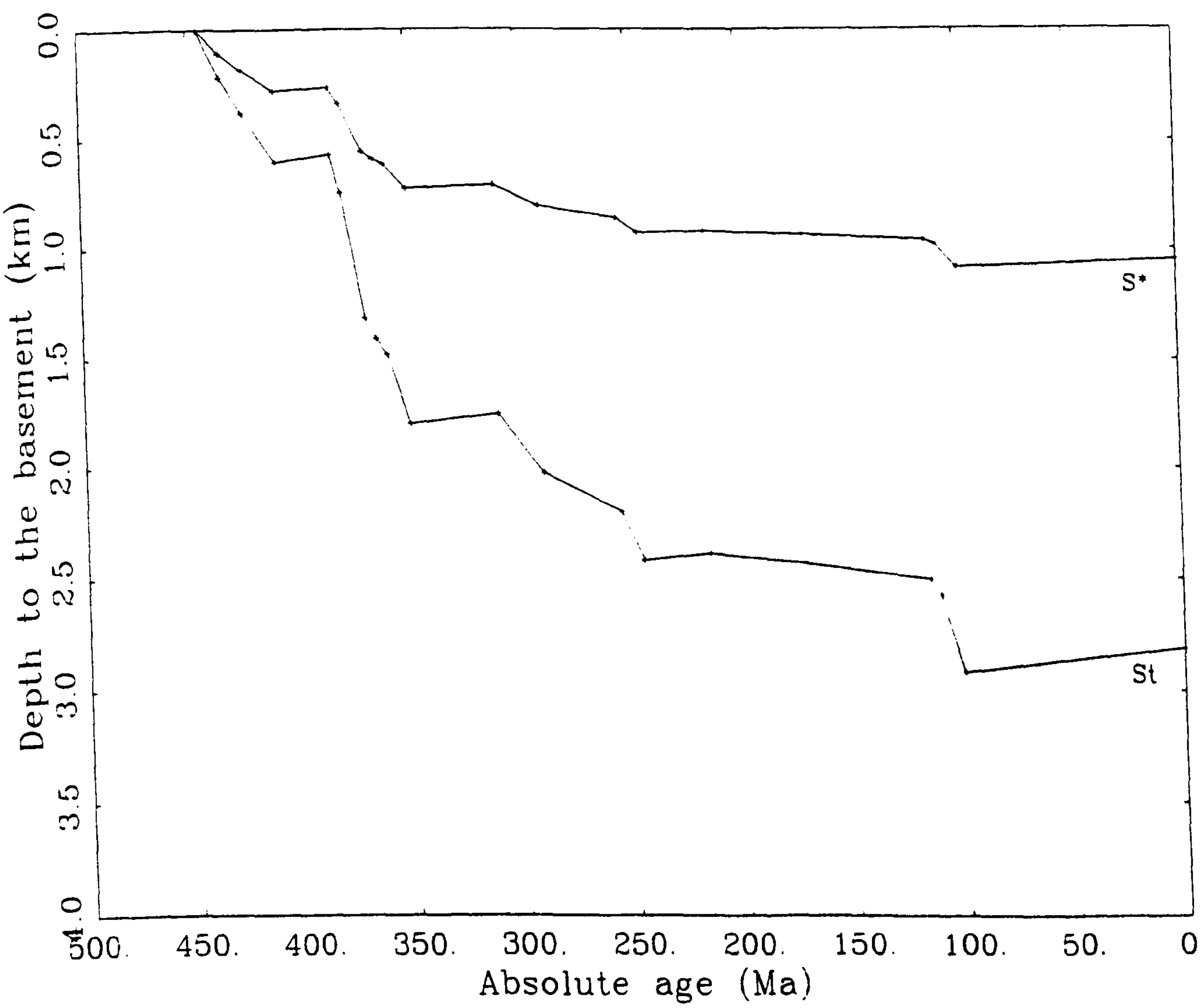

Fig. 5.6 Total (S_t) and tectonic (S^*) backstripped subsidence curves for well 1-PA-01-MA (4.2^{0}S, 45.7^{0}W, Fig. 5.1). Local loading model.

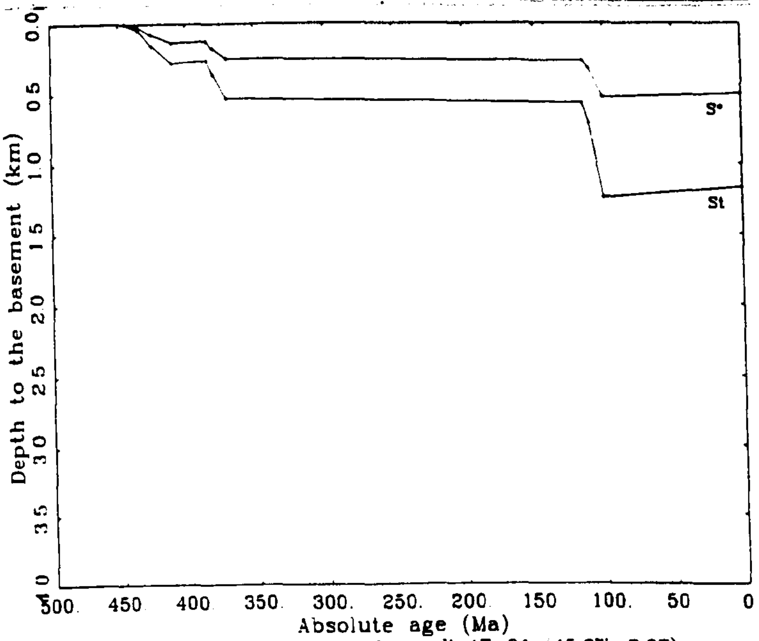

Backstripping curves for well AT-01 (45.6W, 2.9S).

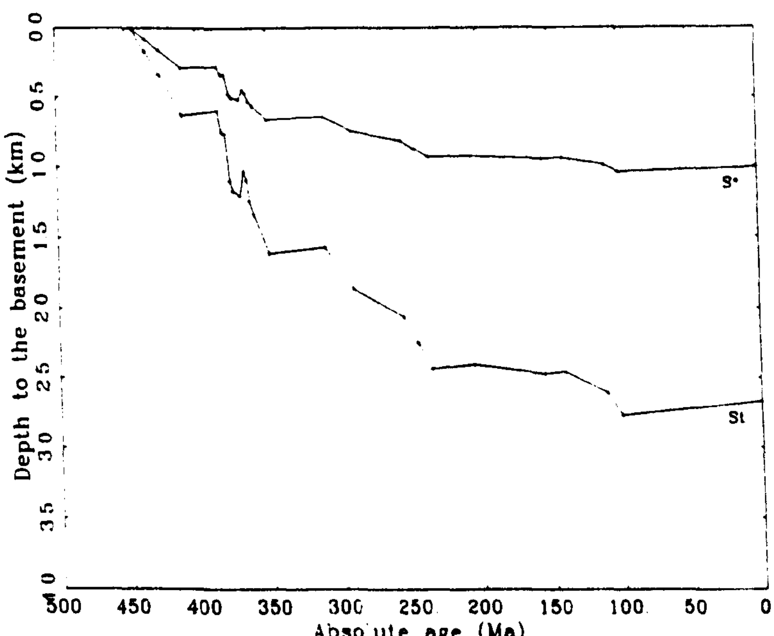

Backstripping curves for well BAC-1 (45.4W, 5.3S)

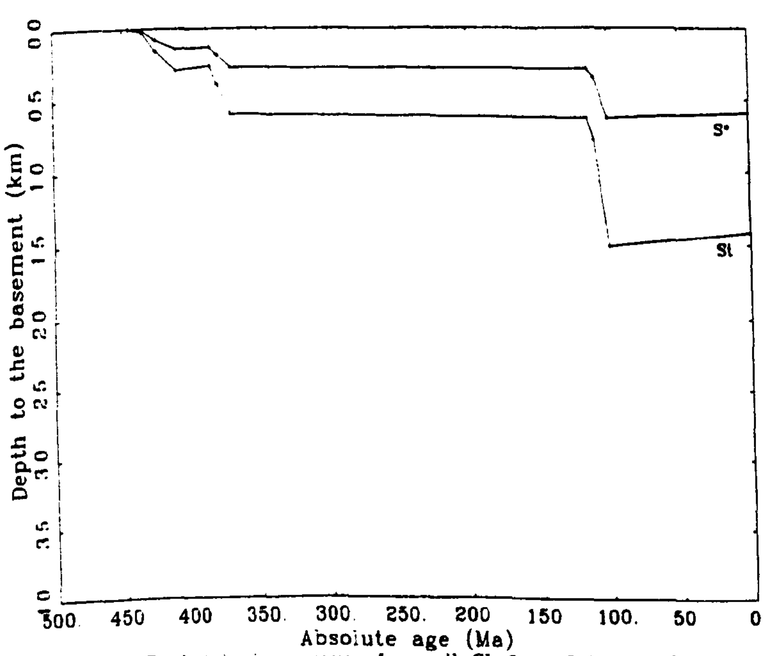

Backstripping curves for well CI-01 (45.4W, 3.0S)

Fig. 5.7 Total (S_t) and tectonic (S^*) backstripped subsidence curves for oil & gas exploration wells in the Parnaíba Basin. Local loading model.

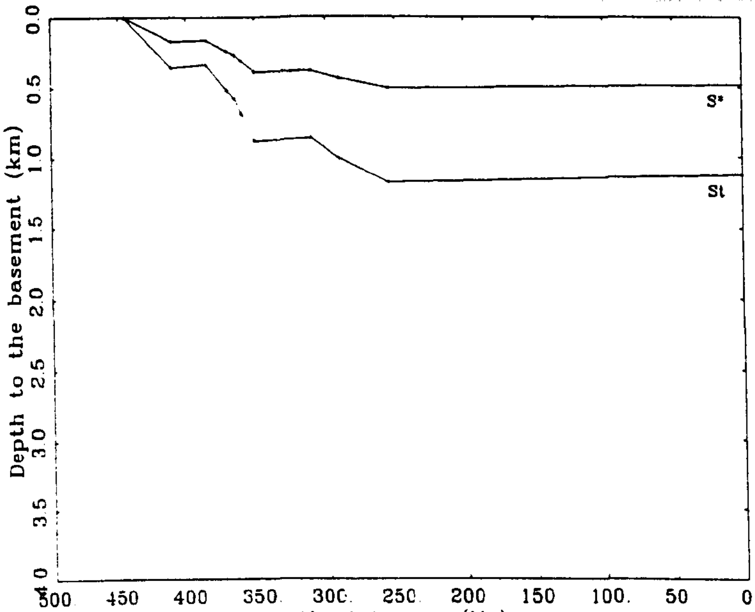

Backstripping curves for well CL-01 (47.5W, 7.3S).

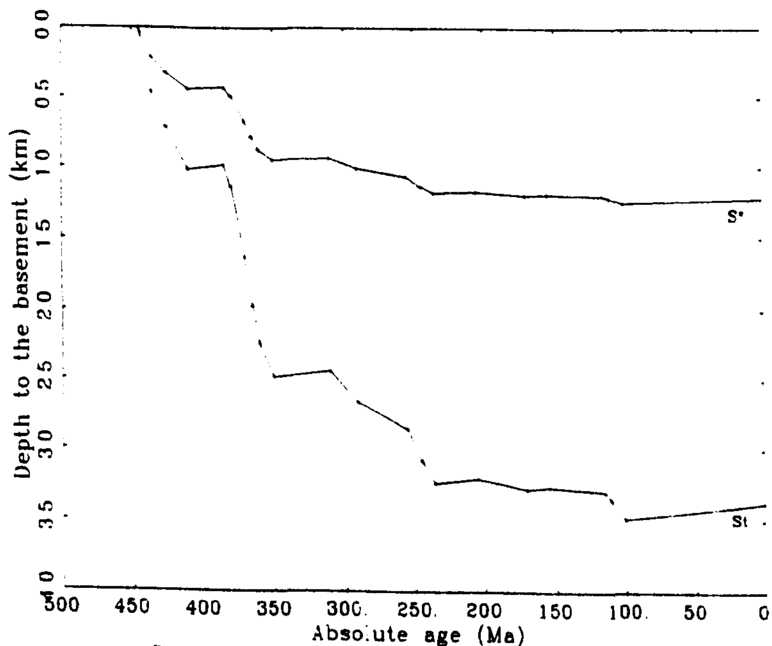

Backstripping curves for well CP-01 (44.3W, 4.8S)

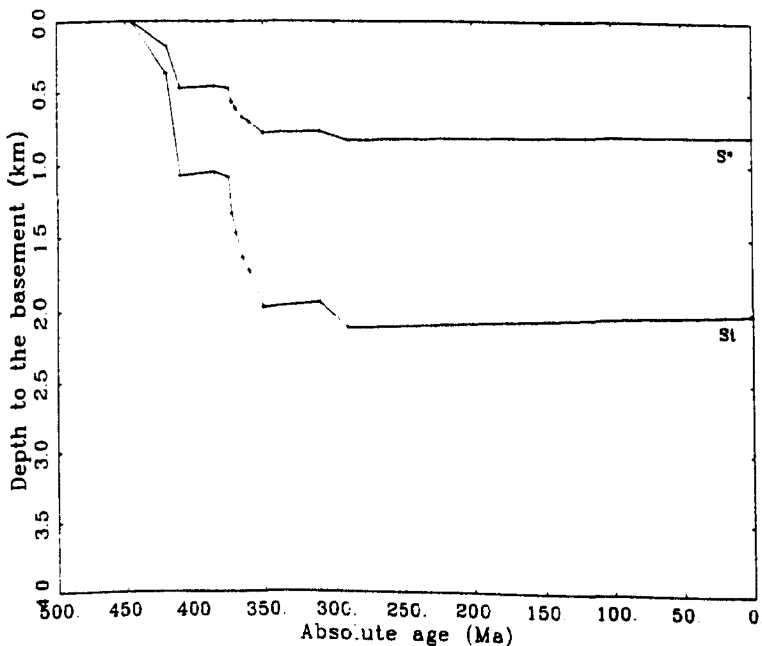

Backstripping curves for well FL-01 (42.8W, 6.5S).

Fig. 5.7 (cont.) Total (S_t) and tectonic (S^*) backstripped subsidence curves for oil & gas exploration wells in the Parnaíba Basin. Local loading model.

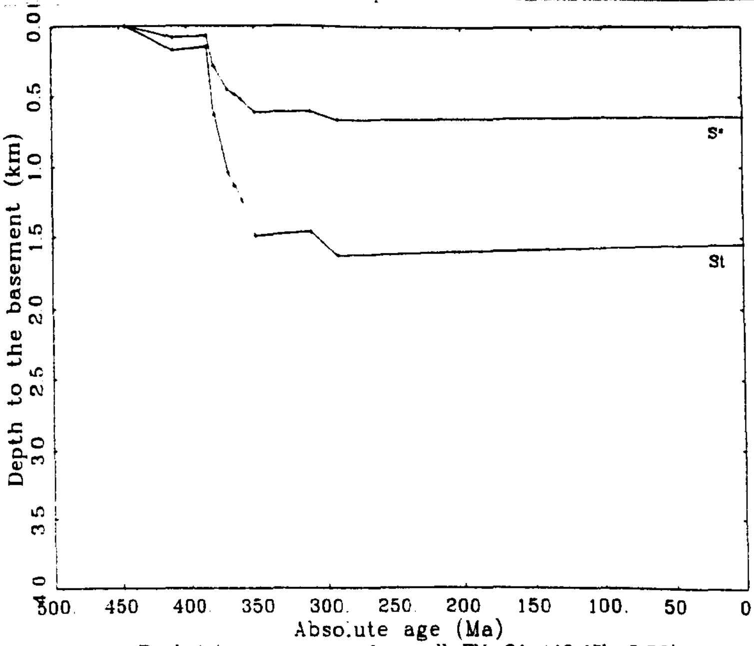

Backstripping curves for well FM-01 (46.1W, 8.3S).

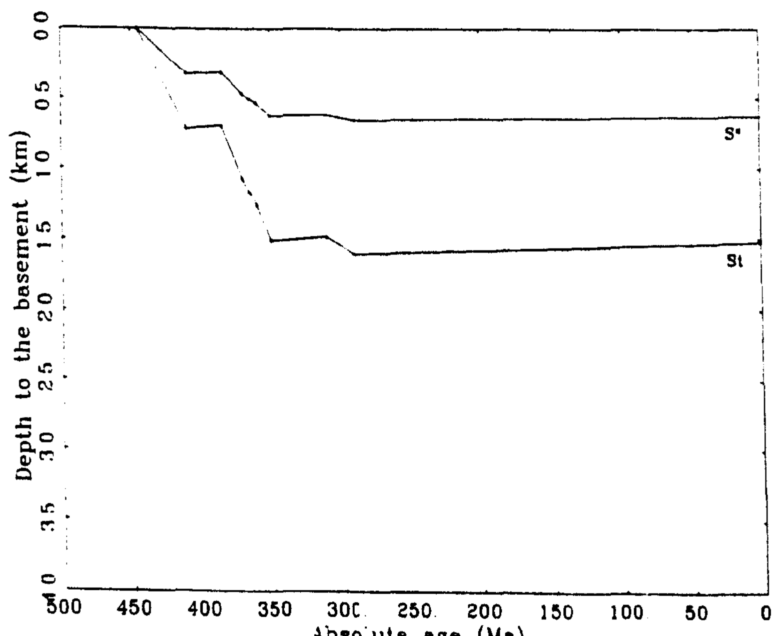

Backstripping curves for well FO-01 (46.2W, 8.3S)

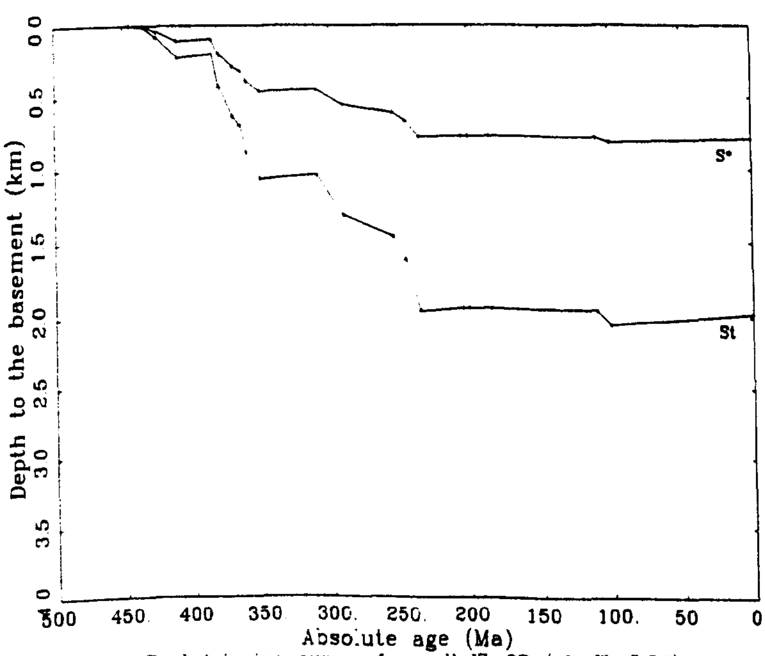

Backstripping curves for well IZ-02 (47.4W, 5.5S).

Fig. 5.7 (cont.) Total (S_t) and tectonic (S^*) backstripped subsidence curves for oil & gas exploration wells in the Parnaíba Basin. Local loading model.

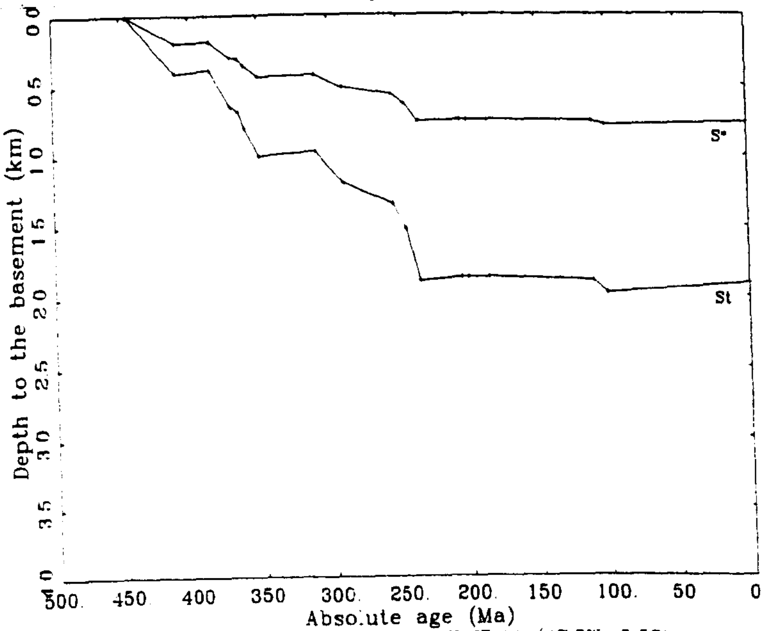

Backstripping curves for well 1Zst1 (47.5W, 5.5S).

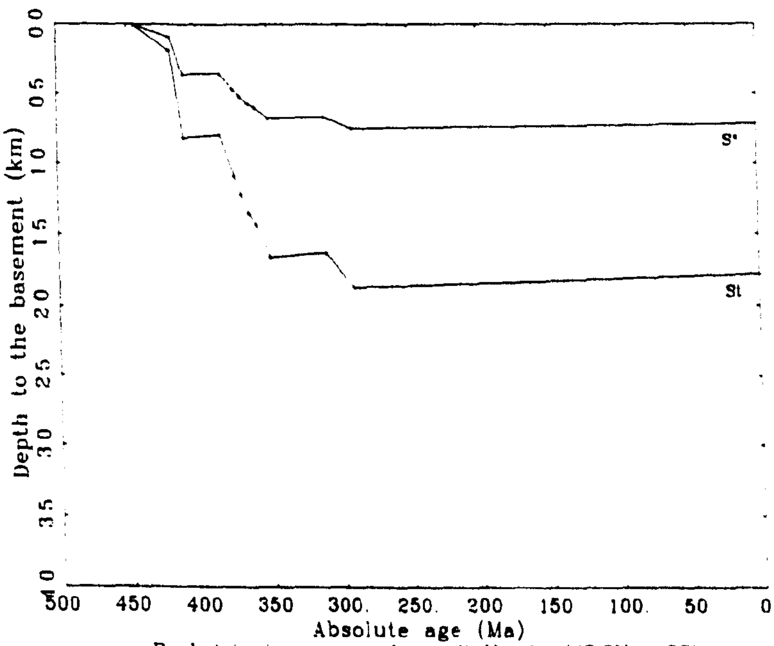

Backstripping curves for well MA-01 (42.8W, 4.8S).

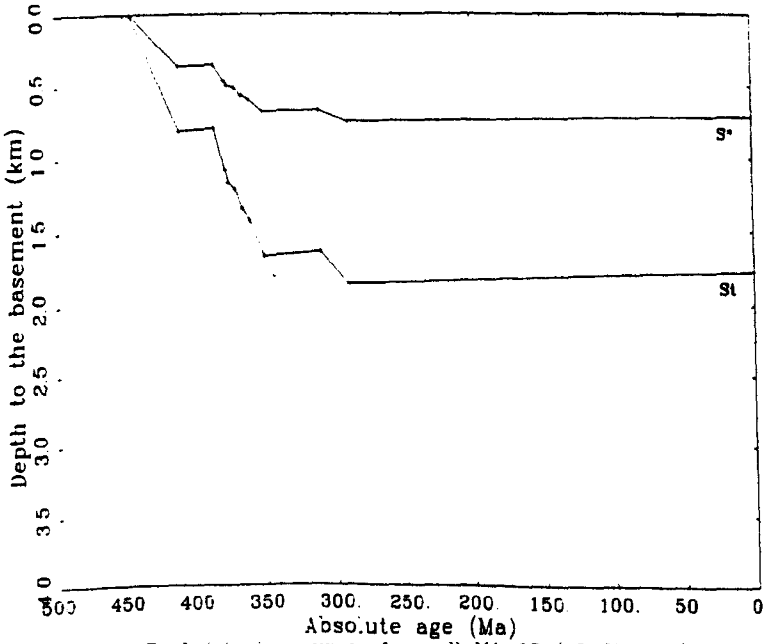

Backstripping curves for well MA-02 (42.8W, 4.6S).

Fig. 5.7 (cont.) Total (S_t) and tectonic (S^*) backstripped subsidence curves for oil & gas exploration wells in the Parnaíba Basin. Local loading model.

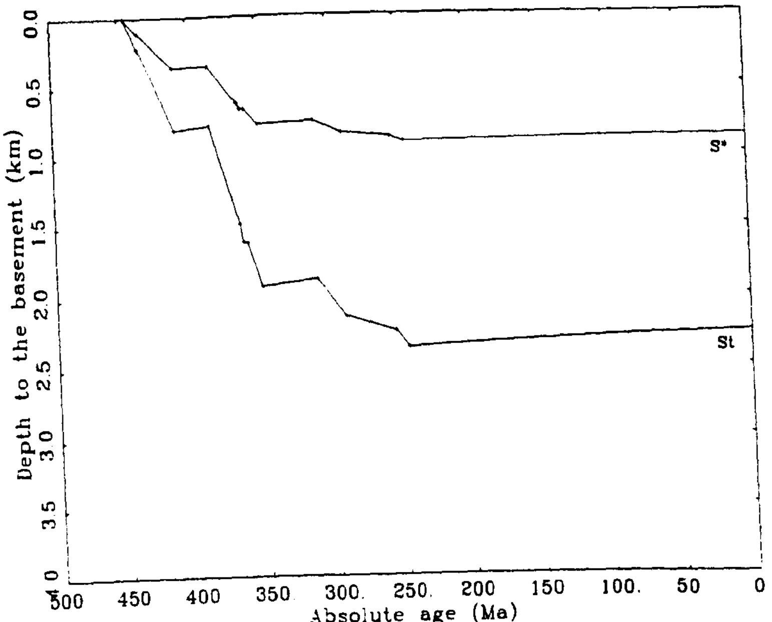

Backstripping curves for well MD-01 (44.3W, 6.4S).

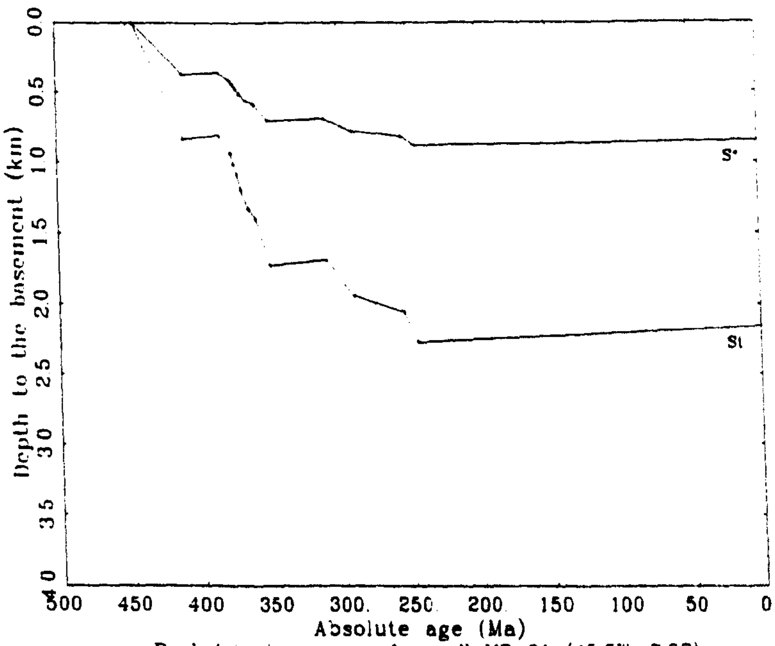

Backstripping curves for well MS-01 (45.5W, 7.0S).

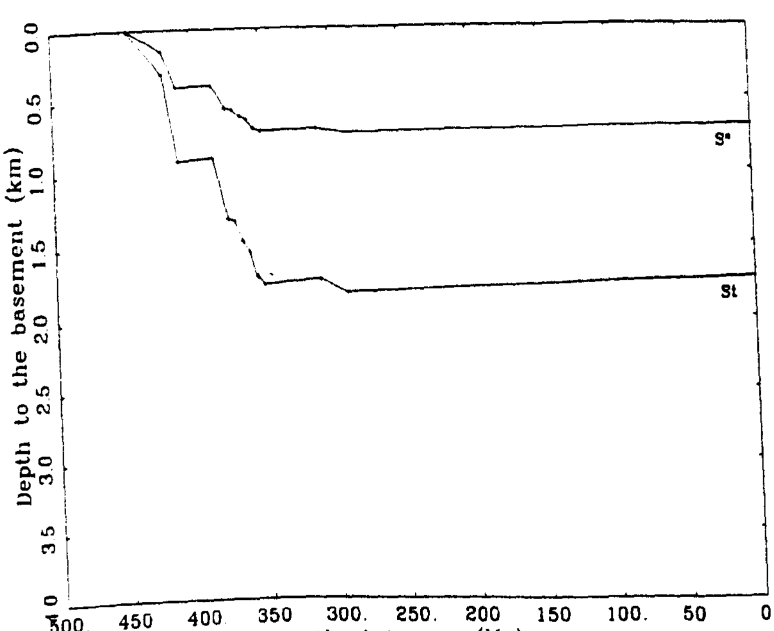

Backstripping curves for well NLst1 (42.6W, 5.6S).

Fig. 5.7 (cont.) Total (S_t) and tectonic (S^*) backstripped subsidence curves for oil & gas exploration wells in the Parnaíba Basin. Local loading model.

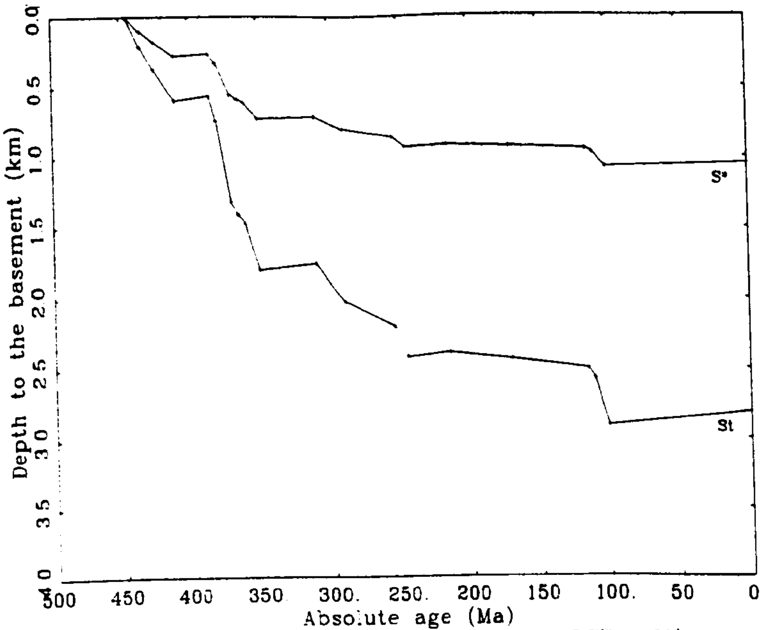

Backstripping curves for well PA-01 (45.7W, 4.2S)

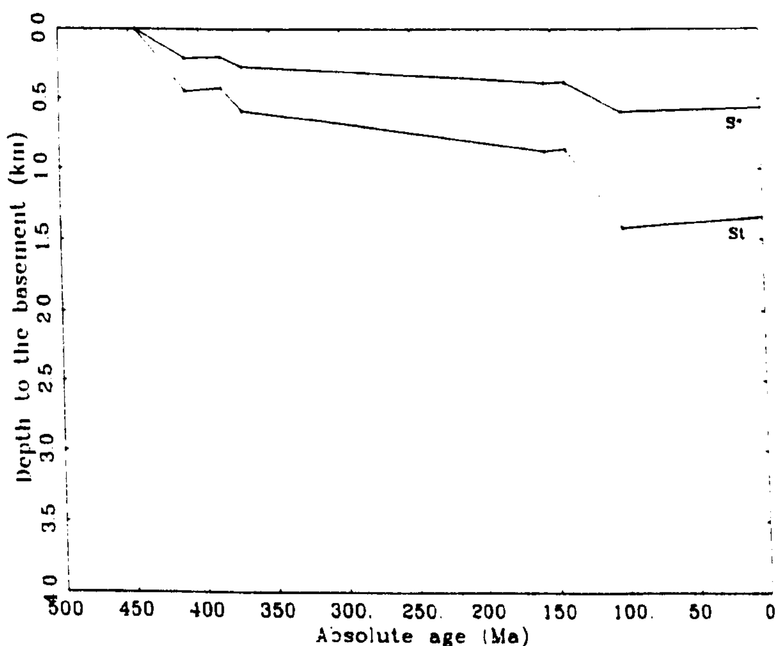

Backstripping curves for well PAF-7 (44.4W, 3.3S)

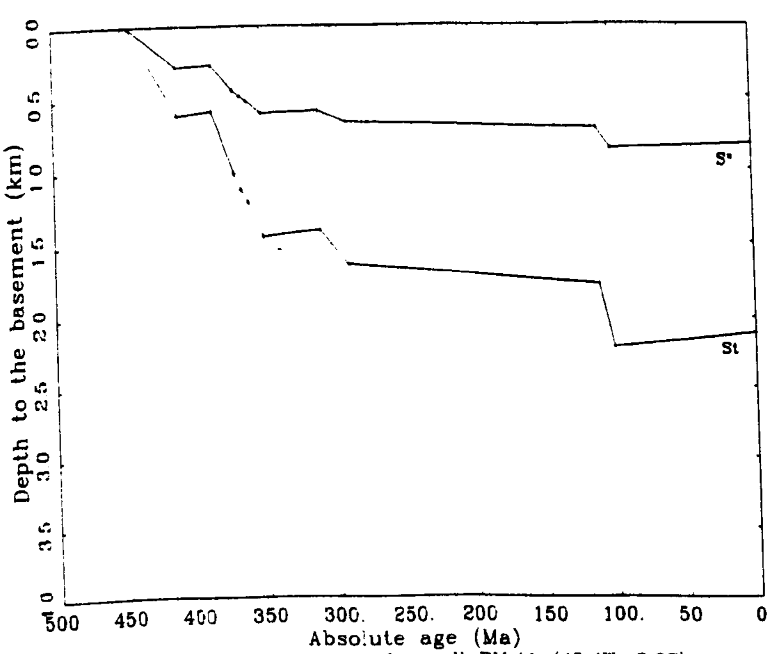

Backstripping curves for well PMst1 (45.4W, 3.8S).

Fig. 5.7 (cont.) Total (S_t) and tectonic (S^*) backstripped subsidence curves for oil & gas exploration wells in the Parnaíba Basin. Local loading model.

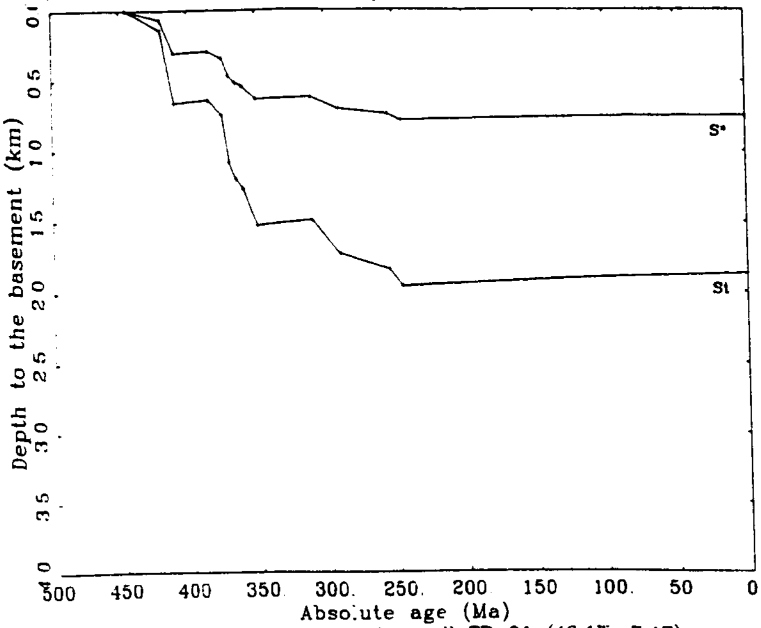

Backstripping curves for well TB-01 (46.1W, 7.4S).

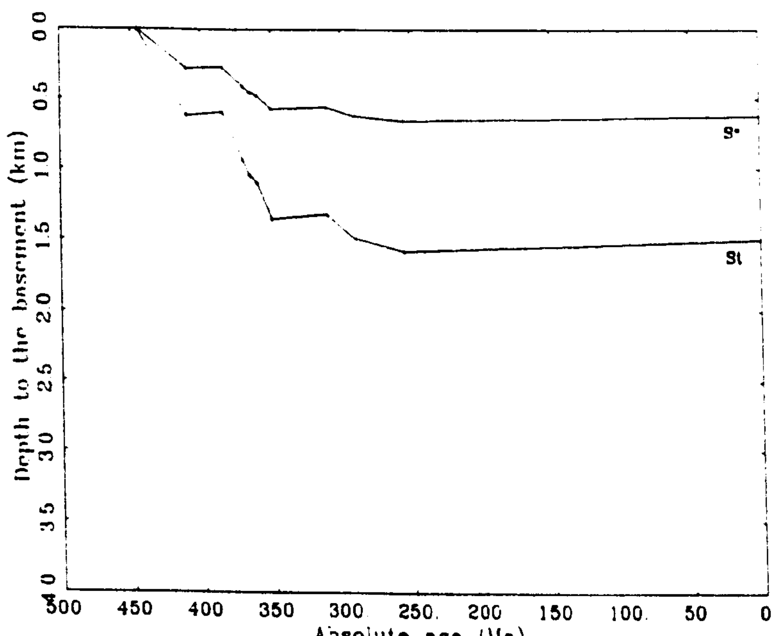

Backstripping curves for well TM-01 (46.9W, 8.7S).

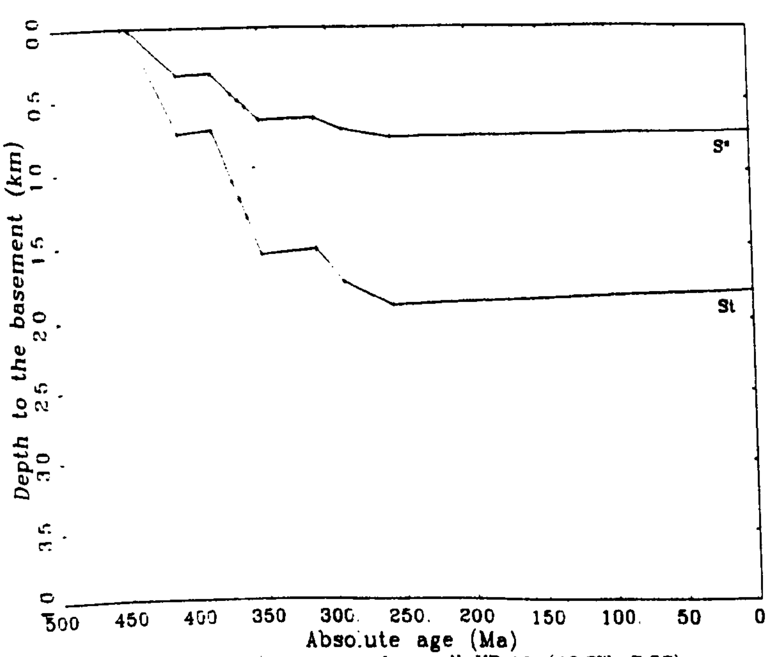

Backstripping curves for well VBst1 (46.3W, 7.5S).

Fig. 5.7 (cont.) Total (S_t) and tectonic (S^*) backstripped subsidence curves for oil & gas exploration wells in the Parnaíba Basin. Local loading model.

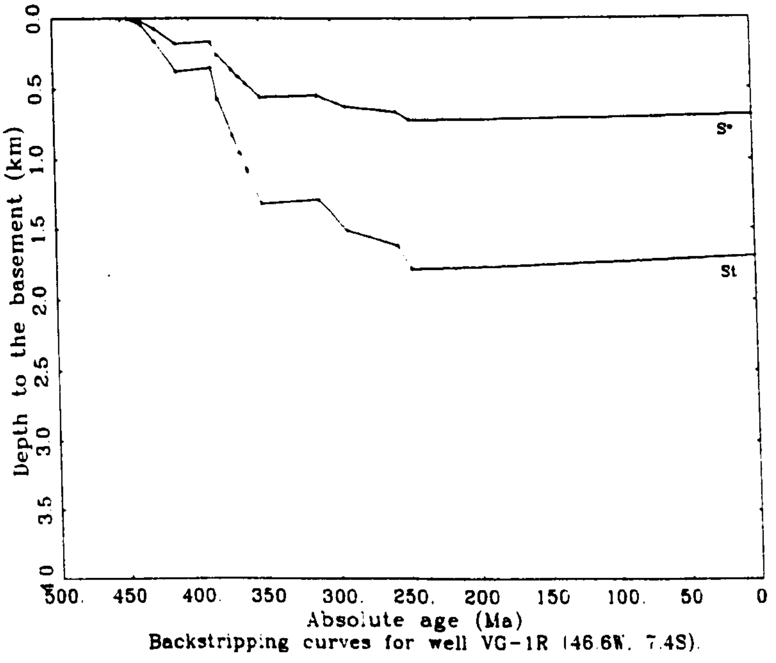

Fig. 5.7 (cont.) Total (S_t) and tectonic (S^*) backstripped subsidence curves for oil & gas exploration wells in the Parnaíba Basin. Local loading model.

Total subsidence and tectonic subsidence rates across the basin were estimated for each lithostratigraphic group. Mean values, taking all groups for the basin as a whole, do not seem to be meaningful since the true amount of erosion is unknown. Rates computed for each well are shown in Table 5.2.

Table 5.2 Total and tectonic subsidence rates (in m Myr^{-1}) for wells in the Parnaíba Basin.

Stratigraphic Groups/Absolute Ages (Ma)									
		Serra Grande/445-410	Canindé/385-350	Balsas/310-235	Mearim/180-155	Serra Grande/445-410	Canindé/385-350	Balsas/310-235	Mearim/180-155
Well	Coordinates	$(\Delta S_t/\Delta t)$				$(\Delta S^*/\Delta t)$			
1-AT-01-MA	2.9°S, 45.6°W	8.1	8.0	0.1	0.1	3.8	3.6	0.1	0.1
2-BAC-01-MA	5.3°S, 45.4°W	18.0	28.7	11.5	1.3	8.2	11.0	3.8	0.4
1-CI-01-MA	3.0°S, 45.4°W	8.4	9.5	0.1	0.1	4.0	4.2	<0.1	<0.1
1-CL-01-MA	7.3°S, 47.5°W	10.3	15.6	5.7	ND	4.9	6.6	2.2	ND
2-CP-01-MA	4.8°S, 44.3°W	29.1	42.9	10.8	0.1	12.7	14.8	3.3	<0.1
1-FL-01-PI	6.5°S, 42.8°W	30.7	26.4	8.6	ND	13.3	9.4	2.8	ND
1-FM-01-MA	8.3°S, 46.1°W	4.9	38.6	8.3	ND	2.4	15.7	2.9	ND
1-FO-01-MA	8.3°S, 46.2°W	20.5	23.5	5.7	ND	9.3	8.9	2.0	ND
1-IZ-02-MA	5.5°S, 47.4°W	6.5	24.8	12.3	0.3	3.1	10.5	4.4	0.1
2-IZst-01-MA	5.5°S, 47.5°W	11.7	17.6	12.3	0.3	5.5	7.3	4.4	0.1
1-MA-01-PI	4.8°S, 42.8°W	23.2	24.9	12.2	ND	10.4	9.3	4.2	ND
1-MA-02-PI	4.8°S, 42.8°W	23.2	25.0	11.0	ND	10.3	9.3	3.8	ND
1-MD-01-MA	6.4°S, 44.3°W	23.1	32.1	7.6	ND	10.3	11.9	2.5	ND
1-MS-01-MA	7.0°S, 45.5°W	23.9	26.2	9.0	ND	10.6	9.7	3.0	ND
2-NLst-01-PI	5.6°S, 42.6°W	26.0	24.8	4.7	ND	11.5	9.1	1.6	ND
1-PA-01-MA	4.2°S, 45.7°W	17.2	35.2	8.7	1.2	7.9	13.3	2.9	0.4
9-PAF-07-MA	3.3°S, 44.4°W	12.7	5.4	1.3	1.3	5.9	2.3	0.5	0.5
2-PMst-01-MA	3.6°S, 45.4°W	17.5	24.5	3.6	0.8	8.0	9.5	1.3	0.3
1-TB-01-MA	7.4°S, 46.1°W	19.1	25.5	7.1	ND	8.7	9.8	2.4	ND
1-TM-01-MA	8.7°S, 46.9°W	17.7	21.8	4.7	ND	8.1	8.5	1.7	ND
1-VBst-01-MA	7.5°S, 46.3°W	21.0	24.3	6.9	ND	9.4	9.2	2.4	ND
1-VG-1R-MA	7.4°S, 46.6°W	10.9	27.4	7.6	ND	5.1	11.1	2.7	ND

(ND - the specific group was not drilled)

Table 5.3 summarizes the total and tectonic rates found. The scatter observed suggests that the subsidence, although regional in nature, was strongly influenced by local structures like faulted blocks and the palaeotopography of the basement. This variability seems to be larger for the Carboniferous-Triassic and Jurassic depositional sequences. The mean values of $\overline{(\Delta S^*/\Delta t)}$ do not exceed 40-45% of the mean total subsidence rates demonstrating the large influence of the sedimentary load. The rates (in m Myr^{-1}) for Parnaíba are much lower than those reported by Oliveira (1987) for the rift phases of the NE coast Potiguar Basin ($20 < \Delta S^*/\Delta t < 84$, $46 < \Delta S_t/\Delta t < 205$) and Sergipe/Alagoas

($33 < \Delta S^*/\Delta t < 97$, $64 < \Delta S_t/\Delta t < 208$). Quintas (1995) reports comparable total and tectonic rates for the Silurian, Devonian, Triassic, Jurassic and Cretaceous sequences of the Paraná Basin. In marked contrast to the corresponding Carboniferous-Triassic sequence of Parnaíba, the Carboniferous-Permian sequence of Paraná shows much larger rates $\overline{\Delta S^*/\Delta t} = 49$ and $\overline{\Delta S_t/\Delta t} = 111$ m Myr^{-1}.

Table 5.3 Summary of total and tectonic subsidence rates for the Parnaíba Basin.

Stratigraphic Group	Absolute Ages (Ma)	$\Delta S_t/\Delta t$ (m Myr^{-1})	$\Delta S^*/\Delta t$ (m Myr^{-1})
Mearim	180-155	0.6 ± 0.5	0.2 ± 0.2
Balsas	310-235	7 ± 4	2 ± 1
Canindé	385-350	24 ± 9	9 ± 3
Serra Grande	445-410	17 ± 7	8 ± 3

5.3 Thermo-Mechanical Modelling

The accumulated geological and geophysical evidence points to the importance of an extensional tectonic regime in Parnaíba prior to, and during, the development of the regional subsidence. Therefore, it is justifiable to investigate how the tectonic subsidence curves obtained compare to lithospheric stretching models and their implications for the crustal structure beneath the basin.

Values for the parameters used in the thermo-mechanical modelling are listed in Table 5.4. Among them, the choice of realistic estimates of crust and lithosphere thicknesses are obviously critical. Nelson (1991) reports Precambrian crust as slightly thicker (41 ± 6 km) than Phanerozoic crust (28 ± 2 km). Precambrian crust thickness was further separated in two classes by Durhein & Mooney (1991): Archean cratons with ~35 km and Proterozoic cratons with ~45 km. According to Pearson *et al.* (1993) the lithospheric thickness in cratonic areas is in the range 150-200 km.

Table 5.4 Parameters used in the thermo-mechanical and flexural modelling of the Parnaíba Basin.

Parameter	Symbol	Value	
Lithospheric initial thickness	z_L	170	km
Crustal initial thickness	z_c	35	km
Temperature at the base of the lithosphere	T_m	1,603	K
Mantle density at 273 K	ρ_m^0	3,330	kg m^{-3}
Crust density at 273 K	ρ_c^0	2,800	kg m^{-3}
Water density	ρ_w	1,030	kg m^{-3}
Volumetric thermal expansion coefficient	α_v	3.0 x 10^{-5}	K^{-1}
Lithospheric thermal diffusivity	κ	0.8 x 10^{-6}	m^2 s^{-1}
Lithospheric thermal time constant	τ	116	Myr
Young's modulus	E	70	GPa
Poisson's ratio	ν	0.25	

In Brazil, Oliveira (1989) and Quintas (1995) used crust and lithosphere thicknesses in the range of 35-45 km and 150-170 km, respectively. The isostatic analysis carried out by Ussami (1986) for the adjacent São Francisco Craton considered a crustal thickness of 35 km. Marangoni *et al.* (1995) carried out the gravity modelling of the Araguaia Fold Belt bordering Parnaíba to the west. The Bouguer gravity of this fold belt was successfully modelled using the *suture zone* concept of Gibb & Thomas (1976) for the Canadian Shield. Crust thickness in this collision zone of two lithospheric blocks was estimated as 40 km, locally thickening to 48 km. Ussami *et al.* (1993) suggested a "normal" crust value of 40 km in Brazil.

There are no previous crust and lithosphere thickness estimates beneath the Parnaíba Basin. The geological evidence is of an area which underwent extensional pulses since the Upper Proterozoic and a reasonable thermal input in the last stages of the Brasiliano Cycle. These geological inferences led to the choice of 35 and 170 km as the preextensional crust and lithosphere thicknesses, respectively.

McKenzie (1978) considered quantitatively a stretching model where crustal and lithospheric extensions are the same, showing no dependence on depth. Isostatic equilibrium is maintained due to passive upwelling of hot aesthenospheric material. It is assumed that the continental lithosphere follows Airy isostasy ($D = 0$) with its initial surface at sea level and heat flux is essentially vertical with no radioactive heat production been considered. For an extensional basin the model describes a total subsidence made up of two components:

1 an instantaneous (less than 20 Myr) fault-controlled subsidence depending on the initial thicknesses of the crust and the lithosphere as well as on the amount of stretching;

2 a subsequent (stretch-dependent only) thermal subsidence due to the exponential dissipation of the heat anomaly with time, resulting in cooling and contraction of the lithosphere.

Some studies of Atlantic-type margins *e.g.* Steckler & Watts (1978) and De Charpal *et al.* (1978), claimed the viability of McKenzie's model in evaluating and predicting the subsidence history of continental margins. A rifting stage initiates with lithospheric extension and crustal attenuation due to stretching. There is an increase in the thermal gradient due to passive upwelling of the aesthenosphere and the crust extends uniformly by normal faulting, possibly listric, in the brittle upper crust and by ductile deformation of the lower crust. The amount of extension as well as the initial thicknesses of crust and lithosphere govern the initial isostatic subsidence.

The theoretical development of McKenzie's model can be summarized as follows: tensional stresses cause the continental crust to fail by brittle fracture, whereas the mantle lithosphere fails by ductile necking. Introducing the notation z_c and z_L for the thicknesses of the crust and lithosphere respectively, ρ_c and ρ_{sc} as the average densities of crustal and subcrustal material and g as the (mean) gravitational acceleration; before rifting the lithostatic column is made up of two components (Fig. 5.8) and the lithostatic stress is given by

$$\rho_c g z_c + \rho_{sc} g (z_L - z_c).$$

Assuming that the geotherms are linear from T_m at the base of the lithosphere to T_0 at the surface and the densities also have a linear relationship to temperature, ρ_c and ρ_{sc} are written as

$$\rho_c = \rho_c^0(1 - \alpha_v T_c)$$

and

$$\rho_{sc} = \rho_m^0(1 - \alpha_v T_{sc}),$$

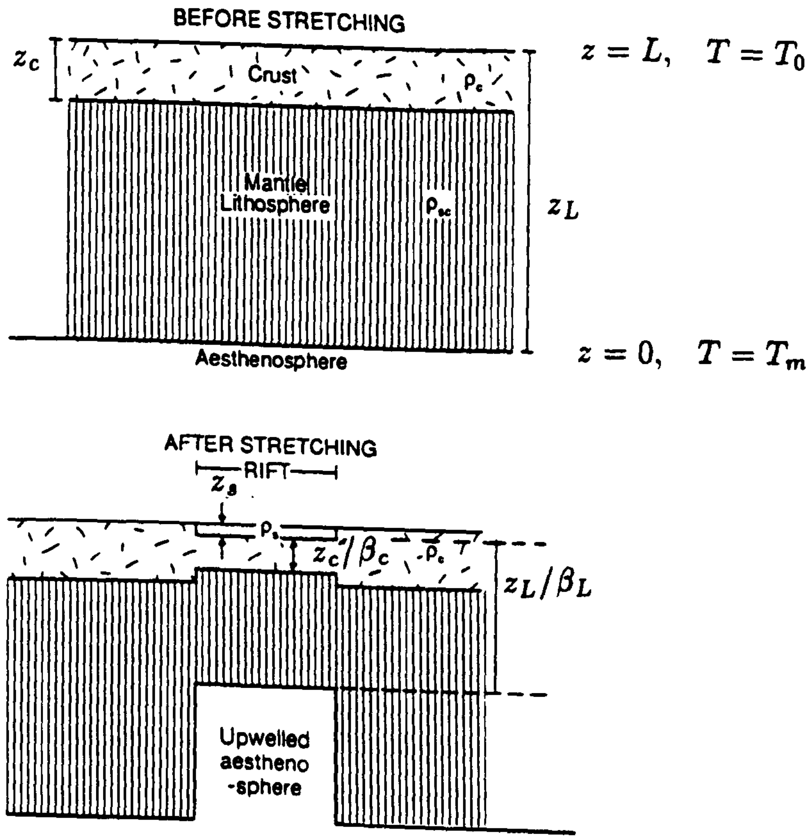

Fig. 5.8 Schematic diagram of the uniform stretching model (McKenzie, 1978). The crustal and lithospheric stretch factors are β_c and β_L. For uniform stretching $\beta_c = \beta_L$ (after Allen & Allen, 1990).

where ρ_c^0 and ρ_m^0 are crustal and mantle densities at 273 K (0°C), α_v is the volumetric coefficient of thermal expansion for crust and mantle and T_c, T_{sc} are the average crustal and subcrustal temperatures, respectively.

Considering linear geotherms, the temperature profile can be written as

$$T(z) = T_m - \frac{T_m - T_0}{z_L} z,$$

and the average values of $T = T(z)$ over the crust and subcrustal lithosphere are

$$\begin{aligned} T_c &= \frac{1}{z_L - (z_L - z_c)} \int_{z_L - z_c}^{z_L} \left(T_m - \frac{T_m - T_0}{z_L} z \right) dz \\ &= T_0 + \frac{T_m - T_0}{2} \frac{z_c}{z_L} \end{aligned}$$

and

$$\begin{aligned} T_{sc} &= \frac{1}{z_L - z_c} \int_0^{z_L - z_c} \left(T_m - \frac{T_m - T_0}{z_L} z \right) dz \\ &= \frac{1}{2} \left[T_0 + T_m + (T_m - T_0) \frac{z_c}{z_L} \right]. \end{aligned}$$

When the surface temperature is 0°C the last expressions simplify to

$$T_c = \frac{T_m}{2}\frac{z_c}{z_L}$$

and

$$T_{sc} = \frac{T_m}{2}\left(1 + \frac{z_c}{z_L}\right).$$

After rifting, both the crust and the lithosphere have been stretched by the same amount. Crust and lithosphere thicknesses are reduced to z_c/β and z_L/β, respectively. Parameter β gives the percentual change in thickness; when $\beta = 0$ there is no extension and when $\beta = \infty$ complete oceanization has occurred.

The lithostatic stress at the depth of the original lithospheric thickness is now

$$\rho_s g z_s + \rho_c g(z_c/\beta) + \rho_{sc} g[(z_L/\beta) - (z_c/\beta)] + \rho_m g[z_L - (z_L/\beta) - z_s],$$

where z_s is the sediment thickness, β is the uniform stretching factor for crust and lithosphere and $\rho_m = \rho_m^0(1 - \alpha_v T_m)$ is the mantle density at temperature T_m. Subcrustal average density ρ_{sc} is assumed to be approximately the same before and after stretching.

Balancing the columns before and after uniform stretching,

$$\rho_c g z_c + \rho_{sc} g(z_L - z_c) = \rho_s g z_s + \rho_c g(z_c/\beta) + (\rho_{sc}/\beta) g(z_L - z_c) + \rho_m g(z_L - z_L/\beta - z_s)$$

and the syn-rift subsidence can be written as

$$z_s = z_L\left(1 - \frac{1}{\beta}\right)\frac{\left[(\rho_m^0 - \rho_c^0)\frac{z_c}{z_L}\left(1 - \alpha_v\frac{T_m}{2}\frac{z_c}{z_L}\right) - \alpha_v\frac{T_m}{2}\rho_m^0\right]}{\rho_m^0(1 - \alpha_v T_m) - \rho_s}. \qquad (5.6)$$

The uniform stretching model of the lithosphere implies in:

1 the *permanent* fault-controlled subsidence of the brittle upper crust; and

2 the *transient* subsidence caused by the thermal anomaly due to the upwelling of hot aesthenosphere.

The initial subsidence is estimated by Equation (5.6) and for the cooling of the lithosphere the model neglects the radioactive heat production and assumes the boundary conditions

$$T = \begin{cases} 0, & \text{at } z = L \quad \text{(surface)} \\ T_m, & \text{at } z = 0 \quad \text{(base of the lithosphere)} \end{cases}$$

with lateral temperature gradients much smaller than vertical gradients

$$\frac{\partial T}{\partial x} \approx \frac{\partial T}{\partial y} \approx 0.$$

Use of the heat conduction equation (Fourier's law) allows the computation of the surface heat flux and the post-rift subsidence, $S(t)$, caused by thermal contraction is given by

$$S(t) \approx \frac{4 z_L \rho_s \alpha_v T_m}{\rho_m^0 - \rho_s} \frac{\beta}{\pi^3} \sin\left(\frac{\pi}{\beta}\right)[1 - \exp(-t/\tau)], \tag{5.7}$$

where $\tau = z_L^2/\pi^2\kappa$ is known as the *thermal time constant* of the lithosphere and κ is its thermal diffusivity.

Initial and thermal subsidence can be estimated from plots of depths versus time, the backstripping curves, and compared to the theoretical estimates of Equations (5.6) and (5.7). Crust/lithosphere extension (β) can be estimated through numerical solution of the transcendental Equation (5.7).

A single extensional event lasting for ~5 Myr was considered in applying the uniform stretching model to the 22 boreholes in Parnaíba, as is shown in Fig. 5.9 for well 1-PA-01-MA. The agreement between the tectonic subsidence curve and the theoretical curve of expression (5.7) is extremely poor. The main observed discrepancy is that the Serra Grande Group lays uncomformably on basement rocks but, according to the uniform stretching model, continuous basinal subsidence should have occurred with usually over 1 km of syn-rift subsidence. Similar discrepancies were observed for all other boreholes. The disparity of McKenzie's model to the tectonic subsidence in Parnaíba has been also observed elsewhere. Several other workers e.g. Sclater *et al.* (1980), Royden & Keen (1980), Oliveira (1987) and Quintas (1995), already observed that McKenzie's model, despite being an important advance in the theoretical framework of understanding basin subsidence, fails to predict the tectonic subsidence in some geological situations. The crustal extension and initial subsidence predicted by the model are usually much larger than the observed values. Equivalently, the observed thermal subsidence is much greater than that predicted from the observed crustal extension.

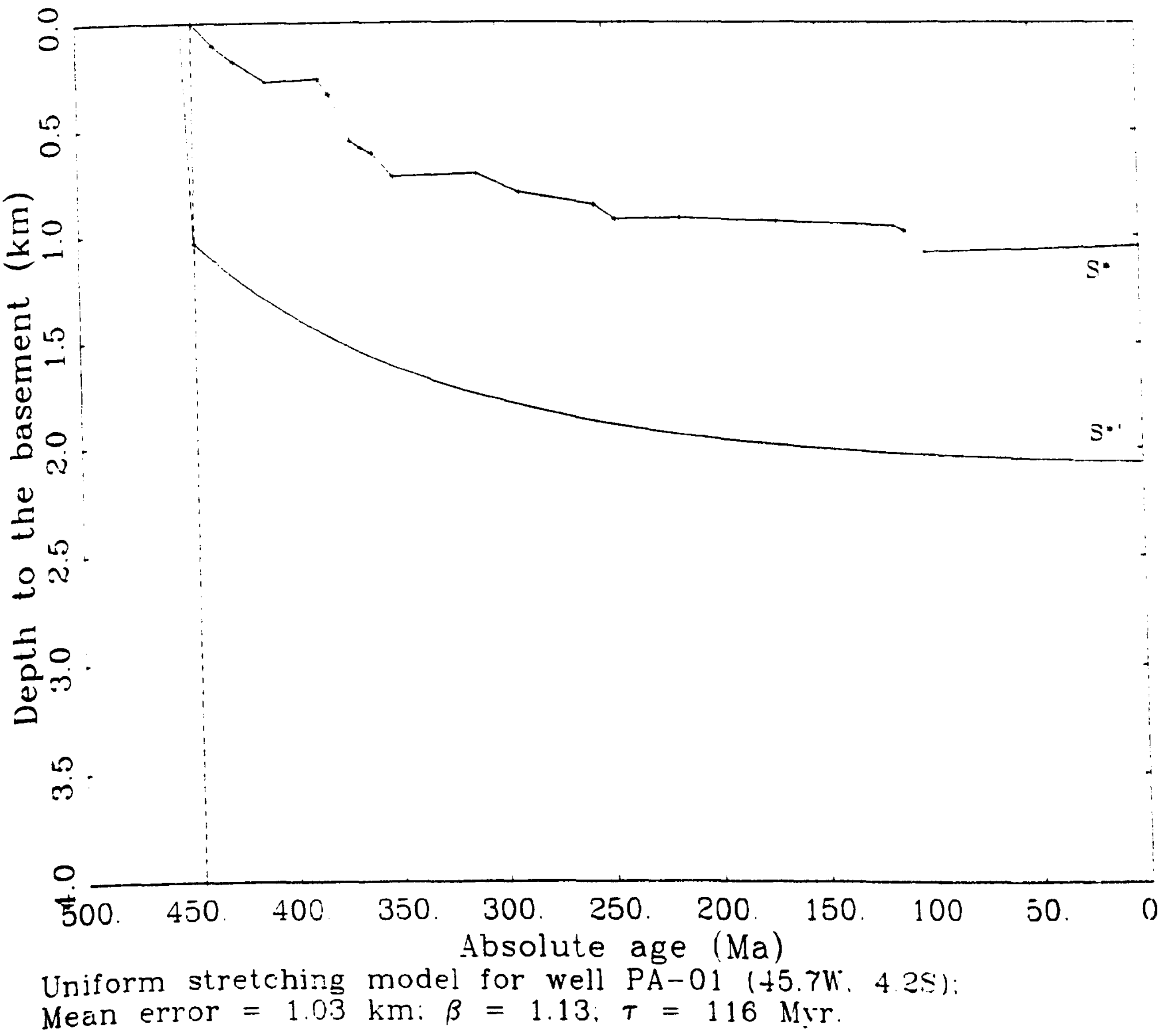

Fig. 5.9 Example of the application of McKenzie's model (uniform stretching) to well 1-PA-01-MA. Note the large predicted syn-tectonic subsidence and the overall poor agreement between the tectonic curve S^* and the theoretical curve $S^{*\prime}$. Rifting assumed to have lasted for 5 Myr under Airy isostasy.

Lithospheric extension is likely to be non-uniform. Royden & Keen (1980) and Hellinger & Sclater (1983) further refined the original, unrealistic uniform stretching model by developing a two-layer instantaneous extensional model. This model was proposed primarily to explain the observed tectonic subsidence of rifted intracratonic basins under the assumptions of:

1 broad-based, predominantly vertical heat input to the subcrustal region during the rifting process;

2 the heat loss is unaffected by sedimentation (*sedimentary blanketing*);

3 effects of crustal radioactivity and dyke intrusion can be ignored; and

4 local isostatic equilibrium is maintained throughout.

The Royden-Keen model considers that extension occurring in an upper, brittle layer is not coupled to what happens to the lower, ductile layer. Under extension, the brittle layer is stretched by a factor β while the ductile layer is stretched by factor δ ($= \beta_L$ in Fig. 5.8). The brittle-ductile transition zone is commonly thought of as occurring at the base of the crust. The evidence comes from structural studies showing that steep faults near the surface quite often become listric and penetrate the continental crust to deep levels (lower crust). Also, focal depths of earthquakes in old cratons (tectonic age ≥ 800 Ma) further confirm that while the upper crust is a seismically active zone of relatively high strength, the lower crust is essentially aseismic, being a zone of lower strength where ductile deformation mechanisms take place.

The formulation of the Royden-Keen model is similar to the McKenzie model. At $t = 0$ the lithosphere undergoes an instantaneous extensional event. A unit length crust is extended to a length β and a unit length of subcrustal lithosphere is extended to δ. The total lithospheric attenuation, ε, is related to the crustal and subcrustal rates as

$$\varepsilon = \frac{z_L}{z_c/\beta + (z_L - z_c)/\delta}.$$

It is convenient to introduce the parameters $\gamma_L = 1 - 1/\varepsilon$, $\gamma_c = 1 - 1/\beta$ and $\gamma_{sc} = 1 - 1/\delta$ where γ represents the reduction in thickness as a percentage of the original thickness. The initial, fault-controlled subsidence is given by (Hellinger & Sclater, 1983)

$$z_s = \frac{\left[\left(\rho_m^0 - \rho_c^0\right) z_c \left(1 - \frac{\alpha_v T_m z_c}{2 z_L}\right) - \frac{\alpha_v \rho_m^0 T_m z_c}{2}\right] \gamma_c - \left[\frac{\alpha_v \rho_m^0 T_m (z_L - z_c)}{2}\right] \gamma_L}{\rho_m^0 (1 - \alpha_v T_m) - \rho_w} \tag{5.8}$$

while the thermal subsidence (Friedinger, 1988) is

$$S(t) = z(0) - z(t), \tag{5.9}$$

where the (waterloaded) depth z at time t after the end of the extension phase is

$$z(t) = \frac{4 z_L \alpha_v \rho_m^0 T_m}{\pi^2 (\rho_m^0 - \rho_w)} \sum_{m=0}^{\infty} \frac{x_{2m+1}}{(2m+1)^2} \exp[-(2m+1)^{2t/\tau}] \tag{5.10}$$

When there are no dyke intrusions the x_n are defined as

$$x_n = \frac{(-1)^{n+1}}{n\pi} [(\beta - \delta) \sin n\pi H + \delta \sin n\pi G]$$

with

$$H = 1 - \frac{z_c}{z_L \beta} \quad \text{and} \quad G = H - \frac{1 - z_c/z_L}{\delta}.$$

Notice that

1 z_s is a linear function of γ_c and γ_L and therefore also of γ_{sc};

2 z_s depends on a much larger scale on crustal thinning than on whole lithosphere thinning; and

3 $S(t)$ involves a weakly convergent infinite series and the summation must be evaluated to a reasonably large value.

Friedinger (1988) wrote a computer algorithm to model basin subsidence and thermal evolution under the assumptions of either the McKenzie or Royden-Keen models. Program **BASTA** uses Equations (5.8)-(5.10) to compute the best match (in the L_2 sense) of β and δ factors for a given range of admissible values to the subsidence tectonic pattern of an exploratory borehole. The summation in Equation (5.10) is evaluated up to the first 50 terms.

The borehole data set for Parnaíba was submitted to **BASTA** with the same parameter values of Table 5.4. A short rifting phase was assumed to have lasted

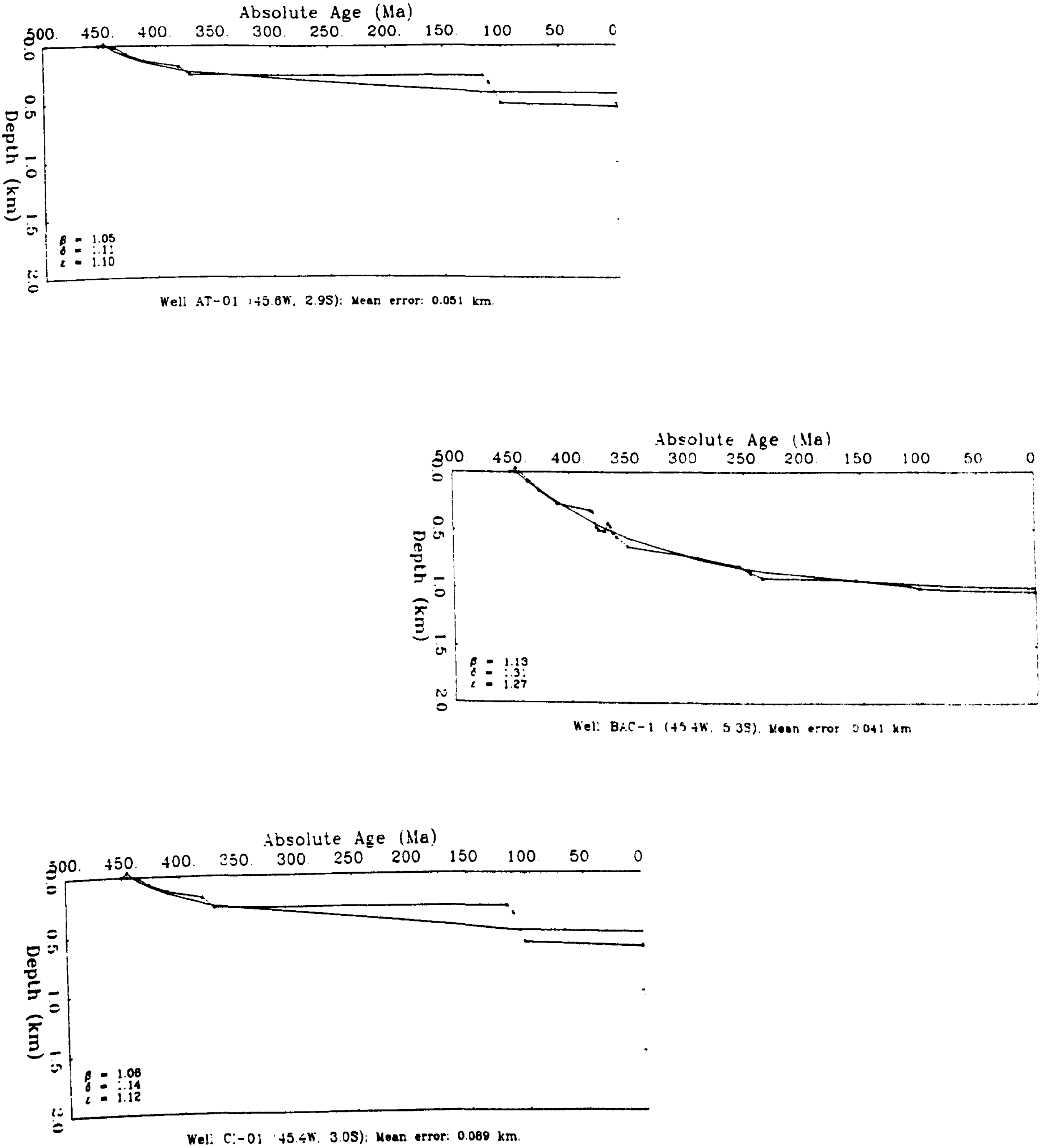

Fig. 5.10 Graphical comparison of the predicted tectonic curves of the Royden-Keen model with the observed tectonic subsidence curves of wells in the Parnaíba Basin. A small initial uplift is often seen and does not contradict the observed erosion prior to the regional thermal subsidence.

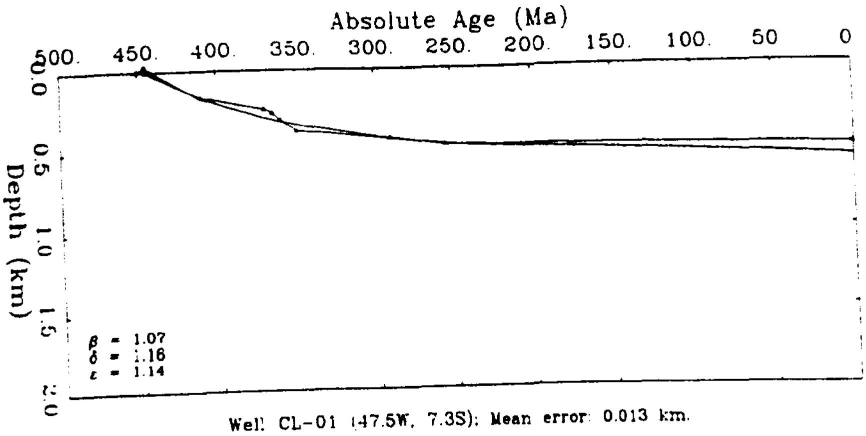

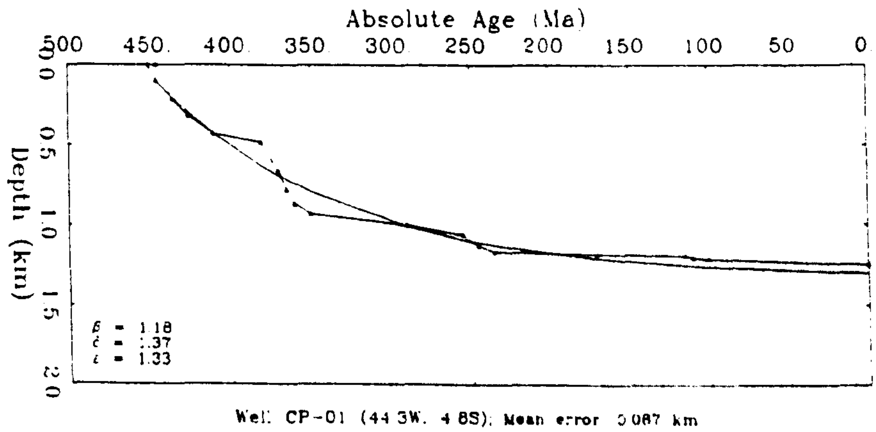

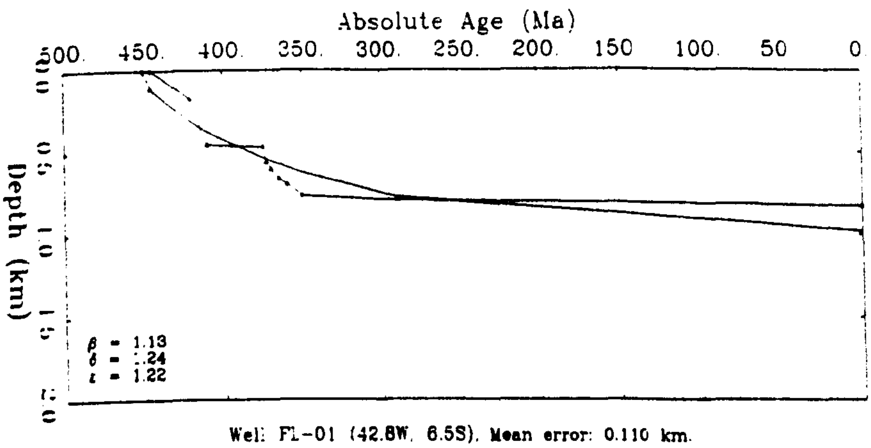

Fig. 5.10 (cont.) Graphical comparison of the predicted tectonic curves of the Royden-Keen model with the observed tectonic subsidence curves of wells in the Parnaíba Basin. A small initial uplift is often seen and does not contradict the observed erosion prior to the regional thermal subsidence.

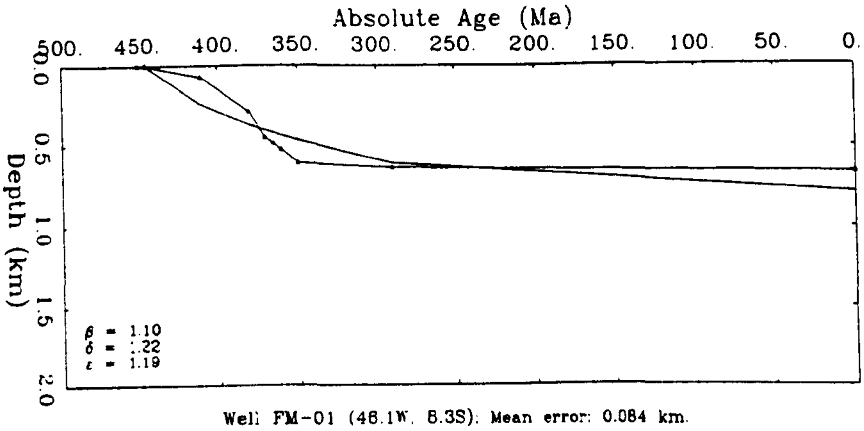

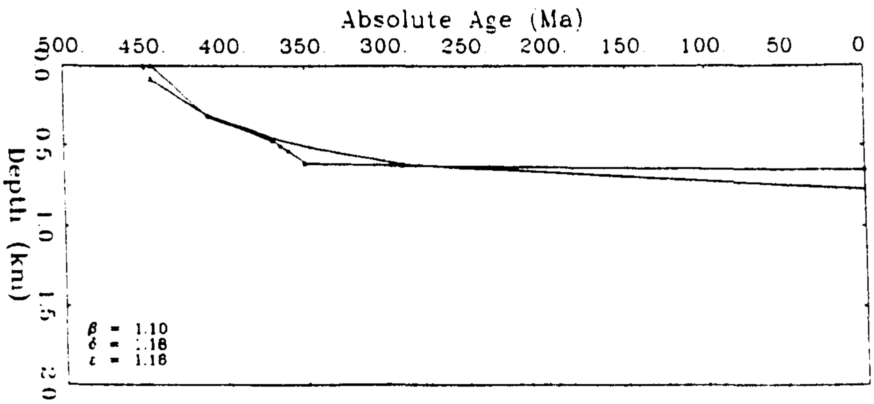

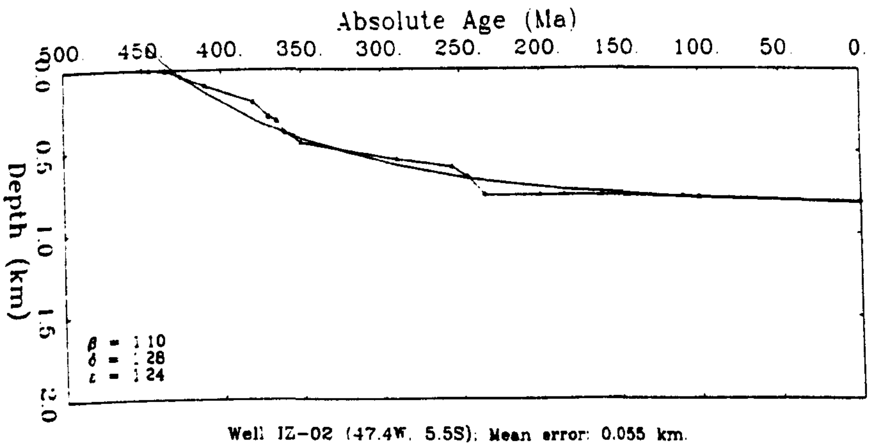

Fig. 5.10 (cont.) Graphical comparison of the predicted tectonic curves of the Royden-Keen model with the observed tectonic subsidence curves of wells in the Parnaíba Basin. A small initial uplift is often seen and does not contradict the observed erosion prior to the regional thermal subsidence.

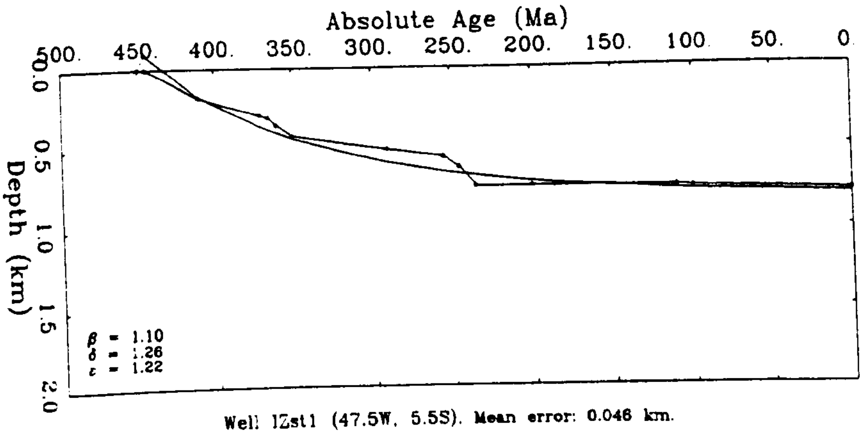

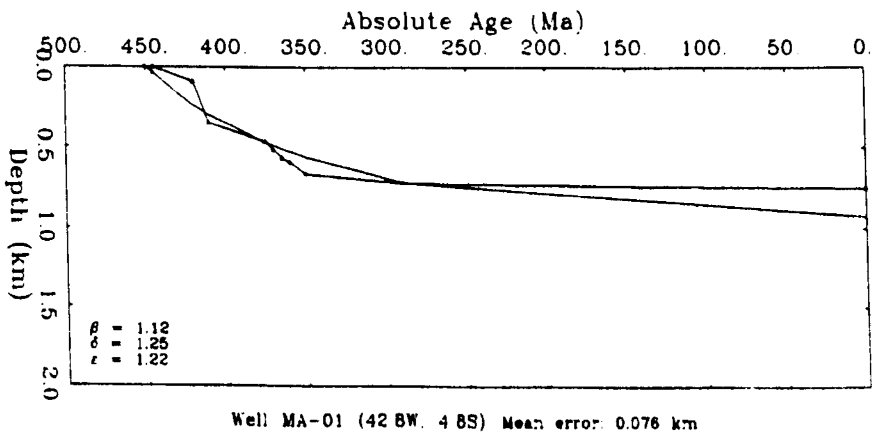

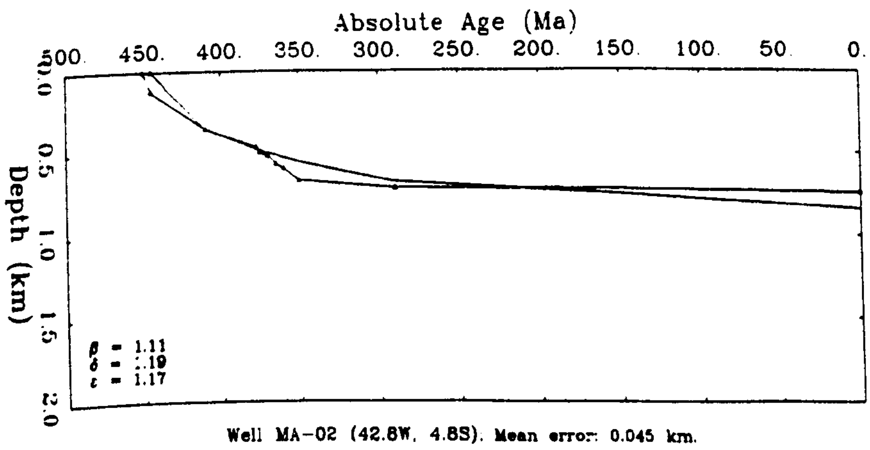

Fig. 5.10 (cont.) Graphical comparison of the predicted tectonic curves of the Royden-Keen model with the observed tectonic subsidence curves of wells in the Parnaíba Basin. A small initial uplift is often seen and does not contradict the observed erosion prior to the regional thermal subsidence.

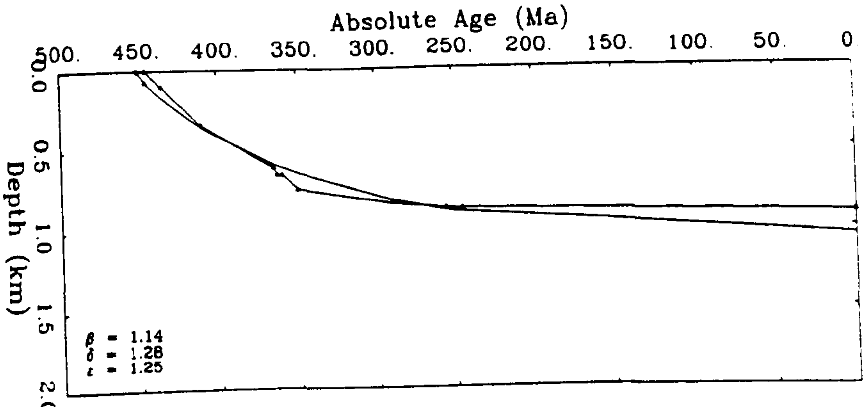

Well: MD-01 (44.3W, 6.4S); Mean error: 0.047 km.

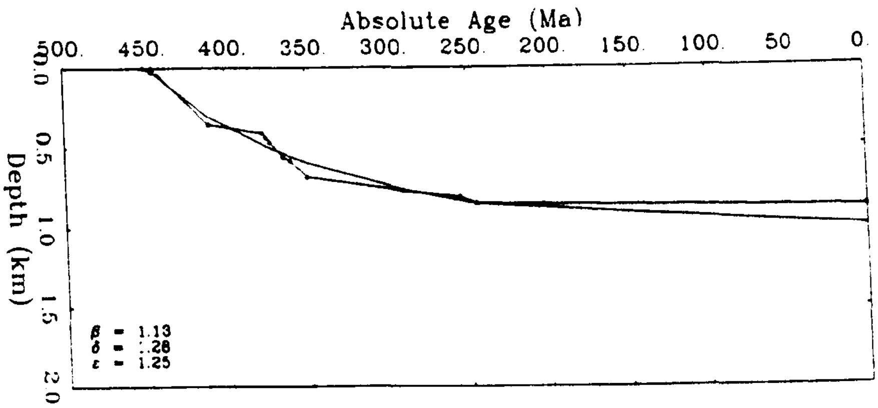

Well MS-01 (45.5W, 7.0S). Mean error 0.036 km.

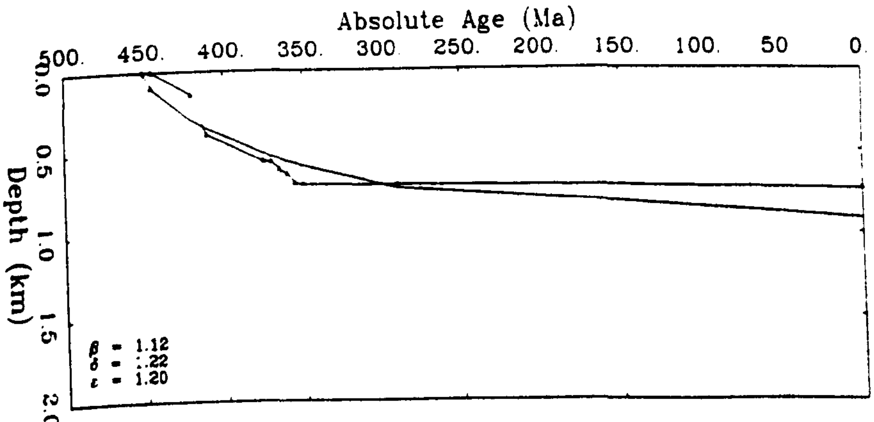

Well NLst1 (42.6W, 5.6S); Mean error: 0.109 km.

Fig. 5.10 (cont.) Graphical comparison of the predicted tectonic curves of the Royden-Keen model with the observed tectonic subsidence curves of wells in the Parnaíba Basin. A small initial uplift is often seen and does not contradict the observed erosion prior to the regional thermal subsidence.

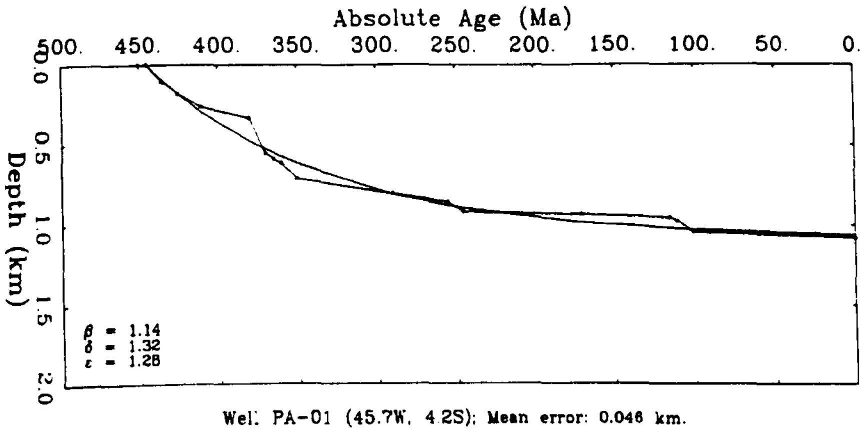

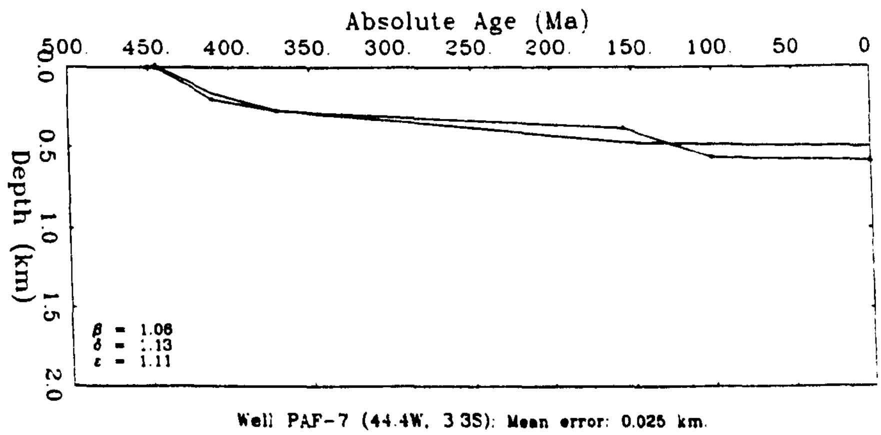

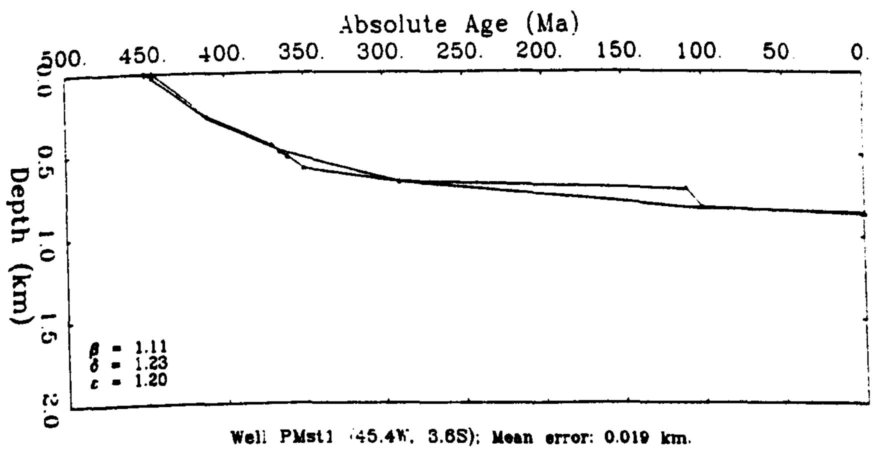

Fig. 5.10 (cont.) Graphical comparison of the predicted tectonic curves of the Royden-Keen model with the observed tectonic subsidence curves of wells in the Parnaíba Basin. A small initial uplift is often seen and does not contradict the observed erosion prior to the regional thermal subsidence.

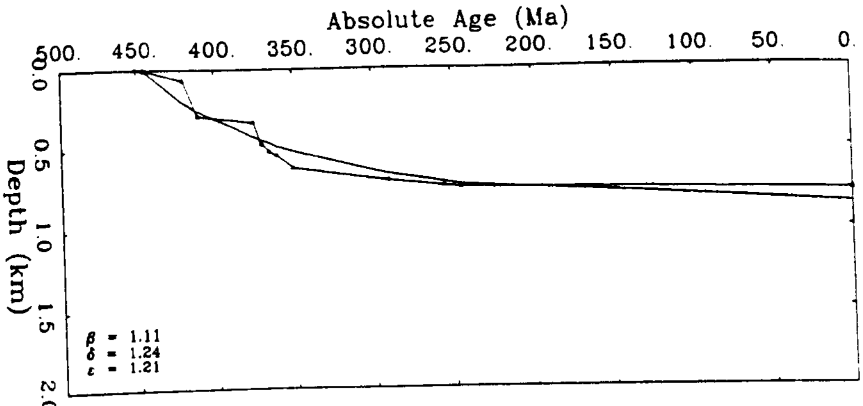

Well TB-01 (46.1W, 7.4S); Mean error: 0.054 km.

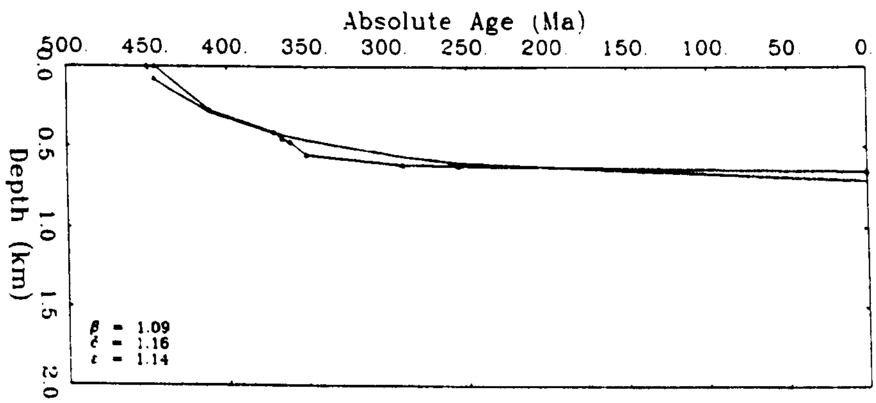

Well TM-01 (46.9W, 8.7S). Mean error: 0.024 km

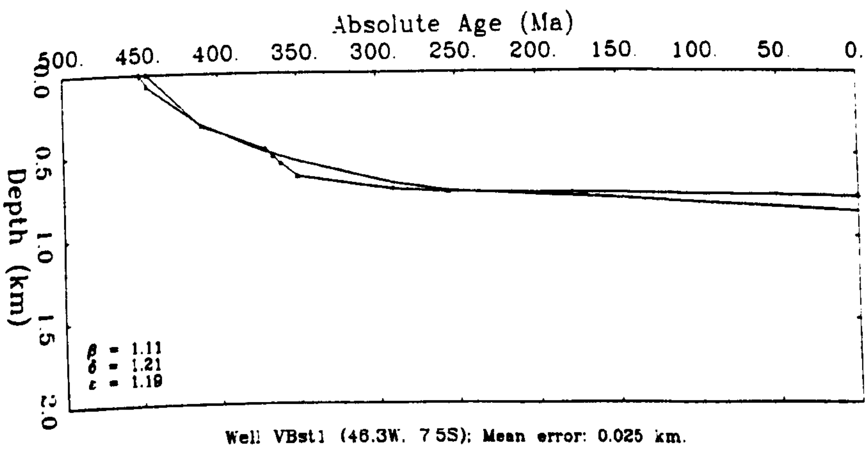

Well VBst1 (46.3W, 7.5S); Mean error: 0.025 km.

Fig. 5.10 (cont.) Graphical comparison of the predicted tectonic curves of the Royden-Keen model with the observed tectonic subsidence curves of wells in the Parnaíba Basin. A small initial uplift is often seen and does not contradict the observed erosion prior to the regional thermal subsidence.

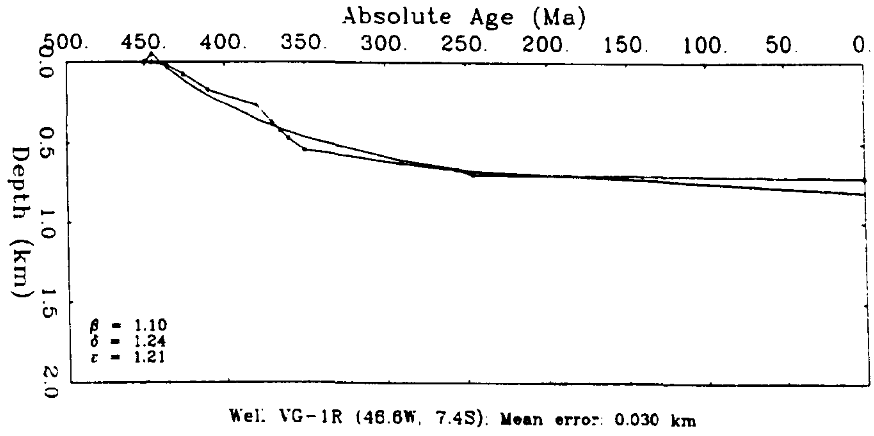

Fig. 5.10 (cont.) Graphical comparison of the predicted tectonic curves of the Royden-Keen model with the observed tectonic subsidence curves of wells in the Parnaíba Basin. A small initial uplift is often seen and does not contradict the observed erosion prior to the regional thermal subsidence.

for (at least) 5 Myr, since instantaneous rifting is absurd of the geological point of view. Expressions (5.8)-(5.10) were evaluated with β, $\delta \in [1., 2.]$ and combinations were iteratively considered with 0.01 steps. Results are grouped in Fig. 5.10 which shows the best matches for all boreholes. Note that small uplifts are considered to have occurred prior to general subsidence, agreeing with the geological evidence of an erosional uncomformity between the basement rocks and the Silurian depositional sequence. The superiority of the Royden-Keen model is clearly visible as compared to the McKenzie model example shown in Fig. 5.9 and Table 5.5 summarizes the results obtained.

Table 5.5 Estimated values of crustal and subcrustal extension rates and total lithospheric attenuation (percentages).

Well	β	δ	ε
1-AT-01-MA	1.05	1.11	1.10
2-BAC-01-MA	1.13	1.30	1.26
1-CI-01-MA	1.06	1.14	1.12
1-CL-01-MA	1.07	1.15	1.13
2-CP-01-MA	1.18	1.36	1.32
1-FL-01-PI	1.13	1.23	1.21
1-FM-01-MA	1.10	1.22	1.19
1-FO-01-MA	1.10	1.17	1.15
1-IZ-02-MA	1.10	1.27	1.23
2-IZst-01-MA	1.10	1.25	1.22
1-MA-01-PI	1.12	1.24	1.21
1-MA-02-PI	1.12	1.22	1.20
1-MD-01-MA	1.14	1.28	1.25
1-MS-01-MA	1.13	1.27	1.24
2-NLst-01-PI	1.12	1.21	1.19
1-PA-01-MA	1.14	1.32	1.28
9-PAF-07-MA	1.07	1.14	1.12
2-PMst-01-MA	1.11	1.22	1.20
1-TB-01-MA	1.11	1.24	1.21
1-TM-01-MA	1.09	1.16	1.14
1-VBst-01-MA	1.11	1.20	1.18
1-VG-1R-MA	1.10	1.24	1.21

Figure 5.11 shows the geographic distribution of the total lithospheric attenuation estimates within the basin. Larger values are noticeably closer to the mapped or inferred NNW-SSE graben structures and along the Transbrasiliano Lineament. Attenuation values systematically decrease towards the borders of the basin. Wells 2-BAC-01-MA (ε = 1.26), 2-CP-01-MA (ε = 1.32) and 1-PA-01-MA (ε = 1.28) are in between the grabenlike structures and show the largest attenuation values. The lithospheric attenuation values have also been contoured and are shown in Fig. 5.12. The zone of largest attenuation is consistent with the maximum basinal sediment thickness and the residual gravity high of Fig. 4.21. Crustal, subcrustal and total attenuation values for Parnaíba are lower than those estimated for the

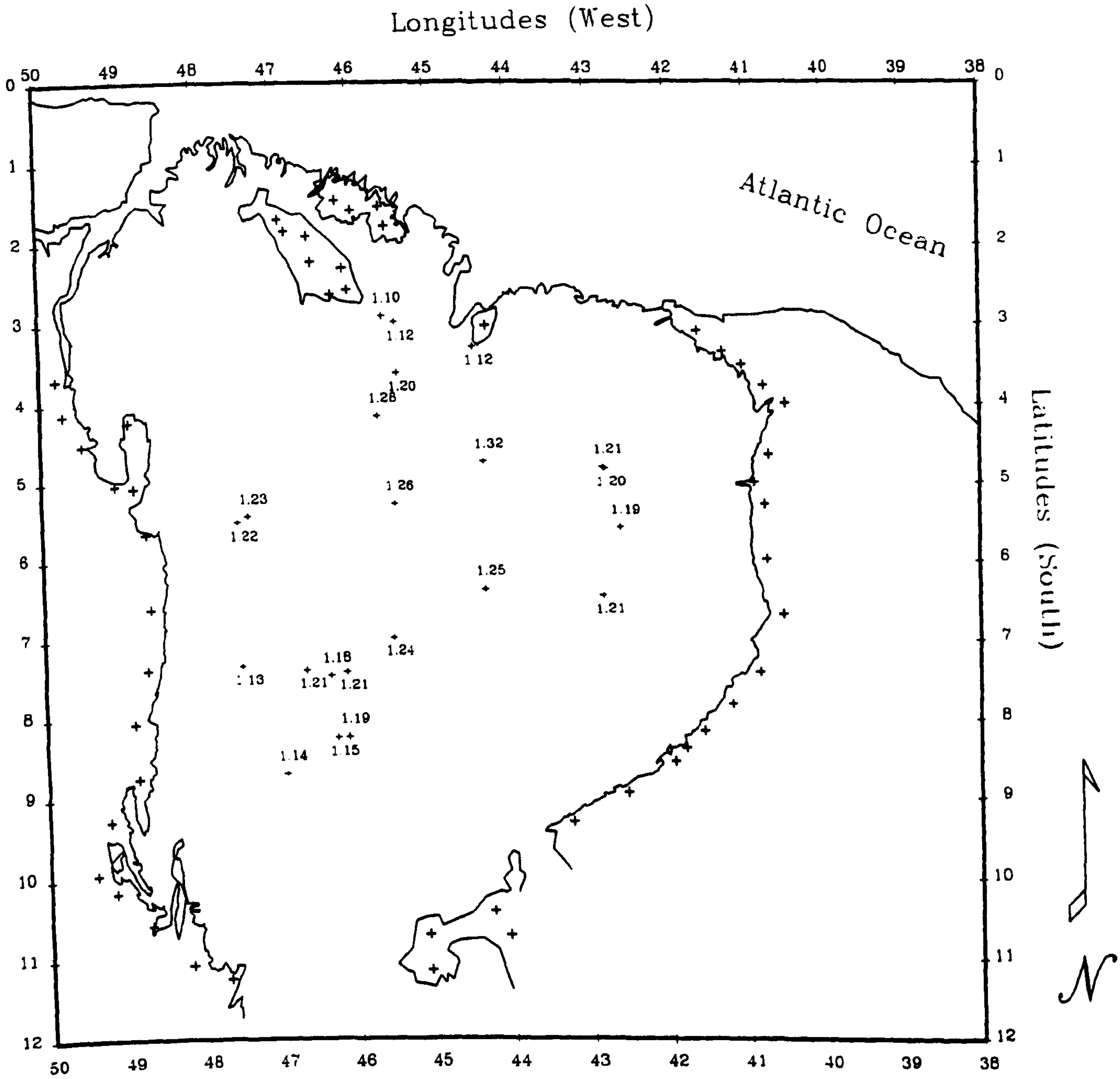

Fig. 5.11 Total lithospheric attenuation (ε) estimated at borehole sites in the Parnaíba Basin. Largest values are found in wells close to the inferred graben structures. Conic projection.

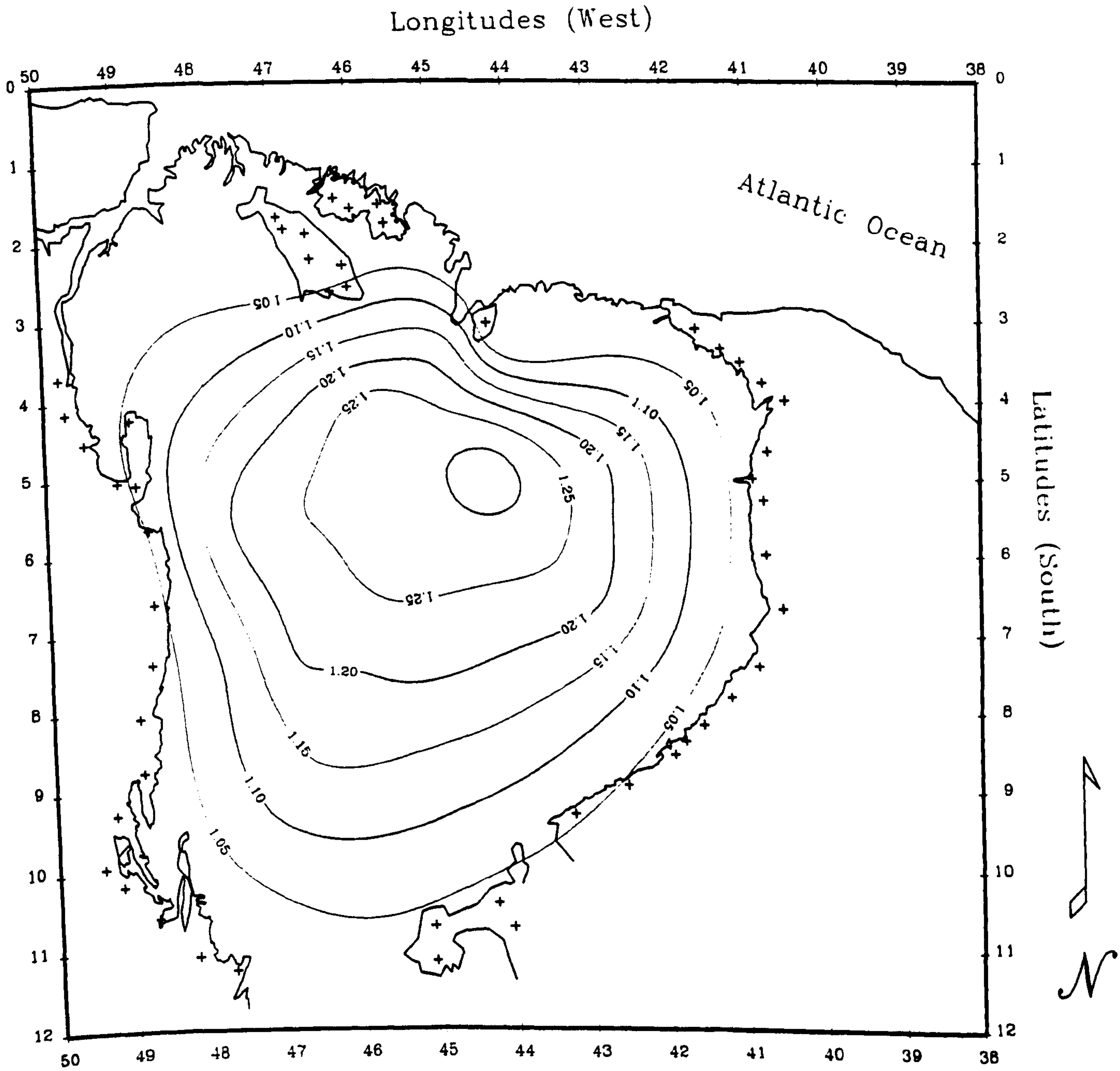

Fig. 5.12 Isoattenuation map of the lithosphere beneath the Parnaíba Basin. Contour interval: 5%, conic projection.

Paraná Basin. Quintas (1995) assigned three extensional pulses acting in Paraná with total lithospheric attenuation in excess of 60% in many sites.

Changes in the depocentre and basin shape through geologic time were analyzed by sketching W-E and S-N profiles at times coincident with the end of sedimentation of each of the stratigraphic groups (Fig. 5.13). The chosen epochs were 410 Ma, after the Serra Grande sedimentation; 350 Ma, when the Canindé Group had been deposited; 235 Ma, when the Balsas Group had also been deposited, 155 Ma, including the Mearim Group; 100 Ma, after the Cretaceous sequence was deposited and magmatism had occurred in the basin; and the present time, after thermal reequilibration and basin exposure. These profiles are shown in Figures 5.14 (profile W-E, 5 wells) and 5.15 (profile S-N, 7 wells).

What these profiles basically outline are cross-sections of the post-rift thermal phase of the Parnaíba Basin and both profiles show quiescent sedimentation. A slight change with time in the depocentre towards west, causing a more symmetrical basin shape is seen in the W-E profile. The change in the depocentre could signal the earlier, stronger influence of the NE-SW crustal weakness zones followed by widespread subsidence. The small number of wells to the east of 43°W precludes a better assessment of the influence of the Transbrasiliano Lineament on the first stages of subsidence of Parnaíba. The S-N profile displays the same gentle sedimentation pattern with a more elongated basin to the south and a steeper northern border due to the truncation process that Parnaíba suffered in the Mesozoic.

The gradual regional subsidence observed in the W-E and S-N profiles have been interpreted as the result of thermal cooling and loading that followed the rift phases of the grabenlike structures. A simple rheological model was considered in an attempt to estimate the flexural subsidence effects of this loading.

5.4 Flexural Loading of the Lithosphere

Numerous authors have considered the flexure of the lithosphere under various loads *e.g.* Brotchie & Silvester, 1969; Walcott, 1970; Turcotte (1979) and Ussami, 1986. Essentially, the tectonic plates defining the lithosphere are treated as rigid plates overlaying the mantle, whose behaviour is that of a fluid substratum on

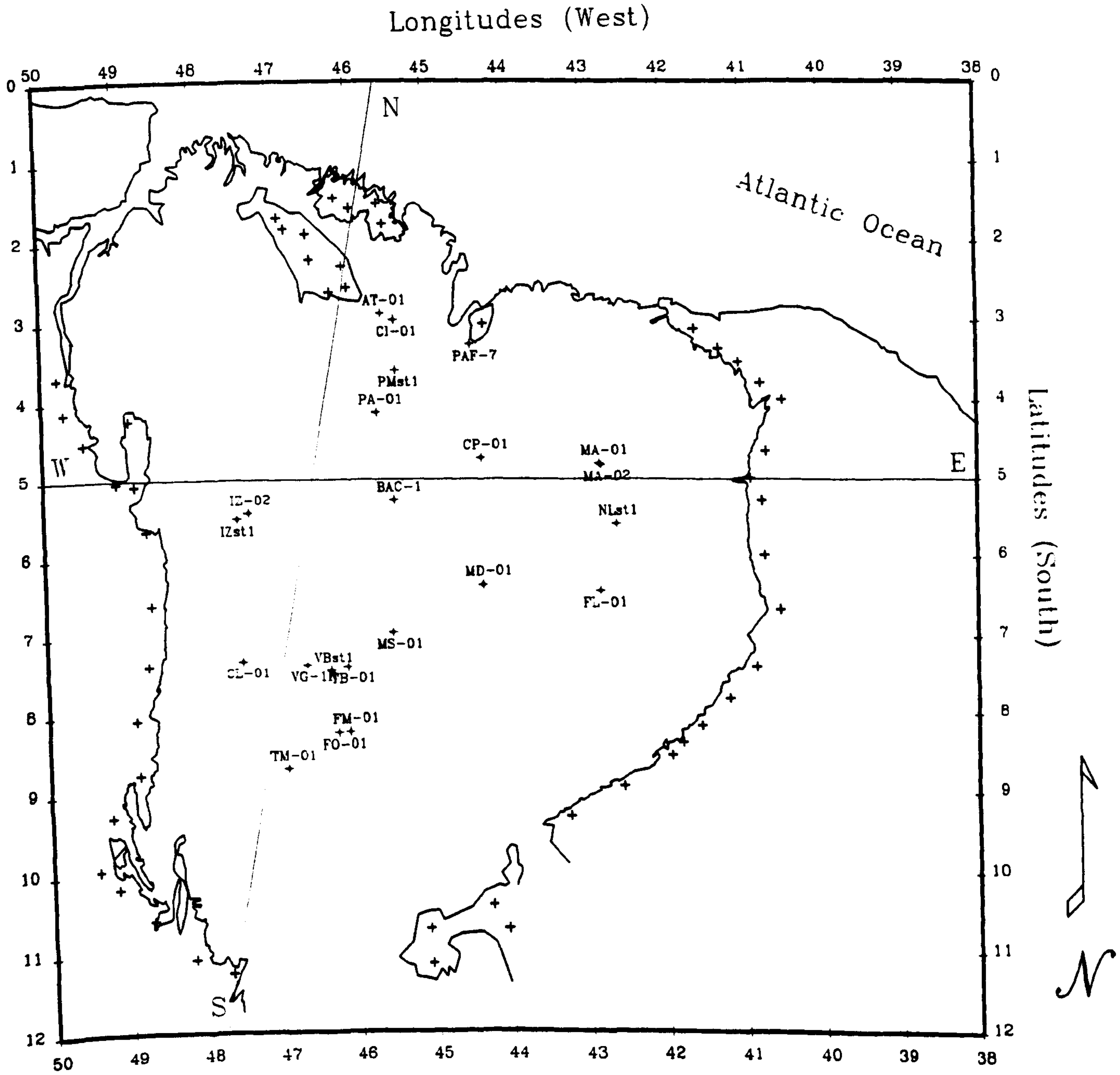

Fig. 5.13 Subsidence profiles across the Parnaíba Basin. Profile W-E includes wells 2-IZst-01-MA, 2-BAC-01-MA, 2-CP-01-MA, 1-MA-01-PI and 2-NLst-01-PI. Profile S-N includes wells 1-TM-01-MA, 1-FO-01-MA, 1-VG-1R-MA, 2-BAC-01-MA, 1-PA-01-MA, 2-PMst-01-MA and 1-AT-01-MA.

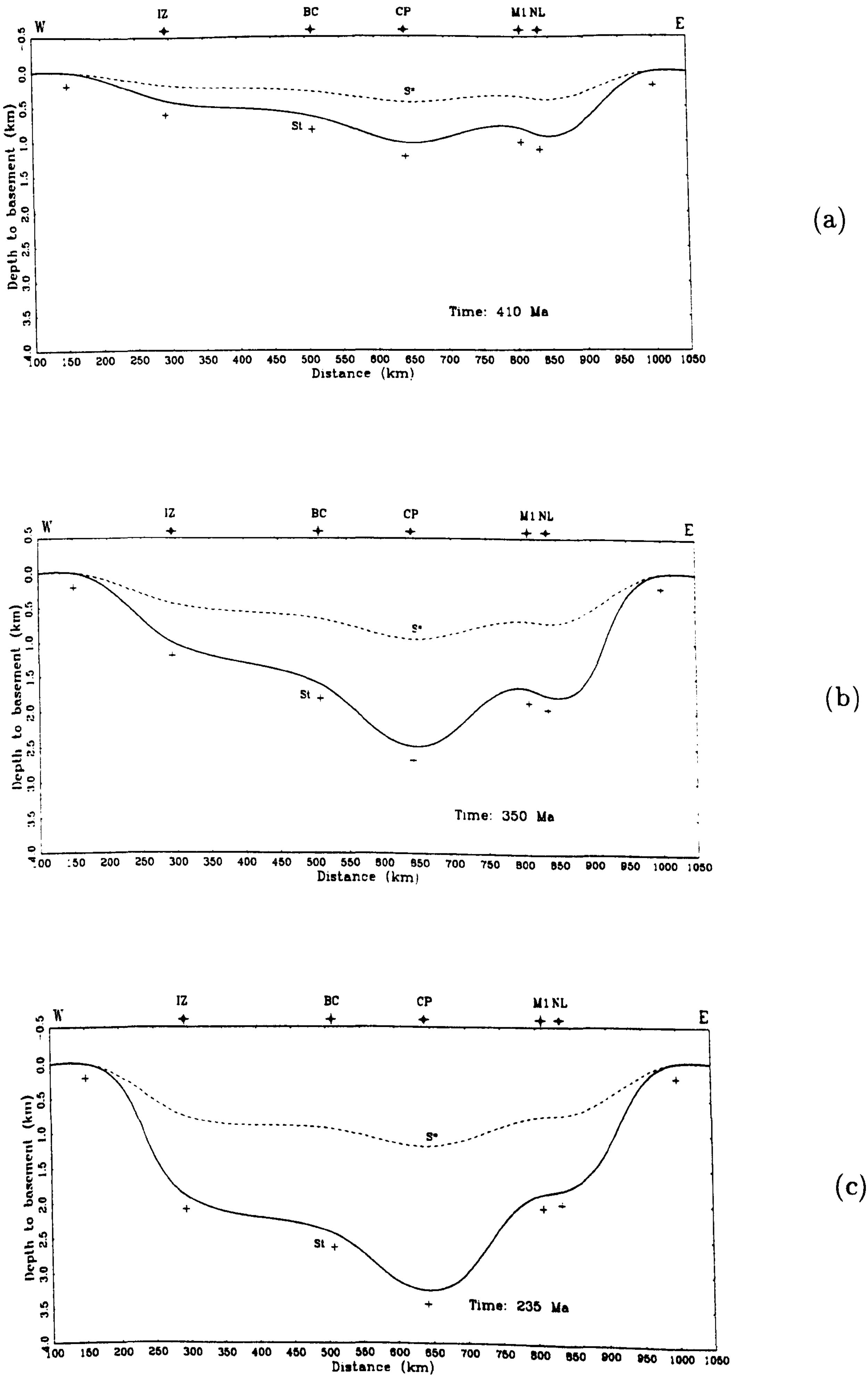

Fig. 5.14 West-East subsidence profile across the Parnaíba Basin; (a) after the Silurian deposition; (b) after the Devonian deposition; (c) after the Carboniferous-Triassic deposition.

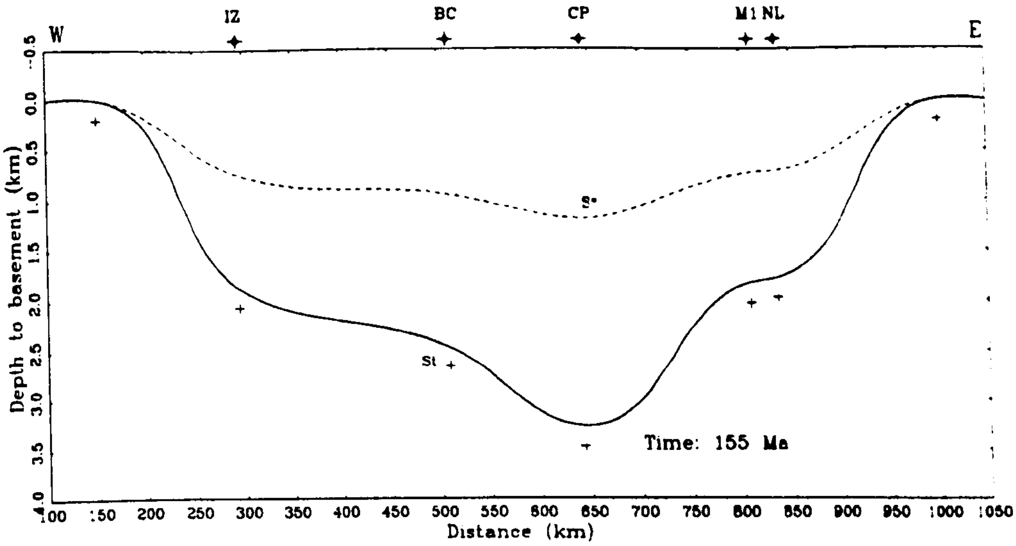

(d)

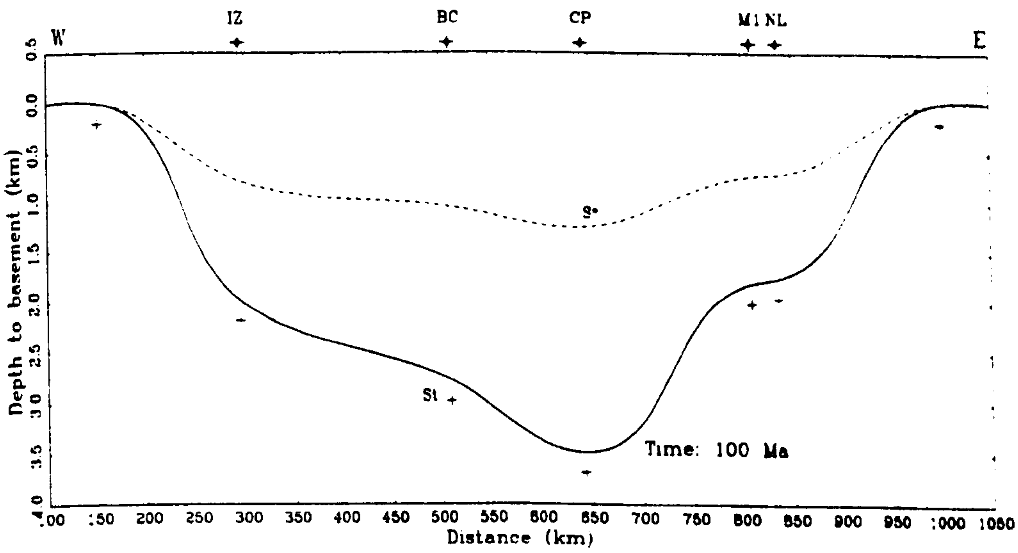

(e)

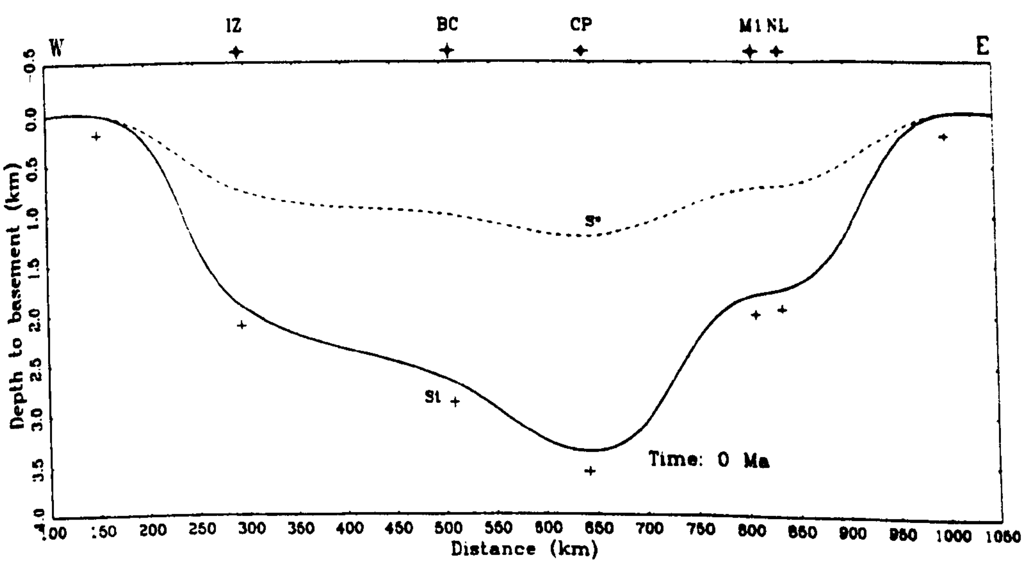

(f)

Fig. 5.14 (cont.) West-East subsidence profile across the Parnaíba Basin; (d) after the Jurassic deposition; (e) after the Cretaceous deposition; and (f) at the present time.

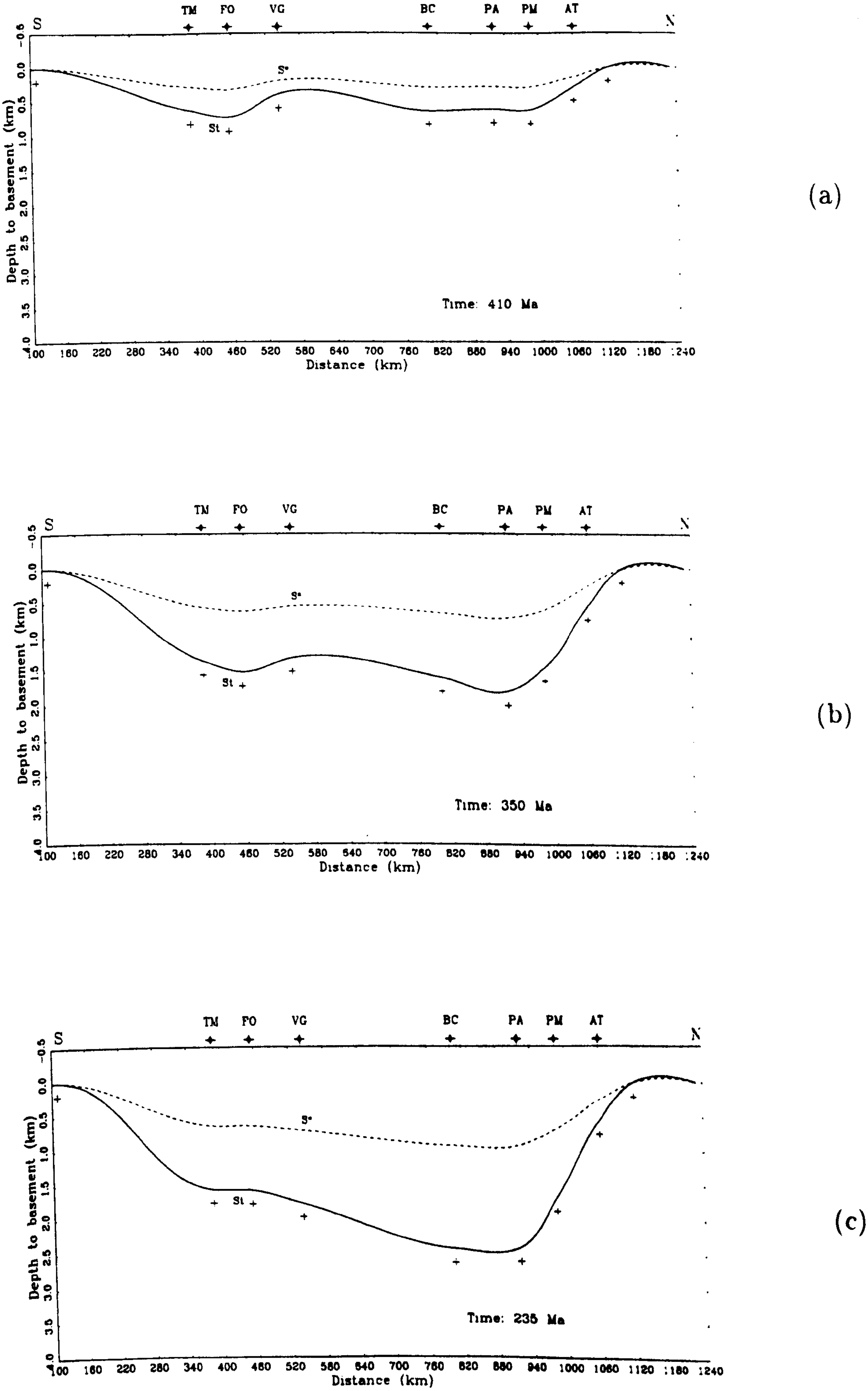

Fig. 5.15 South-North subsidence profile across the Parnaíba Basin; (a) after the Silurian deposition; (b) after the Devonian deposition; (c) after the Carboniferous-Triassic deposition.

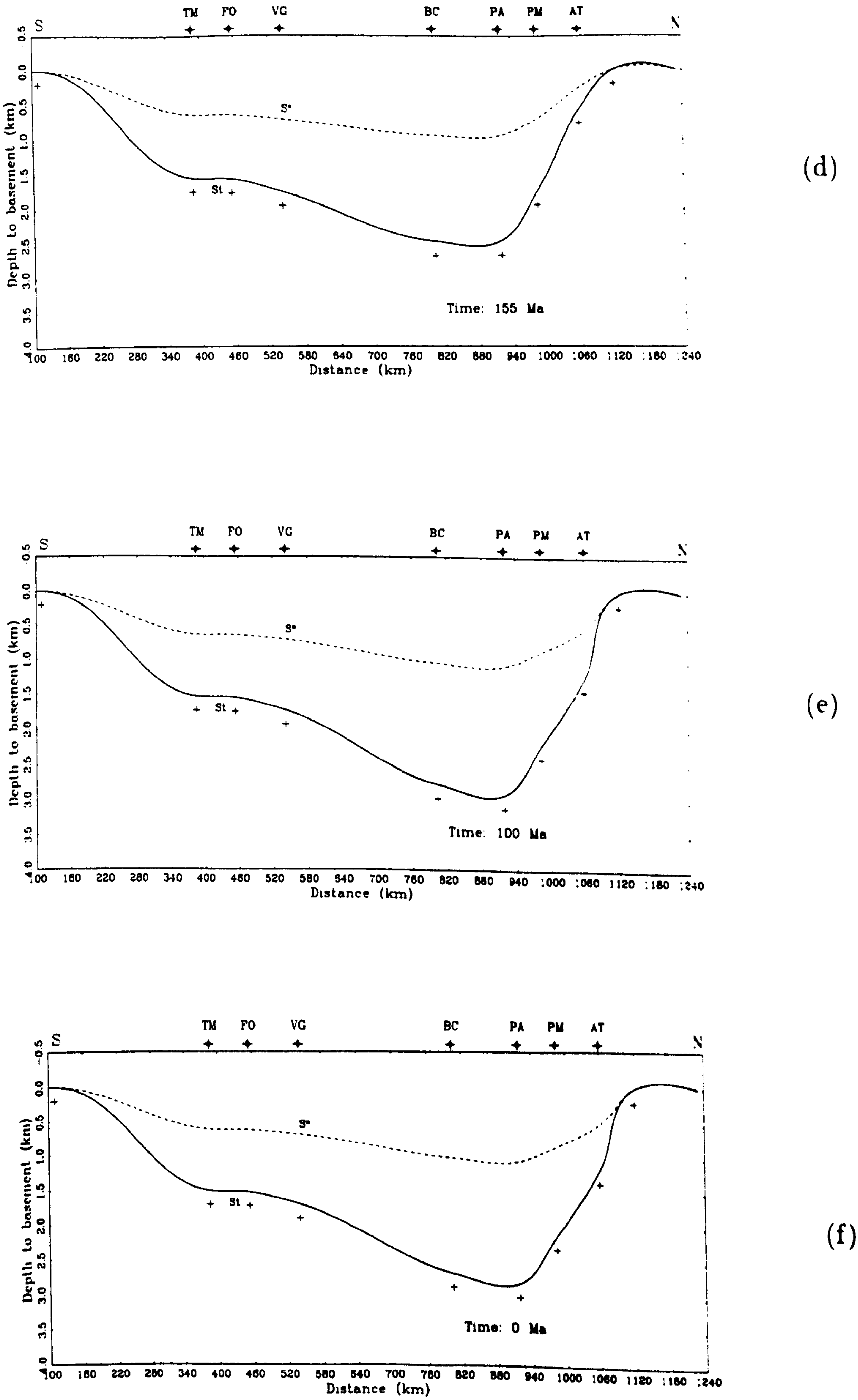

Fig. 5.15 (cont.) South-North subsidence profile across the Parnaíba Basin; (d) after the Jurassic deposition; (e) after the Cretaceous deposition; and (f) at the present time.

geological time scales. A thermal boundary, usually the $450 \pm 100^{\circ}$C (Watts *et al.* 1982), would define the elastic portion of the lithosphere, the transition from rigid to ductile behaviour. There is considerable observational evidence that surface loads like mountains, sedimentary basins, islands and seamounts cause flexure of the lithosphere.

The concept that the lithosphere behaves as an elastic plate overlaying a fluid substratum goes back to the middle of the nineteenth century when the absence of large gravity anomalies over mountain ranges was explained in terms of low density roots. Mountain loading depressed the crust, displacing the denser mantle rocks. Usually, thin plate theory or shell approximation has been applied to problems involving lithospheric flexure; *i.e.* the wavelength of the flexure is considered to be long compared to the thickness of the plate. Loads are supported by the bending ridigity of the plate and in this limit the shear stresses due to vertical loading are neglected compared to bending stresses. Also, a flat Earth approximation is taken since the loads commonly have a wavelength much shorter than the Earth radius.

Of particular interest to this study is the problem of axisymmetric loading of the lithosphere with an applied load $p = p(r)$ per unit area, depending only on the radial coordinate. The governing equation valid for such situation is

$$D\left(\frac{d^2}{dr^2} + \frac{1}{r}\frac{d}{dr}\right)^2 w(r) = p(r) - \textit{restoring force},$$

where D is the effective flexural ridigity of the lithosphere and $w(r)$ is its vertical deflection.

The nature of the restoring force can be understood from the examination of Fig. 5.16. This schematic diagram shows a waterloaded basin model where the axisymmetric load driving the tectonic subsidence has been approximated by one disk lying at the lowermost crust and the uppermost mantle. The disk load with density ρ_c^* is denser than the normal lower continental crust of density ρ_c, thus forcing its way down into the mantle underneath of density ρ_m ($> \rho_c^*$) and experiencing an upward buoyancy force.

The continental lithospheric plate includes crust of thickness z_c and density ρ_c separated by the Moho from the rest of the lithosphere of density ρ_m and thickness z. The plate lies on top of a fluid lithospheric mantle of density ρ_m and has been

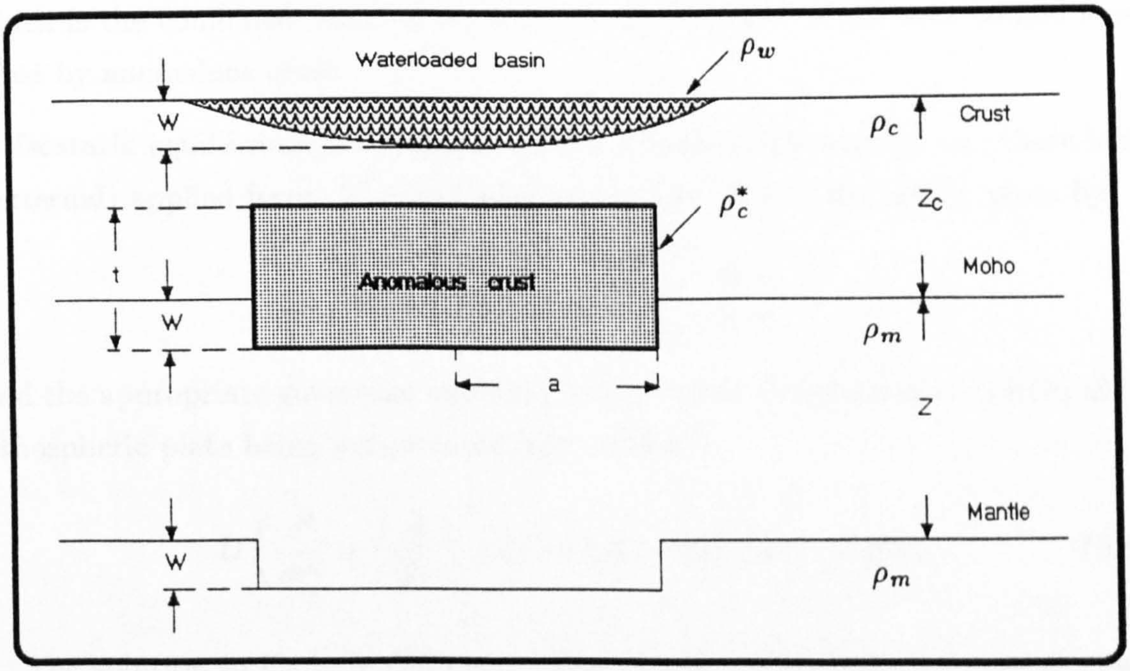

Fig. 5.16 Schematic diagram showing the tectonic subsidence of a waterloaded basin caused by an axisymmetric load at the lowermost crust-uppermost mantle. Densities are $\rho_m > \rho_c^* > \rho_c > \rho_w$.

deflected downward by the disk load of radius a and thickness t. The crust nearest to the load is effectively thickened by the same amount w which the Moho is depressed. The weight per unit area of a vertical column extending from the base of the deflected plate to the surface is

$$\rho_w g w + \rho_c g[z_c - w - (t - w)] + \rho_c^* g t + \rho_m g z$$

while the pressure at a depth $z_c + z + w$ in the surrounding mantle far from the deflected plate is

$$\rho_c g z_c + \rho_m g(z + w).$$

The upward hydrostatic restoring force per unit area is given by the difference

$$\rho_c g z_c + \rho_m g z + \rho_m g w - \rho_w g w - \rho_c g z_c + \rho_c g t -$$
$$-\rho_c^* g t - \rho_m g z = (\rho_m - \rho_w) g w - (\rho_c^* - \rho_c) g t$$

which is the combined result of replacing mantle rock by water and normal lower crust by anomalous crust.

Isostatic equilibrium is assumed to be maintained throughout *i.e.* there is no (external) applied force. The disk load exerts a force per unit area p given by

$$p(r) = \begin{cases} (\rho_c^* - \rho_c) g t, & r \leq a \\ 0, & r > a \end{cases}$$

and the appropriate governing equation for the vertical deflection $w = w(r)$ of the lithospheric plate being axisymmetrically loaded is

$$D \left(\frac{d^2}{dr^2} + \frac{1}{r} \frac{d}{dr} \right)^2 w(r) + (\rho_m - \rho_w) g w(r) = p(r). \tag{5.11}$$

The solution to Equation (5.11) has been given by Brotchie & Silvester (1969) and Haxby *et al.* (1976). The predicted tectonic subsidence is written as

$$w(r) = \begin{cases} \dfrac{(\rho_c^* - \rho_c)t}{\rho_m - \rho_w} \left[\dfrac{a}{\alpha} \mathrm{ker}' \left(\dfrac{a}{\alpha} \right) \mathrm{ber} \left(\dfrac{r}{\alpha} \right) - \dfrac{a}{\alpha} \mathrm{kei}' \left(\dfrac{a}{\alpha} \right) \mathrm{bei} \left(\dfrac{r}{\alpha} \right) + 1 \right], & r \leq a \\ \dfrac{(\rho_c^* - \rho_c)t}{\rho_m - \rho_c} \left[\dfrac{a}{\alpha} \mathrm{ber}' \left(\dfrac{a}{\alpha} \right) \mathrm{ker} \left(\dfrac{r}{\alpha} \right) - \dfrac{a}{\alpha} \mathrm{bei}' \left(\dfrac{a}{\alpha} \right) \mathrm{kei} \left(\dfrac{r}{\alpha} \right) \right], & r > a \end{cases} \tag{5.12}$$

where ker, ber, kei and bei are the Bessel-Kelvin functions of zero order, with primes denoting derivatives with respect to the argument. The associated ***flexural parameter*** α is defined as $\alpha = \left[\dfrac{4D}{(\rho_m - \rho_w) g} \right]^{\frac{1}{4}}$ and polynomial approximations (Abramowitz & Stegun, 1965) were used to evaluate the Bessel-Kelvin functions and their derivatives for arguments in the range

$$0 \leq \left(\frac{a}{\alpha} \right), \left(\frac{r}{\alpha} \right) \leq 8.$$

Equation (5.12) has been coded as a FORTRAN program to model the present-day tectonic subsidence as found in the profile W-E shown in Fig. 5.14f. The best-fit iteration for the axisymmetric loading model is shown in Fig. 5.17 and the following parameters were found:

- Effective flexural ridigity $D = 0.2 \times 10^{24}$ N m;
- Flexural parameter $\alpha = 77$ km; and
- Disk load: radius = 370 km, thickness = 14.5 km, centered at 630 km.

Thin plate theory relates the effective flexural ridigity of the plate to its elastic thickness T_e as

$$D = \frac{ET_e^3}{12(1-\nu^2)}.$$

Given the value of D and taking into account the Poisson's ratio and Young's modulus of Table 5.4, this correlates to an elastic lithospheric thickness of 32 km. This elastic thickness is similar to those found for the continental lithosphere as a whole (Beaumont, 1981; Watts, 1992), for the Michigan Basin (Haxby *et al.* 1976; Nunn & Sleep, 1984), Paris Basin (Brunet & Le Pichon, 1982), the interior basins of Australia (Lambeck, 1983) and the Paraná Basin (Oliveira, 1989). Figure 5.18 positions the elastic thickness computed in the present study among other estimates for the continental lithosphere (Watts, 1992). Note the bimodal distribution of continental values in contrast to oceanic values.

Karner (1993) has suggested that care should be taken in understanding the meaning of any figures obtained for the effective elastic thickness of the lithosphere. The lithospheric elastic plate model is simply a mechanical analogue (derived from civil engineering) and the results eventually obtained do not imply that the lithosphere is elastic down to a certain depth and plastic, viscoelastic beyond that. Our results do not necessarily mean that the lithosphere is elastic at all! The model merely demonstrates that the depth-integrated behaviour of the lithosphere over geologic time is similar to that of an elastic plate of given thickness.

5.5 Discussion

The first systematic application of the backstripping technique to exploration boreholes in the Parnaíba Basin has been carried out in the present study. Estimates of the separate tectonic (40-45%) and sediment (60-55%) contributions to

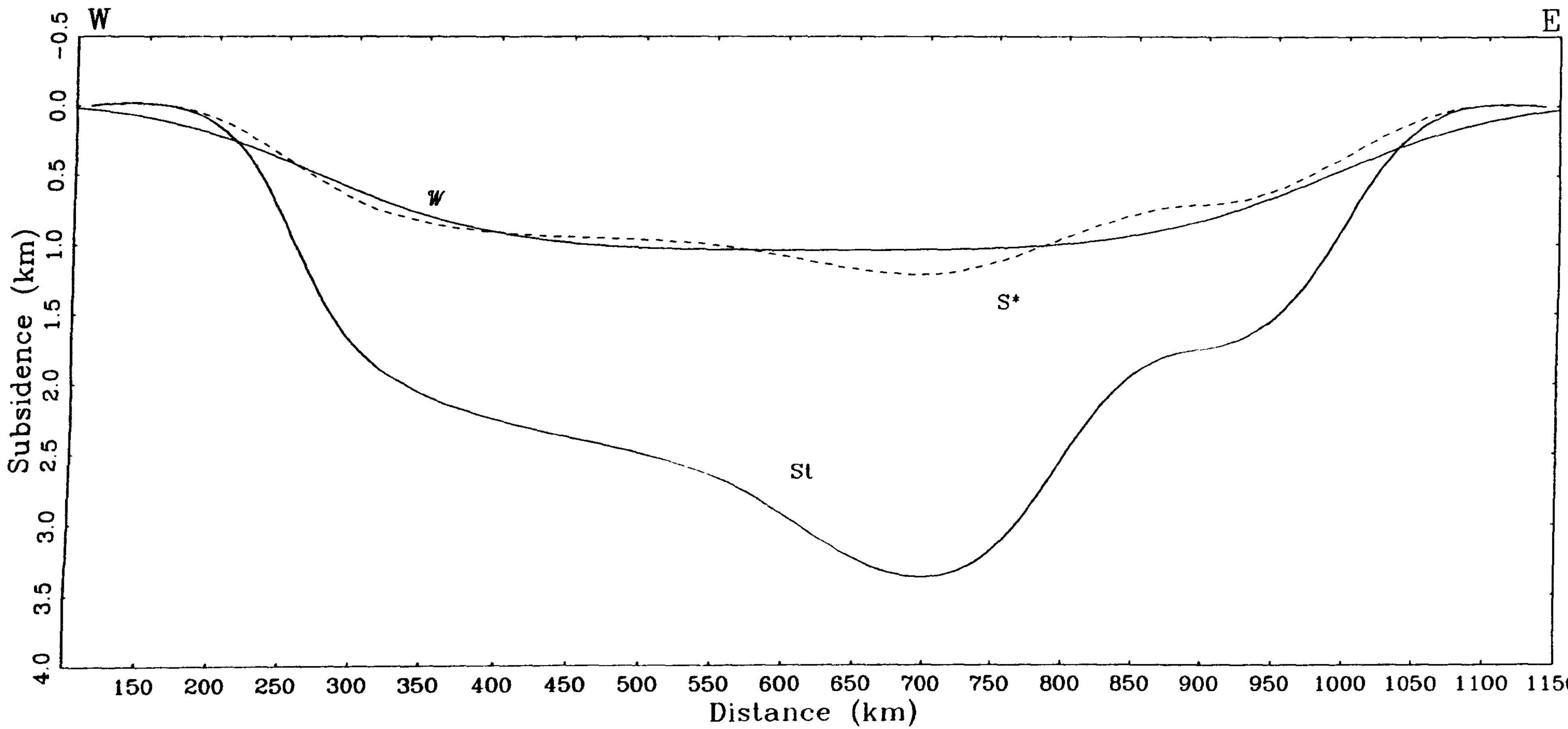

Fig. 5.17 West-East profile across the Parnaíba Basin showing present-day total (S_t) and tectonic (S^* - dashed) subsidences. Also shown is the predicted (W) subsidence curve due to an axisymmetric load.

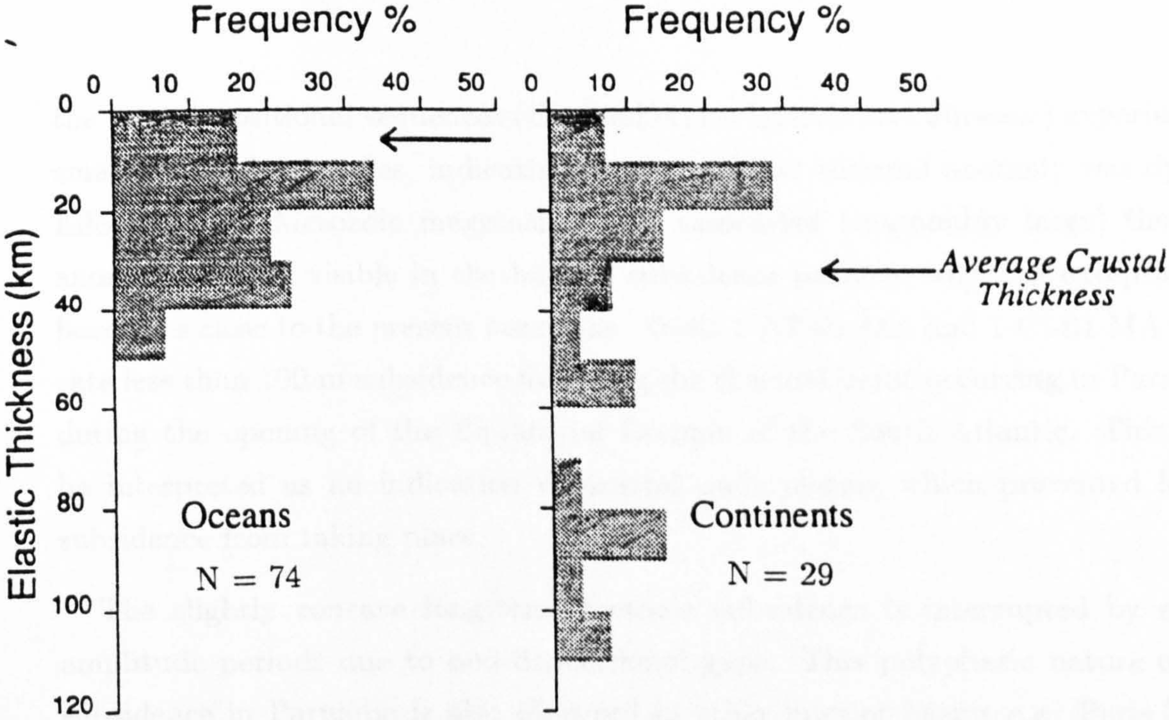

Fig. 5.18 Frequency plot of oceanic and continental estimates of the elastic thickness of the lithosphere. All loads are considered to be older than 10^4 years to sample the long-term mechanical properties of the lithosphere (modified from Watts, 1992).

the observed subsidence curves were obtained using the general chrono-lithostratigraphic column for Parnaíba and decompacting sediments under Airy isostasy assumption. The backstripping algorithm developed takes into account **i** the sediment compaction through an exponential dependence of rock porosity on depth; **ii** erosion estimates by computing a local erosion rate; and **iii** the removal of thicknesses of intruded volcanics from the stratigraphic column. Flexural backstripping was not considered due to the expected low lithospheric flexural ridigity and the large dimensions of the basin. Better spatial and temporal knowledge of the regional erosional mechanism which affected Parnaíba will obviously improve the present subsidence estimates.

The backstripping diagrams show the strong influence of the sediment load since the onset of regional subsidence in the basin. The general geohistory of Parnaíba shows a quiescent Silurian sedimentation often followed by up to twice as large Devonian subsidence. After the basinal exposure in the Lower Carboniferous, the next depositional sequences (Carboniferous-Triassic and Jurassic) experienced smaller subsidence rates, indicating that the initial thermal anomaly was dying. Effects of the Mesozoic magmatism and associated (reasonably large) thermal anomaly are not visible in the basinal subsidence pattern, with the exception of boreholes close to the present coast line. Wells 1-AT-01-MA and 1-CI-01-MA indicate less than 100 m subsidence following the thermal input occurring in Parnaíba during the opening of the Equatorial Domain of the South Atlantic. This may be interpreted as an indication of crustal underplating which prevented larger subsidence from taking place.

The slightly concave long-term tectonic subsidence is interrupted by short-amplitude periods due to non-depositional gaps. This polyphasic nature of the subsidence in Parnaíba is also observed in other interior basins *e.g.* Paris Basin (Loup & Wildi, 1994) and in the Michigan basin (Nunn *et al.*, 1984).

The geological record shows that the Transbrasiliano Lineament and other fault systems were active during the entire development of Parnaíba. Therefore, the regional subsidence should be understood as resulting from intermittent distensional pulses occurring in the region since (at least) the Upper Proterozoic up to the Upper Ordovician. Extension was prevalent up to the Mesozoic when the pattern became disrupted due to the opening of the Equatorial Domain of the South Atlantic Ocean.

Estimates of crust/lithosphere attenuation using the simple uniform stretching model (McKenzie) had to be abandoned due to failure of the model to adequately predict the observed tectonic subsidence. Modelled syn-rift subsidences and stretch rates (β) were excessive as a result of model inadequacies. The application of the Royden & Keen two-layer extension model, although still a simple working hypothesis, allowed estimation of lithosphere attenuation values on a regional basis and it appears that larger stretching values are close to the main inferred extension zones. Note that the three largest attenuation values found are for wells in between the graben structures, therefore being the most affected by the extensional regime. Also, these wells are located on a gravity high of the Bouguer map, consistent with the proposed situation of being closer to the anomalous (denser) crustal material.

A single stretching event was used in the modelling of basin subsidence that started possibly at 450 $\pm$ 5 Ma. Although the tectonic subsidence curves (in particular those for wells 1-PA-01-MA, 2-BAC-01-MA and 2-CP-01-MA) might suggest another stretching event at about 390 $\pm$ 10 Ma, the present resolution of the litho-chronostratigraphic column casts doubt on the mere superimposition of two theoretical curves. Other cratonic basins display a similar variable subsidence pattern *e.g.* the Paris Basin (Loup & Wildi, 1994), often interpreted as changes in the regional stress field or the thermal regime affecting the basin.

For the contemporaneous Middle Amazon Basin, Nunn & Aires (1988) proposed a second rifting/intrusion event in their explanation of Palaeozoic subsidence. Their suggestion was mostly based on the rapid cumulative subsidence in Upper Carboniferous-Permian observed at the centre of the Middle Amazon Basin, a feature not found at Parnaíba. However, their study did not correct for sediment load and compaction as has been done here. Fig. 5.7 shows that the backstripped curves do not demonstrate this second, rapid tectonic subsidence and a second rifting/intrusion event is not well defined to model the regional basin subsidence. Most of the Devonian accelerated subsidence can be accounted for by the sediment loading. Nunn (1994) proposed free convection of fluids in upper crust rocks as the cause of short-lived ($\sim$ 5 Myr) thermal anomaly in the overlaying sediments. Renewed subsidence could be induced in intracratonic basins provided basement rocks are sufficiently permeable and basinal sediments are underlain by a large igneous body. None of these assumptions have been confirmed for Parnaíba.

A further refinement to the Royden-Keen model is *continuous stretching with depth* (Rowley & Sahagian, 1986), which considers lithospheric extension being depth-dependent. This model removes the following objections related to the discontinuous non-uniform mechanism:

- the existence of an intralithospheric discontinuity region where the crust is effectively decoupled from subcrustal lithosphere; and
- a mechanism capable of detaching and stretching the subcrustal lithosphere by a different amount to the overlying crust.

Other postulated initiation mechanisms e.g. deep crustal metamorphism (Middleton, 1980) or small-scale convective downwelling in the mantle (Middleton,

1989) were considered not applicable to Parnaíba, given the geological boundary conditions known either at the surface or through the exploration boreholes.

Total and tectonic subsidence profiles across the basin show the quiescent thermal phase sedimentation with a slight change of the depocentre towards west after the first depositional cycle. The tectonic subsidence was reasonably modelled by an axisymmetric subsurface load at the Moho interface. The flexural ridigity was taken as constant in time and space, given the regional interpretation sought as well as the less complicated mathematical details required. The estimated elastic thickness of 32 km is similar to the 30-35 km estimated by Oliveira (1989) for the Paraná Basin. These low elastic thicknesses are characteristic of basins which underwent a strong thermal anomaly (Watts, 1992; Sahagian, 1994). The lithosphere presents a rather complex rheology but it is believed that the upper, cooler portions at temperatures below 450°C are stiffer than the lower portions. The elastic-ductile transition varies with composition and has been determined as 350°C for quartz and 550°C for olivine rheologies. The continental lithosphere evolves as if its olivine-dominated mantle thickens, from an elastic thickness defined by 350°C to one defined by 550°C (Kusznir & Karner, 1985; Sahagian & Holland, 1993). A constant, intermediate value of 450°C is often used since it seems to be a reasonable approximation for the continental lithosphere *e.g.* Watts *et al.* (1982).

A thin plate elastic rheology for the lithosphere with amplification of subsidence by sediment loading was considered. Given the present limitations of the data sources and the good correlation between the tectonic subsidence profile and the curve predicted by the axisymmetric model, it seems to be premature to consider more complex rheologies.

CHAPTER 6

DISCUSSION AND CONCLUSIONS

6.1 Gravity Modelling

The present gravity coverage, although not evenly distributed, allowed obtaining the first gravity anomaly maps of the Parnaíba Basin. Elongated gravity lows associated with thicker accumulation of sediments along the Transbrasiliano Lineament and NNW-SSE grabens are clearly seen in the Bouguer map. These features were not previously detected. Contrary to what might be expected for a Palaeozoic, aseismic basin in clear isostatic equilibrium, the free-air map consistently shows negative anomalies ranging from -10 to -30 mGal, which has been interpreted as an indication that Airy isostasy due to simple crustal thinning should not be a model applicable to Parnaíba.

Subsequent gravity analysis exploring the basin geometry suggested the existence of a zone located at the lowermost crust-uppermost mantle where normal lower crust has been replaced/intruded by denser, mantle-differentiated material. In contrast to a normal lower crust density of 2,800 kg m^{-3}, an average density of 2,900 kg m^{-3} has been assigned to this altered material. This is geochemically feasible (Cox, 1980) for rocks at the base of the crust contaminated with mantle material. Figure 6.1 presents a NW-SE gravity profile across the Parnaíba Basin and the proposed geological model. There is general agreement between observed and modelled Bouguer anomalies and the predicted free-air anomalies are compatible with the isostatic equilibrium situation of Parnaíba.

According to this regional gravity model a maximum thickness of ~13.5 km of anomalous crust should be occurring beneath the basin depocentre. Further analysis, involving the separation of the Bouguer field into regional and residual components, led to the construction of regional, resultant and residual anomaly maps. Despite several gaps in the gravity data set used, the regional map correctly shows gradual crustal thickening towards the São Francisco Craton and crustal thinning towards the continental plate margin. A slight increase in the depth to the Moho is seen at the centre of the basin with a gravity expression of ~5

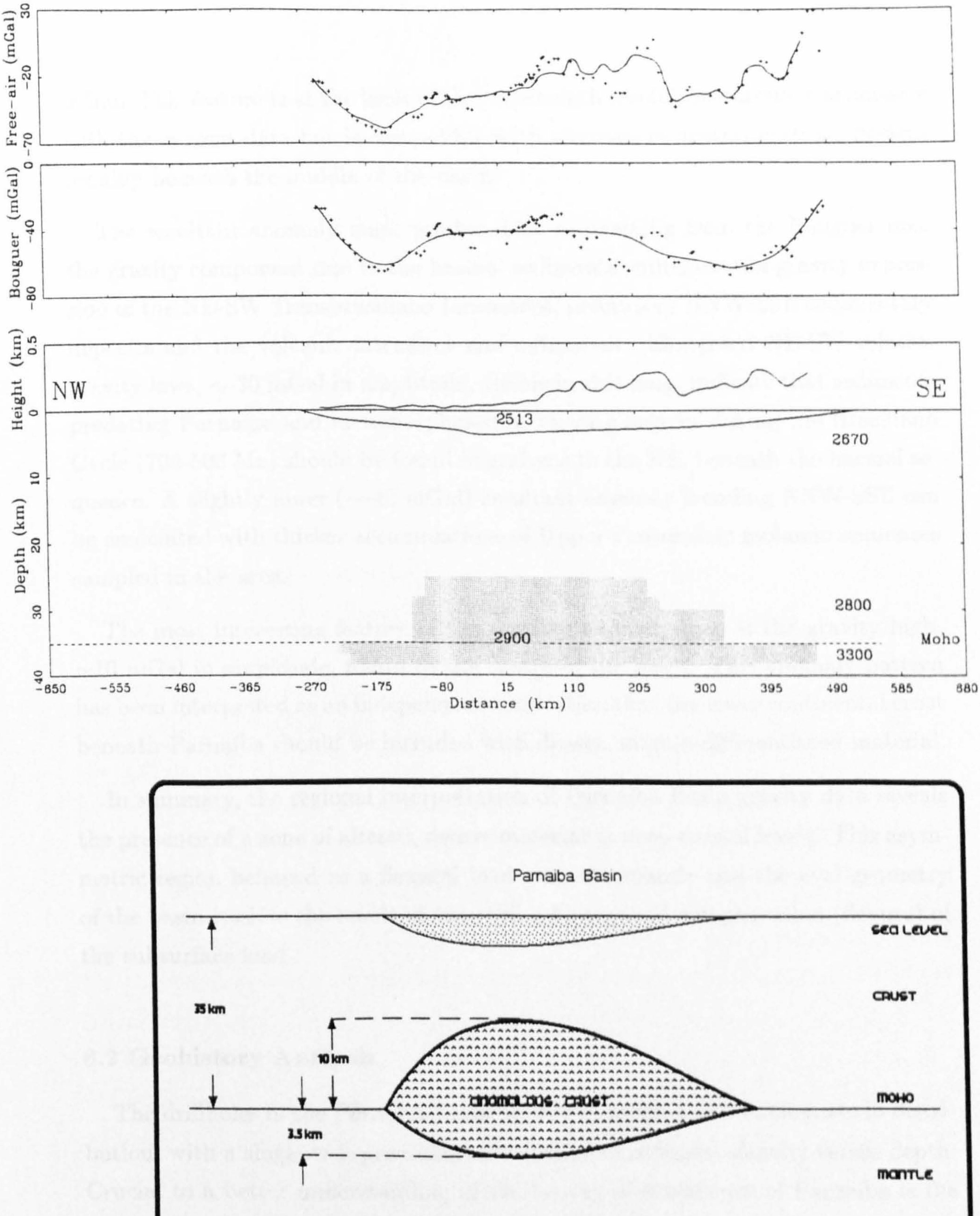

Fig. 6.1 Proposed gravity (top) and geological (bottom) models for the Parnaíba Basin. The continuous lines are the model-predicted gravity anomalies and the scattered crosses are the observed anomalies. Two loads have been considered: **i** the basinal sediments with mean density contrast of -157 kg m^{-3} (but nearly continuous compaction has been taken into account) and **ii** a subsurface load consisting of anomalous crust of intermediate density between normal lower crust and mantle.

mGal. This feature is at the limit of the wavelength resolution currently attainable with the current data but is compatible with a remanent central cratonic nucleus roughly beneath the middle of the basin.

The resultant anomaly map, produced by subtracting from the Bouguer map the gravity component due to the basinal sediments, enhances the gravity expression of the NE-SW Transbrasiliano Lineament, precursory NNW-SSE sedimentary deposits and the volcanic intrusives and extrusives. Elongated NE-SW relative gravity lows, ~-30 mGal in amplitude, visible in this map, indicate that sediments predating Parnaíba and metamorphosed in varying degrees during the Brasiliano Cycle (700-500 Ma) should be found in grabens to the NE, beneath the basinal sequence. A slightly lower (~-40 mGal) resultant anomaly trending NNW-SSE can be associated with thicker accumulations of Upper Proterozoic molassic sequences sampled in the area.

The most interesting feature of the residual anomaly map is the gravity high, ~10 mGal in amplitude, found to the centre of the basin. This anomaly pattern has been interpreted as an independent verification that the lower continental crust beneath Parnaíba should be intruded with denser, mantle-differentiated material.

In summary, the regional interpretation of Parnaíba Basin gravity data reveals the presence of a zone of altered, denser material at deep crustal levels. This asymmetric region behaved as a flexural load onto the mantle and the oval geometry of the basin itself is the result of smoothing by regional compensation (flexure) of the subsurface load.

6.2 Geohistory Analysis

The drillholes in the Parnaíba basin are few in number and inadequate in distribution, with a single well providing information of sediment density versus depth. Crucial to a better understanding of the history of subsidence of Parnaíba is the refinement of its chrono-lithostratigraphic column and boreholes more regularly distributed.

The present assessment of the geohistory of the Parnaíba Basin shows a quiescent sedimentation process in all 22 exploration boreholes analyzed. Both total and tectonic rates were low to moderate throughout its long history, never being larger than 43 m Myr^{-1} and 15 m Myr^{-1}, respectively. A slight, episodic acceleration in the Devonian can be mostly accounted for by the sediment load amplification of subsidence. The other large Brazilian intracratonic basins (Amazon and Paraná) show larger accumulation rates throughout the Phanerozoic. Typical decompacted sediment and backstripped curves are shown in Fig. 6.2 for well 2-CP-01-MA, the deepest well in the basin, close to the present depocentre. Regional uncomformities have been mapped in Parnaíba. Non-depositional gaps lasting for many millions of years have been recognized at **i** the end of the Silurian (~410-385 Ma); **ii** the Lower Carboniferous (~350-310 Ma); **iii** the Lower Triassic (~245-215 Ma); **iv** the Middle Jurassic (~184-180 Ma); **v** the Upper Jurassic-Lower Cretaceous (~155-140 Ma); and **vi** from ~100 Ma to the present. These gaps have been taken into account in the backstripping.

The geological evidence found in the basin, in its metamorphic and sedimentary basement rocks and in adjacent terranes suggest an extensional regime associated with a thermal origin as the basin-forming mechanism of Parnaíba. It may also be considered that **i** the late stages of the Brasiliano Cycle were characterized by regional thermal metamorphism in the basinal area, reaching granulite facies to the east and southeast; **ii** the long-term evolution of the basin is compatible with a thermal input event due to extension; and **iii** a large thermal anomaly again affected most of the basin from the Lower Jurassic to Lower Cretaceous, at the time of the South Atlantic opening.

The geological and geophysical evidence indicate the adequacy of an extensional mechanism initiating the regional subsidence. Uniform lithospheric stretching (McKenzie's model) was discarded as a viable process given the exaggerated predicted syn-rift subsidence. No boreholes showed a subsidence pattern compatible with this model. An alternative model was used instead: the two-layer extensional model (Royden-Keen), which accounts for the different rheological properties of the continental crust and subcrustal lithosphere, thus allowing for different stretch rates. The Royden-Keen model befits the estimated tectonic subsidence curves in all wells, considering a single stretching event at 450 $\pm$ 5 Ma.

Crustal and subcrustal lithosphere stretch rates were low throughout the entire basinal development, with maximum values of 18% for the first and 36% for

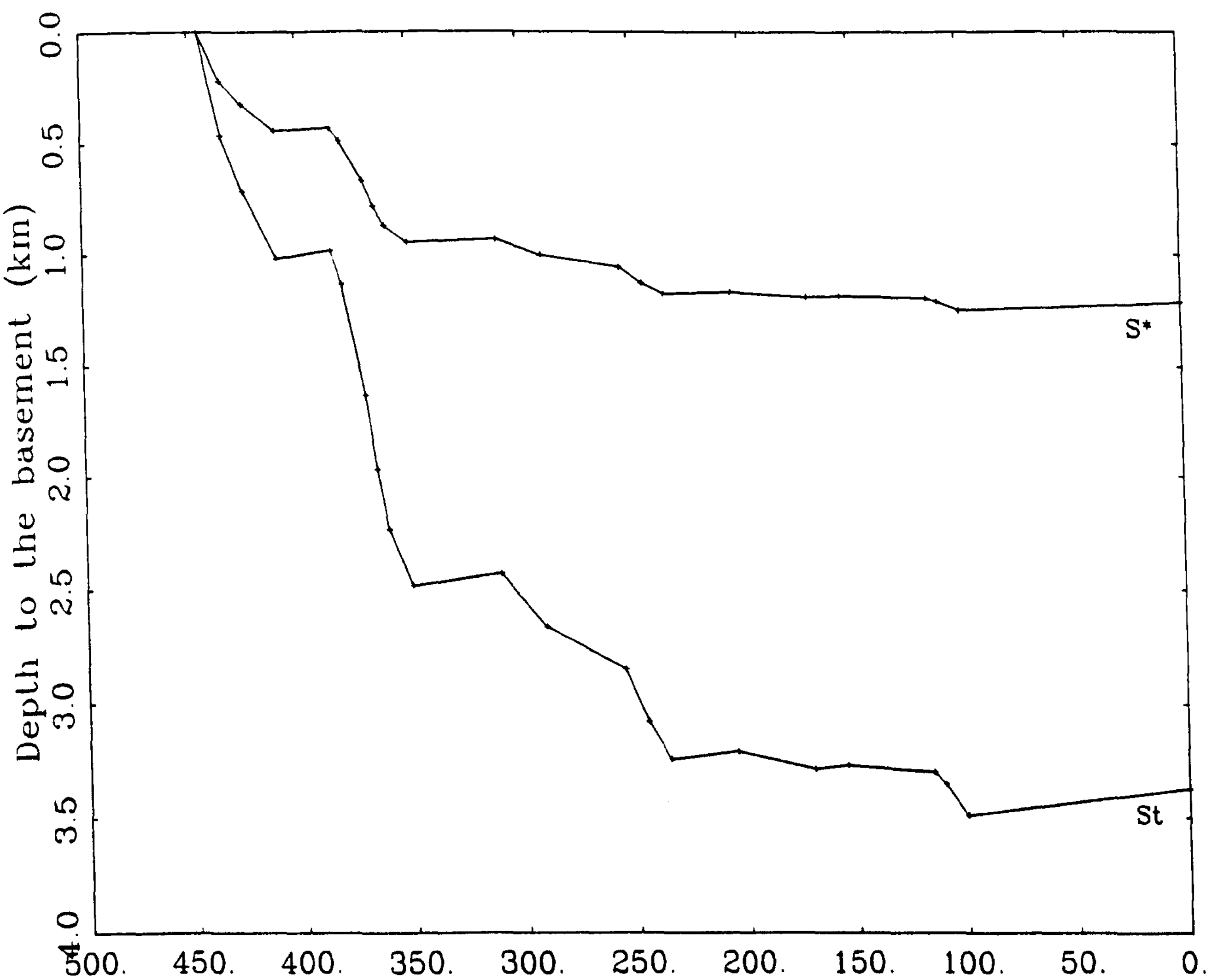

Backstripping curves for well CP-01 (44.3W, 4.8S).

Fig. 6.2 Decompacted sediment (S_t) and backstripped (S^*) curves for well 2-CP-01-MA, close to the depocentre. Most of the subsidence is due to the sediment load and the long-term tectonic subsidence is disturbed by non-depositional gaps.

the latter. Total and purely tectonic subsidence profiles across the basin suggest the earlier influence of crustal weakness zones parallel or subparallel to the Transbrasiliano Lineament, shortly followed by other extension zones.

Considering an elastic rheology for the lithosphere, a regional W-E tectonic subsidence profile could be reproduced employing an axisymmetric subsurface load. Being aware that ridigity estimates using a constant ridigity plate are only a first-order approximation, the best iterative solution yielded an effective flexural ridigity $D = 0.2 \times 10^{24}$ N m for the lithospheric plate. The low equivalent elastic thickness $T_e = 32$ km is compatible with a thermally affected continental lithosphere and similar to the range of 30-35 km estimated for the Paraná Basin by Oliveira (1989). Computation of the compensation coefficient gave $C = 0.98$ confirming that the local isostatic model used in the backstripping and thermo-mechanical studies was appropriate. A graphical comparison of the elastic thickness estimate of the present study with other flexural sites is seen in Fig. 6.3 (modified from Willet *et al.*, 1985). It is assumed the T_e estimate for Parnaíba varies in the range 30-35 km and the average heat flow of 62 ± 14 mW m^{-2} was taken from Pereira & Hamza (1991).

The low elastic thickness has been interpreted as due to the inability of the continental lithosphere to recover its ridigity after a thermal stress phase (Watts, 1992). The low T_e value is often taken as an indicator of a sedimentary basin developed on a stretched lithosphere.

In the Upper Cretaceous the Parnaíba Basin locked and stopped subsiding. Rifting followed by rapid sedimentation started in the neighbouring offshore basins *e.g.* Barreirinhas and São Luís Basins and, by the time these newly-formed basins entered their drift phase, Parnaíba was definitely exposed and erosion restarted. The lack of post-Cretaceous subsidence is also observed in the other large intracratonic Palaeozoic basins of Brazil.

The injection of volcanics in the basin at the time of the South Atlantic opening, although associated with extensional stresses, did not reactivate the tectonic subsidence, perhaps due to crustal underplating. There is petrological and geochemical evidence that parental picritic magmas derived from the mantle very rarely reach the surface in extensional areas. Cox (1980) suggested that basaltic

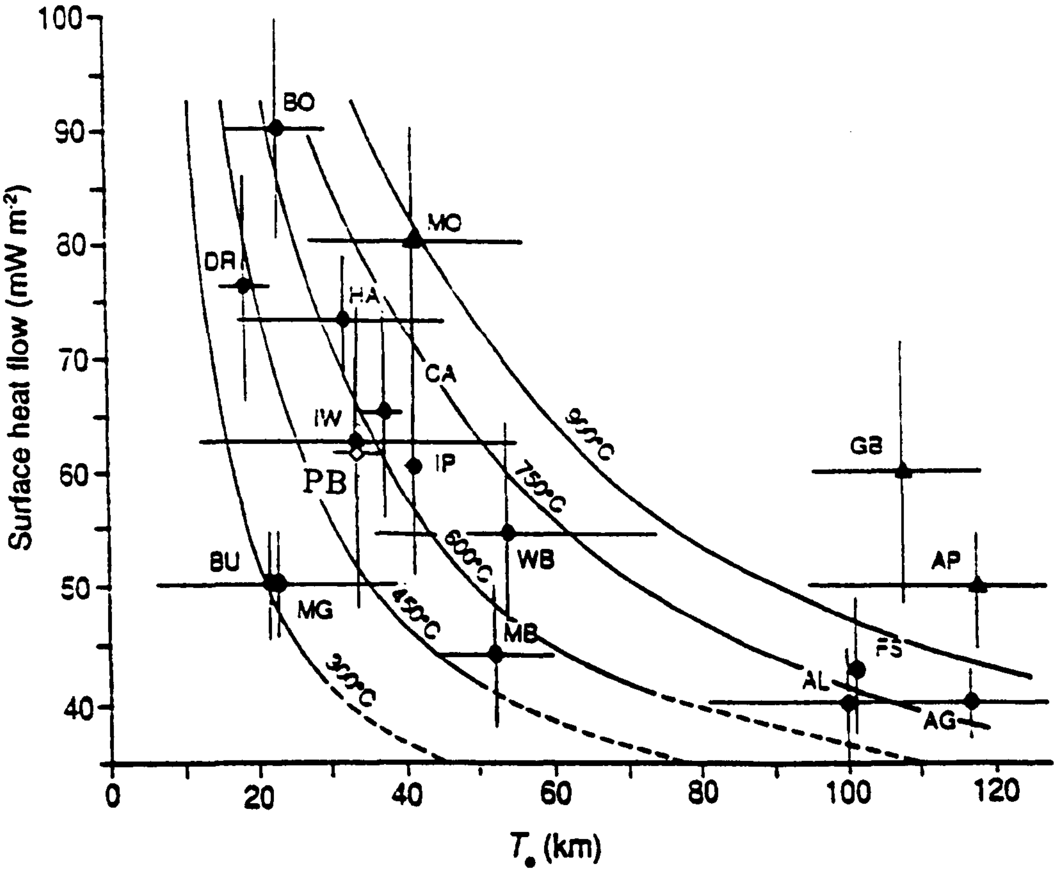

Fig. 6.3 Plot of the equivalent elastic thickness versus surface heat flow for a number of sites of flexure. The continuous curves indicate depths to isotherms at a given surface heat flow for a steady-state thermal model. It is seen the wide range in temperature (300^0C to > 900^0C) for the base of the elastic lithosphere. Flexure sites: AG - Lake Agassis, AL - Lake Algonquin, AP - Appalachian Foreland Basin, BO - Lake Bonneville, BU - Boothnia Uplift, CA - Caribou Mountains, DR - North Great Dividing Range, FS - Fennoscandia, GB - Ganges Basin, HA - Lake Hamilton, IP - Interior Plains, IW - Idaho-Wyoming Thrust Belt, MB - Michigan Basin, MG - Midcontinent Gravity High, MO - Molasse Basin, PB - Parnaíba Basin, WB - Williston Basin (modified from Willet *et al.*, 1985).

material should be trapped/intruded in the lower crust. Picritic magmas in the base of the crust or intruded as sills in the lower crust would differentiate into ultramafic cumulates and low-Mg basalts that could be then brought up to the surface.

6.3 Integrated Geophysical Modelling

The confident interpretation of the history of the Parnaíba Basin requires a better gravity and chrono-lithostratigraphic data sets than what is currently available. The geological evidence, the Bouguer and free-air gravity *anomalies* and the geohistory analysis are in favour of an extensional mechanism to initiate the subsidence of the Parnaíba Basin. This was possibly a tectonic response to a global process.

Two periods in the Earth history have been recognized as important for the initiation of intracratonic basins: the Upper Precambrian-Lower Palaeozoic (~590-500 Ma) and the Lower Jurassic-Lower Cretaceous (~180-100 Ma). Both periods are associated with the break-up of supercontinental assemblies. Palaeozoic examples come from North America (Hudson Bay, Illinois, Michigan and Williston), South America (Amazon, Parnaíba and Paraná) and Australia (Bonaparte, Ord, Warburton and Wiso). Mesozoic examples are the cratonic basins of NW Europe (North Sea and Paris - Permo-Triassic?) and Africa (Chad and Iullmedden). Sometimes, older, Upper Proterozoic basins are known to have experienced further subsidence either in the Upper Precambrian (Amadeus, Georgina, Ngalia and Officer Basins in Australia) or in the Upper Jurassic (Taoudeni and Congo Basins in Africa).

Some intracratonic basins have been observed to have their depocentres developed a few hundreds of kilometres from the present-day coastline (Hartley & Allen, 1994). The present depocentre of Parnaíba is within ~400 km of the coast and the basin itself is clearly linked to the South American plate margin by a failed rift arm *(aulacogen)* trending at a high angle to the regional strike of the margin. De Brito Neves *et al.* (1984) note that for about two thirds of their lengths the present coastlines of Brazil and Africa follow ancient basement structures. For the remaining segments e.g. the northeast Brazil, where the coast cuts across the

Precambrian trend, transverse features within the basins are common and affect the sedimentation history of the marginal basins.

The prolonged development of Parnaíba, when compared to the two other large intracratonic Brazilian basins, shows overall similar sedimentation histories with minor differences caused by changes in the tectonic regime affecting each basin individually at a certain time of its evolution and local changes in the sediment supply. The Amazon Basin lacks the (modest) Jurassic depositional sequences found in Parnaíba and Paraná.

Sandstones are the dominant lithology in all three basins and, although Mesozoic magmatism is also a common feature, the massive volcanism is unique to the Paraná Basin. The Parnaíba basalts show mineralogical and chemical similarities to the equivalent extrusives of Paraná: the older Mosquito basalts correspond chemically to the low Ti-type, tholeiitic basalts found in southern Paraná whereas the younger Sardinha basalts are similar to those of high Ti-type of northern Paraná.

The characteristic oval shape of Parnaíba is not reflected in the Bouguer map. The gravity lows trending NE-SW and NNW-SSE help identify ancient crustal weakness zones which controlled basinal evolution. A pronounced gravity high on the basin depocentre is not observed, in contrast to the Middle Amazon Basin, where a chain of gravity highs transects the basin roughly coincident with the axis of maximum deposition. A sequence of NNE-SSW trending gravity highs localized over and along the Paraná River is coincident with the maximum depths to the basement and thicknesses of basaltic rocks. Similar to Parnaíba, the free-air map of the Paraná Basin also shows negative anomalies, demonstrating that simple Airy isostasy is not followed in both basins. Continental underplating or passive upwelling of partial melt resulting in intrusion/partial replacement of the lower crust by mantle-differentiated material is a mechanism capable to explain the regional pattern of gravity anomalies over the Middle Amazon and Northern Paraná Basins (Nunn & Aires, 1988; Molina *et al.* 1989). The downward deflection of the Moho caused by the subsurface load produces a regional negative free-air anomaly within the basins and accounts for the drop in the Bouguer anomalies towards the basins, even after correcting for the gravity component due to the low-density sediments infill.

The comparative geohistory of the Amazon, Parnaíba and Paraná Basins shows a consistent pattern of subsidence initiated in the Lower Ordovician-Lower Silurian up to the Middle-Upper Cretaceous. Several non-depositional gaps which lasted for tens of million years are found in the stratigraphic record of all three basins with roughly synchronous changes in sediment volume. However, a few contrasts should be noticed. The gently dipping sediments of Parnaíba were slowly deposited with an episodic larger rate in the Devonian. The Devonian depositional acceleration is observed neither in the Middle Amazon nor in the Paraná Basins. In contrast, the Amazon and Paraná had large depositional rates in the Carboniferous-Permian which were not matched in Parnaíba. The sediment contribution to the total subsidence in Parnaíba is about the same as estimated for the Paraná Basin (Quintas, 1995). However, total and tectonic subsidence rates in Paraná were computed assuming that three extensional pulses occurred at 440, 296 and 144 Ma, while the subsidence curves for Parnaíba do not indicate any renewed subsidence mechanism apart from the Devonian acceleration. Nunn & Aires (1988) proposed that rapid subsidence pulses might be due to lithospheric relaxation, horizontal buckling or another rifting/intrusion event.

Given the present chrono-lithostratigraphic data, it is noticeable that regional subsidence in the Parnaíba Basin iniated (at least) ~60 Myr after tectonic activity in the adjacent mobile belts had come to an end with the last pulses of the Brasiliano Cycle. Having the observations above in mind and using all available data, an integrated interpretation of the gravity anomalies and tectonic subsidence as *observed today* suggest the simplest explanation for the Phanerozoic development of the Parnaíba Basin is:

1 Following the break-up of a supercontinent in the Upper Precambrian-Lower Palaeozoic, a rifting zone trending NE-SW starts developing. The lithosphere had been thermally weakened during the last stages of the Brasiliano Cycle, at Cambro-Ordovician times. Restricted extension and fissural volcanism occurred in these grabens. Rifting ceases and rift flanks are eroded for about 50-55 Myr. Conglomeratic and coarse-grained (proximal) sediments infill the grabens. With time, progressively pelitic facies (distal) top up the sequence known as the Mirador Formation;

2 A renewed, broad thermal anomaly regionally affects the area and induces regional uplift in the Upper Ordovician. Small extension pulses occur along the already defined NNE-SSW trend and, shortly after, along an approximately orthogonal NW-SE trend. The Silurian sedimentation (the Serra Grande Group) is deposited preferably along these trends. No volcanism happens this time and basaltic partial melts starts intruding the lower crust. The newly-formed basin enters a thermal phase and deposited sediments flexurally uplift the margins. As result of the Caledonian Orogeny and maybe due to another thermal pulse the basin is exposed and a non-depositional gap lasts for ~25 Myr. Subaerial erosion follows;

3 Glacial conditions prevail. Renewed extension occurs and ancient, Upper Proterozoic grabens trending NW-SE are reactivated. Diffuse spreading centres are found in the basin. An open sea environment is established and Devonian marine deposits of the Canindé Group fill the basin. Coeval with the Hercynian Orogeny the basin is gradually uplifted and eventually exposed. Erosion occurs for approximately 40 Myr and is accompanied by dramatic climate changes;

4 After (extensional) stress relaxation the basin could subside thermally from the Upper Carboniferous to the Lower Triassic. Continental deposition under hot climate conditions characterize the rocks of the Balsas Group. Anhydrite is sometimes found. The remanent, epicontinental sea progressively retreats and desert conditions were established in Parnaíba. The basin is regionally uplifted due to the South Atlantic opening and erosion occurs for ~30 Myr;

5 The first signs of magmatism in the basin happen in the Lower Jurassic and the main feeders are along preexisting fractures in the basement. The basalts of the Mosquito Formation and associated intrusives do not show significant crustal contamination and are characterized by low TiO_2 and incompatible element contents. These extrusives were eroded for about 4 Myr and are similar to the southern Paraná Basin basalts;

6 Relaxation of the first extensional pulse allows a small transgressive-regressive cycle in the Middle Jurassic. The basin is again uplifted and the sea retreats definitely from the Parnaíba Basin. Erosion follows for about 15 Myr;

7 Restricted magmatism occurs in the central parts of the basin in the Lower Cretaceous. The Sardinha basalts and intrusives have high TiO_2 and incompatible element contents. The appreciable crustal contamination of these volcanics supports the gravity interpretation that the lower crust was progressively intruded/replaced by mantle-differentiated material;

8 After the lithosphere cools down, there is no appreciable subsidence with the exception of its northern tip, where a rift flank developed and was eroded. Isostatic reequilibration brings this part of the basin to a lower level with the restricted sedimentation of the Itapecuru Formation taking place in the Middle Cretaceous;

9 Finally, sedimentation is transferred to the NE coast where complete oceanization occurs. Some tectonism (mainly transcurrent faulting) affects the northern Parnaíba Basin. The evolutionary cycle ends in the Upper Cretaceous and erosion has been occurring ever since.

6.4 Suggestions for Future Work

A deep seismic survey across the Parnaíba Basin, preferably crossing its depocentre in the NW-SE direction would show the extent and depth of syn-rift sediments in the precursory grabens and provide direct assessment of the Moho topography. A better gravity coverage including the adjacent areas would greatly improve the present regional interpretation. Coherence estimate studies could be carried out to obtain an independent estimate of the elastic thickness of the lithosphere. Accurate separation of high- and low-frequency components of the magnetic anomalies in the basin would help identify dykes and probable feeders associated with fractures zones in the crust.

REFERENCES

ABRAMOWITZ, M. and Stegun, I. A. (1965), "Handbook of mathematical functions: With formulas, graphs and mathematical tables", *Dover Publishers, New York*, 104pp.

ALLEN, P. A. and Allen, J. R. (1990), "Basin analysis: Principles and applications", *Blackwell Scientific Publications, Oxford*, 451pp.

ATHY, L. F. (1930), "Density, porosity and compaction of sedimentary rocks", *Bull. Am. Ass. Petrol. Geol.*, **14:** 1-24.

AUDET, D. M. and McKonell, J. D. C. (1992), "Forward modelling of porosity and pore pressure evolution in sedimentary basins", *Basin Res.*, **4:** 147-162.

BALCH, S. J., and Thompson, G. T. (1989), "An efficient algorithm for polynomial surface fitting", *Comp. & Geosci.*, **15(1):** 107-119.

BALLY, A. W. and Snelson, S. (1980), "Realms of subsidence", *Can. Soc. Petr. Geol., Mem. Number 6*, 9-24.

BARANOV, W. (1975), "Potential fields and their transformations in applied geophysics", *Geoexploration Monographs Series 1 - Number 6, Berlin*, 121pp.

BARRODALE, I. and Young, A. (1966), "Algorithms for best L_1 and L_∞ linear approximation in a discrete set", *Num. Math.*, **8:** 295-306.

BAUMONT, C. (1981), "Foreland basins", *Geophys. J. Royal Astron. Soc.*, **65:** 291-329.

BELLIENI, G., Piccirillo, E. M., Cavazzini, G., Petrini, R., Chomin-Chiaramonti, P., Nardy, A. J. R., Civetta, L., Melfi, A. J., and Zantedeschi, P. (1990), "Low- and high-TiO_2 Mesozoic tholeiitic magmatism of the Maranhão Basin (NE-Brazil): K/Ar age, geochemistry, petrology, isotope characteristics and relationships with Mesozoic low- and high-TiO_2 flood basalts of the Paranà Basin (SE-Brazil)", *Neues Jahrb. Mineral., Abh.*, **162:** 1-33.

BELLIENI, G., Macedo, M. H. F., Petrini, R., Piccirillo, E. M., Cavazzini, G., Chomin-Chiaramonti, P., Ernesto, M., Macedo, J. W. P., Martins, G., Melfi, A. J., Pacca, I. G. and De Min, A. (1992), "Evidence of magmatic activity related to Middle Jurassic and Lower Cretaceous rifting from northeastern Brazil (Ceará-Mirim): K/Ar age, palaeomagnetism, petrology and Sr-Nd isotope characteristics", *Chem. Geol.*, **97:** 9-32.

BELTRÃO, J. F., Silva, J. B. C. and Costa, J. C. (1991), "Robust polynomial fitting method for regional gravity estimation", *Geophys.*, **56(1):** 80-89.

BOND, G. C., Nickeson, P. A. and Kominz, M. (1984), "Break-up of a supercontinent between 625 Ma and 555 Ma: New evidence and implications for continental histories", *Earth Planet. Sci. Lett.*, **70:** 325-345.

BRUNET, M. and Le Pichon, X. (1982), "Subsidence of the Paris Basin", *J. Geophys. Res.*, **87:** 8547-8560.

BROTCHIE, J. F. and Silvester, R. (1969), "Crustal flexure", *J. Geophys. Res.*, **74:** 5240-5252.

BUCK, W. R. and Mutter, J. C. (1987), "Convection and density changes due to partial melting: Relation to passive margin volcanism", *Eos Tras. AGU*, **68:** 414.

CAPUTO, M. V. and Lima, E. C. (1984), "Estratigrafia, idade e correlação do Grupo Serra Grande", *Annals of the XXXIII Congresso Brasileiro de Geologia*, **2:** 740-759.

CLAERBOUT, J. F. and Muir, F. (1973), "Robust modelling with erratic data", *Geophys.*, **38:** 826-844.

CORDANI, U. G., Neves, B. B.de B., Fucks, R. A., Porto, R., Thomaz Fº, A. e Cunha, F. M. B. (1984), "Estudo preliminar do Pré-Cambriano com os eventos tectônicos das bacias sedimentares brasileiras", *Ciênc. Téc. Petr., PETROBRÁS*, **15,** 70pp.

COSTA, A. F. U., Chemale, F. Jr., Magro, F., Dias, N. L. (1995), "Modelagem gravimétrica da bacia do Camaquã (RS)", *Annals of V Simpósio Nacional de Estudos Tectônicos, Gramado*, **1:** 234-235.

COWIE, P. A. and Karner, G. D. (1990), "Gravity effect of sediment compaction: Examples from the North Sea and Rhine graben", *Earth & Plan. Sci. Lett.*, **99:** 141-153.

COX, K. G. (1980), "A model for flood basalt volcanism", *J. Petrol.*, **21:** 629-650.

CUNHA, F. M. B. (1986), "Evolução paleozóica da bacia do Parnaíba e seu arcabouço tectônico", *MSc. Thesis, Universidade Federal do Rio de Janeiro,*, 106pp.

CUNHA, F. M. B. and Góes, A. M. O. (1989), "Geologia da parte norte da Bacia do Parnaíba", *PETROBRÁS-SIEX Report 130-07044*, 28pp.

DE BRITO NEVES, B. B. (1990), "Processos orogênicos no Pré-Cambriano do Brasil", *In: Origem e evolução de bacias sedimentares (Ed. by G. P. Raja Gabaglia and E. J. Milani, PETROBRÁS, Rio de Janeiro*, 99-114.

DE BRITO NEVES, B. B., Fuck, R. A., Cordani, U. G. and Thomaz, A. (1984), "Influence of basement structures on the evolution of major sedimentary basins of Brazil: A case of tectonic heritage", *J. Geodyn.*, **1:** 495-510.

DE CHARPAL, O., Guenoch, P., Montadert, L. and Roberts, D. G. (1978), "Rifting, crustal attenuation and subsidence in the Bay of Biscay", *Nature*, **275:** 706-711.

DEMIDOVITCH, B. P. and Maron, I. A. (1976), "Computational mathematics", *MIR Publishers, Moscow*, 691pp.

DE RITO, R. F., Cozzarelli, F. A. and Hodge, D. S. (1983), "Mechanism of subsidence of ancient cratonic rift basins", *Tectonophys.*, **94:** 141-168.

DE SÁ, N. C. and Blitzkow, D. (1986), "Uma tentativa de homogeneizar os dados gravimétricos existentes no Brasil", *Rev. Bras. Geofís.*, **4(2):** 73-77.

DE SÁ, N. C., Ussami, N. and Molina, E. C. (1993), "Gravity map of Brazil 1. Representation of free-Air and Bouguer anomalies", *J. Gephys. Res.*, **98(B2):** 2187-2197.

DE SOUSA, M. A. (1983), "Distribuição de elementos traços no perfil Guatá - Bom Jardim da Serra, Formação Serra Geral", *MSc. Thesis, Universidade de São Paulo*, 176pp.

DE SOUSA, M. A. and Moreira, E. M. (1994), "Referring the old gravity network of the National Observatory to the IGSN 71/absolute datum. Part I: The LC & R 61 data set", *Bull. d'Inf. Bureau Gravimetrique International*, **74:** 30-43.

DE SOUSA, M. A. and Seixas, N. A. B. (1995), "GRR - Gravity reduction routines for fieldwork data" (submitted), *Comp. & Geosci.*, 9pp.

DONATO, J. A. and Tully, M. C. (1981), "A regional interpretation of North Sea gravity data", *In: Petroleum Geology of the Continental Shelf of North-West Europe (Ed. by L. V. Illing and G. D. Hobson), London*, 521pp.

DURHEIN, R. J. and Mooney, W. D. (1991), "Archean and proterozoic crustal evolution: Evidence from crustal seismology", *Geology*, **19:** 606-609.

EASON, G., Noble, B. and Sneddon, I. N. (1955), "On certain integrals of Lipschitz-Hankel type involving products of Bessel functions, *Phil. Trans. Royal Soc.*, **247A:** 529-551.

EBONG, M. B. (1981), "A study and analysis of the geodetic levelling of Nigeria", *Ph.D. Thesis, University of Newcastle upon Tyne*, 424pp.

EBONG, M. B. (1985), "The least sum adjustment of a geodetic levelling network", *Manuscr. Geodaet.*, **10:** 33-36.

ECKSTEIN, B. A. (1989), "Evaluation of spline and weighted average interpolation algorithms", *Comp. & Geosci.*, **15(1):** 79-94.

FACHETTI, F. A. (1961), "Levantamento gravimétrico do Maranhão", *PETROBRÁS-SIEX Report 130-01439*, 48pp.

FAIRHEAD, J. D. and Okereke, C. S. (1987), "A regional gravity study of the West African rift system in Nigeria and Cameroon and its tectonic interpretation", *Tectonophys.*, **143:** 141-159.

FAIRHEAD, J. D., Okereke, C. S. and Nnange, J. M. (1991), "Crustal structure of the Mamfe basin, West Africa, based on gravity data", *Tectonophys.*, **186:** 351-358.

FORTES, F. P. (1990), "A matriz Brasiliana e sua cinemática no embasamento do setor sudeste da Bacia do Parnaíba", *PETROBRÁS-SIEX Report 130-07775*, 28pp.

FORTES, F. P. (1992), "Os grabens sigmoidais do sudeste da Bacia do Parnaíba", *PETROBRÁS-SIEX Report 130-08163*, 24pp.

FRIEDINGER, P. J. J. (1988), "BASTA - Subsidence and paleotemperature modeling of rift basins", *Comp. & Geosci.*, **14(4):** 505-526.

FUCHS, H. (1982), "Contributions to the adjustment by minimizing the sum of absolute residuals", *Manuscr. Geodaet.*, **7:** 151-207.

FURLONG, K. P. and Fountain, D. M. (1986), "Continental crust underplating: Thermal considerations and seismic-petrologic consequences", *J. Geophys. Res.*, **91:** 8285-8294.

GAMA, L. I. and Gualda, J. (1968), "Base gravimétrica do Corcovado", *Internal Report Number 1 O.N.-M.E.C.*, 15pp.

GAMA, L. I. (1971), "Valores de gravidade no nordeste e região centro-leste do Brasil", *Internal Report Number 2 O.N.-M.E.C.*, 45pp.

GAMA, L. I. (1972), "Valores da gravidade nas regiões centro e sul do Brasil", *Internal Report Number 4 O.N.-M.E.C.*, 78pp.

GAMA, L. I. (1973), "Extensão da rede do nordeste", *Internal Report Number 6 O.N.-M.E.C.*, 37pp.

GEMAEL, C., Leite, O. H. S., Rosier, F. A., Torge, W., Röder, R. H. and Schnüll M. (1990), "Large-scale absolute gravity controls in Brazil", *In: Gravity, Gradiometry and Gravimetry (Ed. by R. Rummel and R. Hipkin), Springer-Verlag, Berlin*, 181pp.

GIBB, R. A. and Thomas, M. D. (1976), "Gravity signature of fossil plate boundaries in the Canadian Shield", *Nature*, **262:** 199-200.

GIBB, R. A. (1968), "The densities of Precambrian rocks from northern Manitoba", *Can. J. Earth Sci.*, **5** 433-438.

GÓES, A. M. O. (1991), "Relatório de viagem a Teresina - Coletânea de dados de alguns poços perfurados para captação de àguas subterrâneas no Estado do Piauí - Bacia do Parnaíba", *PETROBRÁS-SIEX Report 130-07905*, 18pp.

GÓES, A. M. O. and Feijó, F. J. (1994), "Bacia do Parnaíba", *B. Geoc. PETROBRÁS*, **8(1):** 57-67.

GÓES, A. M. O., Souza, J. M. P. and Teixeira, L. B. (1990), "Estágio exploratório e perspectivas petrolíferas da bacia do Parnaíba", *B. Geoc. PETROBRÁS*, **4(1):** 55-64.

GÓES, A. M. O., Travassos, W. A. and Nunes, K. C. (1993), "Projeto Parnaíba-Reavaliação da bacia e perspectivas exploratórias", *PETROBRÁS-DEXNOR-DINTER*, 97pp.

GUPTA, V. K. and Ramani, N. (1980), "Some aspects of regional-residual separation of gravity anomalies in a Precambrian terrain", *Geophys.*, **45:** 1412-1426.

HACK, B. U. and Van Eysinga, B. U. (1987), "Geological time table", *Fourth edition, revised and enlarged, Elsevier Science Publishers B. V.*, Amsterdam..

HALLS, H. C. (1982), "Crustal thickness in the Lake Superior region", *In: Geology and tectonics of the Lake Superior Basin, Geol. Soc. Am. Mem.*, **156:** 239-245.

HAMZA, V. M. and Muñoz, M. (1996), "Heat flow map of South America", *Geothermics*, **25(6)** , in press..

HAMDANI, Y., Mareschal, J.-C. and Arkani-Hamed, J. (1991), "Phase changes and thermal subsidence in intracontinental sedimentary basins", *Geophys. J. Int.*, **106:** 657-665.

HAQ, B. U., Hardenbol, J. and Vail, P. R. (1987), "Chronology of fluctuating sea levels since the Triassic (250 Myr ago to present)", *Science*, **235:** 1156-1167.

HARLAND, W. B., Armstong, R. L., Cox, A. V., Craig, L. E., Smith, A. G. and Smith, D. G. (1990), "A geologic time scale, 1989", *Cambridge University Press, Cambridge*, 263pp.

HARTLEY, R. W. and Allen, P. A. (1994), "Interior cratonic basins of Africa: Relation to continental break-up and role of mantle convection", *Basin Res.*, **6:** 95-113.

HASUI, Y. (1984), "Província Tocantins, setor setentrional", *In: O Pré-Cambriano do Brasil (Ed. by F. F. M. Almeida and Y. Hasui), Editora Edgard Blücher, São Paulo*, 205-264.

HAXBY, W. F., Turcotte, D. L. and Bird, J.M. (1976), "Thermal and mechanical evolution of the Michigan Basin", *Tectonophys.*, **36:** 57-75.

HELLINGER, S. J. and Sclater, J. G. (1983), "Some comments on two-layer extensional models for the evolution of sedimentary basins", *J. Geophys. Res.*, **88(B10):** 8251-8269.

HINZE, W. J., von Frese, R. R. B., Longacre, M. B., Braile, L. W., Lidiak, E. G. and Keller, G. R. (1982), "Regional magnetic and gravity anomalies of South-America", *Geophys. Res. Lett.*, **9(4):** 314-317.

HODGSON, R. A. (1979), "Precision altimeter survey procedu-res", *American Paulin System, Educational Division*, 59pp.

HURTER, S. J. and Pollack, H. N. (1995), "Effect of the Cretaceous Serra Geral igneous event on the temperatures and heat flow of the Paraná Basin, southern Brazil", *Basin Res.*, **7:** 215-220.

JACOBSEN, B. H. (1987), "A case for upward continuation as a standard separation filter for potential-field maps", *Geophys.*, **52:** 1138-1148.

KARNER, G. D. (1986), "Effects of lithospheric in-plane stress on sedimentary basin stratigraphy", *Tectonics*, **5:** 573-588.

KARNER, G. D. (1993), "The thermal and mechanical response of the continental lithosphere to compressional and extensional forces: Implications for the development of sedimentary basins", *Notes of the Tectonophysics Course, Universidade Federal de Ouro Preto*, 53pp.

KUSZNIR, N. and Karner, G. D. (1985), "Dependence of the flexural ridigity of the continental lithosphere on rheology and temperature", *Nature*, **316:** 138-141.

KLEIN, G.de V. (1991), "Origin and evolution of North American cratonic basins", *S. Afr. J. Geol.*, **94(1):** 3-18.

KLEIN, G.de V. and Hsui, A. T. (1987), "Origin of cratonic basins", *Geology*, **15:** 1094-1098.

KOLATA, D. R. and Nelson, W. J. (1991), "Basin-forming mechanisms of the Illinois Basin", *In: Cratonic Basins (Ed. by M. W. Leighton, D. R. Kolata, D. F. Oltz and J. J. Eidel), Mem. Am. Ass. Petrol. Geol.*, **51:** 729-797.

LAMBECK, K. (1983), "Structure and evolution of the intracratonic basins of central Australia", *Geophys. J. Royal Astron. Soc.*, **74:** 843-886.

LESQUER, A., Beltrão, J. F. and Abreu, F. A. M. (1984), "Proterozoic links between northeastern Brazil and west Africa: A plate tectonic model based on gravity data", *Tectonophys.*, **110:** 9-26.

LINDSAY, J. F. (1991),"Origin and evolution of North-American cratonic basins", *S. Afr. J. Geol.*, **94(1):** 3-18.

LINDSAY, J. F. and Korsch, R. J. (1989), "Interplay of tectonics and sea-level changes in basin evolution: An example from the intracratonic Amadeus Basin, central Australia", *Basin Res.*, **2:** 3-25.

LINDSAY, J. F., Korsch, R. J. and Wilford, J. R. (1987), "Timing the breakup of a Proterozoic supercontinent: Evidence from Australian intracratonic basins", *Geology*, **15:** 1061-1064.

LITINSKY, V. A., (1989), "Concept of effective density: Key to gravity depth determinations for sedimentary basins", *Geophys.*, **54(11):** 1474-1482.

LOCZY, L. and Ladeira, E. A. (1976), "Geologia estrutural e introdução à geotectônica", *Editora Edgard Blücher, São Paulo*, 528pp.

LONGMANN, I. M. (1959), "Formulas for computing the tide acceleration due to the Moon and the Sun", *J. Geophys. Res.*, **64:** 2351-2356.

LOUP, B. and Wildi, W. (1994), "Subsidence analysis in the Paris Basin: A key to Northwest European intracontinental basins?", *Basin Res.*, **6:** 159-177.

LUGNANI, J. B. (1983), "Introdução ao Ajustamento", *Universidade Federal do Paraná, Curitiba*, 137pp.

MANTOVANI, M. S. M., Marques, L. S., De Sousa, M. A., Civetta, L., Atalla, L. and Innocenti, F. (1985), "Trace element and strontium isotope constraints on the origin and evolution of Paraná flood basalts of Santa Catarina State (Southern Brazil)", *J. Petrol.*, **26(1):** 187-209.

MARANGONI, Y. R., Assumpção, M. and Fernandes, E. P. (1995), "Gravimetria em Goiás, Brasil", *Revta. Bras. Geofís.*, **13(3):** 205-219.

MARINI, O. J. (1984), "Província Tocantins, setores central e sudeste", *In: O Pré-Cambriano do Brasil (Ed. by F. F. M. Almeida and Y. Hasui), Editora Edgard Blücher, São Paulo,* 205-264.

MCCONNELL, R. K., Mazzini, V., Marsh, C. and Winter, P.J. (1973), "An evaluation of six LaCoste & Romberg gravimeters for use on the Latin American Primary Gravity Net", *Report published by the Earth Physics Branch (Ottawa), Servicio de Hidrografia Naval (Buenos Aires) and the Hawaii Institute of Geophysics (Honolulu)-Draft,* 12pp.

MCGINNIS, L. D., Heilgold, C. P., Ervin, C. P. and Heidi, M. (1976), "The gravity field and tectonics of Illinois", *Tech. Rept. 494, Illinois State Geological Survey Circular,* 27pp.

MCKENZIE, D. (1978), "Some remarks on the development of sedimentary basins", *Earth Planet. Sci. Lett.*, **40(1):** 25-32.

MCKENZIE, D. (1984), "A possible mechanism for epeirogenic uplift", *Nature*, **307:** 616-618.

MENESES, P. T. L. (1990), "Uma nova abordagem na interpretação de anomalias gravimétricas em bacias sedimentares - exemplo da Bacia do Recôncavo, Bahia, Brasil", *MSc. Thesis, Universidade Federal do Pará,* 156pp.

MIDDLETON, T. L. (1980), "A model of intracratonic basin formation entailing deep crustal metamorphism", *Geophys. J. Royal Astron. Soc.*, **62** 1-14.

MIDDLETON, T. L. (1989), "A model for the formation of intracratonic sag basins", *Geophys. J. Royal Astron. Soc.*, **99:** 665-676.

MOLINA, E. C., Ussami, N., De Sá, N. C. and Blitzkow, D. (1989), "Interpretação dos dados gravimétricos da parte norte da bacia do Paraná", *Revta. Bras. Geoc.*, **19(2):** 187-196.

MOONEY, W. D., Andrews, M. C., Ginzsburg, A., Peters, D. A. and Hamilton, R. M.(1983), "Crustal structure of the northern Mississippi Embayment and a comparison with other continental rift zones", *Tectonophys.*, **94:** 327-348.

MORELLI, C. (1972), "The International Gravity Standardization Net 1971 - IGSN 71", *Special Report Number 4 of the Central Bureau of the I.U.G.G., Paris*, 194pp.

NARASINHA RAO, B., Ramakrishna, P. and Markandeyulu, A. (1995), "GMINV: A computer program for gravity or magnetic data inversion", *Comp. & Geosci.*, **21(2):** 301-319.

NARASINHA RAO, B., Ramakrishna, P. and Markandeyulu, A. (1996), "MAPROS - A computer program for basement mapping and filtering of gravity and magnetic data using a Hartley Transform", *Comp. & Geosci.*, **22(3):** 197-218.

NELSON, K. D. (1991), "A unified view of craton evolution motivated by recent deep seismic reflection and refraction result", *Geophys. J. Int.*, **105:** 25-35.

NETTLETON, L. L. (1976), "Gravity and magnetics in oil prospecting", *McGraw-Hill Book Co., New York*, 172pp.

NUNN, J. A. (1994), "Free thermal convection beneath intracratonic basins: Thermal and subsidence effects", *Basin Res.*, **6:** 115-130.

NUNN, J. A. and Aires, J. R. (1988), "Gravity anomalies and flexure of the lithosphere at the Middle Amazon Basin, Brazil", *J. Geophys. Res.*, **93(B1):** 415-428.

NUNN, J. A. and Sleep, N. H. (1984), "Thermal contraction and flexure of intracratonal basins: A three-dimensional study of the Michigan basin, *Geophys. J. Royal Astron. Soc.*, **76:** 587-635.

NUNN, J. A., Sleep, N. H. and Moore, W. E. (1984), "Thermal subsidence and generation of hydrocarbons in Michigan basin", *AAPG Bull.*, **68(3):** 296-315.

OLIVEIRA, L. O. A. (1989), "Aspectos da evolução termomecânica da bacia do Paraná no Brasil", *Revta. Bras. Geoc.*, **19(3):** 330-342.

PARASNIS, D. S. (1961), "Exact expressions for the gravitational attraction of a circular lamina at all points of space and of a right vertical cylinder at points external to it", *Geophys. Prosp.*, **9:** 382-398.

PAWLOWSKI, R. S. and Hansen, R. O. (1990), "Gravity anomaly separation by Wiener filtering", *Geophys.*, **55(5):** 539-548.

PEARSON, D. G., Shirey, S. B., Carlson, R. W., Boyd, F. R. and Pokhilenko, N. P. (1993), "Re-Os isotope evidence for ancient lithosphere beneath the Siberian and Kaapvaal cratons linked to crust generation", *Terra Nova*, **5:** 40.

PENNYBAKER, K. A. (1988), "Borehole gravity drift correction: A new approach", *Geophys.*, **53(10):** 1343-1346.

PEREIRA, A. J. O. and Hamza, V. M. (1991), "Fluxo geotérmico na Bacia do Parnaíba", *Annals 2nd. International Congress Brazilian Geophysical Society, Salvador*, **2:** 177-182.

PETRI, S. and Fúlfaro, V. J. (1983), "Geologia do Brasil (Fanerozóico)", *Editora Universidade de São Paulo*, 558pp.

PIPER, J. D. A. (1983), "Proterozoic paleomagnetism and single continent plate tectonics", *Geophys. J. Royal Astron. Soc.*, **74:** 163-197.

POPOFF, M. (1988), "Du Gondwana à l'Atlantique sud: Les connexions du fossé de la Bénoué avec les bassins du nord-est brésilien jusqu'á l'ouverture du golfe de Guinée au Crétace inférieur", *J. Afr. Earth Sci.*, **7:** 409-431.

PRESS, W. H., Flannery, B. P., Teukolsky, S. A. and Vetterling, W. T. (1992), "Numerical Recipes: The art of scientific computing", *Cambridge University Press, Cambridge*, 818pp.

QUINTAS, M. C. (1995), "O embasamento da Bacia do Paraná: Reconstrução geofísica de seu arcabouço", *PhD. Thesis, Universidade de São Paulo*, 213pp.

RAO, B. S. R. and Radhakrishnamurty (1966), "An expression for the gravitational attraction of a circular plate", *Indian J. Pure Appl. Phys.*, **4:** 276-278.

RAO, D. B. (1986), "Modelling of sedimentary basins from gravity anomalies with variable density contrast", *Geophys. J. Royal Astron. Soc.*, **84:** 207-212.

RAO, D. B. and Babu, N. R. (1991), "A FORTRAN-77 program for three-dimensional analysis of gravity anomalies with variable density contrast", *Comp. & Geosci.*, **17(5):** 655-667.

RICCI-LUCCHI, F. (1986), "The Oligocene to Recent foreland basins of the northern Apennines", *In: Foreland Basins (Ed. by P. A. Allen and P. Homewood), Spec. Publ. Int. Assoc. Sedimentol., Blackwell Scientific Publications, Oxford*, **8:** 105-140.

RICHARDUS, P. and Adler, R. K. (1972), "Map projections for geodesists, cartographers and geographers", *North Holland Publ. Co., Amsterdam*, 174pp.

RODRIGUES, R. (1967), "Estudo sedimentológico e estratigráfico dos depósitos silurianos e devonianos da Bacia do Parnaíba", *PETROBRÁS-DENOR Report*, 48pp.

ROWLEY, B. D. and Sahagian, D. (1986), "Depth-dependent stretching: A different approach", *Geology*, **14:** 32-35.

ROYDEN, L. and Keen, C. E. (1980), "Rifting process and thermal evolution of the continental margin of eastern Canada determined from subsidence curves", *Earth & Plan. Sci. Lett.*, **51(2):** 343-361.

SAHAGIAN, D. (1993), "Structural evolution of African basins: Stratigraphic synthesis", *Basin Res.*, **5:** 41-54.

SAHAGIAN, D. and Holland, S. M. (1993), "On the thermo-mechanical evolution of continental lithosphere", *J. Geophys. Res.*, **98(B5):** 8261-8274.

SCHOBBENHAUS, C., Campos, D. A., Derze, G. R. and Asmus, H. E. (1984), "Geologia do Brasil - Texto explicativo do mapa geológico do Brasil e da área oceânica adjacente, incluindo depósitos minerais, escala 1:2.500.000", *Departamento Nacional da Produção Mineral, Brasília (DF)*, 501pp.

SCLATER, J. G. and Christie, P. A. F. (1980),"Continental stretching: An explanation of the post Mid-Cretaceous subsidence of the central North Sea basin", *J. Geophys. Res.*, **85(B7):** 3711-3739.

SEVILLA, M. J., Gill, A. J. and Romero, P. (1990), "Adjustment of the first-order gravity net in the Iberian peninsula", *Bull. Inf. Bureau Gravimetrique International*, **66:** 21-54.

SINGH, S. K. (1977), "Gravitational attraction of a circular disc", *Geophys.*, **42(1):** 111-113.

SLEEP, N. H. (1971), "Thermal effects of the formation of Atlantic continental margins by continental break up", *Geophys. J. Royal Astron. Soc.*, **24:** 325-350.

SLEEP, N. H. and Snell, N. S. (1976), "Thermal contraction and flexure of mid-continent and Atlantic marginal basins", *Geophys. J. Royal Astron. Soc.*, **45:** 125-154.

SLEEP, N. H., Nunn, J. A. and Chou, L. (1980), "Platform basins", *Ann. Rev. Earth Planet. Sci.*, **8:** 17-34.

SLOSS, L. L. (1972), "Synchrony of Phanerozoic sedimentary-tectonics events in the North American craton and the Russian platform", *Annals 24th. International Geological Congress, Montreal*, **6:** 24-32.

STECKLER, M. S. and Watts, A. B. (1978), "Subsidence of the Atlantic-type continental margin off New York", *Earth Plan. Sci. Lett.*, **41(1):** 1-13.

STEPHENSON, R. S. (1984), "Flexural models of continental lithosphere based on the long-term erosional decay of topography", *Geophys. J. Royal Astron. Soc.*, **77:** 385-414.

THOMPSON, G. T. and Balch, S. J. (1988), "An efficient algorithm for polynomial curve fitting", *Comp. & Geosci.*, **14(5):** 547-556.

TORQUATO J. R. and Cordani, U. (1981), "Brazil-Africa geological links", *Earth-Sci. Rev.*, **17:** 155-176.

TURCOTTE D. L. (1979), "Flexure", *Advances in Geophys.*, **21:** 51-86.

TURCOTTE D. L. and Schubert, G. (1982), "Geodynamics. Application of continuum physics to geological problems", *John Wiley & Sons, New York*, 450pp.

UOTILA, U.A. (1967), "Introduction to adjustment computations with matrices", *The Ohio State University*, 84pp.

USSAMI, N (1986), "Interpretation of the gravity anomalies of Bahia State, Brazil", *Ph.D Thesis, University of Durham*, 138pp.

USSAMI, N., Karner, G. D. and Bott, M. H. P. (1986), "Crustal detachment during South Atlantic rifting and formation of Tucano-Gabon basin system", *Nature*, **322:** 629-632.

USSAMI, N., De Sá, N. C. and Molina, E. C. (1993), "Gravity map of Brazil 2. Regional and residual isostatic anomalies and their correlation with major tectonic provinces", *J. Geophys. Res.*, **98(B2):** 2199-2208.

USSAMI, N. and Padilha, A. L. (1982), "Density and magnetic susceptibility measurements of crystalline rocks of Bahia State", *unpublished report, Instituto Astronômico e Geofísico, Universidade de São Paulo*, 21pp.

VAIL, P. R., Mitchum, R. M. Jr. and Thompson, S. (1977), "Seismic stratigraphy and global changes of sea level, Part 4: Global cycles of relative changes of sea level", *In: Seismic Stratigraphy - Applications to Hydrocarbon Exploration (Ed. by C. E. Payton), Am. Assoc. Petrol. Geol. Mem.*, **26:** 83-97.

WALCOTT, R. I. (1970), "Flexural rigidity, thickness and viscosity of the lithosphere", *J. Geophys. Res.*, **75:** 3941-3954.

WATTS, A. B. (1992), "The effective elastic thickness of the lithosphere and the evolution of foreland basins", *Basin Res.*, **4:** 169-178.

WATTS, A. B., Karner, G. D. and Steckler, M. S. (1982), "Lithospheric flexure and the evolution of sedimentary basins", *Phil. Trans. Royal Soc.*, **A305:** 249-281.

WILLET, S. D., Chapman, D. S. and Neugebauer, H. J. (1985), "A thermo-mechanical model of continental lithosphere", *Nature*, **314:** 520-523.

WOOLLARD, G. P., Black, W. A. and Bonini, W. E. (1954), "World gravity measurements 1952-1954", *Woods Hole Oceanographic Institution, Technical Report Reference 54-53*, 128pp.

XIA, J. and Sprowl, D. R. (1995), "Moho depths in Kansas from gravity inversion assuming exponential density contrast", *Comp. & Geosci.*, **21(2):** 237-244.

YOUNG, T. L. and Van Woert, M. L. (1990), "PLOT88 - Software library reference manual", *Plotworks, Inc.*, 342pp.

ZENG, H. (1989), "Estimation of the degree of polynomial fitted to gravity anomalies and its application", *Geophys. Prospec.*, **37:** 959-973.

COEFF.FOR

```
      PROGRAM COEFF
C
C     This program computes upward continuation coefficients C(k, n) as
C     appears in equation 6.12 of Baranov (1975).
C
      PARAMETER(M = 10, PI = 3.141592654, DOPIDO = 19.7392088,
     &          DELTA = .001)
      CHARACTER COEFFNAME * 5
      REAL C(-M:M, -M:M)
      COMMON / KNUZ / K, N, U, Z
      EXTERNAL FUNCAO
      WRITE(*, *) 'Program COEFF.FOR.  Execution begins.'
      WRITE(*, '(A\)')
     &      ' Enter number of units for upward continuation: '
      READ(*, '(A5)') COEFFNAME
      READ(COEFFNAME(1:5), '(F5.3)') Z
      OPEN(1, FILE = COEFFNAME)
      WRITE(1, *) '              Upward continuation coefficients'
      WRITE(1, '(''Z = '', F5.3, '' Unit(s), Order = '', I2,
     &     '' Delta = '', F4.3)') Z, M, DELTA
      WRITE(*, *)
      DO K = 0, M
        DO N = K, M
          DO U = -1., 1., DELTA
            CALL QROMB(FUNCAO, 0., PI, SS)
            C(K, N) = C(K, N) + SS * DELTA
          END DO
          C(K, N) = C(K, N) / DOPIDO
          C(N, K) = C(K, N)
          WRITE(*, '(''+Computation finished for (k, n) = ('', I2,
     &          '', '', I2, '')'')') K, N
        END DO
      END DO
      DO K = -M, -1
        DO N = -M, 0
          C(K, N) = C(-K, -N)
        END DO
      END DO
      DO K = -M, 0
        DO N = 1, M
          C(K, N) = C(-K, N)
        END DO
      END DO
      DO K = 0, M
        DO N = -M, -1
          C(K, N) = C(K, -N)
        END DO
      END DO
      SOMA = 0.
      DO K = -M, M
        DO N = -M, M
          SOMA = SOMA + C(K, N)
        END DO
      END DO
      WRITE(1, '(''Non-normalized sum of all coefficients = '',
     &     F3.2)') SOMA
      EPSILON = (1. - SOMA) / 80.
      WRITE(*, '('' Amount to be added to the last coefficients: '',
     &     F8.6)') EPSILON
      DO I = -M, M
        C(I, M) = C(I, M) + EPSILON
        C(I, -M) = C(I, -M) + EPSILON
      END DO
      DO I = -(M - 1), M - 1
        C(M, I) = C(M, I) + EPSILON
```

```
      C(-M, I) = C(-M, I) + EPSILON
    END DO
    SOMA = 0.
    DO K = -M, M
      DO N = -M, M
        SOMA = SOMA + C(K, N)
      END DO
    END DO
    WRITE(1, '(21(F8.6, 1X))')((C(K, N), K = -M, M), N = -M, M)
    WRITE(1, '(''Normalized sum of all coefficients = '', F6.4)')
   &    SOMA
    STOP
    END
C
    SUBROUTINE QROMB(FUNCAO, A, B, SS)
    PARAMETER(EPS = 1.E-3, JMAX = 30, JMAXP = JMAX + 1, K = 5,
   &       KM = K - 1)
    EXTERNAL FUNCAO
    REAL S(JMAXP), H(JMAXP)
    H(1) = 1.
    DO J = 1, JMAX
      CALL TRAPZD(FUNCAO, A, B, S(J), J)
      IF(J .GE. K) THEN
        CALL POLINT(H(J - KM), S(J - KM), K, 0., SS, DSS)
        IF(ABS(DSS) .LT. EPS * ABS(SS)) RETURN
      END IF
      S(J + 1) = S(J)
      H(J + 1) = .25 * H(J)
    END DO
    PAUSE 'Convergence not reached after 30 iterations!'
    END
C
C*******************************************************************
C
    SUBROUTINE TRAPZD(FUNCAO, A, B, S, N)
    EXTERNAL FUNCAO
    IF(N .EQ. 1) THEN
      S = .5 * (B - A) * (FUNCAO(A) + FUNCAO(B))
      IT = 1
    ELSE
      TNM = IT
      DEL = (B - A) / TNM
      X = A + .5 * DEL
      SUM = 0.
      DO I = 1, IT
        SUM = SUM + FUNCAO(X)
        X = X + DEL
      END DO
      S = .5 * (S + (B - A) * SUM / TNM)
      IT = 2 * IT
    END IF
    RETURN
    END
C
C*******************************************************************
C
    FUNCTION FUNCAO(ALFA)
    COMMON / KNUZ / K, N, U, Z
    FUNCAO = EXP(-ALFA * Z * SQRT(1. + U ** 2)) * ALFA *
   &       (COS((K + N * U) * ALFA) + COS((K * U + N) * ALFA))
    RETURN
    END
C
C*******************************************************************
C
    SUBROUTINE POLINT(XA, YA, N, X, Y, DY)
    PARAMETER(NMAX = 10)
    REAL XA(N), YA(N), C(NMAX), D(NMAX)
    NS = 1
    DIF = ABS(X - XA(1))
    DO I = 1, N
      DIFT = ABS(X - XA(I))
```

```
      IF(DIFT .LT. DIF) THEN
        NS = I
        DIF = DIFT
      END IF
      C(I) = YA(I)
      D(I) = YA(I)
    END DO
    Y = YA(NS)
    NS = NS - 1
    DO M = 1, N - 1
      DO I = 1, N - M
        HO = XA(I) - X
        HP = XA(I + M) - X
        W = C(I + 1) - D(I)
        DEN = HO - HP
        IF(DEN .EQ. 0.) PAUSE
        DEN = W / DEN
        D(I) = HP * DEN
        C(I) = HO * DEN
      END DO
      IF(2 * NS .LT. N - M) THEN
        DY = C(NS + 1)
      ELSE
        DY = D(NS)
        NS = NS - 1
      END IF
      Y = Y + DY
    END DO
    RETURN
    END
```

STRIPP.FOR

```
      PROGRAM STRIPP
C
C     This program performs backstripping analysis of wells
C     according to a local loading model and an exponential
C     dependence of sediments porosity upon depth.
C     Reference: Allen & Allen (1990).
C
      PARAMETER(N = 30, ROW = 1.03, ROSEDG = 2.68, ROM = 3.33,
     &        THOUSAND = 1000.)
      REAL LNPORO(14), AGE(N), Z(N, 0:N - 1), ZSED(N), X(N), S(N),
     &   TSR(N), ZTEC(N), DENS(14), DEPTH(14), POROS(14), TIMES(N),
     &   ERODED(N), TIMEGAP(N)
      CHARACTER WELL * 10, FNAME * 2, R, CODIGO(N) / N * ' ' /
      DATA DENS / 2.2, 2.234, 2.254, 2.362, 2.39, 2.467, 2.496,
     &   2.508, 2.548, 2.59, 2.595, 2.473, 2.665, 2.463 /,
     &   DEPTH / .156, .3595, .4525, .526, .6755, .989, 1.3665,
     &   1.5865, 1.7515, 2.0615, 2.29, 2.444, 2.6145, 2.7595 /,
     &   YL / 200000. /, YC / 35000. /, DIFF / .8 /,
     &   PI / 3.141592645E0 /, ROMAST / 3.3 /, ROCAST / 2.8 /,
     &   TM / 1330. / ALPHAV / 3.E-5 /, X / N * 0./,
     &   ZTEC / N * 0. /, Z / N * N * 0. /
      COMMON / POROSITY / F0, C, F0C, EPSILON
      OPEN(6, FILE = 'PRN')
      EPSILON = .00001
      WRITE(*, '(5(/),
     &'' ***              Program STRIPP.FOR. Execution begins.
     &   ***'', 5(/))')
      TAU = (YL ** 2 / (PI ** 2 * DIFF)) / (365. * 24. * 3600.)
      DO I = 1, 14
        POROS(I) = (ROSEDG - DENS(I)) / (ROSEDG - ROW)
        LNPORO(I) = LOG(POROS(I))
        DEPTH(I) = DEPTH(I) - DEPTH(1)
      END DO
      CALL MEDFIT(DEPTH, LNPORO, 14, F0, C, DEV)
      F0 = EXP(F0)
      F0C = -F0 / C
   10 WRITE(*, *) 'Enter file name with borehole data: '
      READ(*, '(A2)') FNAME
      OPEN(1, FILE = 'C:\PARNAIBA\' // FNAME // '.DAT')
```

```
      OPEN(2, FILE = 'C:\PARNAIBA\' // FNAME // '.STR')
      READ(1, '(A10)') WELL
      WRITE(2, '(''*** Results computed for well '', A10, '' ***''/)')
     &    WELL
      WRITE(6, '(''1'', 5(/), 16X, ''*** Results computed for well '',
     &    A10, '' ***''///)') WELL
C
C     Reading input data file.
C
      DO I = 1, N
        READ(1, '(13X, F5.3, 1X, 2F3.0, 1X, A1)', END = 20) Z(I, 0),
     &     AGE(I), TIMEGAP(I), CODIGO(I)
      END DO
   20 M = I - 1
      DO I = 1, M
        IF(I .EQ. 1) AUX = Z(1, 0)
        Z(I, 0) = -(Z(I, 0) - AUX)
      END DO
      CLOSE(1)
      WRITE(*, '('' File  C:\PARNAIBA\'', A2, ''.DAT holds '', I2,
     &     '' data values for well '', A11)') FNAME, M, WELL // '.'
C
C     Computes Zsed and Ztec at T = T(2) (usually age of top of
C     Itapecuru Formation.
C
      ROMED =  ROSEDG - FOC * (ROSEDG - ROW) * (1. - EXP(C * Z(M, 0)))
      ZSED(2) = Z(M, 0)
      ZTEC(2) = ZSED(2) * (ROM - ROMED) / (ROM - ROW)
      TIMES(2) = AGE(1)
      SEDRATE = Z(M, 0) / AGE(M)
      ERODED(1) = (TIMEGAP(1) * SEDRATE) / 2.
      WRITE(*, '(
     &'' Robust regression of porosity on depth {F = Fo exp(-Cz)}:'',
     &/'' Fo = '', F8.6, '', C = '', F8.6, ''/km''/
     &'' Erosion estimate at this site: '', F5.3, '' km''/
     &'' Sedimentation rate: '', F4.1, '' m/My'')') FO, -C,
     &ERODED(1), SEDRATE * THOUSAND
      WRITE(6, '(
     &''        Robust regression of porosity on depth {F = Fo exp(-Cz)
     &}:''/''        Fo = '', F8.6, '', C = '', F8.6, ''/km''/
     &''        Erosion estimate at this site: '', F5.3, '' km''/
     &''        Sedimentation rate: '', F4.1, '' m/My''//)') FO, -C,
     &ERODED(1), SEDRATE * THOUSAND
C
C     Computes Zsed and Ztec at time T = T(1) = 0 Ma (adds the assumed
C     erosion of the first layer and compacts the whole sediment column).
C
      CALL NEWDEPTH(Z(M, 0), 0., ERODED(1), ZBOTTOM, 1)
      ROMED = ROSEDG - FOC * (ROSEDG - ROW) * (1. - EXP(C * ZBOTTOM))
      ZSED(1) = ZBOTTOM
      ZTEC(1) = ZSED(1) * (ROM - ROMED) / (ROM - ROW)
      TIMES(1) = AGE(1) - TIMEGAP(1)
C
C     Sequentially backstripps sediments from layer 2 (usually Codo') downwar-
ds.
C
      J = 2
      KSTART = 3
      DO L = 1, M - 2
        DO K = KSTART, M
          IF(CODIGO(K) .EQ. 'V') THEN
            Z(K, L) = Z(K, L - 1) - Z(K - 1, L - 1)
            CYCLE
          END IF
          CALL NEWDEPTH(Z(K, L - 1), Z(K - 1, L - 1), Z(K - 1, L),
     &        Z(K, L), K)
        END DO
        ROMED = ROSEDG - FOC * (ROSEDG - ROW) * (1. - EXP(C *
     &        Z(M, L)))
        J = J + 1
        ZSED(J) = Z(M, L)
        ZTEC(J) = ZSED(J) * (ROM - ROMED) / (ROM - ROW)
```

```
      TIMES(J) = AGE(KSTART - 1)
C
C     Should erosion ocurrs...
C     Adds the eroded part of the layer alowing compaction of layers beneath
C     and assigns an age T = T(i) - Time gap(i).
C
      IF(TIMEGAP(KSTART - 1) .NE. 0.) THEN
        ERODED(KSTART - 1) = (TIMEGAP(KSTART - 1) * SEDRATE) / 2.
        ZZ = Z(M, L)
        CALL NEWDEPTH(Z(M, L), 0., ERODED(KSTART - 1), ZBOTTOM,
     &       KSTART)
        ROMED = ROSEDG - FOC * (ROSEDG - ROW) * (1. - EXP(C *
     &          ZBOTTOM))
        AUXZSED = ZBOTTOM
        AUXZTEC = AUXZSED * (ROM - ROMED) / (ROM - ROW)
        AUXTIMES = TIMES(J) - TIMEGAP(KSTART - 1)
        J = J + 1
        ZSED(J) = ZSED(J - 1)
        ZTEC(J) = ZTEC(J - 1)
        TIMES(J) = TIMES(J - 1)
        ZSED(J - 1) = AUXZSED
        ZTEC(J - 1) = AUXZTEC
        TIMES(J - 1) = AUXTIMES
      END IF
      KSTART = KSTART + 1
     END DO
C
C     At time T = T(M) = 450 Ma there are no total and tectonic
C     subsidences.
C
     J = J + 1
     TIMES(J) = 450.
     ZSED(J) = 0.
     ZTEC(J) = 0.
C
C     Starts computing BETA for McKenzie's uniform stretching model.
C     Reference: Allen & Allen (1990).
C
     DO I = 1, J
        TSR(I) = TIMES(I) - 450.
        X(I) = 1. - EXP(TSR(I) / TAU)
     END DO
     CALL MEDFIT(X, ZTEC, J, B, A, DEV)
     E0 = (.004 * YL * ROMED * ALPHAV * TM) / (PI ** 2 *
     &    (ROMAST - ROMED))
     ZZ = 2.
     DIF = 1.
     DO WHILE (DIF .GE. EPSILON)
       ZZZ = ZZ - ((SIN(ZZ) / ZZ) * E0 - A) / ((E0 / ZZ) * (COS(ZZ) -
     &       SIN(ZZ) / ZZ))
       DIF = ABS(ZZZ - ZZ)
       ZZ = ZZZ
       ITER = ITER + 1
       IF(ITER .GT. 10) THEN
         WRITE(*, '('' Convergence not reached after 10 iterations! Che
     &ck input data for BETA.''/)')
         STOP
       END IF
     END DO
     BETA = PI / ZZ
     WRITE(*, '('' BETA computed after'', I2, '' iteration(s): '',
     &    F4.2, /)') ITER, BETA
     ZS = .001 * YL * (1. - 1. / BETA) * ((ROMAST - ROCAST) * (YC /
     &    YL) * (1. - ALPHAV * (TM / 2.) * (YC / YL)) - ALPHAV *
     &    (TM / 2.) * ROMAST) / (ROMAST * (1. - ALPHAV * TM) -
     &    ROMED)
     DO I = 1, J
       S(I) = E0 * (BETA / PI) * SIN(PI / BETA) * X(I)
     END DO
C
C     Starts printing results for this particular well.
C
```

```
      WRITE(2, '(
     &'' Robust regression of porosity on depth {F = Fo exp(-Cz)}:'',
     &/'' Fo = '', F8.6, '', C = '', F8.6, '' km-1''/
     &'' Erosion estimate at this site: '', F5.3, '' km.''/
     &'' Sedimentation rate: '', F4.1, '' m/My'')') FO, -C,
     &ERODED(1), SEDRATE * THOUSAND
      WRITE(2, '('' #  Age   Zsed   Ztec    St Erosion  Tsr'')')
      WRITE(2, '(I3, 2X, I3, 2X, F6.3, 2X, F6.3, 2X, F6.3, 2X, F6.3,
     &2X, I4)') (I, NINT(TIMES(I)), ZSED(I), ZTEC(I), S(I), ERODED(I),
     &NINT(TSR(I)), I = 1, J)
      WRITE(2, '(/''Time constant: '', I3, '' My, Eo: '', F6.3,
     &     '' km'')') NINT(TAU), EO
      WRITE(2, '(''Beta: '', F4.2, '', Zs: '', F4.2,'' km'')') BETA, ZS
      WRITE(6, '(12X, ''#  Age   Zsed   Ztec    St Erosion  Tsr'')
     &')
      WRITE(6, '(10X, I3, 2X, I3, 2X, F6.3, 2X, F6.3, 2X, F6.3, 2X, F6.3
     &, 2X, I4)') (I, NINT(TIMES(I)), ZSED(I), ZTEC(I), S(I), ERODED(I),
     &NINT(TSR(I)), I = 1, J)
      WRITE(6, '(//9X, ''Time constant: '', I3, '' My, Eo: '', F6.3,
     &     '' km''/9X, ''Beta: '', F4.2, '', Zs: '', F4.2,'' km'')')
     &     NINT(TAU), EO, BETA, ZS
C
C   For Serra Grande Group.
C
      BEGIN = 410.
      END = 450.
      CALL INTLIN(J, TIMES, ZSED, BEGIN, YSED2)
      DSTOT1 = (YSED2 - ZSED(J)) * THOUSAND / (END - BEGIN)
      CALL INTLIN(J, TIMES, ZTEC, BEGIN, YTEC2)
      DSTEC1 = (YTEC2 - ZTEC(J)) * THOUSAND / (END - BEGIN)
      WRITE(2, '(/''Stratigraphic  Total Subsidence Tectonic Subsidence'
     &'/4X, ''Group          Rate (m/My)       Rate (m/My)''/
     &''Serra Grande'', 9X, F4.1, 12X, F4.1)') DSTOT1, DSTEC1
      WRITE(6, '(//9X, ''Stratigraphic  Total Subsidence Tectonic Subsid
     &ence''/13X, ''Group          Rate (m/My)       Rate (m/My)''/
     &9X, ''Serra Grande'', 9X, F4.1, 14X, F4.1)') DSTOT1, DSTEC1
C
C   For Caninde' Group.
C
      BEGIN = 300.
      END = 385.
      CALL INTLIN(J, TIMES, ZSED, END, YSED1)
      CALL INTLIN(J, TIMES, ZSED, BEGIN, YSED2)
      DSTOT2 = (YSED2 - YSED1) * THOUSAND / (END - BEGIN)
      CALL INTLIN(J, TIMES, ZTEC, END, YTEC1)
      CALL INTLIN(J, TIMES, ZTEC, BEGIN, YTEC2)
      DSTEC2 = (YTEC2 - YTEC1) * THOUSAND / (END - BEGIN)
      WRITE(2, '(''  Caninde'', 12X, F4.1, 12X, F4.1)') DSTOT2, DSTEC2
      WRITE(6, '(11X, ''Caninde'', 12X, F4.1, 14X, F4.1)')
     &     DSTOT2, DSTEC2
C
C   For Balsas Group.
C
      END = 310.
      CALL INTLIN(J, TIMES, ZSED, END, YSED1)
      CALL INTLIN(J, TIMES, ZTEC, END, YTEC1)
      IF(215. .GE. TIMES(1)) THEN
        BEGIN = 215.
        CALL INTLIN(J, TIMES, ZSED, BEGIN, YSED2)
        DSTOT3 = (YSED2 - YSED1) * THOUSAND / (END - BEGIN)
        CALL INTLIN(J, TIMES, ZTEC, BEGIN, YTEC2)
        DSTEC3 = (YTEC2 - YTEC1) * THOUSAND / (END - BEGIN)
        WRITE(2, '(''  Balsas'', 13X, F4.1, 12X, F4.1)') DSTOT3, DSTEC3
        WRITE(6, '(11X, ''Balsas'', 13X, F4.1, 14X, F4.1)')
     &     DSTOT3, DSTEC3
      ELSE
        YSED2 = ZSED(1)
        YTEC2 = ZTEC(1)
        DSTOT3 = (YSED2 - YSED1) * THOUSAND / (END - BEGIN)
        DSTEC3 = (YTEC2 - YTEC1) * THOUSAND / (END - BEGIN)
        WRITE(2, '(''  Balsas    '', 9X, F4.1, 12X, F4.1)') DSTOT3,
     &     DSTEC3
```

```
      WRITE(6, '(14X, "Balsas", 13X, F4.1, 14X, F4.1)')
     &      DSTOT3, DSTEC3
     END IF
C
C    For Mearim Group.
C
     END = 180.
     IF(145. .GE. TIMES(1)) THEN
       BEGIN = 145.
       CALL INTLIN(J, TIMES, ZSED, END, YSED1)
       CALL INTLIN(J, TIMES, ZSED, BEGIN, YSED2)
       DSTOT4 = (YSED2 - YSED1) * THOUSAND / (END - BEGIN)
       CALL INTLIN(J, TIMES, ZTEC, END, YTEC1)
       CALL INTLIN(J, TIMES, ZTEC, BEGIN, YTEC2)
       DSTEC4 = (YTEC2 - YTEC1) * THOUSAND / (END - BEGIN)
       WRITE(2, '("  Mearim", 13X, F4.1, 12X, F4.1)') DSTOT4,
     &       DSTEC4
       WRITE(6, '(11X, "Mearim", 13X, F4.1, 14X, F4.1)')
     &      DSTOT4, DSTEC4
     ELSE IF(END .GE. TIMES(1)) THEN
       YSED2 = ZSED(1)
       YTEC2 = ZTEC(1)
       CALL INTLIN(J, TIMES, ZSED, END, YSED1)
       DSTOT4 = (YSED2 - YSED1) * THOUSAND / (END - BEGIN)
       CALL INTLIN(J, TIMES, ZTEC, END, YTEC1)
       DSTEC4 = (YTEC2 - YTEC1) * THOUSAND / (END - BEGIN)
       WRITE(2, '("  Mearim", 13X, F4.1, 12X, F4.1)') DSTOT4, DSTEC4
       WRITE(6, '(11X, "Mearim", 13X, F4.1, 14X, F4.1)')
     &      DSTOT4, DSTEC4
     ELSE
       WRITE(2, '("  Mearim", 7X, "Not drilled")')
       WRITE(6, '(11X, "Mearim", 7X, "Not drilled")')
     END IF
     CLOSE(2)
C
C    Calls PLOT88 graphics lybrary.
C
     ZTEC(J + 1) = 4.
     ZTEC(J + 2) = -.5
     ZSED(J + 1) = 4.
     ZSED(J + 2) = -.5
     S(J + 1) = 4.
     S(J + 2) = -.5
     TIMES(J + 1) = 450.
     TIMES(J + 2) = -50.
     CALL PLOTS(0, 97, 97)
     CALL WINDOW(-.3, -.3, 10., 10.)
     CALL FACTOR(.9)
     CALL COMPLX
     CALL PLOT(.5, 1., -3)
     CALL STAXIS(.15, .18, .13, .05, 0)
     CALL AXIS(0., 0., 'Age (Ma)', -8, -9., 0., TIMES(J + 1),
     &        TIMES(J + 2))
     CALL STAXIS(.15, .18, .13, .05, 1)
     CALL AXIS(0., 0., 'Depth to basement (km)', 22, -8., 90.,
     &        ZSED(J + 1), ZSED(J + 2))
     CALL STAXIS(.001, .001, .001, .05, 0)
     CALL AXIS(0., 8., ' ', -0, -9., 0., TIMES(J + 1), TIMES(J + 2))
     CALL AXIS(9., 0., ' ', -0, 8., 90., ZSED(J + 1), ZSED(J + 2))
     CALL COLOR(14, IERRO)
     CALL STLINE(1, .05, 0.)
     CALL LINE(TIMES, ZSED, J, 1, 1, 3)
     CALL COLOR(12, IERRO)
     CALL LINE(TIMES, ZTEC, J, 1, 1, 3)
     CALL COLOR(13, IERRO)
     CALL LINE(TIMES, S, J, 1, 1, 5)
     CALL COLOR(0, IERRO)
     CALL SYMBOL(3., 8.2, .18, 'Local loading model', 0., 19)
     IF(FNAME .EQ. 'BC' .OR. FNAME .EQ. 'bc') THEN
       CALL SYMBOL
     &(9.8, 8., .18, 'Figure 5.8 - Total (St), tectonic (S*) and',
     &          -90., 42)
```

```
      CALL SYMBOL
    &(9.5, 8., .18, 'uniform stretching (S*`) subsidence curves.',
    &-90., 43)
     ELSE
      CALL SYMBOL(9.8, 8., .18,
    &'Figure 5.8 (cont.) - Total (St), tectonic (S*)', -90., 46)
      CALL SYMBOL(9.5, 8., .18,
    &'and uniform stretching (S*`) subsidence curves.', -90., 47)
     END IF
     CALL SYMBOL(-(TIMES(J + 1) - TIMES(1)) / TIMES(J + 2) - .5,
    &          -(ZSED(J + 1) - ZSED(1)) / ZSED(J + 2) - .3,
    &          .15, 'St', 0., 2)
     CALL SYMBOL(-(TIMES(J + 1) - TIMES(1)) / TIMES(J + 2) - .5,
    &          -(ZTEC(J + 1) - ZTEC(1)) / ZTEC(J + 2) - .3,
    &          .15, 'S*', 0., 2)
     CALL SYMBOL(-(TIMES(J + 1) - TIMES(1)) / TIMES(J + 2) - .5,
    &          -(S(J + 1) - S(1)) / S(J + 2) + .2,
    &          .15, 'S*`', 0., 3)
     CALL SYMBOL(-.5, -1., .15,
    &    'Backstripping curves for well: ', 0., 31)
     CALL SYMBOL(999., 999., .15, WELL, 0., 12)
     CALL SYMBOL(999., 999., .15, ', Tau: ', 0., 7)
      CALL NUMBER(999., 999., .15, TAU, 0., -1)
     CALL SYMBOL(999., 999., .15, ' My, Beta: ', 0., 11)
     CALL NUMBER(999., 999., .15, BETA, 0., 2)
     CALL SYMBOL(999., 999., .15, '.', 0., 1)
     CALL PLOT(0., 0., 999)
     WRITE(*, '(/A\)') ' Another well (Y/N)? '
     READ(*, '(A1)') R
     SELECT CASE(R)
     CASE('Y', 'y')
       DO I = 1, N
         AGE(I) = 0.
         ERODED(I) = 0.
         TIMEGAP(I) = 0.
         CODIGO(I) = ' '
         DO J = 0, N - 1
           Z(I, J) = 0.
         END DO
       END DO
       ITER = 0
       GO TO 10
     END SELECT
     CLOSE(6)
     WRITE(*, *) 'Program executed.'
     STOP
     END
C
      SUBROUTINE MEDFIT(X, Y, NDATA, A, B, ABDEV)
C
C     Fitsa Y = A + B * X on the criterion of minimum absolute deviation.
C     Vectors X and Y of length NDATA are the experimental input data.
C     Coefficients A and B are then computed as well as ABDEV which is
C     the mean absolute deviation (in y) of the experimental points
C     relative to the fitted straight line. The subroutine uses function
C     ROFUNC communicating through a commom block.
C
      PARAMETER(NMAX = 30)
      EXTERNAL ROFUNC
      COMMON /ARRAYS/ NDATAT, XT(NMAX), YT(NMAX), ARR(NMAX), AA, ABDEVT
      REAL X(NDATA), Y(NDATA)
      SX = 0.
      SY = 0.
      SXY = 0.
      SXX = 0.
      DO J = 1, NDATA
        XT(J) = X(J)
        YT(J) = Y(J)
        SX = SX + X(J)
        SY = SY + Y(J)
        SXY = SXY + X(J) * Y(J)
        SXX = SXX + X(J) ** 2
```

```
      END DO
      NDATAT = NDATA
      DEL = REAL(NDATA) * SXX - SX ** 2
      AA = (SXX * SY - SX * SXY) / DEL
      BB = (REAL(NDATA) - SX * SY) / DEL
      CHISQ = 0.
      DO J = 1, NDATA
        CHISQ = CHISQ +(Y(J) -(AA + BB * X(J))) ** 2
      END DO
      SIGB = SQRT(CHISQ / DEL)
      B1 = BB
      F1 = ROFUNC(B1)
      B2 = BB + SIGN(3. * SIGB, F1)
      F2 = ROFUNC(B2)
   30 IF(F1 * F2 .GT. 0.) THEN
        BB = 2. * B2 - B1
        B1 = B2
        F1 = F2
        B2 = BB
        F2 = ROFUNC(B2)
        GO TO 30
      END IF
      SIGB = 0.01 * SIGB
   40 IF(ABS(B2 - B1) .GT. SIGB) THEN
        BB = 0.5 * (B1 + B2)
        IF(BB .EQ. B1 .OR. BB .EQ. B2) GO TO 50
        F = ROFUNC(BB)
        IF(F * F1 .GE. 0.) THEN
          F1 = F
          B1 = BB
        ELSE
          F2 = F
          B2 = BB
        END IF
        GO TO 40
      END IF
   50 A = AA
      B = BB
      ABDEV = ABDEVT / REAL(NDATA)
      RETURN
      END
C
      FUNCTION ROFUNC(B)
C
C      Computes the right side of equation 14.6.16 (Press et alli, 1982)
C      for a given B.
C
      PARAMETER(NMAX = 30)
      COMMON /ARRAYS/ NDATA, X(NMAX), Y(NMAX), ARR(NMAX), AA, ABDEV
      N1 = NDATA + 1
      NML = N1 / 2
      NMH = N1 - NML
      DO J = 1, NDATA
        ARR(J) = Y(J) - B * X(J)
      END DO
      CALL SORT(NDATA, ARR)
      AA = 0.5 * (ARR(NML) + ARR(NMH))
      SUM = 0.
      ABDEV = 0.
      DO J = 1, NDATA
        D = Y(J) -(B * X(J) + AA)
        ABDEV = ABDEV + ABS(D)
        SUM = SUM + X(J) * SIGN(1., D)
      END DO
      ROFUNC = SUM
      RETURN
      END
C
C*****************************************************************************
C
      SUBROUTINE NEWDEPTH(X, Y, Z, W, LAYER)
      COMMON / POROSITY / F0, C, F0C, EPSILON
```

```
      ITER = 1
      WO = X
      DIF = 1.
      DO WHILE (DIF .GE. EPSILON)
       W = WO - (WO +  FOC * EXP(C * WO) - (X - Y + Z - FOC *
     &     (EXP(C * Y) - EXP(C * X) - EXP(C * Z)))) / (1. - FO *
     &     EXP(C * WO))
       DIF = ABS(W - WO)
       WO = W
       ITER = ITER + 1
       IF(ITER .GT. 10) THEN
        WRITE(*, '(/'' Convergence not reached after 10 iterations!''/
     &)')
        WRITE(*, '('' Check these data:''/'' X = '', F10.3,
     &        '' Y = '', F10.3, '' Z = '', F10.3, '' W = '', F10.3,
     &        '' WO = '', F10.3/'' Layer: '', I2)')
     &        X, Y, Z, W, WO, LAYER
        STOP
       END IF
      END DO
      RETURN
      END
```